Mississippi River Plume Hydrography:
Second Annual Report

Mississippi River Plume Hydrography: Second Annual Report

Editors

Stephen P. Murray
Jami Donley

Published by

DISCLAIMER

This report was prepared under contract between the Minerals Management Service (MMS) and Louisiana State University. This report has been technically reviewed by the MMS and approved for publication. Approval does not signify that the contents necessarily reflect the views and policies of the Service nor does mention of trade names or commercial products constitute endorsement or recommendation for use. It is however, exempt from review and compliance with MMS editorial standards.

REPORT AVAILABILITY

Extra copies of the report may be obtained from the Public Information Office (MS 5034) at the following address:

U.S. Department of the Interior
Minerals Management Service
Public Information Office (MS 5034)
Gulf of Mexico OCS Region
1201 Elmwood Park Boulevard
New Orleans, Louisiana 70123-2394

Telephone Number: (504) 736-2519 or
1-800-200-GULF

CITATION

PRINCIPAL INVESTIGATORS AND KEY PERSONNEL

Remote Sensing and Image Processing
Nan D. Walker, Coastal Studies Institute, LSU, Baton Rouge, LA
Lawrence J. Rouse, Jr., Coastal Studies Institute, LSU, Baton Rouge, LA
Oscar K. Huh, Coastal Studies Institute, LSU, Baton Rouge, LA

Hydrographic Survey
Stephen P. Murray, Coastal Studies Institute, LSU, Baton Rouge, LA
Curtis C. Ebbesmeyer, Evans-Hamilton, Inc., Seattle, WA
Neal Pettigrew, Department of Oceanography, University of Maine, Orono, ME

Sediment Flux
Wilford D. Gardner, Department of Oceanography, Texas A&M, College Station, TX
Mary Jo Richardson. Department of Oceanography, Texas A&M, College Station, TX

Benthic Boundary Layer
L. Don Wright, School of Marine Science, VIMS, College of William & Mary,
    Gloucester Point, VA
R. W. Sternberg, School of Oceanography, University of Washington, Seattle, WA
C. Sherwood, Battelle Marine Sciences Laboratory, Sequim, WA

Light and Nutrients
R. Eugene Turner, Coastal Ecology Institute, LSU, Baton Rouge, LA

Hypoxia and Pigments
Nancy Rabalais, Louisiana Universities Marine Consortium, Cocodrie, LA

Phytoplankton
Quay Dortch, Louisiana Universities Marine Consortium, Cocodrie, LA

Zooplankton
Richard F. Shaw, Coastal Fisheries Institute, LSU, Baton Rouge, LA

Pollutant Chemistry
Jay C. Means, Aquatic Toxicology Laboratory, School of Veterinary Medicine,
    LSU, Baton Rouge, LA
Debra J. McMillin, Aquatic Toxicology Laboratory, School of Veterinary Medicine,
    LSU, Baton Rouge, LA

Data Management
Mary L. White, Coastal Ecology Institute, LSU, Baton Rouge, LA

Program Management
Stephen P. Murray, Coastal Studies Institute, LSU, Baton Rouge, LA

Field Logistics
Rodney Fredericks, Coastal Studies Institute, LSU, Baton Rouge, LA

TABLE OF CONTENTS

LIST OF FIGURES

LIST OF TABLES

I. INTRODUCTION

The Mississippi River plume Hydrography study (LATEX B) is part of a larger Louisiana-Texas Physical Oceanography Program, which began in October 1991. The overall objective of our study is to determine the fundamental aspects of the velocity structure, volume and sediment flux, pollutant chemistry, and biological characteristics in the coastal plume arising from the discharge of the Mississippi and Atchaflaya Rivers. This report covers LATEX B Cruise III (April 1993) and Cruise IV (July 1994). Figure 1 shows the LATEX study area.

Satellite images and observations of the hydrographic and current regimes of the coastal waters from the Mississippi Delta west and south to the Texas-Mexico border indicate the presence of a brackish water, turbid plume emanating from the discharge of the Atchafalaya-Mississippi Rivers. This plume is strongly modulated and even reversed by the annual cycle of the winds from Louisiana to south Texas. The coastal current formed by this plume is locally influenced by turbid, low salinity outflow plumes from major coastal bays (Sabine and Calcasieu Lakes and Galveston Bay). Intense northerly wind events associated with frontal passages in late fall, winter, and early spring apparently completely disrupt the Atchafalaya source of the coastal current and its dissolved and suspended sediment particulate load. The Mississippi-Atchafalaya River system typically has a peak discharge in April in excess of 30,000 m^3/s and a low in September to October of about 10,000 m^3/s.

These river discharges, mixing with seawater and spreading sediment over the continental shelf, create a region of altered (lowered) salinities and temperatures, a seaward sloping pressure gradient, and a resulting mosaic of water masses and fronts in the estuarine, inshore, and continental shelf areas of the LATEX region. Inner shelf distribution of waters and sediments results from the interaction of momentum, buoyancy forces, winds, waves, longshore currents, and pressure gradients (sea surface slope and density gradients). These runoff-altered shelf waters, loosely referred to as the coastal current are in fact a complex of river and estuarine discharge plumes, mudstreams from rivers, and local zones of resuspended bottom sediment—all in various stages of mixing and dispersal in the ambient gulf waters.

Fresh water distribution has heretofore been the most valuable tracer of large-scale water motion in the LATEX region. The fresh water content in the coastal plume and on the shelf is clearly an annual cycle triggered by the spring flood of the Mississippi-Atchafalaya Rivers. The Mississippi-Atchafalaya discharge is advected westerly and southerly along the LATEX coastline even as far as Mexico by downcoast wind components from the time of spring flood until early summer. The onset of strong southerly and southeasterly winds in early summer off Mexico and south Texas then exert upcoast wind stress components on the low salinity layer near the coast, reversing the flow, causing a convergence in the coastal currents, and advecting low salinity water offshore from the convergence and offshore Ekman transport in the surface layer. The brackish layer is, in a sense, peeled off and plowed offshore by the northward migrating convergence zone. The result of this activity is that nearly the entire LATEX shelf east of Galveston Bay out to the 200 m isobath is covered with low salinity water by late July. With the slackening of the strong southerly and southeasterly winds in late summer, downcast flow returns to the LATEX region and downwelling favorable winds re-establish the low salinity coastal current. Salinity in the south Texas coastal current decreases as water of northerly origin advects back into the region (Smith, 1980). Salinities gradually increase in October all along the LATEX coastal plume region as the major rivers approach low river discharges.
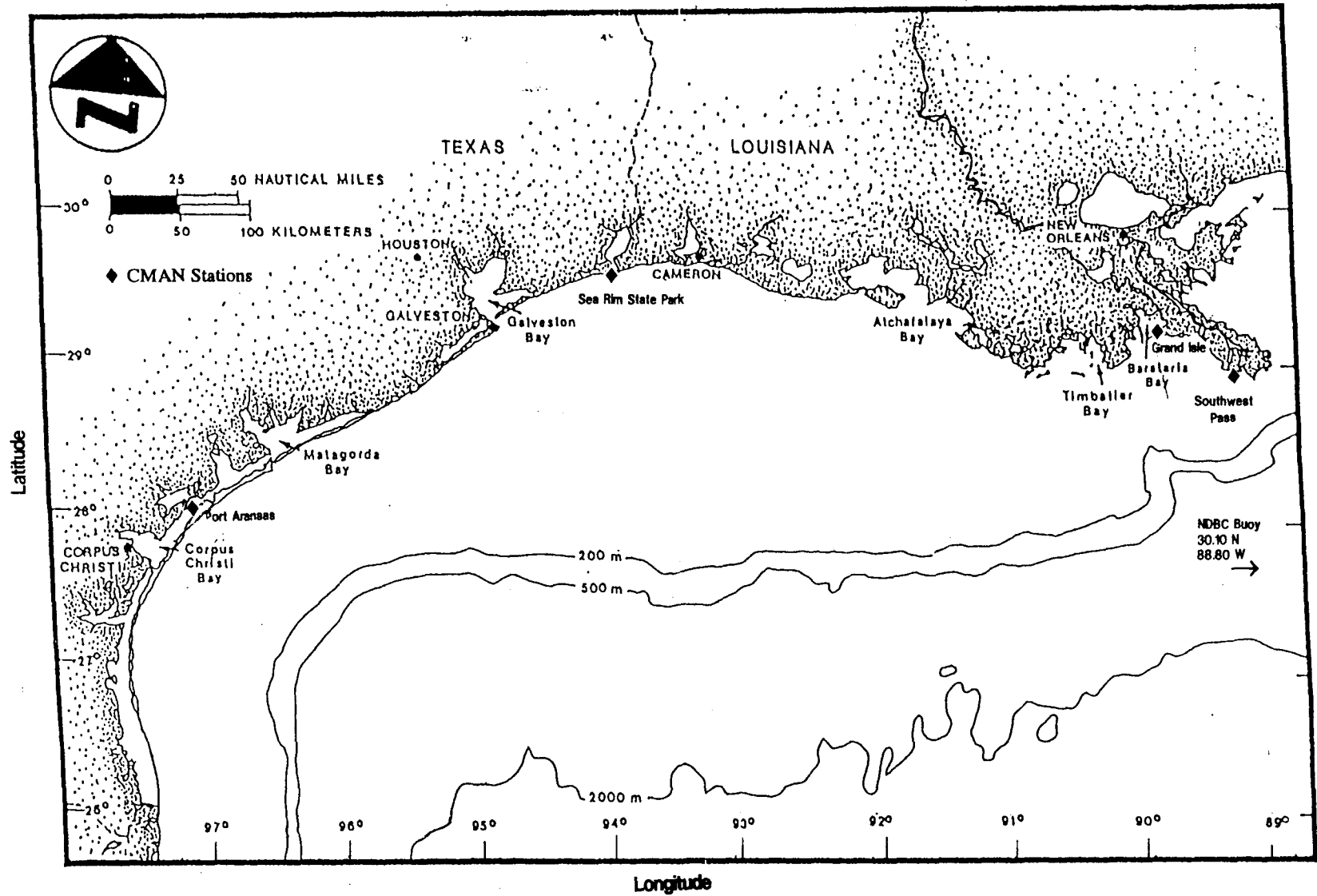
Figure 1.   Map showing the LATEX B study area.

The link between coastal current dynamics, chemistry and biology is nowhere more apparent than off central Louisiana. The Mississippi and Atchafalaya Rivers (a third of the total flow of the Mississippi River system enters the Gulf of Mexico via the Atchafalaya River) are the major source of "new" nutrients to phytoplankton on the inner and mid-shelf. Since the 1950s, water quality in the Mississippi River has changed dramatically (Meade and Parker, 1985; Smith et al., 1987; Turner et al., 1987). Suspended sediments and silicate concentrations have decreased since the 1950s, whereas nitrogen and phosphorus loadings have increased. These large changes, resulting from human activities, provide a basis for concern that this loading, combined with increased water clarity, have resulted in a "eutrophication" effect on the shelf. The area impacted by, and the duration of, hypoxia on the Louisiana shelf is of considerable concern since Louisiana fisheries are 28% of the U.S. total. Fish, shrimp, and benthic annual densities are severely depressed in these hypoxic zones and critical periods of the life history of several commercially important species (Renaud, 1986) may be affected. Of more recent concern is the content of chemical pollutants as they are transported via fresh water into the open Gulf waters.

This report on the second field year of LATEX B studies documents an integrated, multi-disciplinary approach that combines satellite imagery and image processing with ship surveys and scientific analyses (see also Murray, 1994, the annual report from the first year). The shipboard activities include measurements of subsurface currents, temperature, salinity, dissolved pigments, and phytoplankton and zooplankton systematics. The objective of this report is to present the results of Year 2 field observations with minimal synthesis. Field year three will be detailed in a future report. The final report will present an in-depth analysis and synthesis of all data sets.

Station Nomenclature

The CTD stations were assigned distinct numbers that correlate to specific tasks. For example, P931001 reflects the following

P	= R/V Pelican
93	= 1993, the calendar year
1	= the first cruise of that calendar year
001	= the discrete station number assigned to each CTD station and used by every

project task taking samples at that location.

Cruise III, April 1993, followed the basic survey, using numbers beginning with 001. For Cruise IV, July 1993, the basic survey stations were numbers 100 through 399. The plume study is a 400 series, and the convergence study is a 600 series. All cruises follow this system, so that each basic survey stations is as close to the same location as possible.

3

II. HYDROGRAPHIC SURVEY

Figure 2 shows the discharge of the Mississippi River at Tarbert Landing, which is upstream of the controlled diversion of about one-third of this discharge into the Atchafalaya River channel. Cruise III in April 1993 occurs at a discharge of ~35,000 m^3/sec, reasonably representative of the high flows of the previous five years. Cruise IV in July 1993 occurs at a discharge of ~20,000m^3/sec, a value 2 to 3 times the July values of the previous 5 years.

A. Cruise III, April 13-22, 1993 *(Neal R. Pettigrew)*

Cruise III of LATEX B took place the week prior to the crest of the 1993 spring "flood" (Figure 3). The combined discharge from the Mississippi and Atchafalaya rivers during the Cruise III period averaged approximately 3 x 10^4 m^3/s (Figure 3), a value roughly twice that recorded the previous April during Cruise I. Comparison of the two April cruises thus provides a good opportunity to distinguish between regional oceanographic conditions during dry and wet years. While these interannual differences are clear, especially along the Texas coast, the salinity and density fields along the Louisiana Shelf are clearly dominated by the influence of fresh-water inflow from the Mississippi and the Atchafalaya during both dry and wet spring conditions.

1. Background

The shiptrack, hydrostations, and domain for Cruise III are shown in Figure 4. The principal survey sections, which run roughly perpendicular to the coast (from offshore of Terrebonne Bay, Louisiana to beyond Corpus Christi, Texas) are denoted S1 through S8, and X1 through X3. Between these sections are "tie lines" enumerated T2 through T15 along which additional station and underway data were taken while steaming between successive sections.

Even a cursory look at the experimental domain reveals several factors that may substantially complicate the physical oceanography of the study region. In addition to the influences of the Mississippi and Atchafalaya rivers, the Louisiana/Texas (LATEX) shelf is punctuated by a series of smaller rivers and coastal embayments that could add substantially to the variability of the LATEX inner shelf. In addition, there is significant coastal curvature, the importance of which upon the structure of both wind-driven and density-driven circulation has been prominent in the coastal literature since the seminal work of Csanady (1977).

Especially interesting, and potentially troublesome, are complications associated with the size of the domain. The LATEX B study area represents an inner-shelf strip approximately 700 km long. While the coastal survey of such a vast coastal system offers unprecedented opportunity to observe the transitions and interactions of significant alongshore variations in meteorological forcing, the data are likely to be complicated by the existence of temporal fluctuations with time scales shorter than the survey period. In order to distinguish between genuine alongshelf variability and temporal aliasing of the survey data, shipboard winds and survey data were interpreted within the context of time series wind records at multiple alongshore locations. The times of each of the survey lines and sections are listed in Table 1.

5
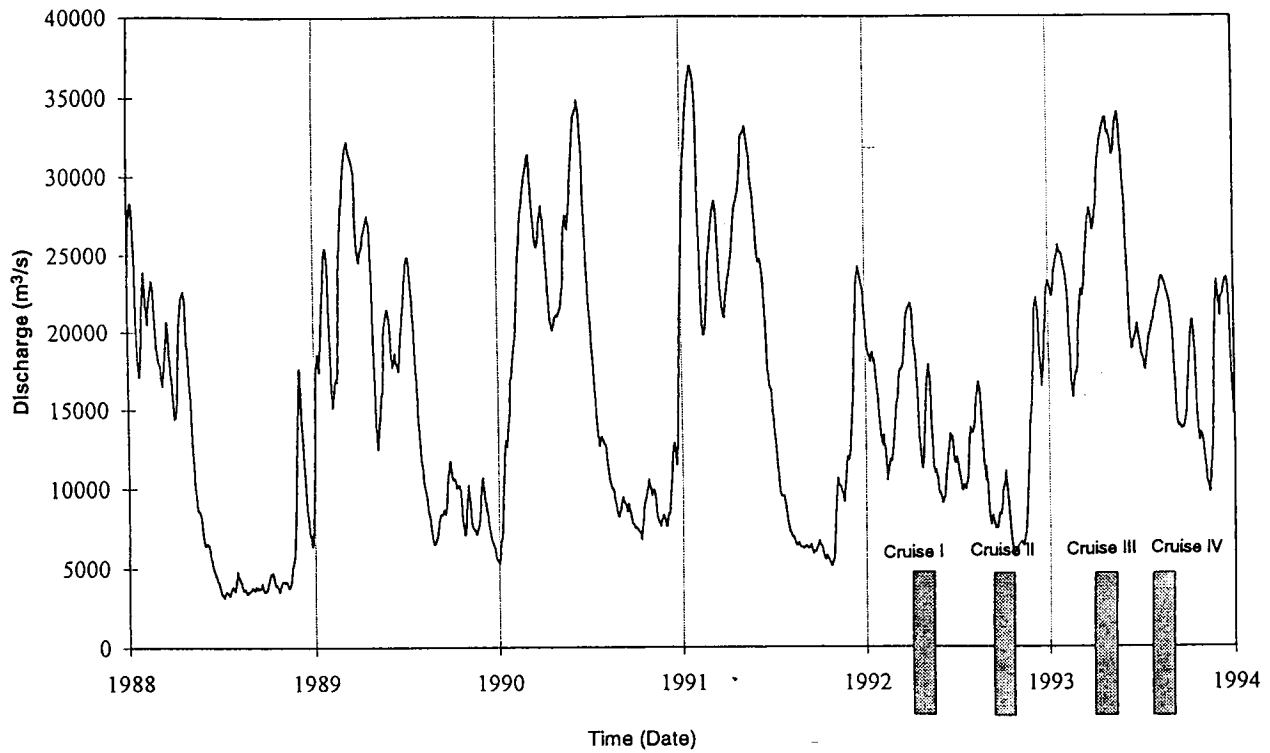
Figure 2. Discharge of the Mississippi River at Tarbert Landing, 1988-1993, highlighting
occurrence of first four Latex B cruises.
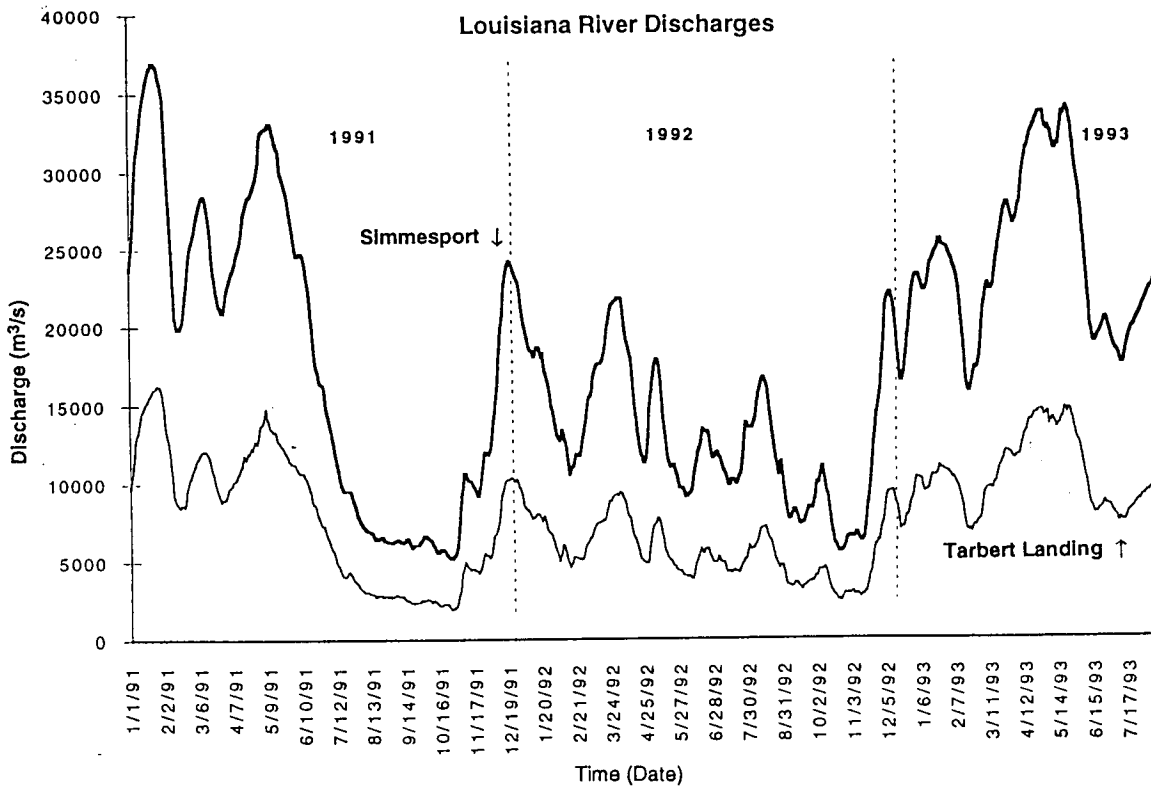
Figure 3. Freshwater discharge down the Mississippi River upstream of the Atchafalaya diversion
and in the Atchafalaya River itself at Simmesport.
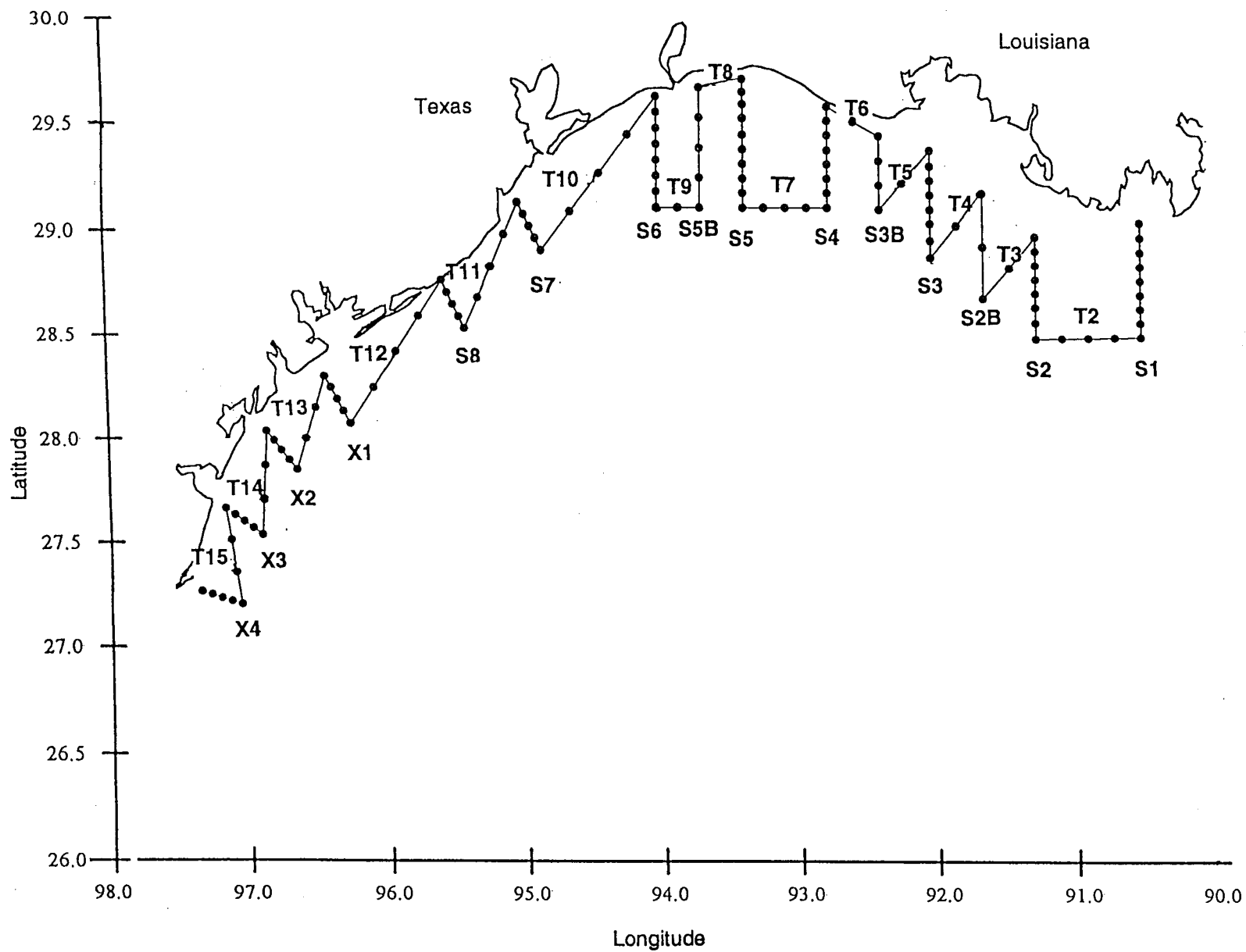
Figure 4. Shiptrack, hydrographic locations, and survey domain for LATEX B, Cruise III, April 13-19, 1993

Table 1. Times and dates of survey lines, Cruise III. All times are in GMT (GMT is CDT plus 5 hours). Dates are noted in Julian days.

Line	Start Time	Start Date	End Time	End Date
S1	1306	13 April	2156	13 April
T2	2156	13 April	0310	14 April
S2	0302	14 April	1123	14 April
T3	1123	14 April	1545	14 April
S2B	1545	14 April	1956	14 April
T4	1956	14 April	0040	15 April
S3	0040	15 April	0717	15 April
T5	0717	15 April	1248	15 April
S3B	1248	15 April	1717	15 April
T6	1717	15 April	2138	15 April
S4	2138	15 April	0337	16 April
T7	0337	16 April	0928	16 April
S5	0928	16 April	1700	16 April
T8	1700	16 April	1955	16 April
S5B	1955	16 April	0133	17 April
T9	0133	17 April	0432	17 April
S6	0432	17 April	1104	17 April
T10	1104	17 April	2140	17 April
S7	2140	17 April	0107	18 April
T11	0107	18 April	0849	18 April
S8	0849	18 April	1218	18 April
T12	1218	18 April	2123	18 April
X1	2123	18 April	0044	19 April
T13	0044	19 April	1622	19 April
X2	0622	19 April	1015	19 April
T14	1015	19 April	1615	19 April
X3	1615	19 April	2022	19 April

2. Wind Velocity Time Series

Time series vector stick plots of velocity are shown for April 1993 in Figure 5. The data are from Coastal Marine Automated Network (CMAN) stations located at New Orleans, Grande Isle, Sabine, and Corpus Christi. The data show April 1993 to have been a month of strong and variable winds. Wind speeds in excess of 20 knots were common, and significant shifts in wind strength and direction occurred over time scales ranging from 1 to 5 days. While there is clear visual coherence between the records, there are also apparent phase shifts across the array with wind episodes generally appearing first at Corpus Christi and propagating northeastward toward New Orleans. There are also clear cases of significant wind convergence and divergence related in part to the northeastward propagation of the wind signal.

The survey (April 13-19) occurred during a period of generally southerly and southeasterly winds that began on April 10 and ended April 15. During this period there were consistent differences in wind speed along the coast, with Grand Isle experiencing winds of roughly 10 knots, while at the other stations winds were characteristically twice as strong. During the principal wind shifts on April 15 and 17, there were significant differences in wind strength and direction between Grand Isle and Sabine.

3. Multiple Interface Data Acquisition System (MIDAS)

a. Underway Wind Measurements. Data logged by the MIDAS included shipboard "absolute winds." These wind records, corrected for ship speed and heading, provide shipboard survey data of the wind field over the cruise. It is anticipated that, while these data provide much

Cruise 3, Winds (April 1-30 1993)
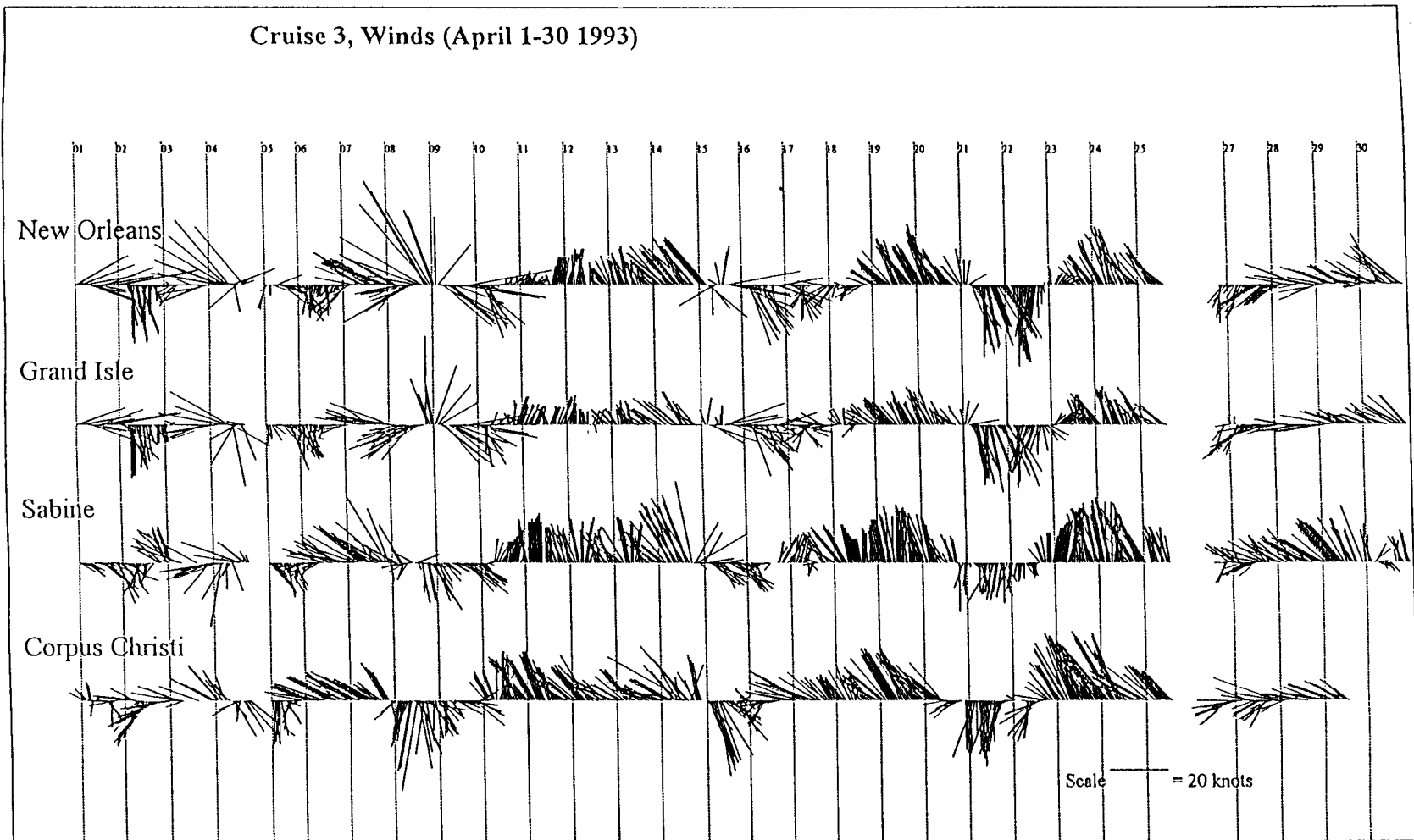
Figure 5. Wind vectors from four Coastal-Marine Automated Network (C-MAN) stations along the coast, April 1993. See Figure 1 for locations of the CMAN instruments.
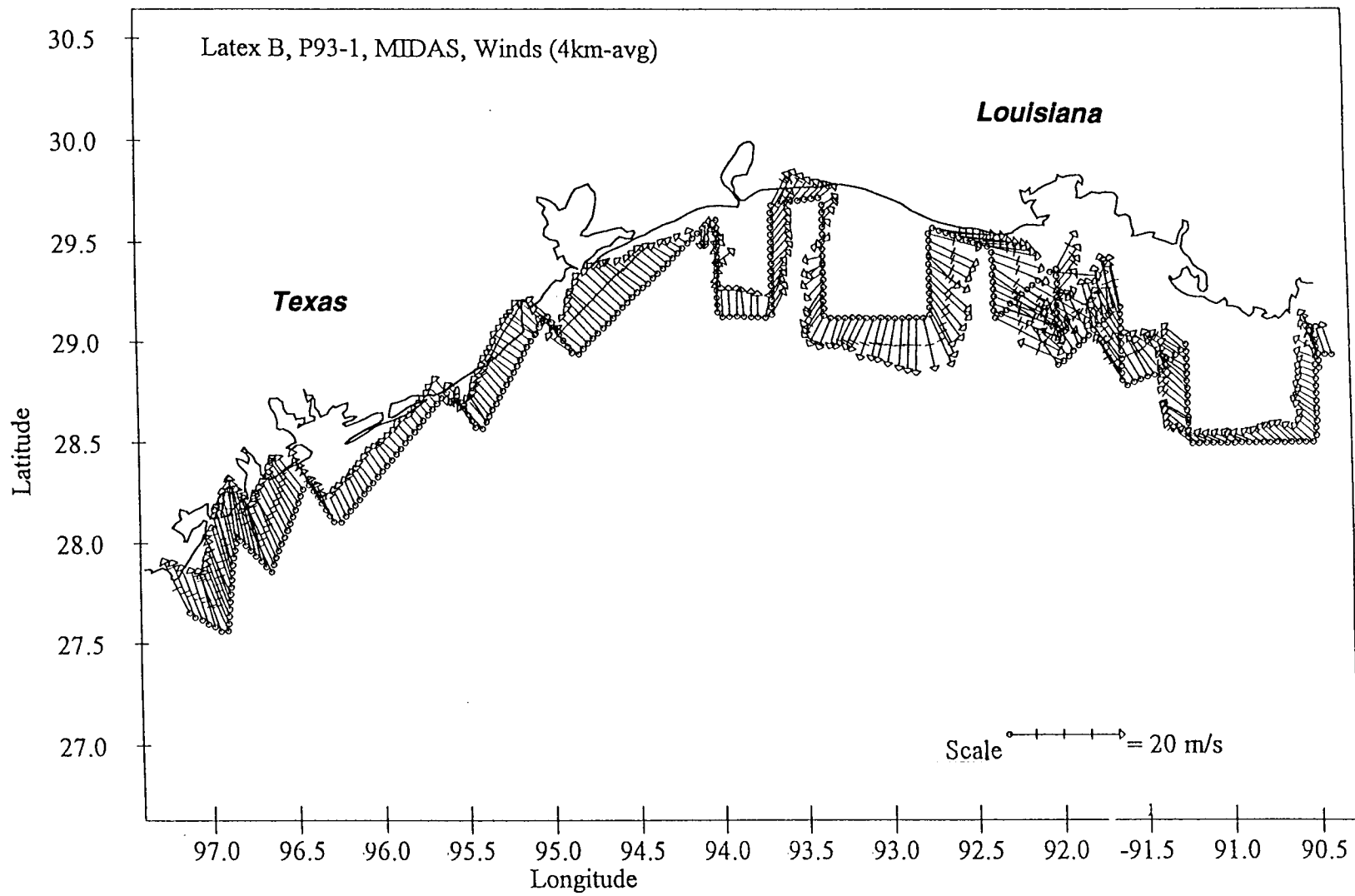
Figure 6. Shipboard "absolute winds, corrected for ship speed and heading, over the cruise survey. These data were collected by the Multiple Interface Data Acquisition System (MIDAS) aboard the R/V *Pelican.*

greater spatial resolution of the wind field than can be attained from CMAN station data, the Midas winds will be aliased by the temporal variability that characterizes the meteorology of the region. Thus care must be exercised in interpreting the spatio-temporal wind field show in Figure 6.

Several generalizations can be made with regard to winds over the survey domain during the study period. The winds along the Texas inner shelf were consistently directed onshore. At the far southwest end of the survey, winds were particularly strong (roughly 30 knots) and had a significant "upcoast" component; that is, in the opposite direction of Kelvin wave propagation. Along the Louisiana shelf the wind direction was far less consistent with wind reversals in both the cross-shore and alongshore components, as well as apparent convergences and divergences of significance occurring in the region between Sabine and Atchafalaya Bay. In the region east of Atchafalaya Bay, the wind was directed primarily "downcoast."

Comparison between MIDAS and CMAN winds, with reference to Table 1 and Figure 4, suggests that, while there was a significant temporal component (aliasing) in the MIDAS wind convergences, there was also a spatial component to the wind convergence, especially between S5 and S6 (Figure 4) in the vicinity of Sabine. These data suggest that interesting oceanographic consequences may be present in the Doppler velocity and/or hydrographic data.

b. Near-surface Velocity and Water Property Fields. Figure 7 shows a plot of shipboard Doppler velocity measurements made at 4.5m depth. Comparison of these vectors with the corresponding shipboard winds measurements shows a clear correlation. This correlation, which holds even during periods of rapidly changing wind (see Figure 6 and Table 1), suggests that the inner shelf flow field responds rapidly to the variable coastal wind forcing.

The near surface currents along the Texas shelf are consistently upcoast, although the cross-shore component alternates between on- and offshore for reasons that are not readily apparent. Along that portion of the LATEX shelf from Sabine to Atchafalaya Bay the Doppler Currents show a pattern that generally reflects the recorded winds; that is, the currents are primarily downwind. The close relationship between the wind and current vectors along in this part of the survey may suggest rapid response to winds varying on time scales short relative to an inertial period. Currents are still largely accelerating downwind, and the rotational adjustment (Ekman response) has not yet fully developed in some cases. East of Atchafalaya Bay the downcoast winds have produced a downcoast surface coastal current, although the offshore component along T2 seems to indicate an offshore surface current not simply related to the local wind.

Contours of MIDAS (underway) measurements of near surface temperature and salinity are presented in Figures 8 and 9, respectively. Temperature contrasts are very slight with only 2° C difference over the 400-mile-long survey area. The warmest surface temperatures are southwest of Corpus Christi, and the coolest are found between Sabine and Atchafalaya Bay. Overall the surface temperatures were 2 to 3° C cooler during Cruise III (April 1993) compared to Cruise I (April 1992).

MIDAS surface salinity distributions showed considerably more structure and variation than did the temperature field. A clear change in character of suface salinity variation occurs near the mouth of Galveston Bay. Southwest of the Bay, the south Texas inner shelf is characterized by increasing alongshore surface salinity with little or no cross-shore variation. In contrast, east of Galveston Bay there are strong cross-shore salinity gradients with the fresher surface waters near shore, as expected. In addition, there are also very significant alongshore salinity variations. Two regions of local salinity minima seem to be associated with fresh water outflow from the Atchafalaya and Lake Calcasieu. In interesting contrast to the salinity field southwest of Galveston, aside from the nearshore salinity minimum associated with Lake Calcasieu, the surface salinity gradients in the region between Galveston and Atchafalaya Bays are directed primarily offshore with the isohalines roughly coast parallel.

11
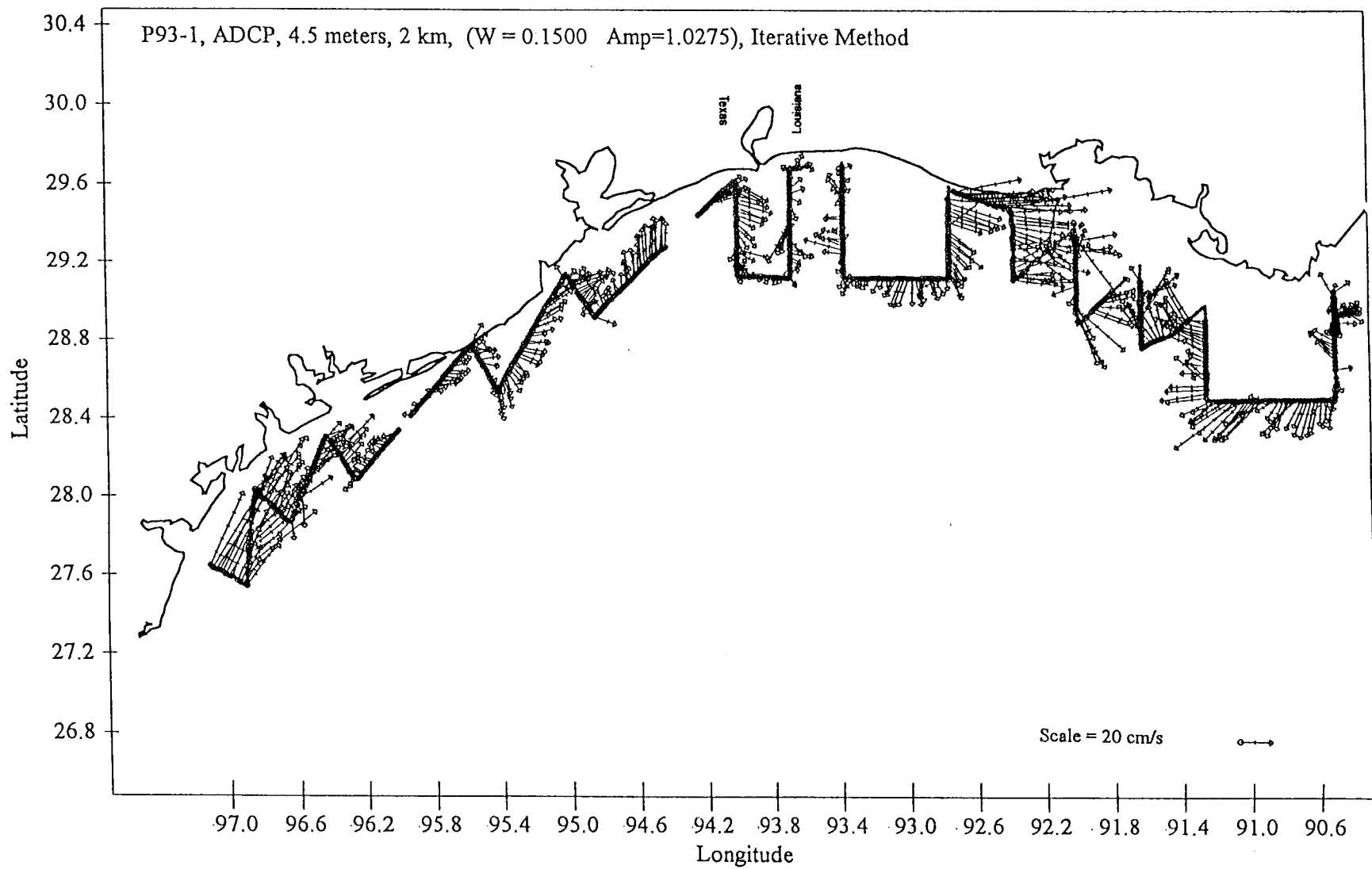
Figure 7. Shipboard survey of Doppler veolcity measurements made at 4.5 m depth.
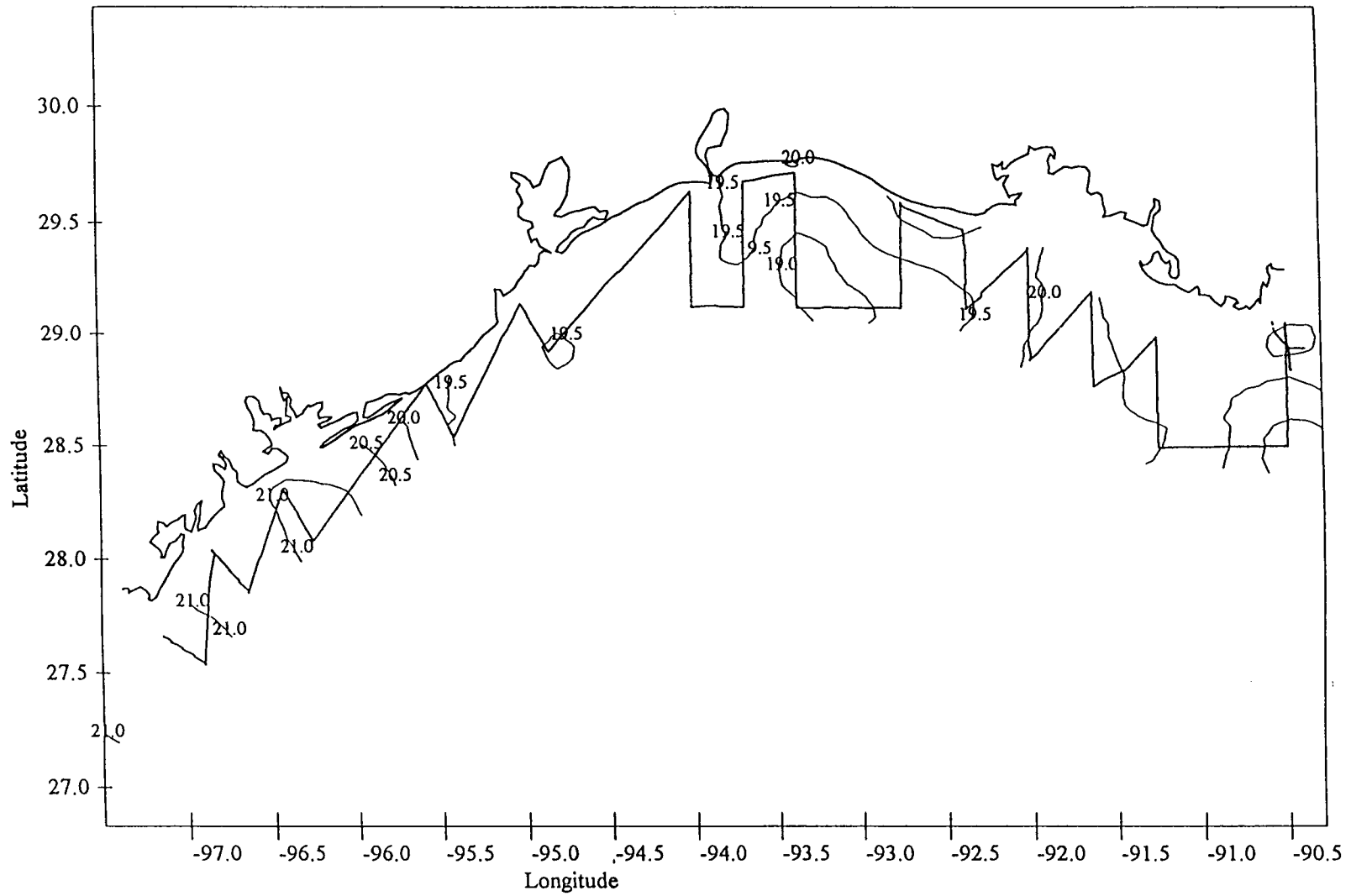
Figure 8. Contours of MIDAS (underway) measurements of near surface temperature for Cruise III, April 13-19,1993.
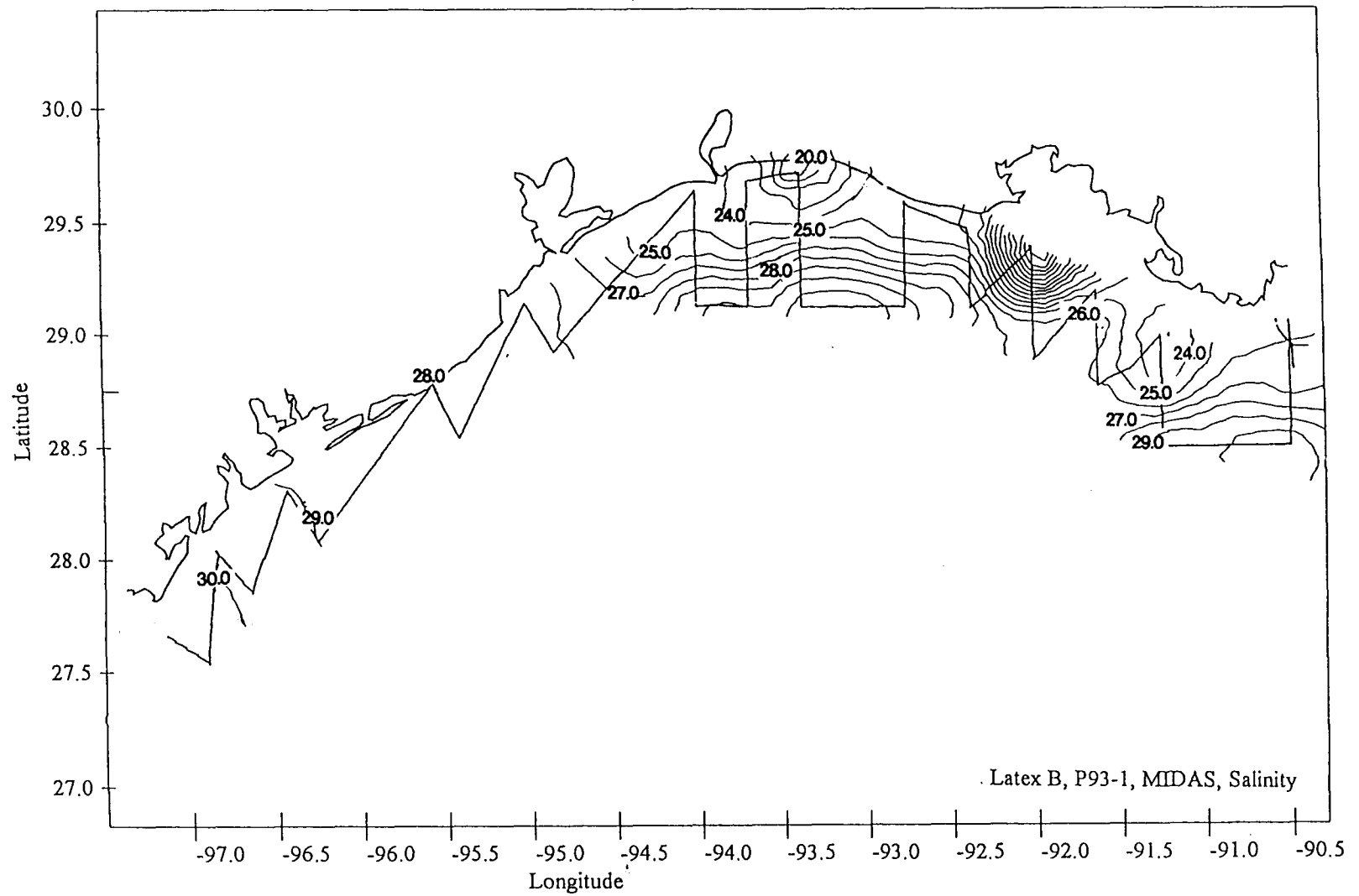
Figure 9. Contours of MIDAS (underway) measurements of near surface salinity for Cruise III, April 13-19,1993.

Since the Mississippi/Atchafalaya runoff was approximately twice as high in April 1993 compared to April 1992, one might anticipate the observed surface salinities in Cruise III to be substantially lower than those observed in Cruise I. Comparison of the two surveys actually shows the opposite case along the coast southwest of Galveston. In this region the surface salinities are several PSU lower during 1992, which we have characterized as the "dry" year. This surprising result is a consequence of the large size of the survey domain and the difference in water shed areas. While 1992 was a relatively dry year for the Mississippi River Basin, it was a wet year for the drainage area of east Texas. In addition, all Latex B cruises indicate the influence of the Mississippi/Atchafalaya outflow plume is not dominant west of Galveston, and that there are distinct differences in the hydrography of the regions east and west of Galveston Bay.

4. Vertical Sections

The principal physical data set from the LATEX B cruises is comprised of vertical sections of salinity, temperature, density, and east-west and north-south components of the Doppler velocity. Below a selection of interesting and/or representative sections are presented in order to characterize the physical oceanographic conditions of the region and to provide preliminary insight into the fundamental dynamical balances operating in the LATEX inner shelf region. Within the LATEX B domain it was found that the temperature distributions are relatively homogenous and make little contribution to the density distribution. Therefore, only the salinity sections are shown below.

Beginning with the eastern most section (S1) off Terrebonne Bay, Figure 10 shows a salinity section that is generally representative of the eastern LATEX region. The retrograde salinity distribution shown in the upper 10 m is characteristic of buoyant coastal plumes. In this particular case, the coastal plume may be characterized as a "foliated" retrograde frontal structure. That is, there are multiple frontal features within the coastal plume that slope upward in the offshore direction. From the data shown in Figure 10, the plume appears to be made up of waters fresher than 31 PSU. However, because of the foliated nature of the front it is very difficult to determine exactly how far offshore the plume may actually extend and what isohalines may eventually surface. Further isohaline outcropping could occur offshore of the seaward end of the survey section. The Doppler current sections at S1 showed a complex spatial structure consistent with the surface current pattern indicated in Figure 7 and are not explored further here.

It is interesting to compare April S1 salinity sections for the wet and dry years of 1993 and 1992. Qualitatively the two sections are very similar. Both clearly exhibit the foliated frontal structure and have their main halocline at roughly 10 m. The lowest salinity values (by ~ 1 PSU) were actually observed nearshore during the dryer year; however, the overall volume of relatively freshwater is substantially reduced . As an example, the 30 PSU isoline outcrops approximately 20 km closer to shore and its greatest depth is 3 m shallower during 1992 compared to 1993. Thus the principal response to increased runoff during relatively wet springs seems to be a seaward expansion of the buoyant coastal water, rather than a dramatic salinity decrease.

Section S2 extends farthest from the coast (~80 km) of all the sections in this study. As shown in Figure 11 in this section the 31.5 PSU isohaline fully outcrops, and several deeper isohalines have a concave distribution. Once again the foliated nature of the front is apparent, and had the section stopped 70 km from shore, one could have concluded that the coastal plume was bounded by the 31 PSU contour. The strongest salinity gradient is observed over the inner 3/4 of the section at a depth of roughly 5 m. Doppler velocity data (Figure 12) show predominantly westward with some indication of a weak counterflow at depth.

The inner half of section S3 (Figure 13) is greatly influenced by the fresh outflow from Atchafalaya Bay. Near-surface salinity values of < 20 PSU and < 10 PSU were respectively observed over the innermost 25 km and 12 km of the section. Reference to Figure 8 shows that
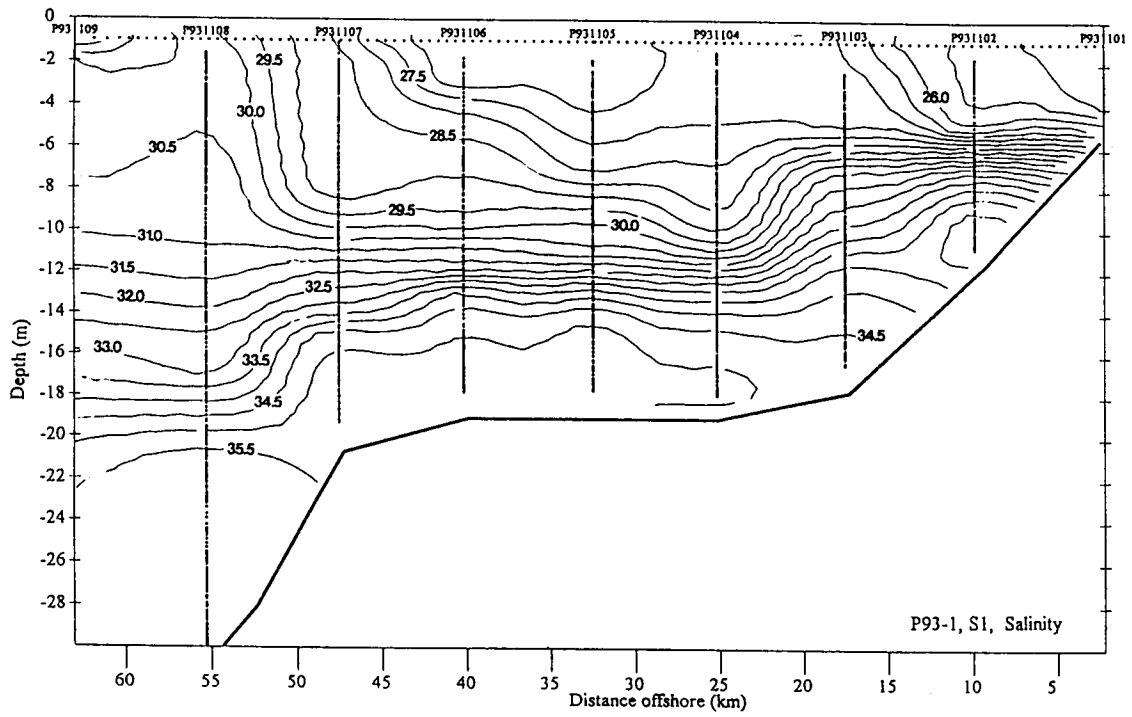
Figure 10. Salinity section at S1 in the eastern LATEX region.
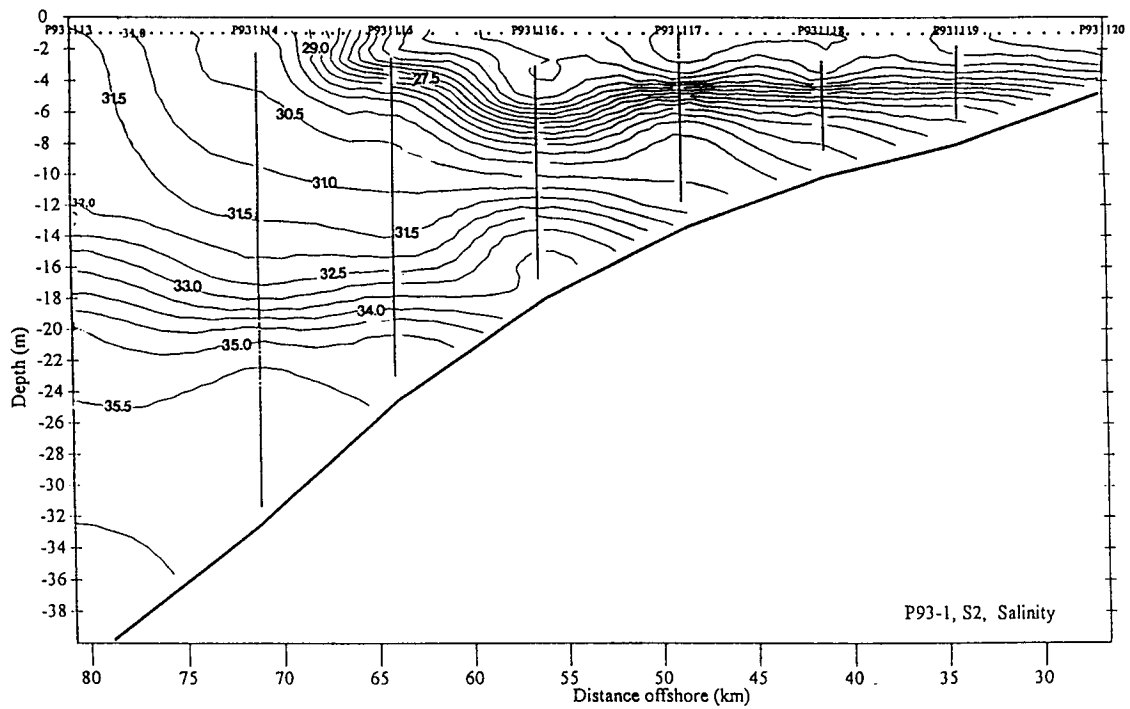
Figure 11. Salinity section from S2, which extends farthest from the coast (~80 km) of all the sections in this study.

16
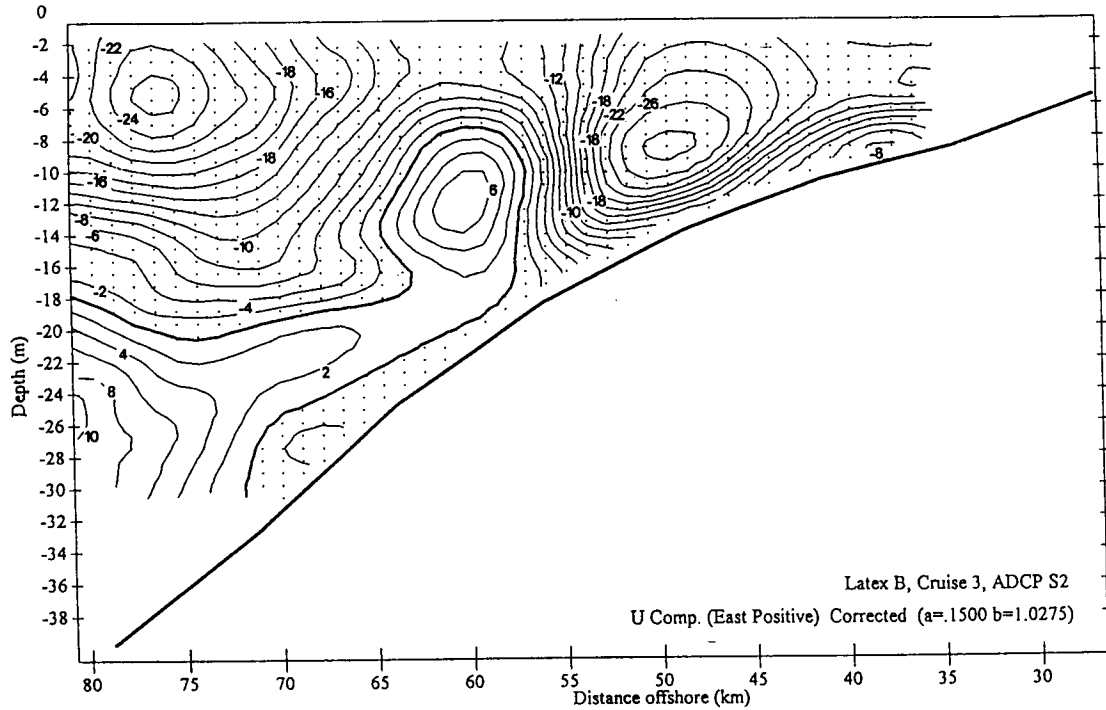
Figure 12. Contour diagram of the eastward component of Doppler velocity measured at S2, showing predominantly westward flow with some indication of a weak counterflow at depth.
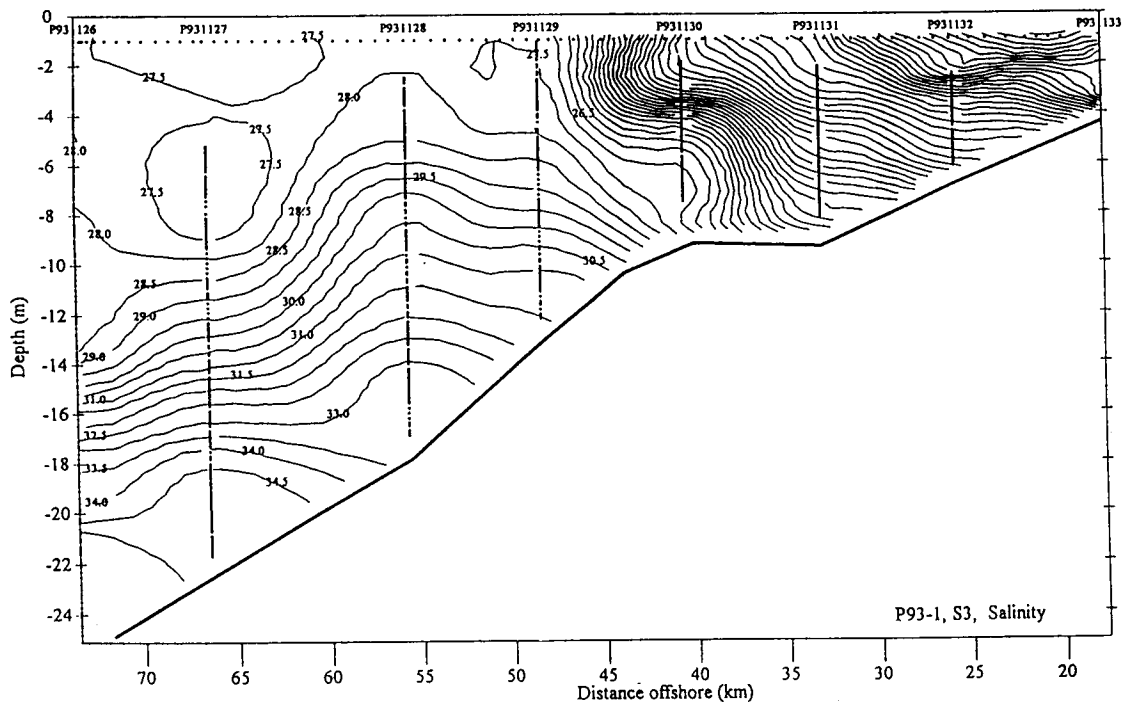
Figure 13. The inner half of the salinity section at S3 is greatly influenced by the fresh outflow from Atchafalaya Bay.

17

the inner portion of S3 was within a distinct lens of fresh water. Surface salinities at the outermost station were < 28 PSU, and one concludes that the coastal plume has been pushed further offshore in this location by the outflow plume from the Atchafalaya. The outer half of the section displayed an upwelled salinity structure and complex velocity structure during a period of rapidly shifting winds.

Section S4 shows a "textbook" example of a lens-shaped halocline resulting from upwelling of a coastal plume. As shown in Figure 14, the lowest salinity water is found in a band separated from shore by a relatively weak prograde front. Figures 9 and 6 show that S4 is outside the near field influence of the Atchafalaya outflow and exposed to the influence of vigorous upwelling-favorable winds. Near the bottom the isohalines are downturned suggesting a bottom mixed layer several meters thick.

Doppler velocity sections shown in Figures 15 and 16 are consistent with the above interpretations. Figure 15 shows a very well-developed upwelling circulation with strong onshore flow in the lower half of the water column, and strong offshore flow in the upper half. Figure 16 shows very strong eastward flow throughout the section. The core of the eastward flow, located at 4-10 m depth 5-15 km from the coast, exceeds 0.35 m/s. The strong near-bottom currents are consistent with the formation of a bottom mixed layer.

It is important to note that the wind-driven coastal current has a subsurface maximum, that it decays offshore, and that it has overcome the buoyancy-driven westward component associated with the runoff from the Mississippi and Atchafalaya rivers during spring runoff in a "wet" year. These data show clearly the dominance of the wind-driven dynamics even along what is often thought of as a runoff dominated inner shelf. Reference to Table 1 and Figure 5 suggests that the strong wind-driven upwelling and coastal current system was established within a fraction of a day of the onset of upwelling winds.

It is instructive at this point to examine the tie-line, T7, that runs between the outer stations of sections S4 and S5. Figure 17 shows an increase in salinity toward the west revealing the expected presence of an eastward baroclinic pressure gradient force that may play a role in the bottom intensified eastward flow at S4. Figure 18 shows an alonghore section of the intense upwelling circulation referred to above in the discussion of the lens-shaped pycnocline.

Section S5 shows a salinity structure (Figure 19) strongly dominated by freshwater runoff. At this location the nearshore freshwater fraction has been enhanced by the influence of the Calcasieu. Over the outer 25 km, the upper 12 m is vertically well-mixed giving the retrograde structure a particularly steep appearance. The winds at this location and time show considerable variation. Over the outer section the winds were downcoast and dowwelling favorable, while at the innermost stations the winds shifted to upcoast, upwelling favorable. As discussed earlier, although there is significant aliasing of the MIDAS wind measurements, there appears to be a spatial convergence of the winds between sections S5 and S5B.

Figure 20 shows the cross-shore flow component as measured by the shipboard Doppler profiler. The flow over most of the section is consistent with the shifting winds onshore except for an apparent local upwelling very close to the coast. The local alongshore component shows a fascinating structure (Figure 21). The upper half of the water column flows downwind in a strong westward core, centered at 6 m depth and 50 km from shore. In the lower layer there is a consistent counter current flowing toward the east. Very near the coast are weak eastward currents surface-to-bottom.

The S5B salinity section (Figure 22), in comparison to S5, is much more saline, reflecting reduced influence of the Calcasieu. Winds are uniformly upwelling favorable, and a lens-shaped halocline is in evidence near shore. Cross-shore velocities (Figure 23) are weak over most of the

18
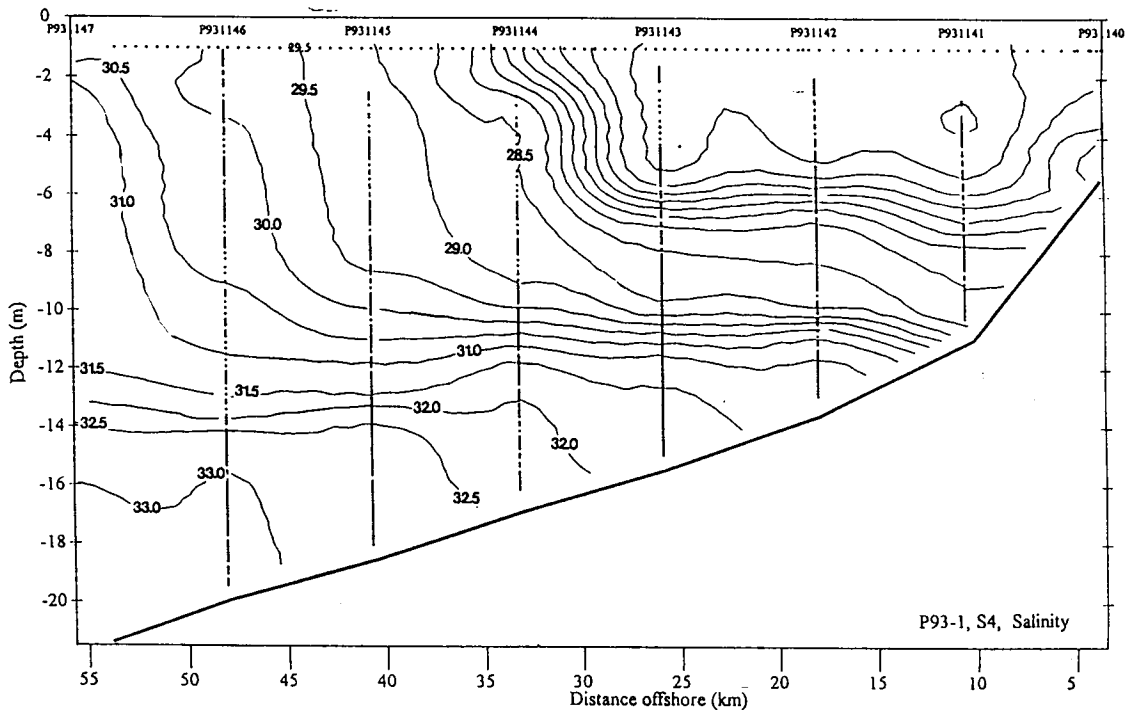
Figure 14. Section S4 exhibited a "textbook" example of a lens-shaped halocline resulting from upwelling of a coastal plume.
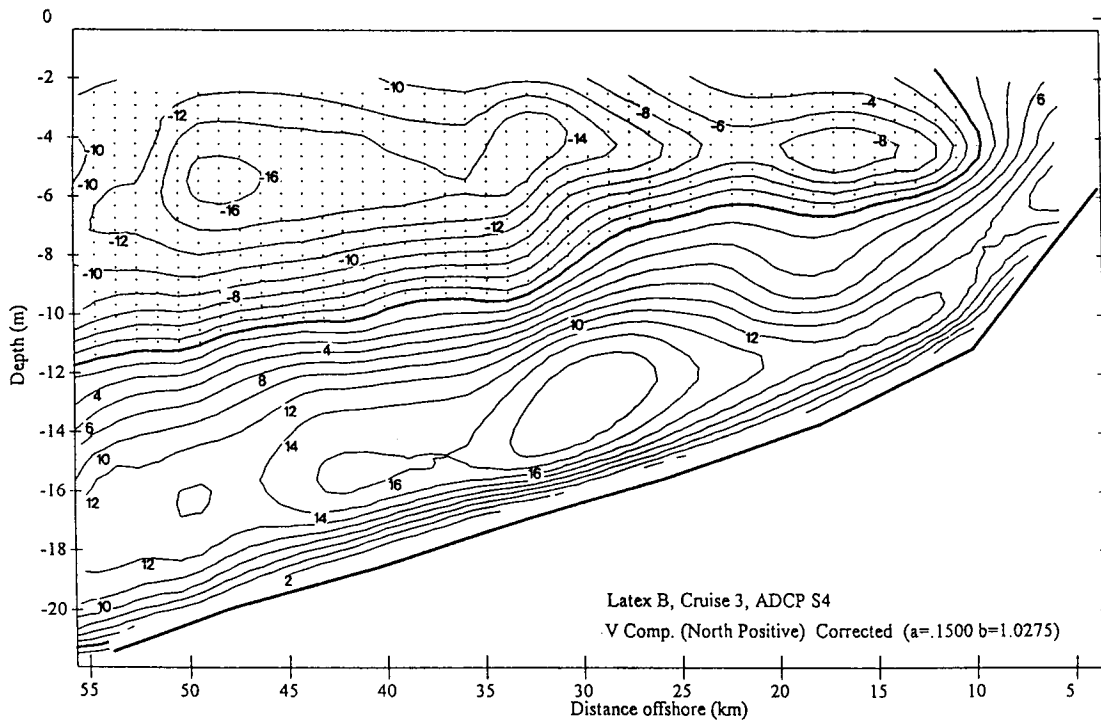
Figure 15. Northward doppler velocity contours at S4 show a very well-developed upwelling circulation with strong onshore flow in the lower half of the water column, and strong offshore flow in the upper half.

19
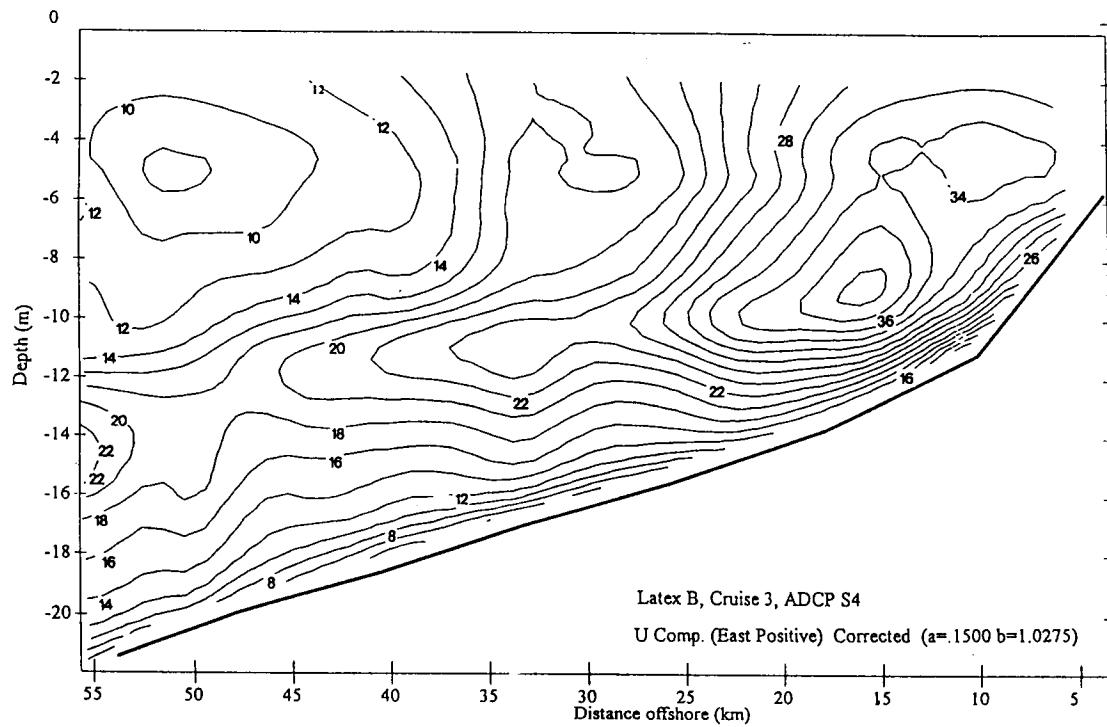
Figure 16. Eastward doppler velocity contours at S4 show very strong eastward flow throughout the section.
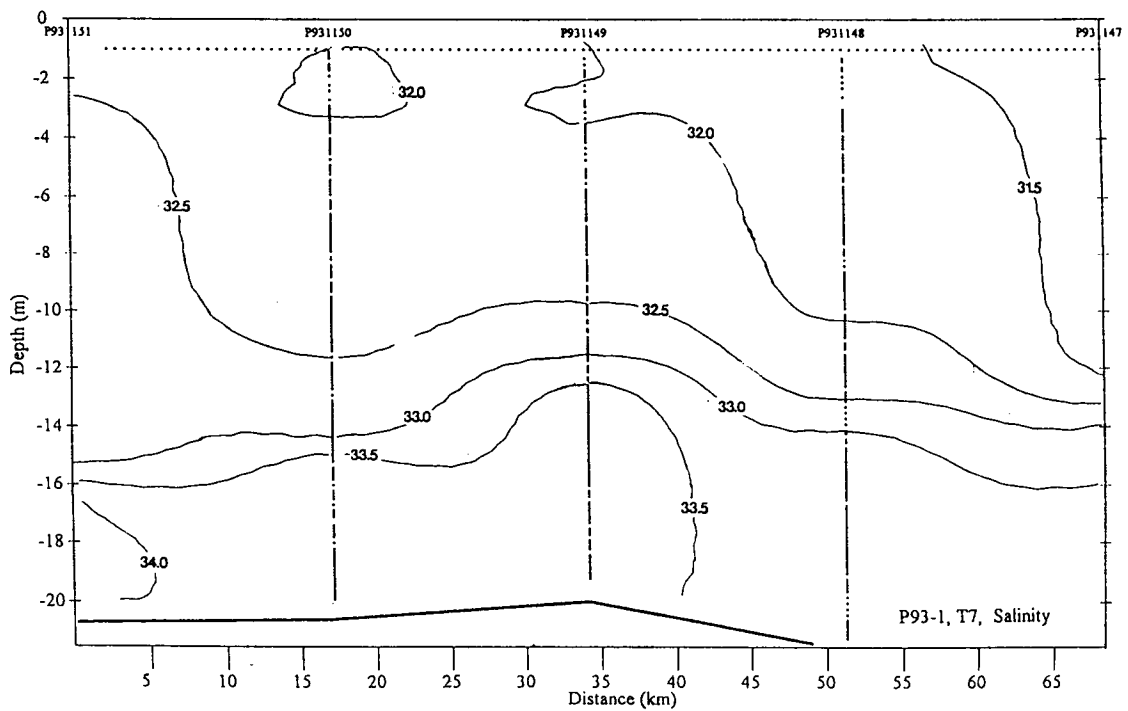
Figure 17. Salinity contours along the east/west line, T7.

20
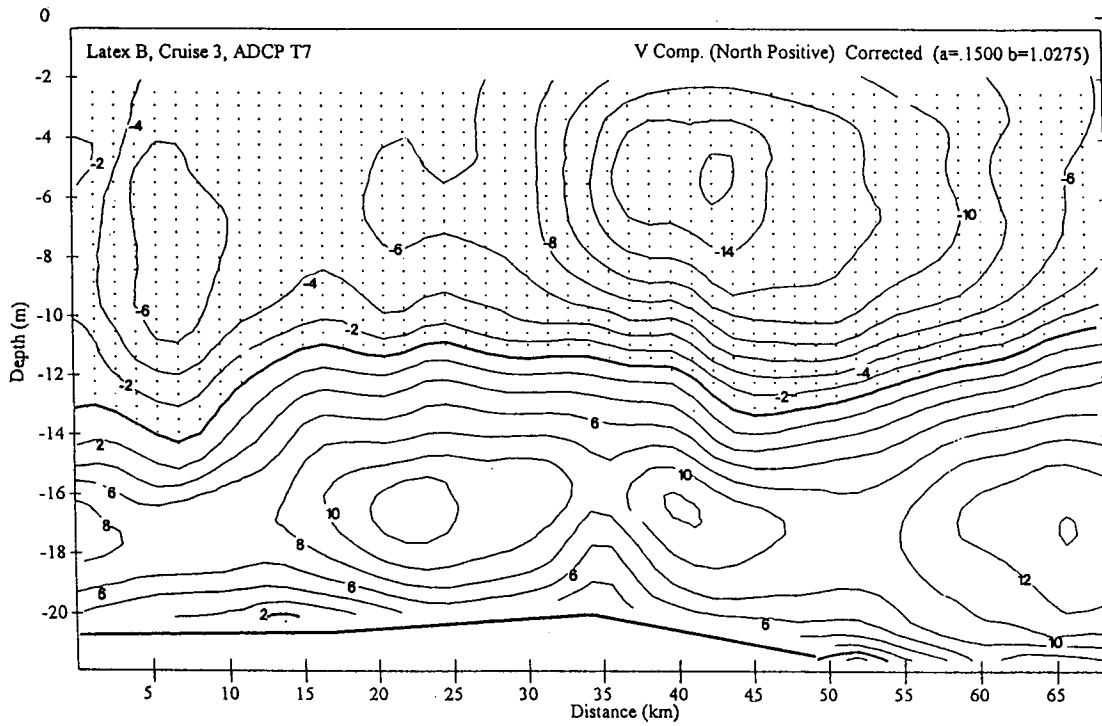
Figure 18. Northward doppler velocity contours along east/west line T7, showing a very well-developed upwelling circulation along this section of the inner shelf.
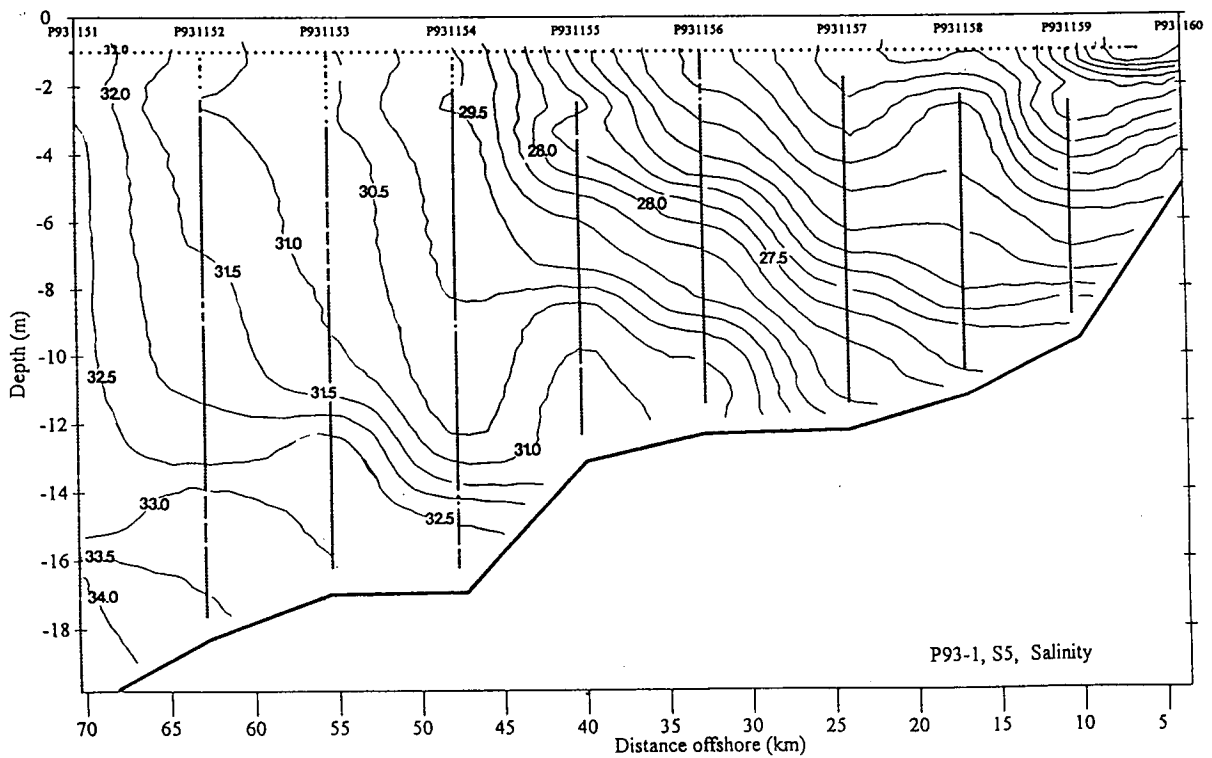
Figure 19. Nearshore salinities along section S5 are apparently reduced by the fresh inflow from the Calcasieu.

21
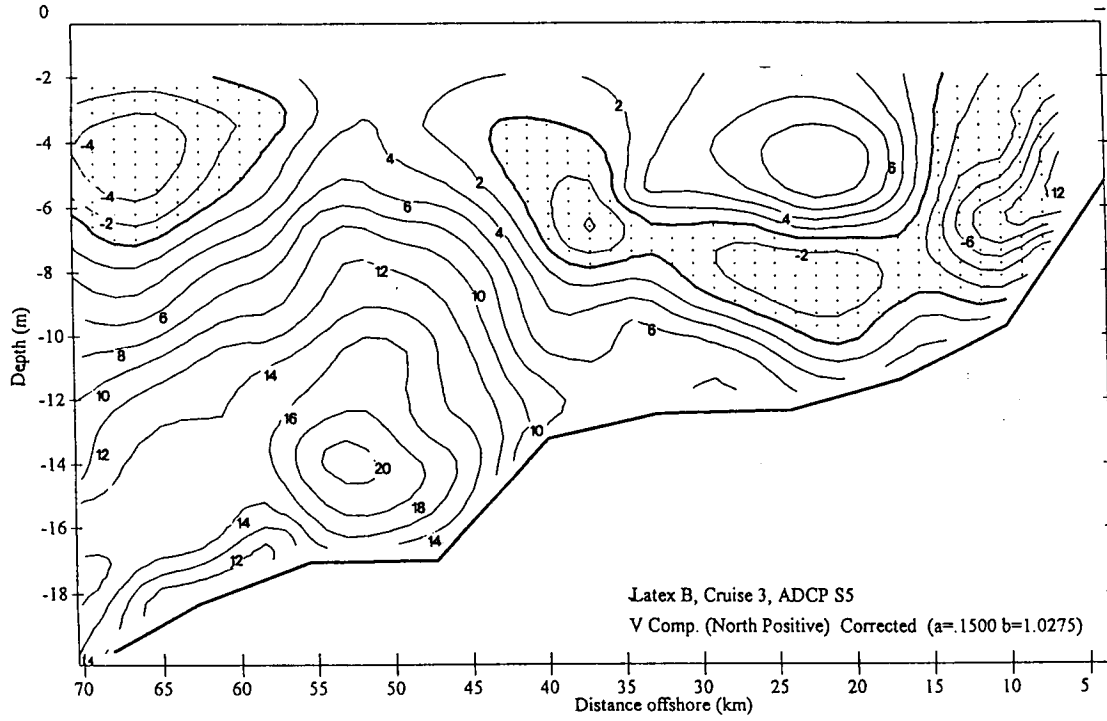
Figure 20. The contours of northward flow speed along section S5.
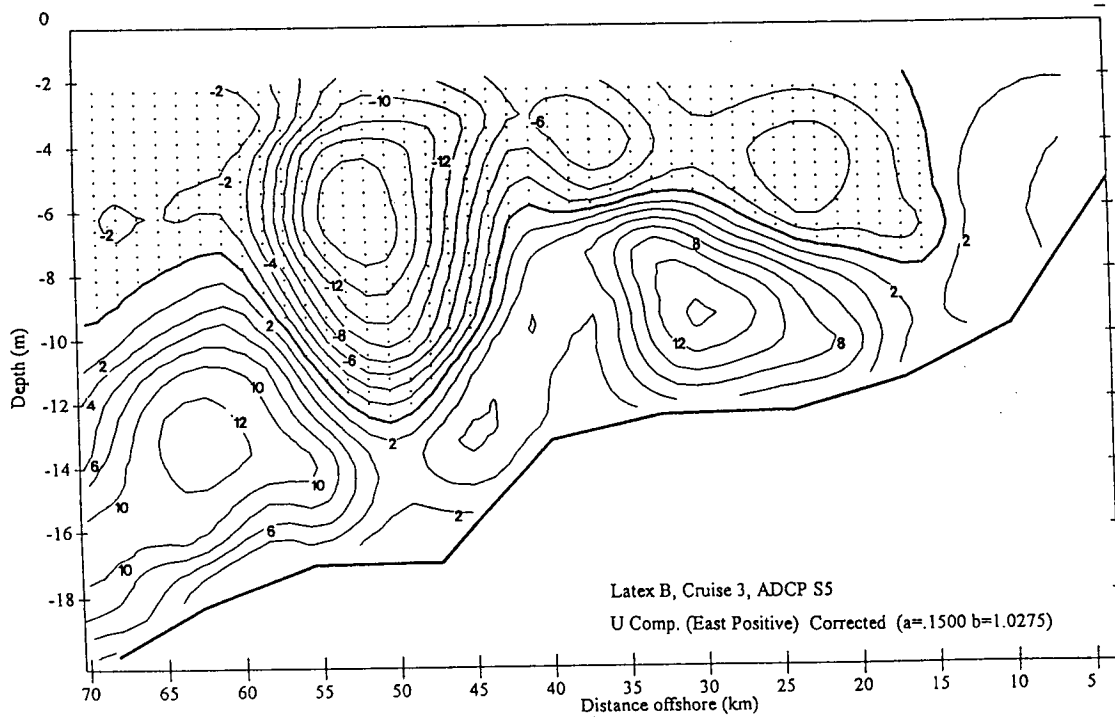
Figure 21. Contours of the eastward flow component at S5 showing downwind (westward) flow in the upper half of the water column, and an upwind counter current in the lower layer.
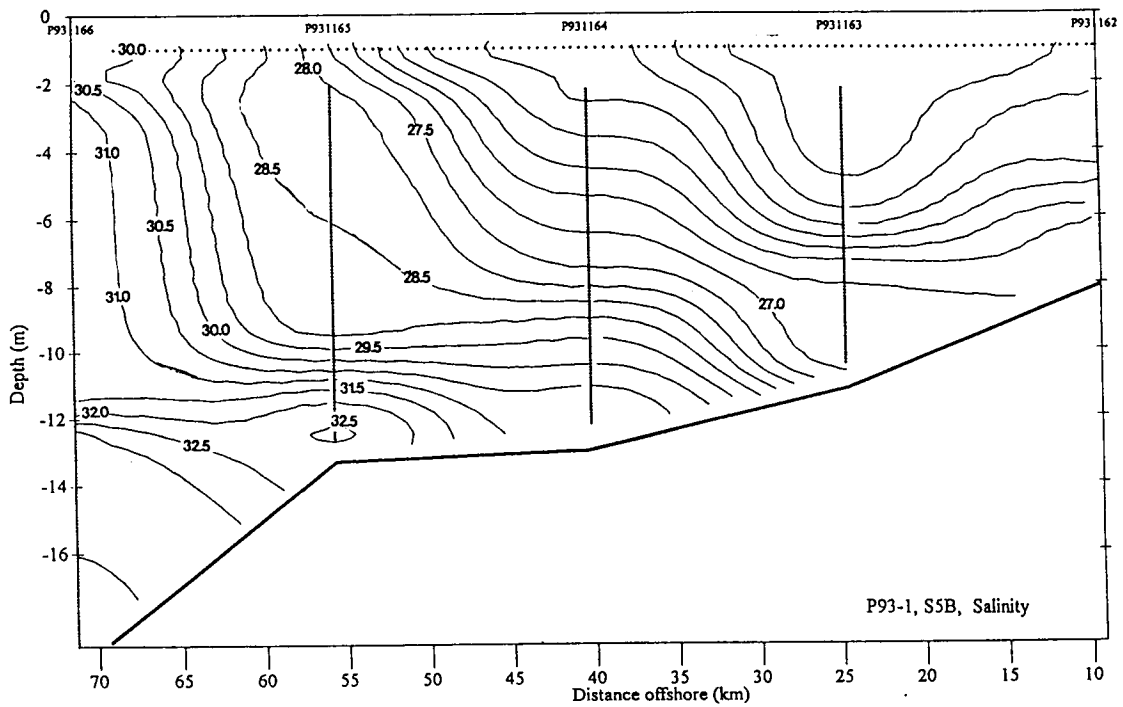
Figure 22. Section S5B salinity contours.
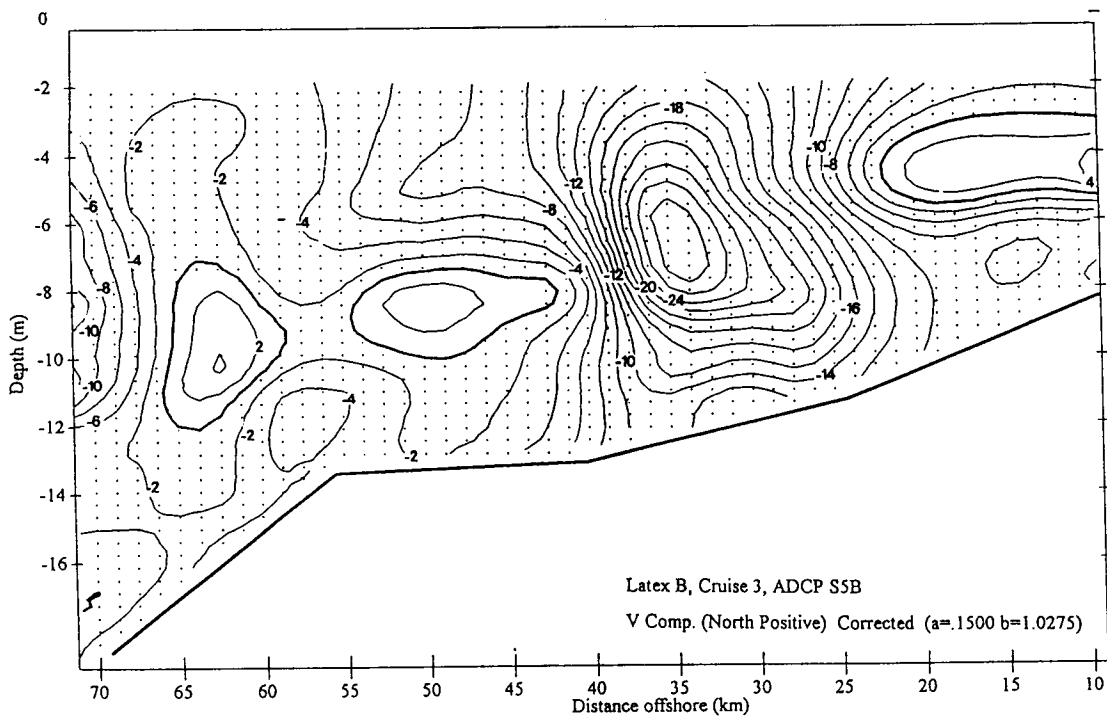
Figure 23. Crossshore velocities are weak over much of section S5B, but a strong onshore flow
was observed over the middle portion that does not satisfy a two-dimensional
continuity constraint.

section, but a strong onshore flow was observed over the middle section that does not satisfy a two-dimensional continuity constraint. Although not as well organized as the alongshore flow at S5, the east/west flow component at S5B, shown in Figure 24, is again predominantly downwind at the surface and upwind at depth. However, because of the wind reversal between the two sections the currents at S5 and S5B are basically mirror images of one another. To the extent that the survey measurements are synoptic, these results suggest that there is an alongshore convergence in the upper layer, and a divergence in the lower layer. The net onshore flow observed at this section may reflect its participation in a complex three-dimensional mass balance in response to the convergent wind field.

The salinity section at S6 is typical of the retrograde distributions observed east of Galveston Bay and is not presented here. Current data, also not presented, show moderate eastward flow and an upwelling cross-shore circulation.

Figure 25 shows the salinity distribution for the first section west of Galveston Bay (S7). The basic nature of the stratification is fundamentally different from that observed east of Galveston Bay. The retrograde structure associated with the buoyant coastal plume is missing, and in its place is hydrography typical of most coastal regions: a tight, horizontal pycnocline that fans shoreward reflecting coastal mixing. Within a few internal Rossby radii of the shore, the halocline (and pycnocline) may be upwelled or downwelled in response to wind-stress forcing. At S7 the wind was directed primarily onshore. Nevertheless, the halocline is slightly upturned, and the Doppler current profiles (Figures 26 and 27) show a vigorous northeastward flow in the upper half of the water column and a south southwestward flow in the lower region.

The next two sections, S8 and X1, are generally similar to S7. The winds are still directed primarily onshore, there is no downward deflection of the strong pycnocline that appears about 10 m off the bottom, and near-surface currents are generally upcoast (Figure 6). In contrast, along X2 there is some indication of a downwelling of the salinity field (Figure 28) by the action of the strong onshore wind. Strong coastal currents with magnitudes exceeding 0.3 m/s were observed within 15 km of shore. Currents were even stronger at X3 where they exceeded 0.5 m/s near shore. No hydrographic data were obtained along section X3.

B. Cruise IV, July 13-22, 1993 *(Stephen P. Murray)*

Cruise IV departed Cocodrie 0000 hours GMT on July 13, 1993, and proceeded to make observations from east to west along the cruise track of the summer regime hydrography and current fields as shown in Figure 29.

Ship-corrected winds along the cruise track (Figure 30) are in essential agreement with the coastal stations, with weak easterly winds at the beginning of the cruise (c.f. Grand Isle Figure 32), changing to stronger southerly winds off the Sabine Pass area, and to stronger southeasterly winds off south central Texas. The ship winds often show local short period weather effects not apparent in the widely separated C Man stations (Figure 31, 32).

1. Background

Cruise IV is of special interest in that in June, the month preceding the cruise, the Surface Current and Lagrangian Drifter Program (SCULP), funded by MMS to Scripps Institution of Oceanography, released an array of test drifters on the Louisiana shelf. Some of these drifters were still being tracked by the time of Cruise IV in mid-July. The movements of these "pre-SCULP" drifters significantly aid in interpreting the cruise results and especially in placing these results in a longer temporal and spatial context.
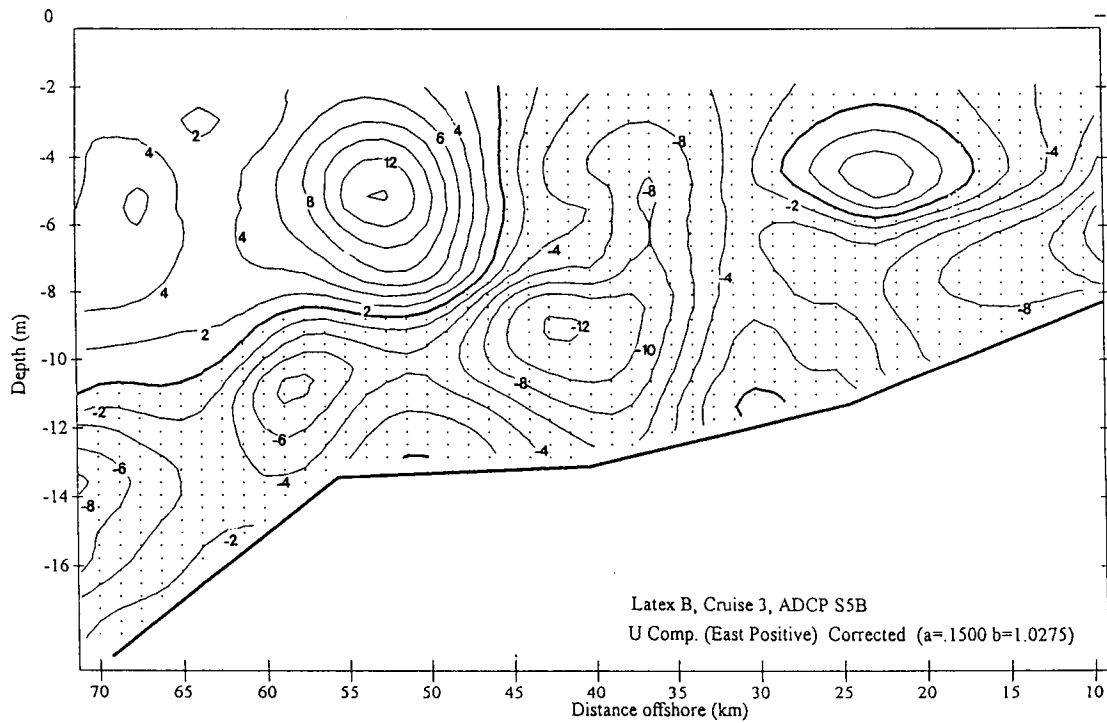
Figure 24. The east/west flow component at S5B is predominantly downwind at the surface and upwind at depth.
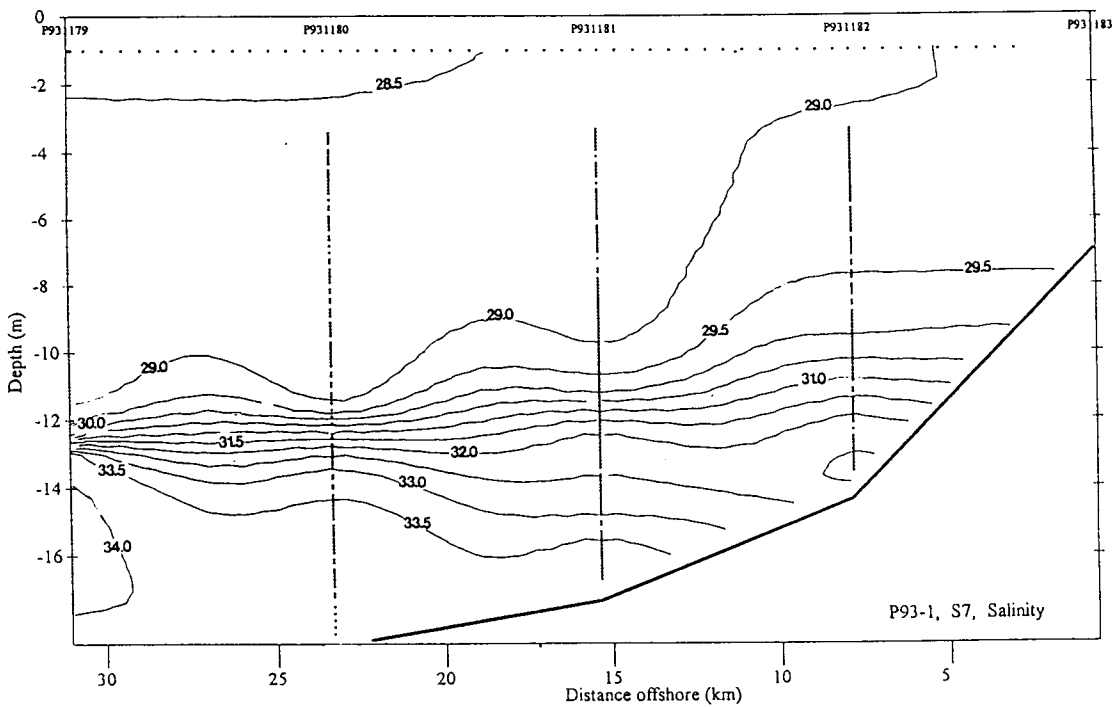
Figure 25. The salinity distribution for the first section west of Galveston Bay (S7).
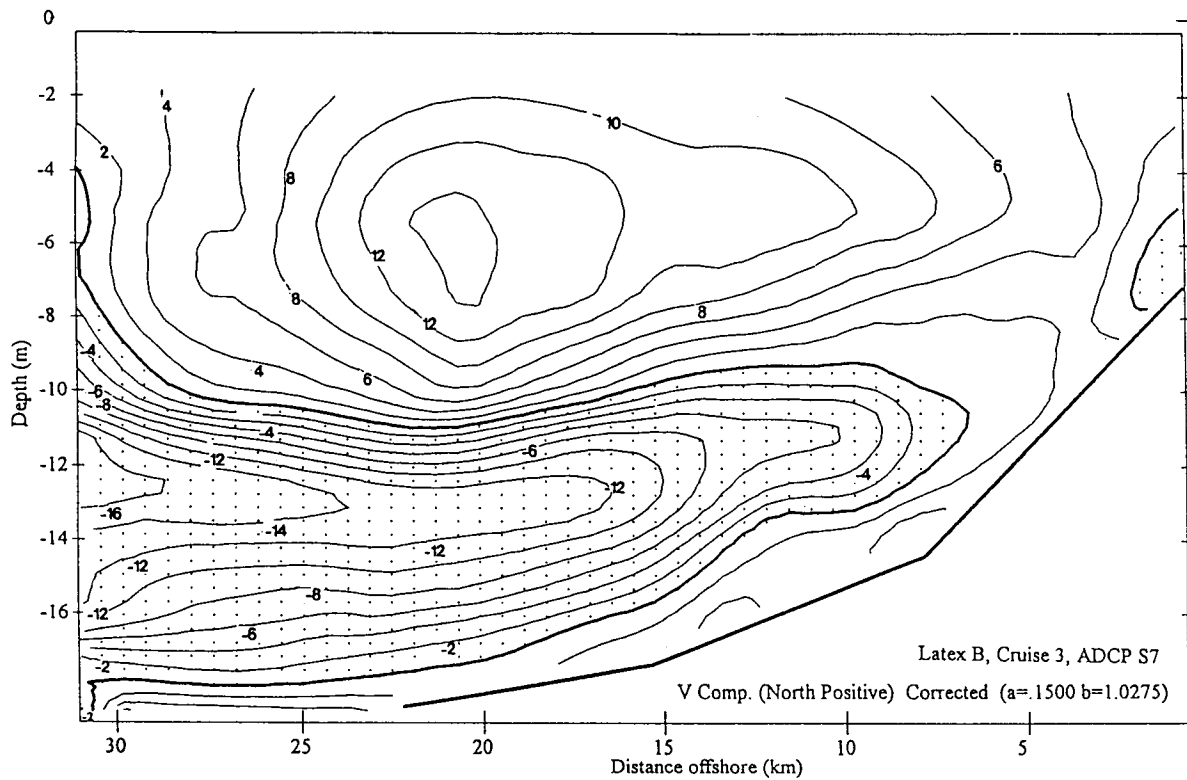
Figure 26. Contours of northward flow along section S7.
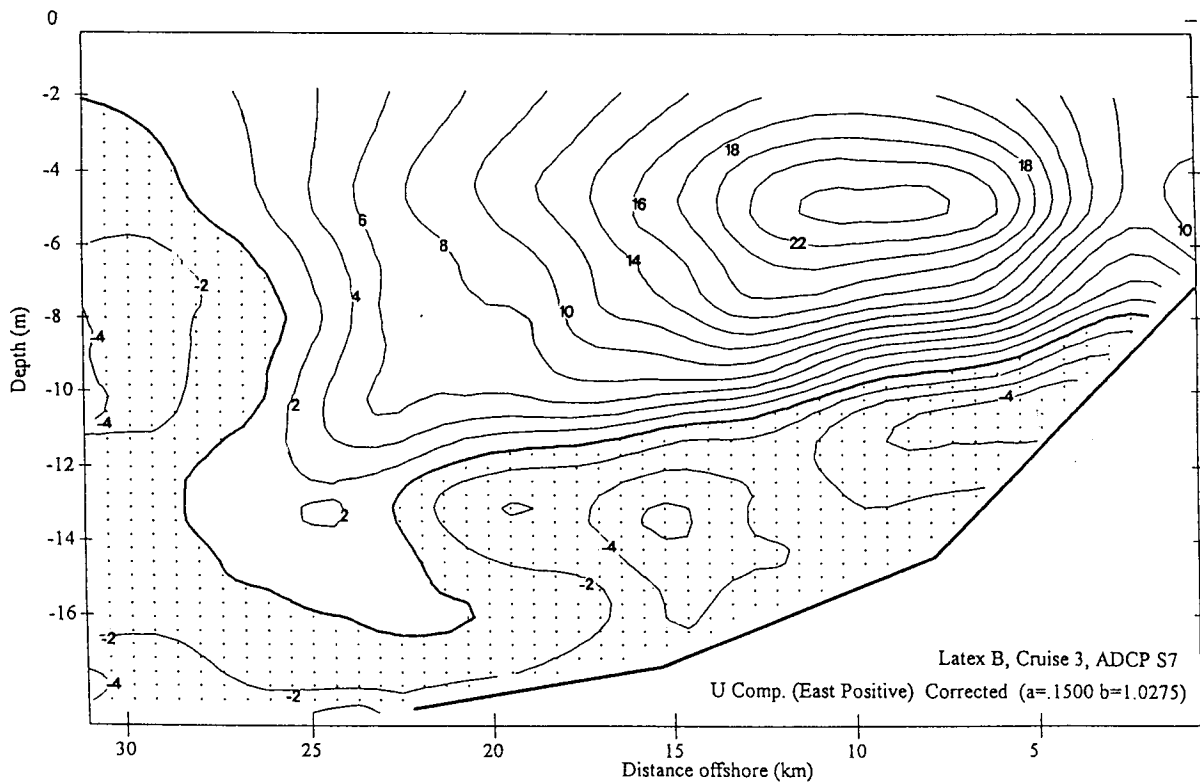
Figure 27. Contours of eastward flow along section S7.
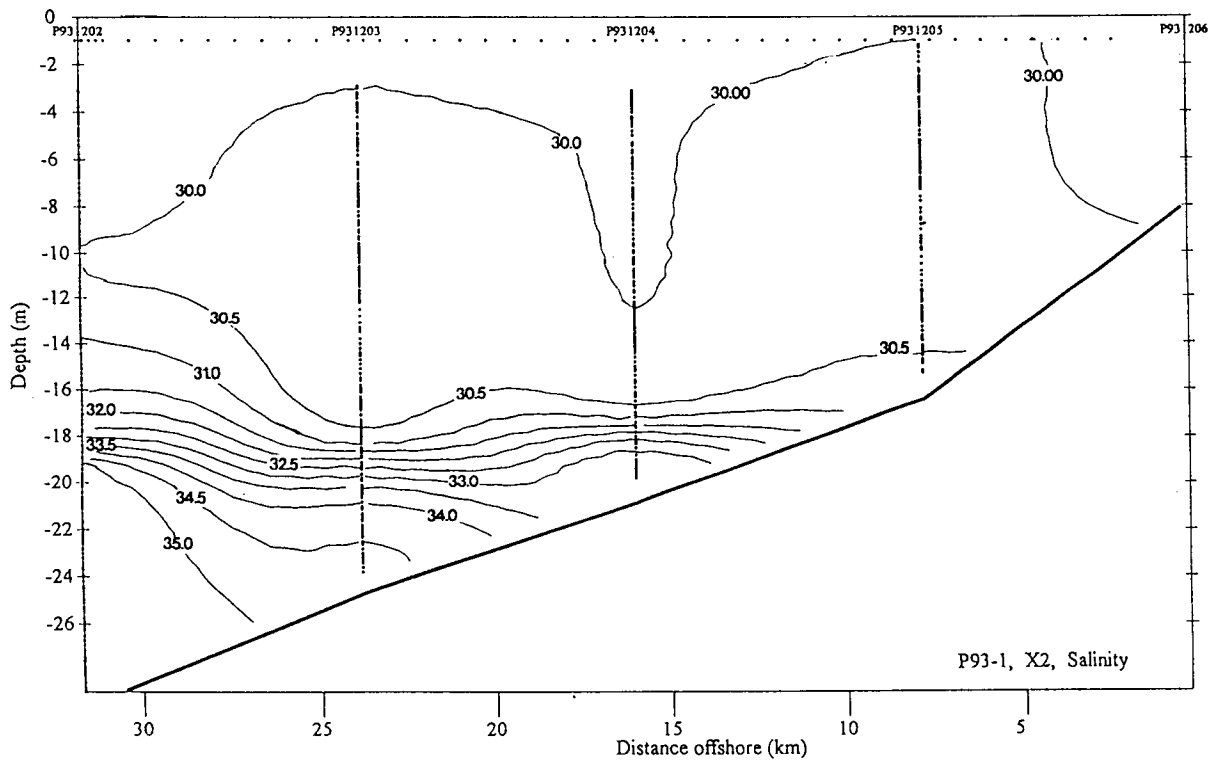
Figure 28. Salinity distribution along X2.

27
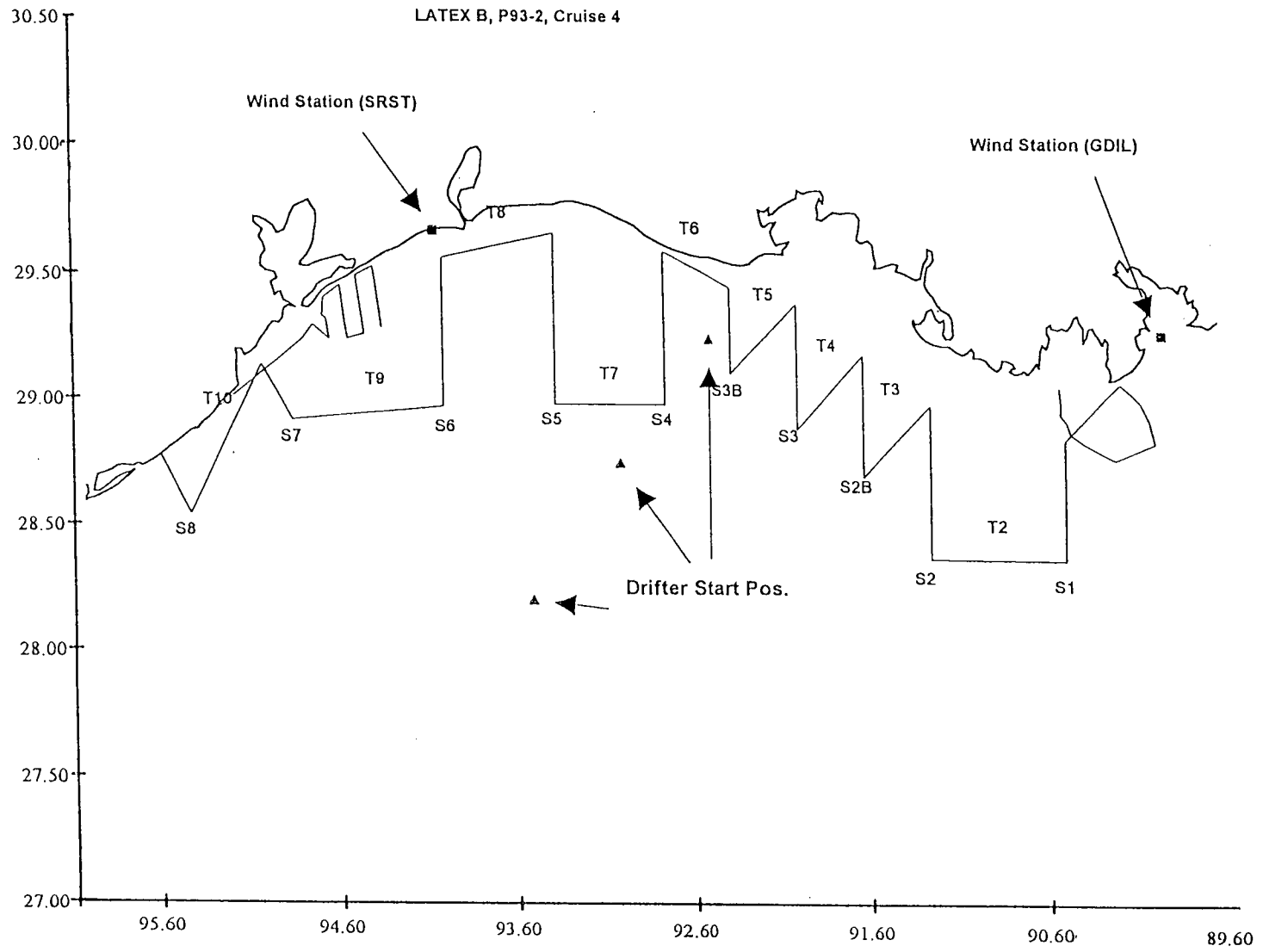
Figure 29. The track of LATEX-B Cruise IV showing locations of meteorological stations and drifter start points.
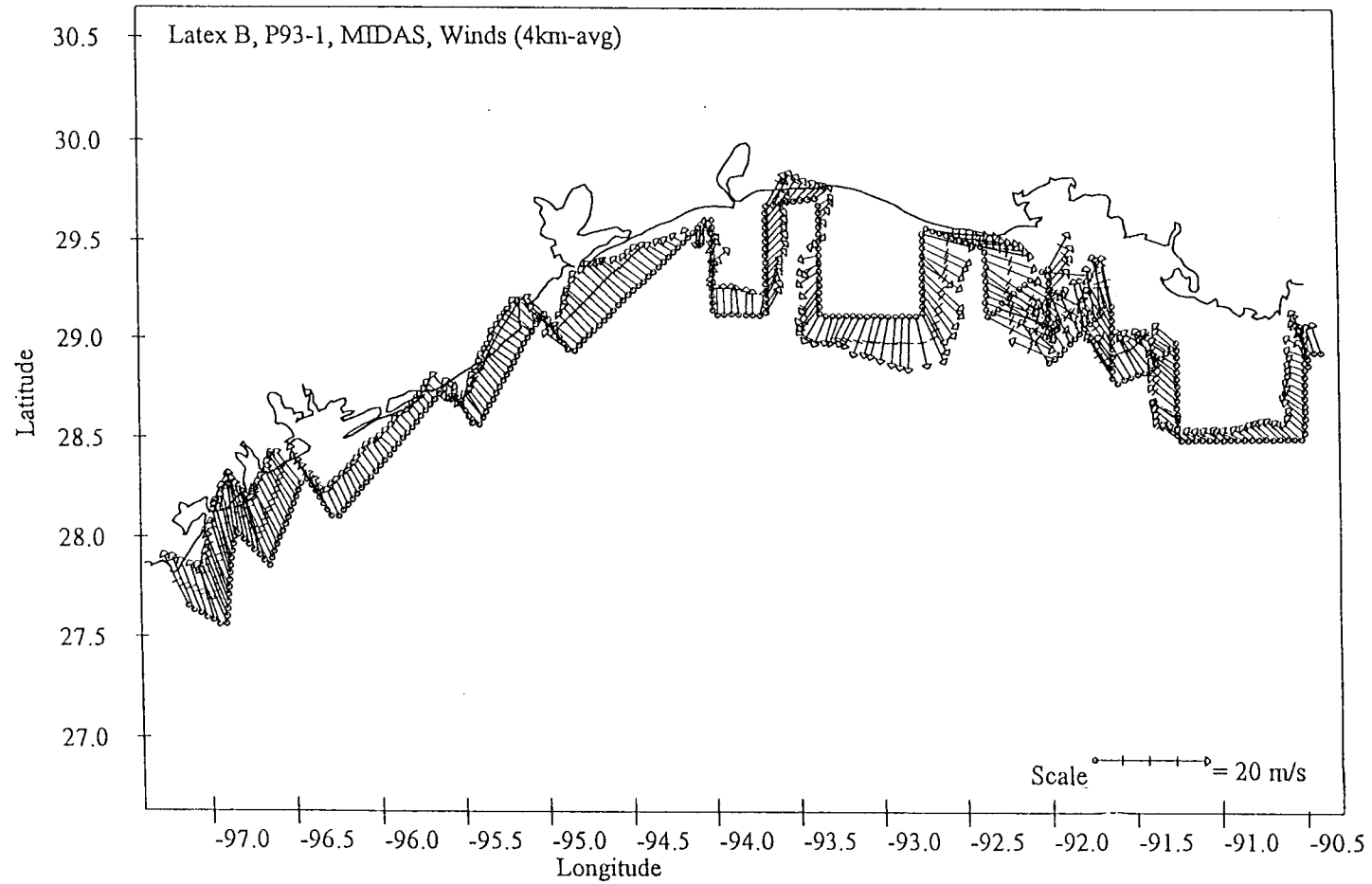
Figure 30. Shipboard "absolute winds, corrected for ship speed and heading, over the cruise survey. These data were collected by the Multiple Interface Data Acquisition System (MIDAS) aboard the R/V *Pelican.*

a. Background Meteorology. In addition to the buoyancy forcing provided by the fresh water discharge from the Mississippi and Atchafalaya Rivers, the coastal wind field is another primary driving force. Study of the Climate Diagnostics Bulletins (NOAA, 1993) in conjunction with the C-MAN coastal wind stations (Figure 31), produces a good understanding of the synoptic scale wind forcing over the coastal current region. By 7 am June 1 CST a cold front had just passed southward over the entire LATEX coast from the Mississippi Delta all the way south to Brownsville. Figure 31 shows that the associated northerly winds behind the front blew all day of June 1 at Grand Isle and Sabine Pass (Sea Rim State Park) while only lasting about 12 hours at the southernmost station at Port Aransas. On June 2 a long period of southerly and southeasterly wind sets in which peak around June 9, but continued with diminishing speeds until June 13. The persistence of a high pressure cell (HPC), a manifestation of the Bermuda high pressure cell, centered over the eastern states (Tennessee, the Carolinas) and the adjacent shelf, was responsible for these southeasterly winds.

By June 13 this HPC had dissipated to the extent that the synoptic wind almost vanished, and Figure 31 clearly shows a sea-land breeze circulation system at the 3 coast stations on June 14, 15, and 16. On June 17 and 18, a new HPC in the same region re-established the easterly-southeasterly wind regime over the LATEX coast. Abruptly on June 19, the intense cyclonic circulation of Tropical Storm Arlene appears off the south Texas coast. The intense curvature of the isobars and strong winds of the storm extended 150 nm north to the Galveston area, and the orientation of Arlene brought strong northeasterly winds to the western Louisiana and Texas coastal region. The signature of Arlene is clearly seen in Figure 31 in the Port Aransas winds on June 18 and 19, blowing from the northeast and east. The Sea Rim-Sabine Pass winds shifted to northeasterly for a shorter interval on June 18-19, and the Grand Isle winds appear unaffected by the storm's passage (Figure 31).

For the remainder of June high pressure cells persisted over the central eastern seaboard states. These HPCs brought strong southeasterly winds to Port Aransas, southerly winds to the Sea Rim Sabine Pass area, and much weaker variable winds with southerly components to the east central Louisiana-Grand Isle coast.

The first half of July (Figure 32) is a classic summer wind pattern. The Daily Weather Maps repeatedly showed only a very weak atmospheric pressure gradient across the northern LATEX region. The central and south Texas region, however, had an appreciably higher pressure gradient. There were strong southeasterly winds off Port Aransas, strong southerly winds off Sea Rim-Sabine Pass, and weaker and more variable southerly and southeasterly winds off Grand Isle. A strong wind stress gradient acted to push the south and central Texas coastal water up to the north and east toward the weak wind stress region off Louisiana.

This summer pattern is perturbed only briefly on July 21-22 when a mesoscale low pressure cell forms over Georgia and Alabama. The ensuing cyclonic circulation brought northwesterly winds to the east central Louisiana coast as seen in the Grand Isle Station data in Figure 32. In the last four days of July, the synoptic scale pressure gradients weakened considerably and diurnal land-sea breeze effects are seen in the Southwest Pass, Grand Isle, and to a lesser extent in the Sea Rim-Sabine Pass wind data (Figure 32).

b. Satellite Data Acquisition. Several satellite image data sets were obtained over the LATEX region during July 1993, which have helped in interpreting the hydrographic measurements. A clear-sky image was obtained on July 8, about 6 days before the cruise started, which revealed an extensive region of warm water (> 30° C) over the northern portion of the LATEX shelf (Figure 33). Between 91° and 95° W longitude, approximately 75% of the continental shelf was covered with this warm water mass. It is thought that this warm water mass reveals the spatial extent of buoyant river waters across the LATEX shelf west of the Mississippi

30

Cruise 4, Winds June

Grand Isle

Sea Rim State Park

Port Aransas

Scale ⊢———⊣ = 20 knots
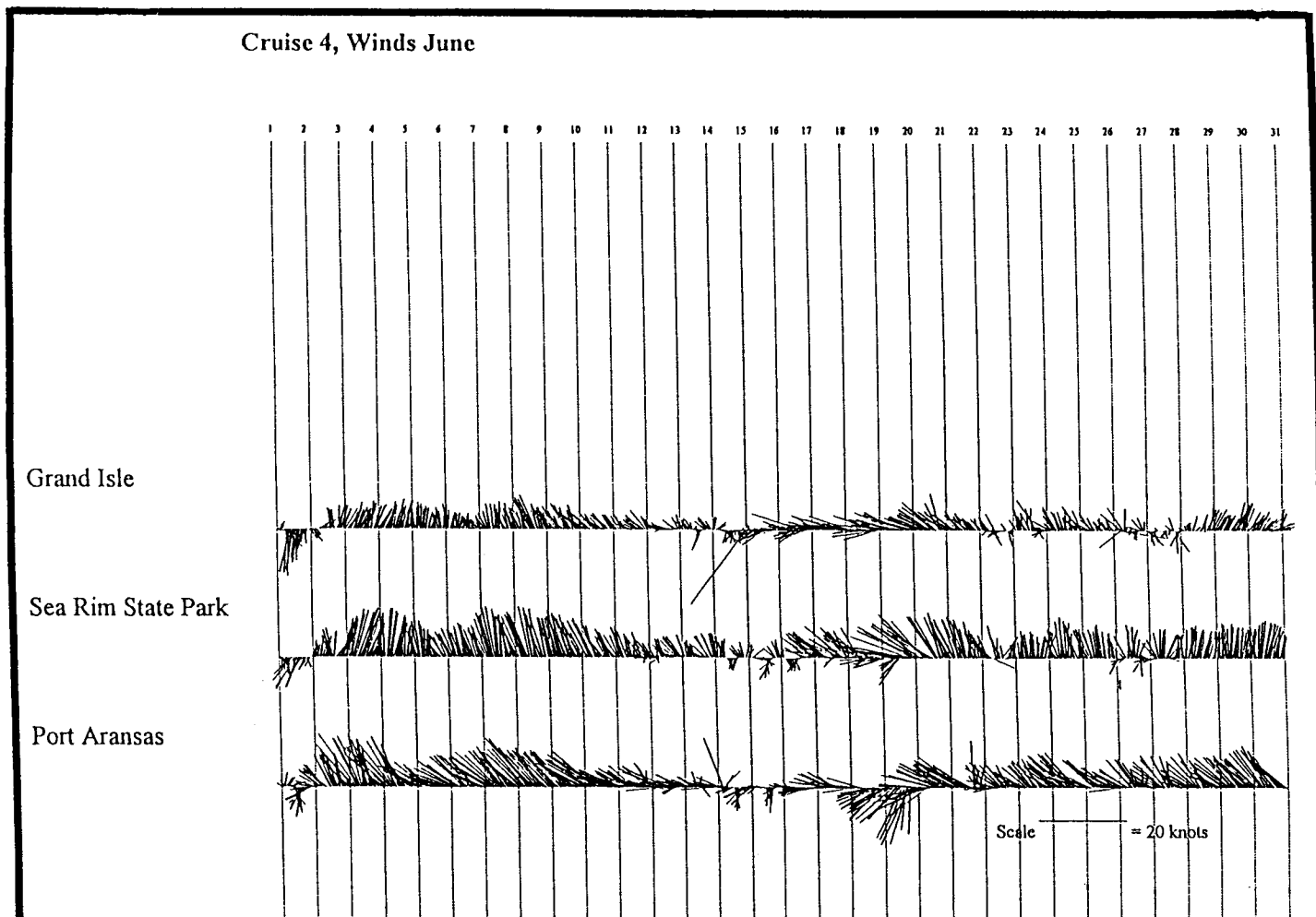
Figure 31. Wind vectors from four Coastal-Marine Automated Network (C-MAN) stations along the coast, June 1993. See Figure 1 for locations of the CMAN instruments.

Cruise 4, Winds July (1-30)

NDBC Buoy 30.10N 88.80W

Southwest Pass

Grand Isle

Sea Rim State Park

Port Aransas

Scale ———— = 20 knots
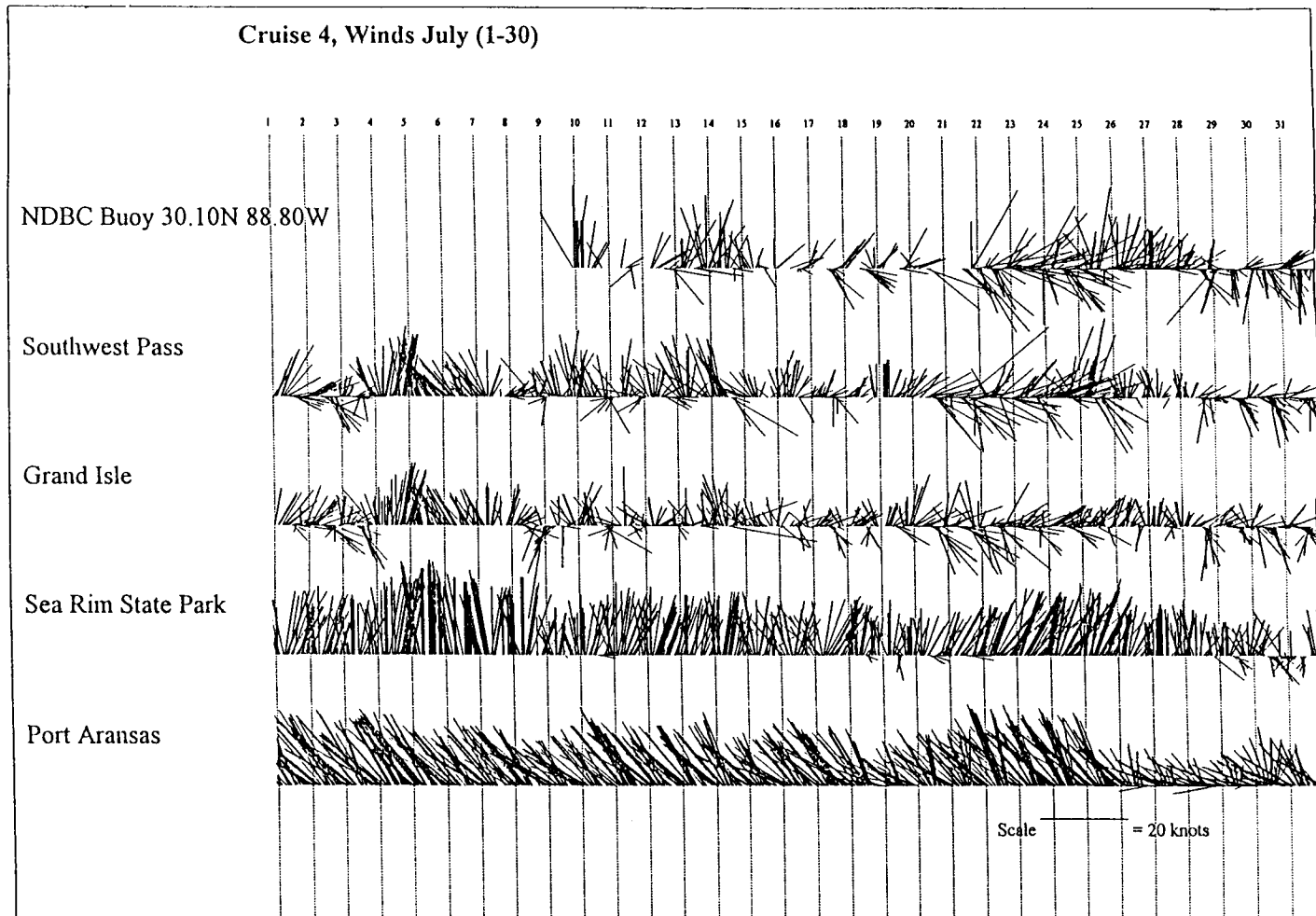
Figure 32. Wind vectors from four C-MAN stations and the NDCB buoy just east of the Mississippi delta, July 1993. See Figure 1 for locations of the instruments.

8 July 93 1039 Z
SST analysis

> 30 C

27 to 30 C

-200

-200

<27 C

< 27 C

28N

96W

94W

92W
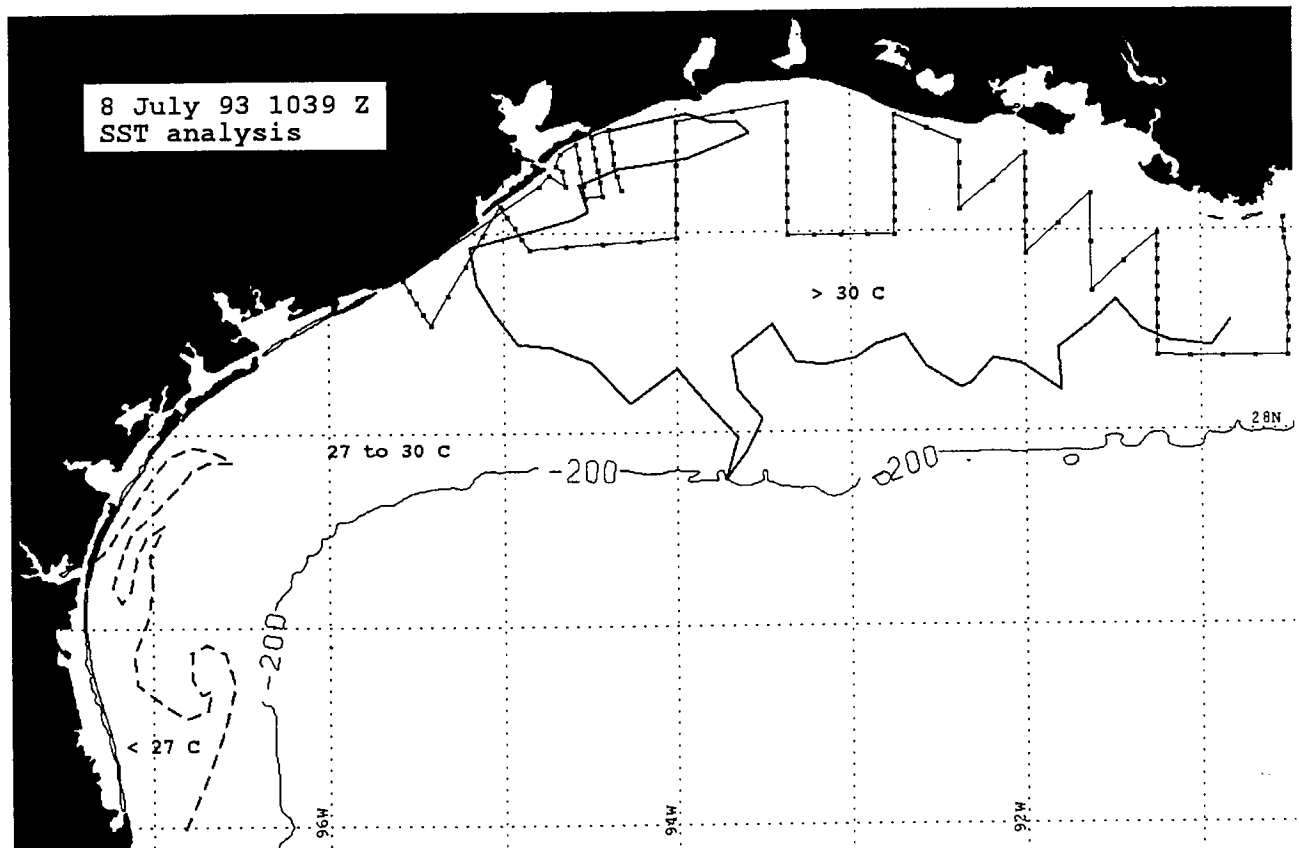
Figure 33. Surface temperature frontal analysis of July 8, 1993, revealing three distinct thermal regimes on the LATEX shelf. Water temperatures >30° C depict the distribution of river waters across the continental shelf. Water temperatures < 27° C reveal the spatial distributionof cool upwelled waters on the south Texas shelf. Waters of 27° to 30° C reveal a mixing zone between the two. The Cruise IV track is overlain for reference.

delta. River discharge was abnormally high during both the spring and summer of 1993 (Figure 34), thus helping to explain its widespread distribution across the shelf. Fortuitously, during the summer months, Atchafalaya and Mississippi River waters are sometimes traceable by their warmer temperatures, particularly in the late afternoon satellite imagery. During July 1993, cruise measurements obtained along S2 revealed the river water to be a thin surface lens of low-salinity water approximately 4-5 meters deep, separated from denser shelf water below by a strong pycnocline (Figures 35a,b). Thus, in regions where river water is found at the surface, the surface mixed layer is relatively shallow and the incoming solar radiation is confined to the top few meters producing relatively warm surface waters.

Further south, along the south Texas coast, cool waters (< 27° C) were observed over a relatively large area from south of Brownsville to 28° N (Figure 33). It is hypothesized that the prevalence of cool water along this coastline and on the shelf was caused by wind-forced upwelling as the coolest waters were located adjacent to the coast and the prevailing wind regime was upwelling favorable. The presence of northward extending cool filaments are suggestive of the prevalence of northward surface flow along the southern and mid-portions of the Texas shelf. Although the LATEX-B cruise did not traverse these cool features, northward flow was encountered along the southernmost lines, even 11 days after acquisition of this July 8 image.

The next image yielding substantial information of surface temperature or suspended sediment distributions was obtained on the afternoon of July 17, 1993 (2142 Z). The 6 mg/l suspended sediment contour reveals that the most turbid region along the coast was located seaward of Atchafalaya Bay (Figure 36). The Atchafalaya sediment plume extended slightly further to the southeast than in any other direction, although the 6 mg/l contour was situated about mid-way along the LATEX-B lines. The synoptic satellite observations compare surprisingly well with the (non-synoptic) surface suspended sediment measurements obtained on the cruise (Figure 37). In both datasets suspended sediment distributions were relatively high along the Chenier coast, in the Sabine and Galveston plumes, and along the coast south of Galveston. The bay/river plumes are often regions of high turbidity as they represent discharges from the more turbid rivers and bays. The high turbidity regions adjacent to the Chenier plain and south of Galveston were probably attributable to wind resuspension of nearshore sediments as the wind was relatively strong and directed onshore for most of the cruise.

The SST information obtained on July 17, 1993, at 2142 Z (Figure 38) is particularly interesting as the ship crossed a coastal temperature/salinity/density front twice within 9 hours of image acquisition (between July 17, 1700 Z, and July 18, 0200 Z). The image data revealed a thermal front ranging from 0.4 to 0.7° C running approximately east-west, becoming narrower towards the west. The ship's location at the time of image acquisition is depicted with an asterisk. The Galveston plume was observed as a warmer water mass lying to the southwest of this coastal front. Lines S5 and S6 crossed the coastal front (Locations, Figure 38). Along line S5, a surface thermal front was encountered in close proximity to the third station from the coast (Figure 39), agreeing well with the frontal position as observed in the satellite imagery. Along S6, the surface thermal front was encountered between the 2nd and 3rd stations from the coast (not shown). The satellite data depicted the front nearer to the 2nd station from the coast. This slight discrepancy may have resulted from a small movement in the front over the 5 hours between satellite image acquisition and the collection of data. The cruise data revealed this relatively warm coastal water mass as a thin lens of low salinity water approximately 4 meters deep, which extended about 25 km from the coast (Figure 39). It is postulated that this near-coastal water mass had its origins in Atchafalaya Bay to the east for several reasons. The combination of cruise measurements and image data revealed that this relatively warm, low salinity coastal water mass became more narrow and shallow in a westward direction suggesting an origin to the east. In addition, the image data revealed the Galveston plume as having its own distinct front, separate from that of this coastal water mass (Figure 38). The low salinity water mass was probably confined close to the coast by
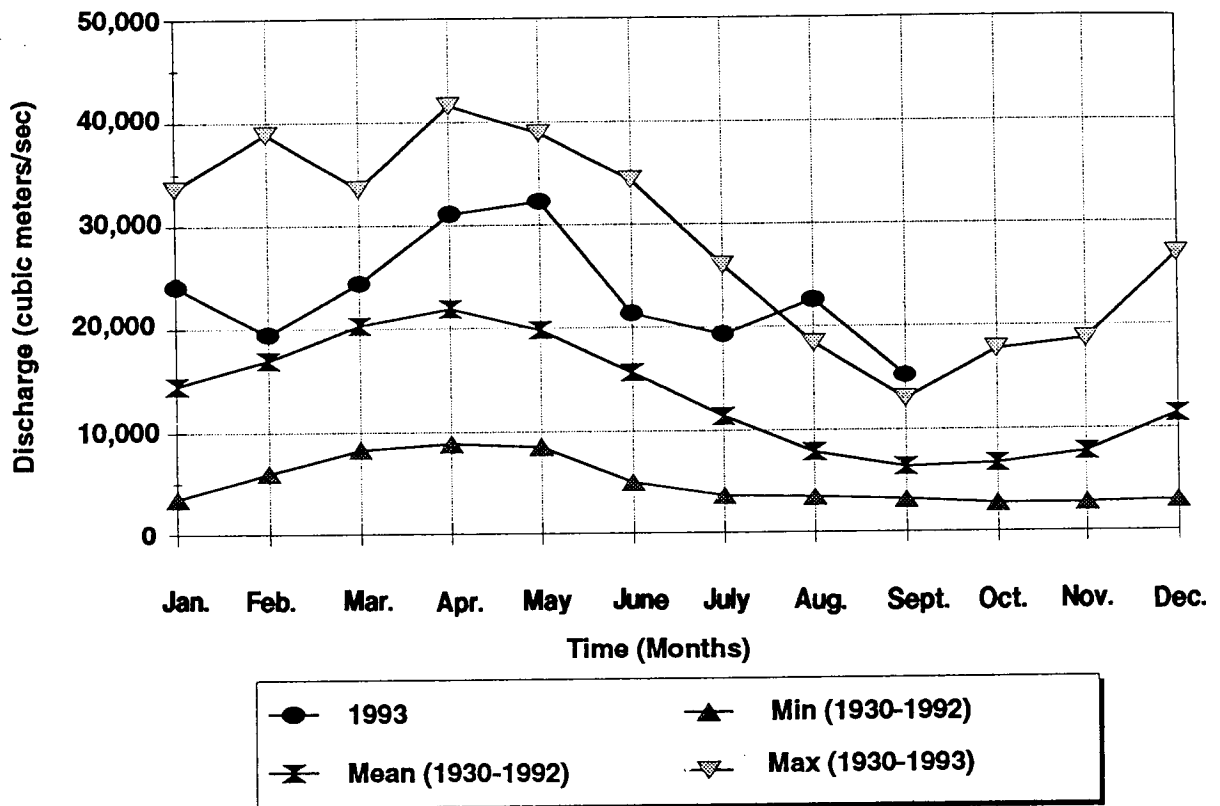
Figure 34. Mississippi River discharge for January through September 1993 in comparison with long-term monthly means, maxima and minima from 1930-1992 (from Walker et al., 1994).
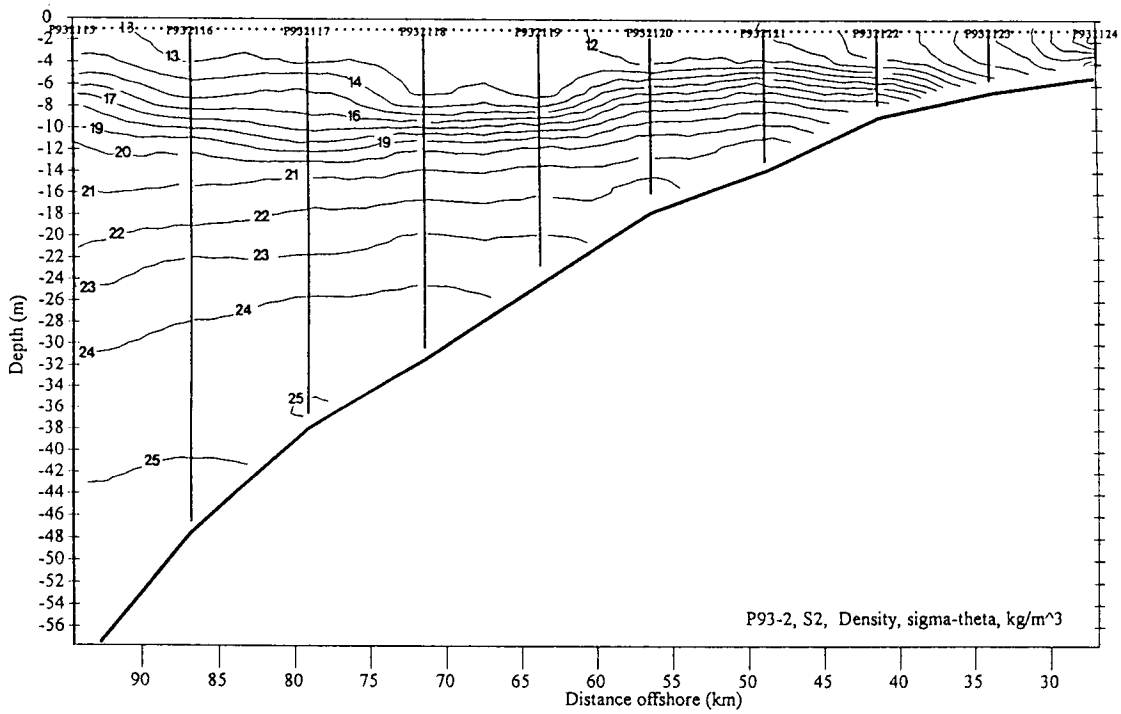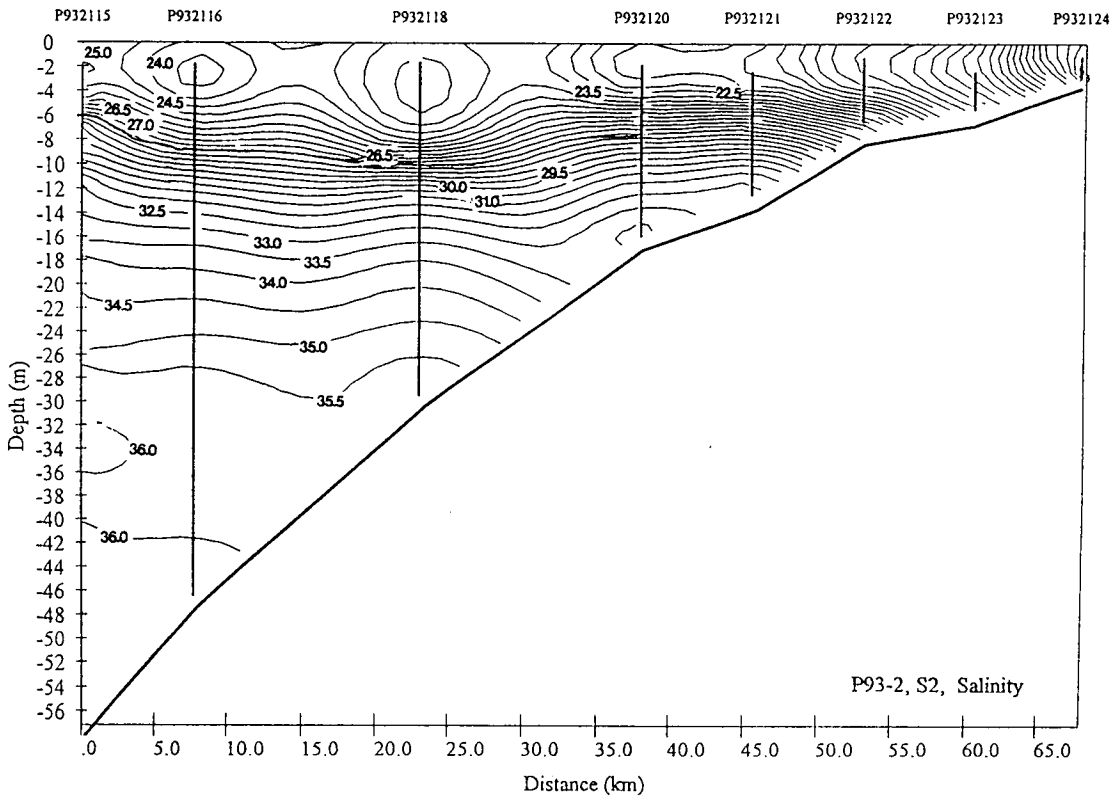
Figure 35. Salinity (upper panel) and density sections (lower panel) along line S2 in July 1993.
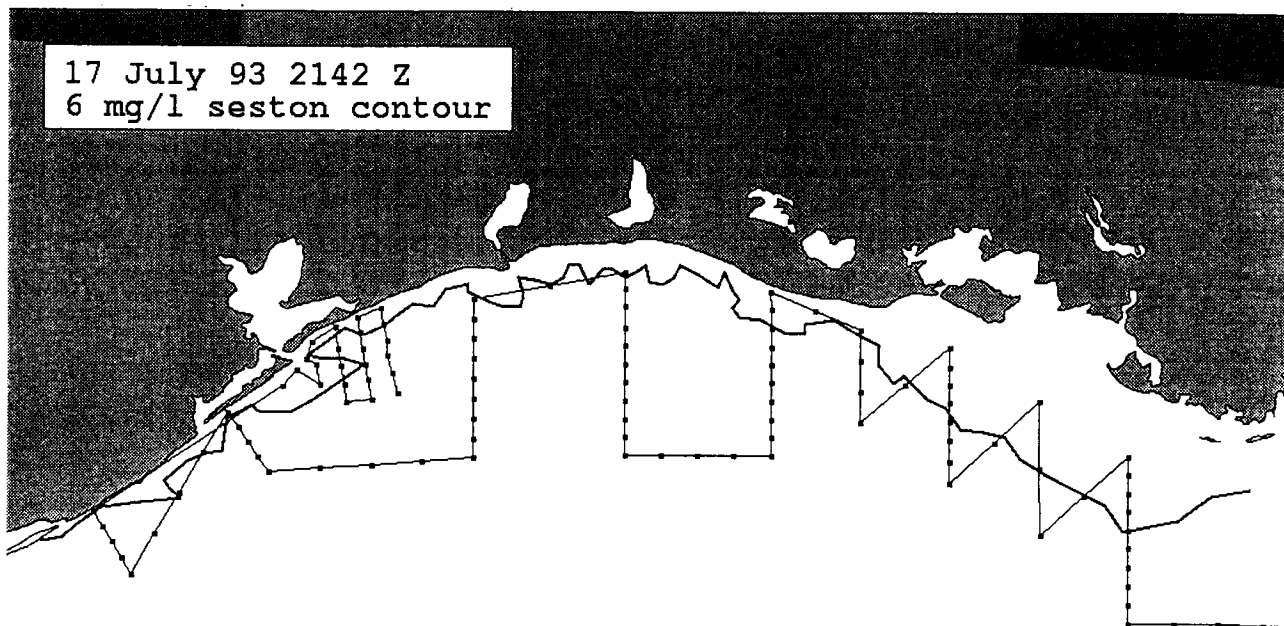
Figure 36. Turbidity patterns as revealed by the 6 mg/l suspended sediment (or seston) contour on July 17, 1993. Cruise IV track has been overlain for reference.
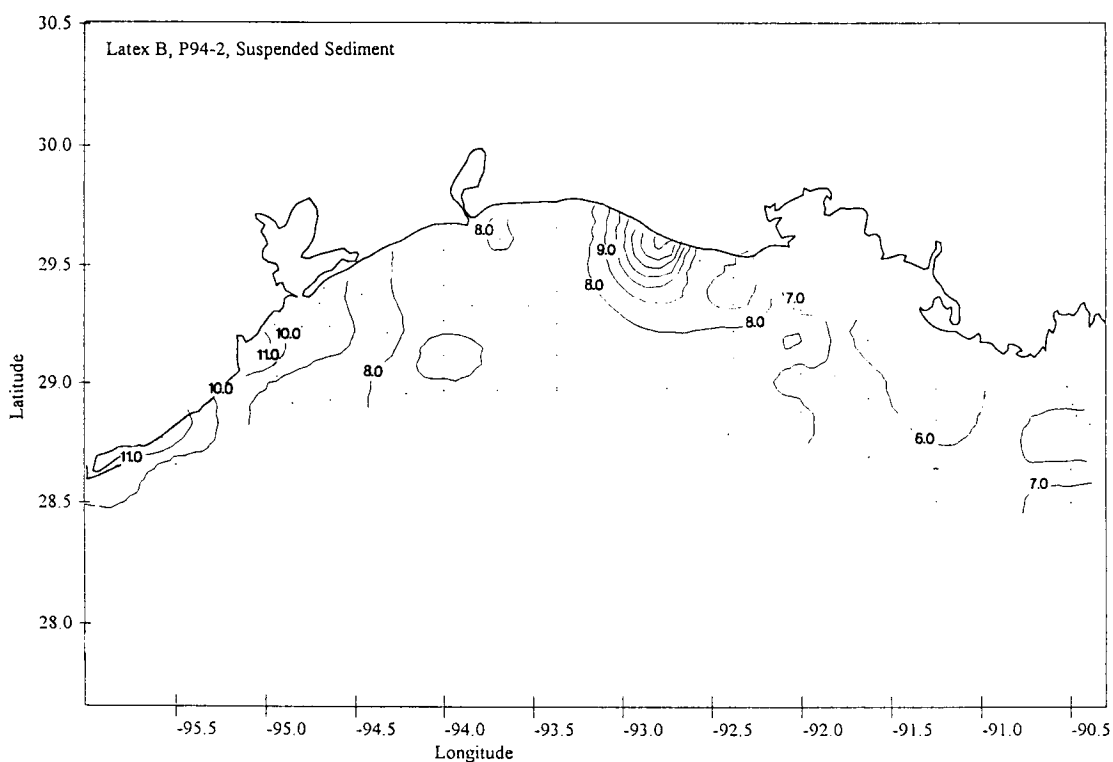
Figure 37. Suspended sediment distributions in mg/l as determined from surface water collection during Cruise IV, July 1993.
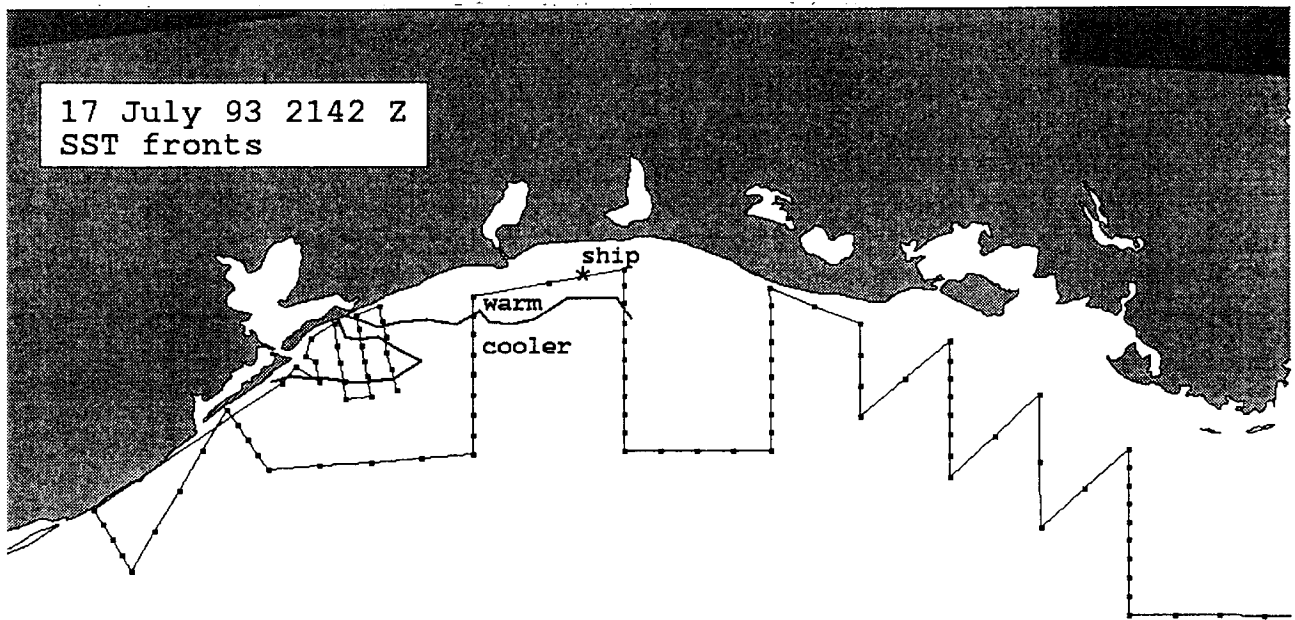
Figure 38. Surface temperature fronts on July 17, 1993 (2142 Z), overlain with the Cruise IV cruise track. The position of the ship is depicted with an asterisk.
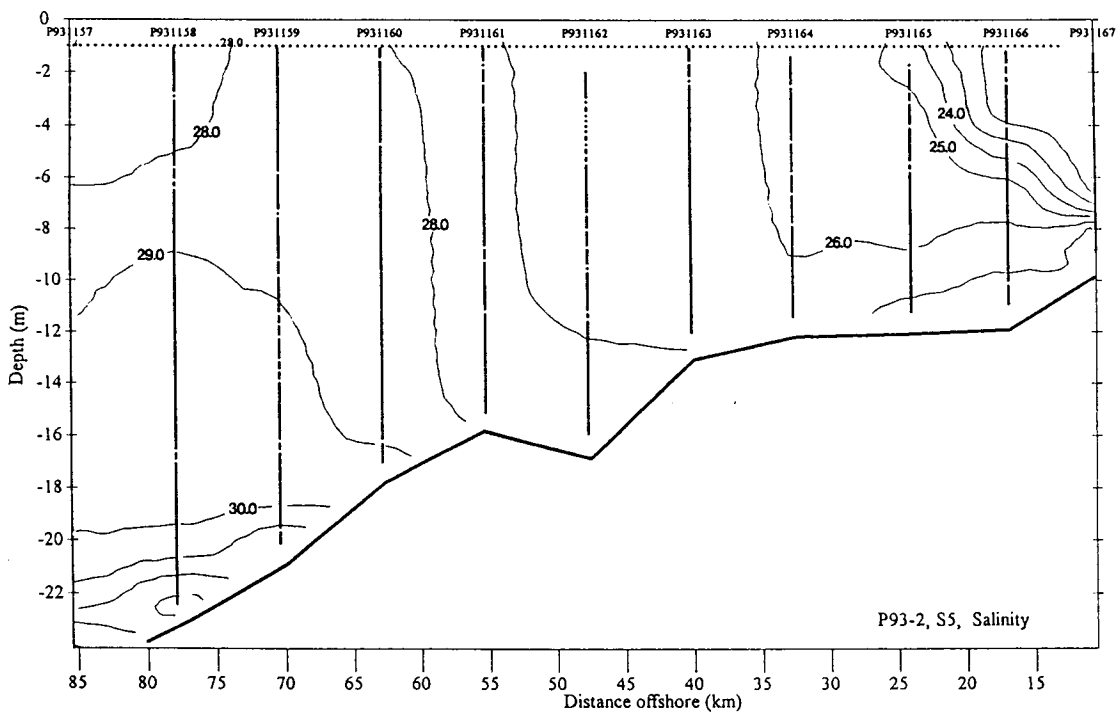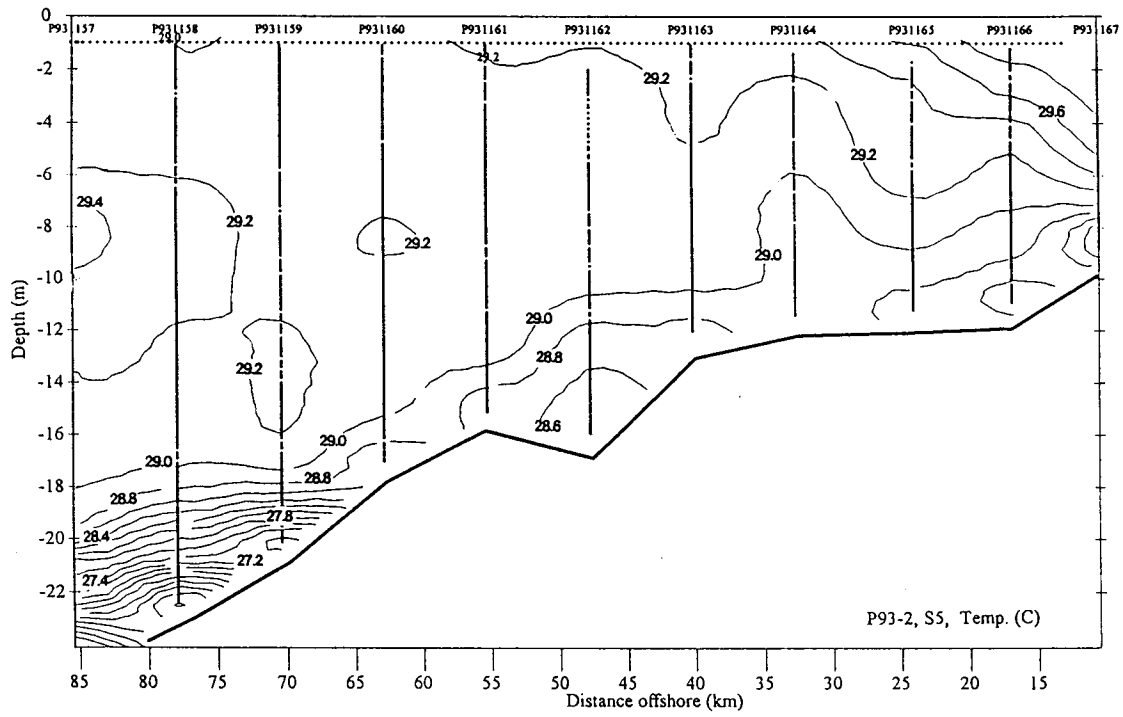
Figure 39. Temperature (upper panel) and salinity (lower panel) sections along line S5 in July 1993.

the persistent southerly winds, which became relatively strong (10 m/s) about 24 hours before image acquisition.

Along the return leg of the cruise, strong currents were measured south of Atchafalaya Bay between July 21 (2300 Z) and July 22 (0400 Z). The ADCP current vectors are overlain on the suspended sediment fronts of July 20, 1993 (2109 Z) in Figure 40. These relatively contemporaneous datasets reveal that the strong currents were encountered just seaward of the main Atchafalaya plume front. In fact, a note in the cruise log reported crossing a distinct front at 2300 on July 21. This observation suggests that the Atchafalaya plume front had moved south over the 26 hours between the time of image acquisition and the onset of strong currents along the return leg. Abnormally strong southeastward setting currents of 0.8 to 1.5 kn were experienced at the Bullwinkle rig (Location, Figure 40) between July 19 (1300 Z) and July 20 (1700 Z) (G. Forristall, OMNET Communication, July 20, 1993). Maximum currents occurred at 0600 Z on July 20. Although this rig was approximately 80 km southeast of the LATEX-B cruise track, the close correspondence in time of the measurements may reveal important information on the spatial scales of circulation on the LATEX shelf. The strong shelf-edge currents at Bullwinkle were attributed to Eddy Whopper, which detached from the Loop Current in early June (Walker et al., 1993). By mid-July/early August Eddy Whopper was oriented north-south such that the northern margin was in close proximity to the shelf edge between 90° and 92° W longitude (Figure 41). If anticyclonic circulation associated with Eddy Whopper was indeed responsible for the strong currents encountered along the return track of the July 1993 LATEX-B cruise then one can conclude that mid- and inner shelf circulation in this region is sporadically affected by detached Loop eddies. It is relevant to point out that Eddy Vasquez affected circulation south of Atchafalaya Bay on the outer and middle shelf regions during October 1992 (Walker et al. in Murray, 1994; Walker et al., in press).

These comparisons of satellite imagery with LATEX-B cruise measurements have revealed that the temperature and turbidity patterns observed in the atmospherically corrected satellite data are often indicative of the surface mixed layer, rather than just the "skin" of the ocean. The satellite data can, in many instances, be used to identify the boundaries between distinct water mass types.

   c. Pre-SCULP Drifters (June-July 1993). A group of 15 surface layer drifter were released across the Louisiana shelf in early June 1993 by an SIO/MMS oil spill-drifter program. The range of the initial positions (the drifter patch) is included in Figure 29. Analysis of the drifter tracks suggest four major flow episodes that are related to the wind records and are illustrated by drifter #15 in Figure 42.

   Episode 1. From June 2 through June 9, the surface layer motion across the drifter patch was onshore to the northeast. This is illustrated by drifters 14, 15, 19, and 21. Beginning about June 11, the wind decelerated steadily into a lull period ending mid-day of June 16.

   Episode 2. Drifter tracks 14, 18, 20, and 21 for June 11 through 17 indicate that during this lull period, the surface layer moved back downcoast to the west, probably because the westward-directed pressure gradient relaxed after being strengthened by the strong upcoast winds prevalent during the first half of June. Note drifter 19 appears trapped just south of the Atchafalaya Bay mouth during this episode.

   Episode 3. Strong easterly winds begin on June 17 at all three C man stations from South Texas to Grand Isle. The strong (25-30 knots) winds from the northeast and north of Tropical Storm Arlene on June 18-19 drove all the drifters downcoast to South Texas at high speeds (1-2 knots). As Arlene moved ashore between Brownsville and Port Aransas, early on June 20, its still strong trailing edge winds from the southeast now opposed the inertia of the coastal jet and dramatically slowed and stopped the drifter movements to the south and west.
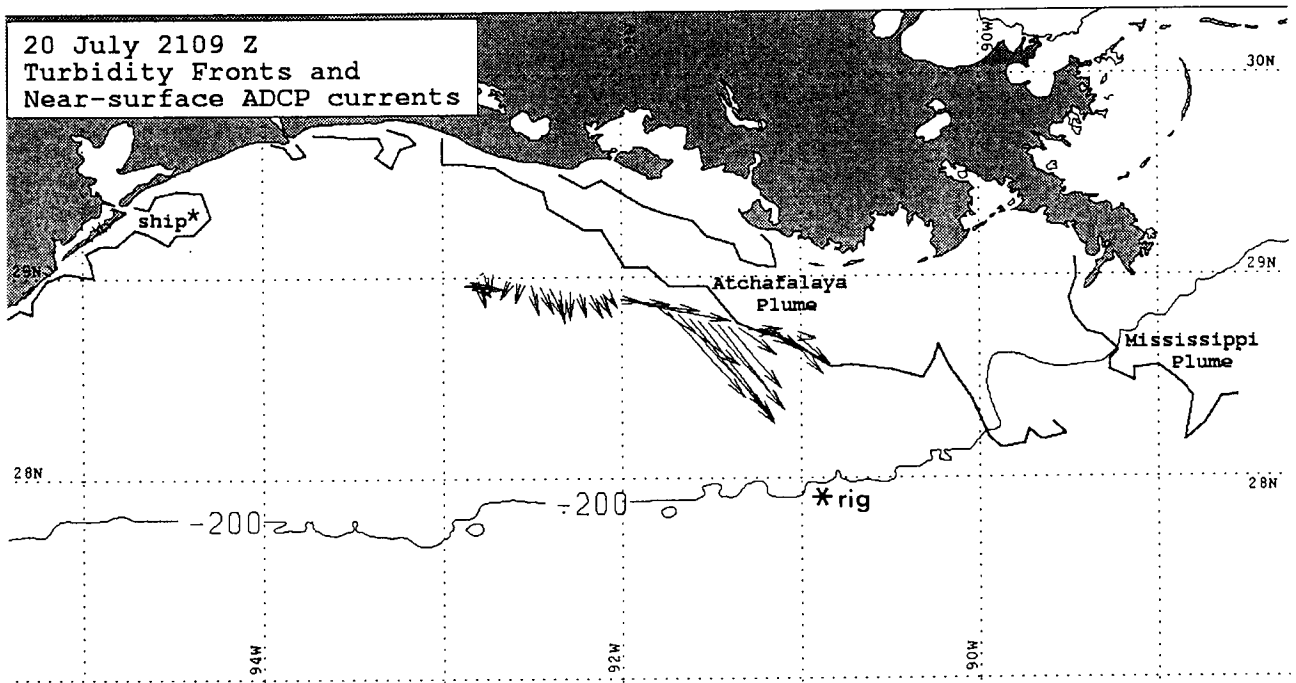
Figure 40. Turbidity fronts as observed in satellite imagery of July 20, 1993 (2109 Z), with near-
surface ADCP current vectors superimposed. The ship was positioned in the
Galveston plume at the time of image acquisition. The position of the Bullwinkle rig is
shown south of the Atchafalaya plume and just seaward of the 200 m isobath.

41

33

-96 -94 -92 -90 -88 -86 -84 -82 -80

W

COOL FILAMENT
W
W

28

COOL UPWELLED WATER

CLOUD

C

EDDY
WHOPPER

VASQUEZ

26

C

COOL UPWELLED
WATER

24

22

20

AUGUST 93 1046 CH 3

COASTAL STUDIES INSTITUTE

LOUISIANA STATE UNIVERSITY
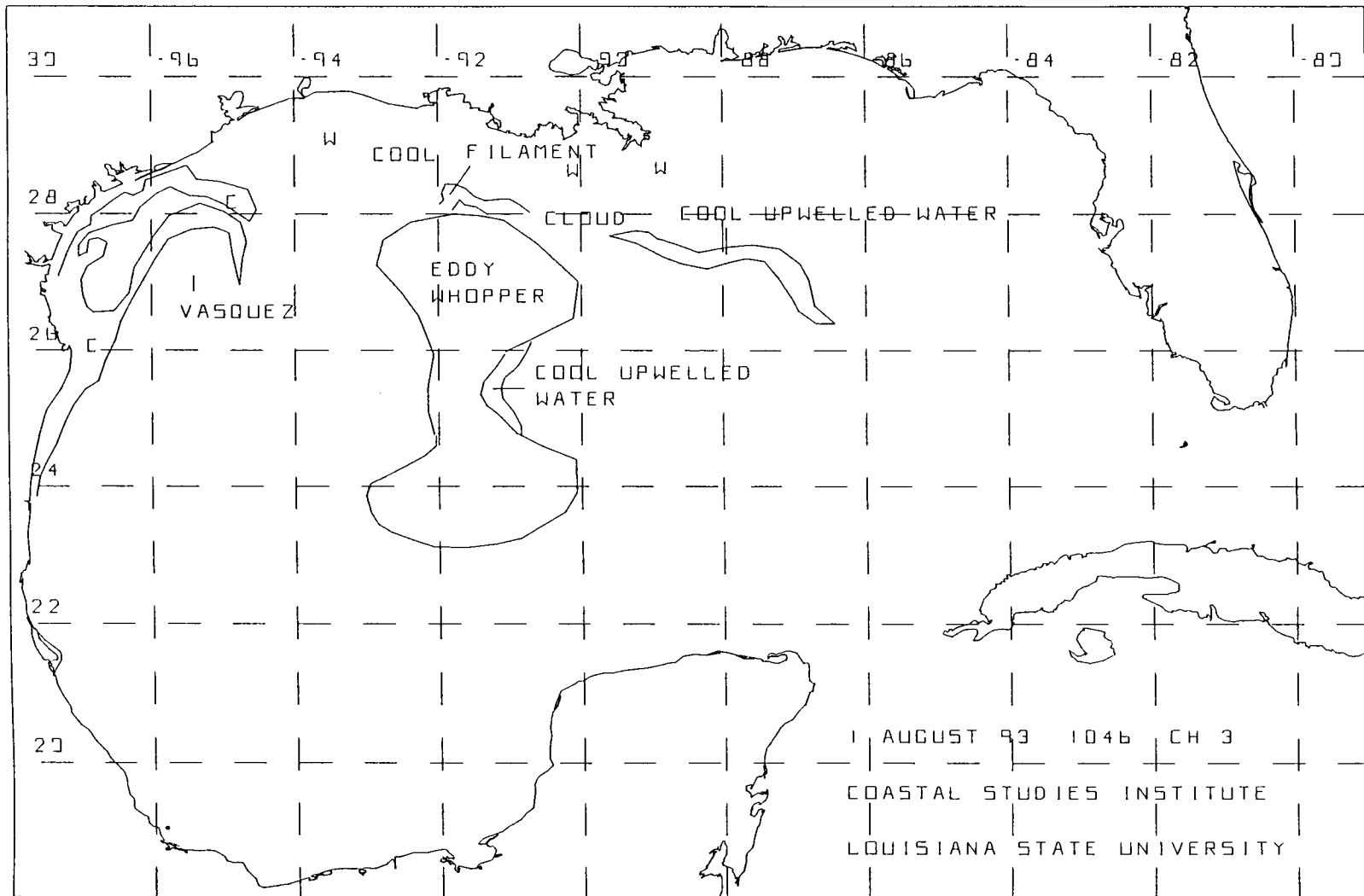
Figure 41. Surface temperature frontal analysis of satellite imagery obtained on August 1, 1993 (1046), depicting the location and morphology of Eddy Whopper.
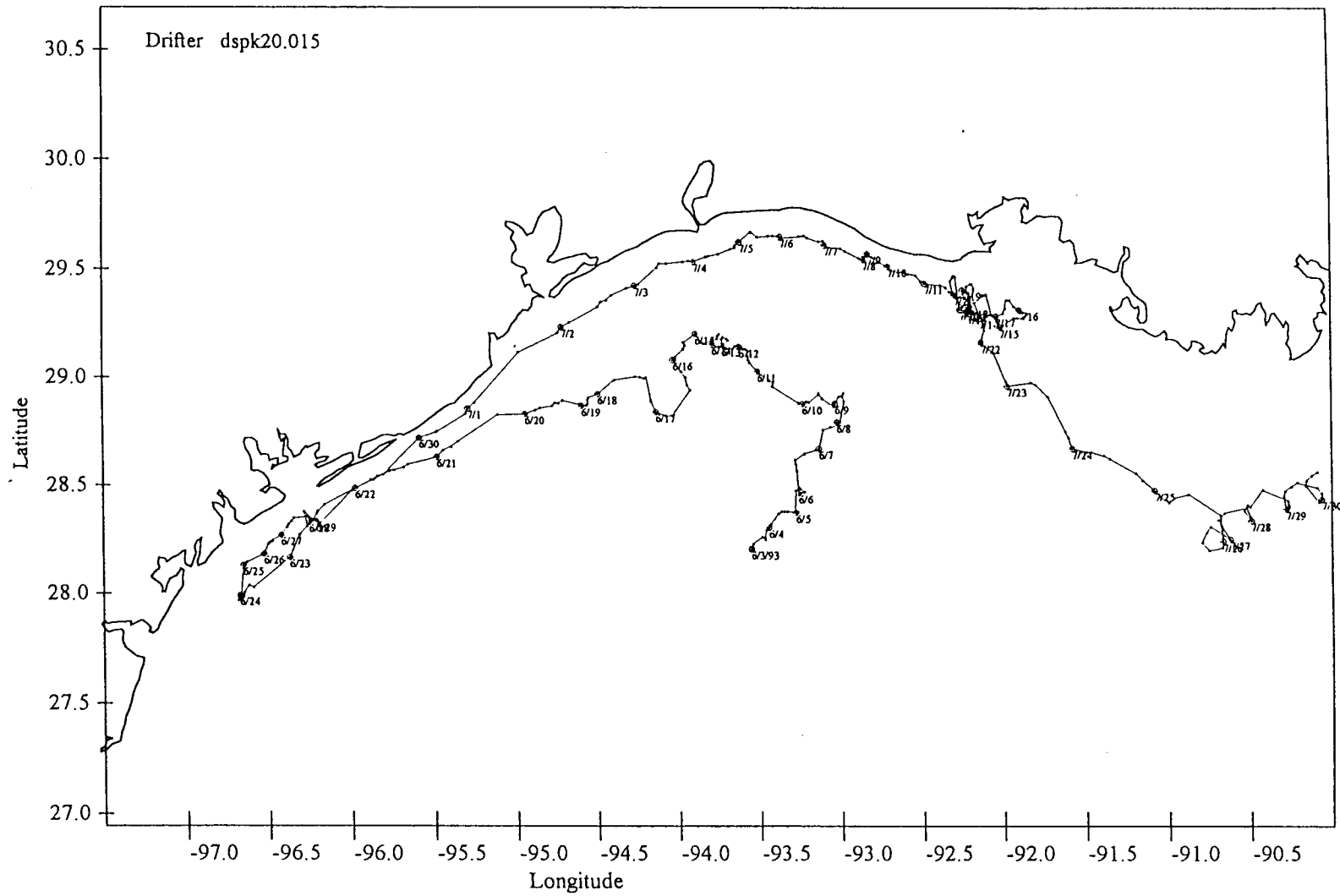
Figure 42. The trajectory of pre-SCULP drifter #15. (Data courtesy of the SCULP program, P Niiler and J. Gaukel.)

Episode 4. The normal summer wind regime set in again on June 23, and by June 25 the drifters resumed the summer current regime of a slow steady march up the coast of Texas to the northeast and eastward along the Louisiana coast. Several pre-SCULP drifters displayed this eastward motion until well into August.

2. Property Fields at Constant Depths

The near-surface salinity field (Figure 43) mapped by the underway thermosalingraph system (MIDAS) presents an excellent integral representation of the hydrographic conditions during Cruise IV. The Atchafalaya River plume is clearly seen along the coast from 91° W to 93° W. The extension of these lowest salinity contours suggests a nearshore flow to the west. There is a marked increase of salinity in the S1-T2-S2 box to the southeast indicating a strong front between the Atchafalaya outflow and the ambient coastal current water.

In the extreme southwest of the study area, surface salinities at S8 and S7 are 33-34 psu, indicating the presence of relatively undiluted Gulf water. The tongue-like distribution of the 23-27 psu isohalines in the S4-S5 region suggests a penetration of this high salinity water from central-south Texas toward the east.

The salinity at the 7m level from the CTD casts shows a pattern similar and proportionally higher to the surface pattern (Figure 44). The salinity at the 15 m level is more uniform, ranging from 30-35 psu, and generally high throughout the whole study area (Figure 45).

3. Acoustic Doppler Velocities at Constant Depth

The velocity field along the cruise track in the 2m bin centered at the 4.5m depth level is shown in Figure 46. The overall velocity field is quite consistent with the circulation pattern suggested by the salinity distribution. Clearly there was a dominant tendency for upcoast or eastward flow all along the Louisiana and Texas coast covered by the cruise track. This is in agreement with the advection of higher salinity water from the Texas coast onto the Louisiana shelf indicated by the salinity field (Figure 43). Off the Atchafalaya Bay the ADCP vectors suggest the eastward coastal current was deflected around the buoyant plume emanating from the Atchafalaya River. This is also consistent with extrapolating the 22-25 psu isohalines from line S3B around the bulge of fresh water formed by the Atchafalaya River linking up with these outflows, and with the salinity values on S1.

There is no evidence in the ADCP data in Figure 46 for the nearshore westward flow of very low salinity Atchafalaya River water toward S3B and S4 as suggested by the salinity field. Several possibilities could explain this discrepancy such as (a) the inshore westward flow of low salinity water was an episodic event that occurred prior to the cruise or (b) the doppler velocities in this very shallow water are unreliable and require further screening.

There are specific zones along the cruise track that exhibit strong cross-shore motion (e.g., intense onshore flow along the western end of T10 and along nearly the entire length of T7). Zones of strong offshore flow are seen along the east end of T9 and at the south end of S3B. Further data screening is necessary, but indications are these are probably real features. The SCULP drifter data indicate a wealth of cyclonic and anticyclonic eddys of a variety of sizes to be common in the region between S4 and S8. It is noteworthy that the strong offshore flow at the seaward end of S3B is associated with a 90° bend in the 22-23 psu isohalines, which we presently interpret as the eastward returning coastal current reflecting around the Atchafalaya fresh water bulge.
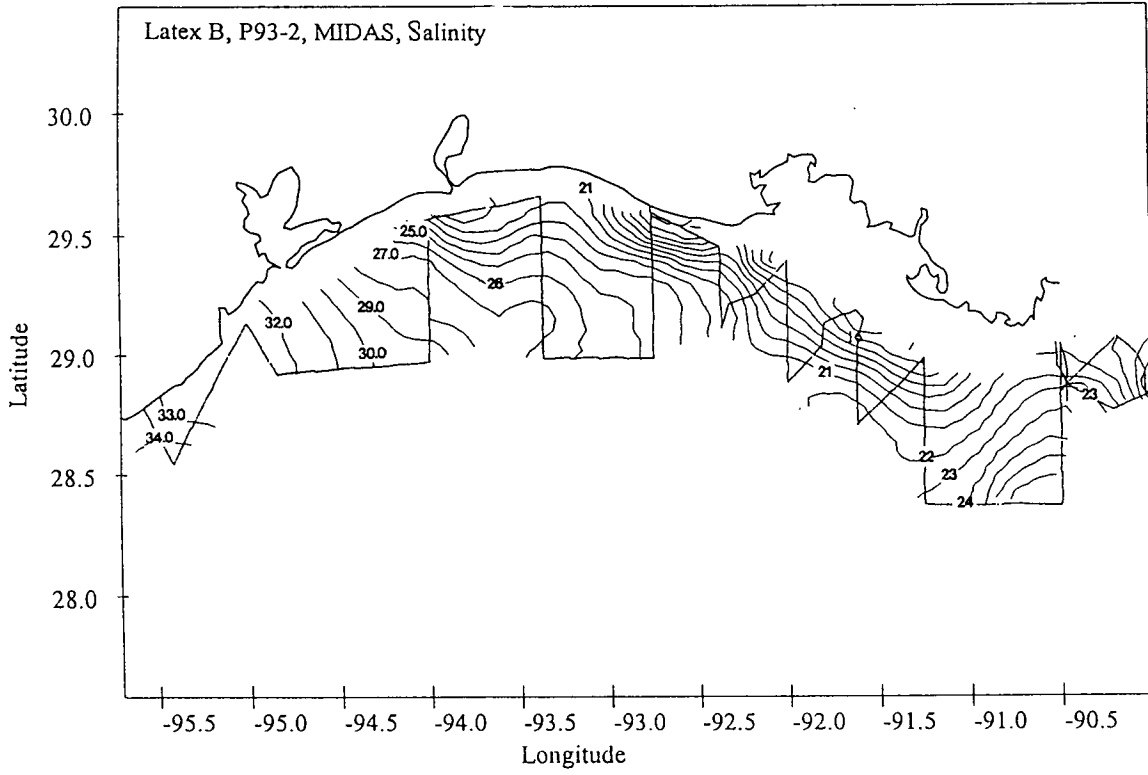
Figure 43. Near-surface salinity along the track of Cruise IV.
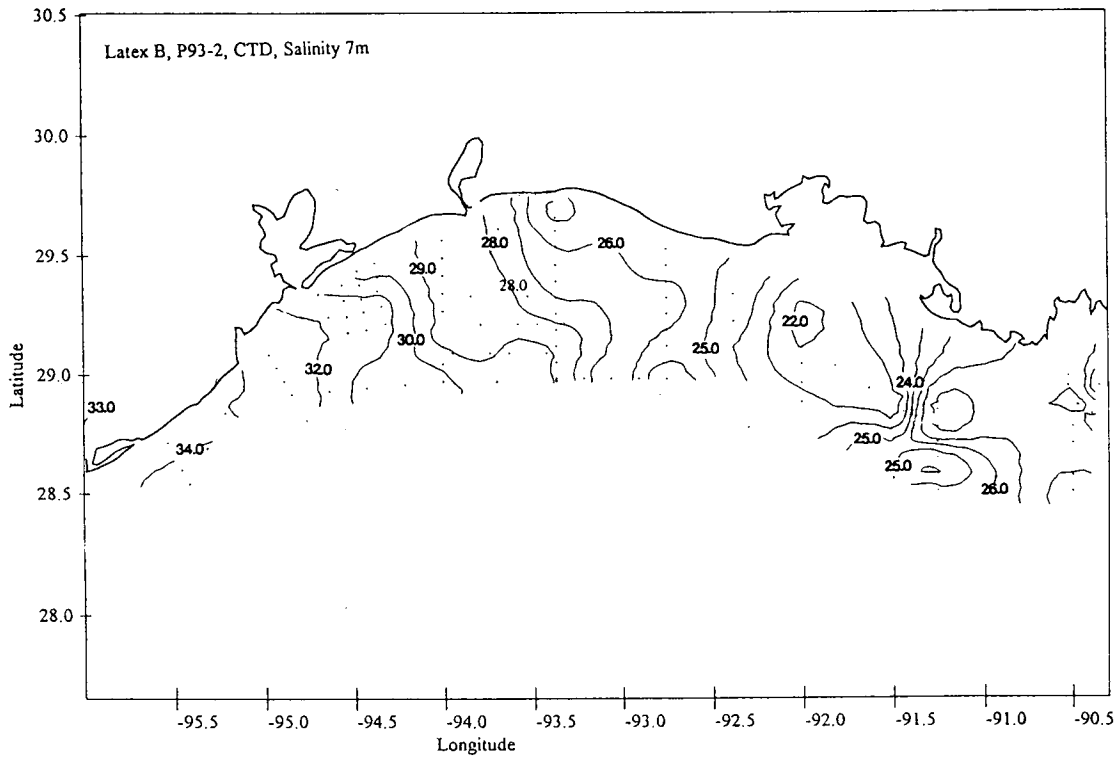
Figure 44. Salinity along the Cruise IV track at the 7 m level.

45
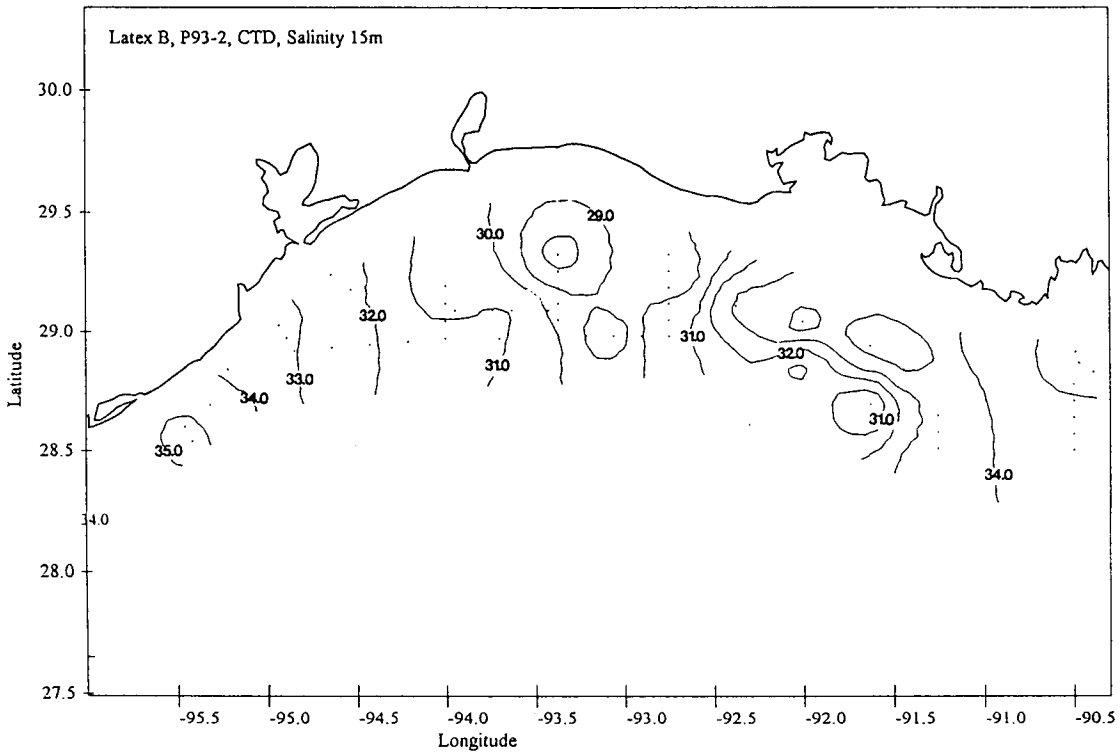
Figure 45. Salinity along the Cruise IV track at the 15 m level.
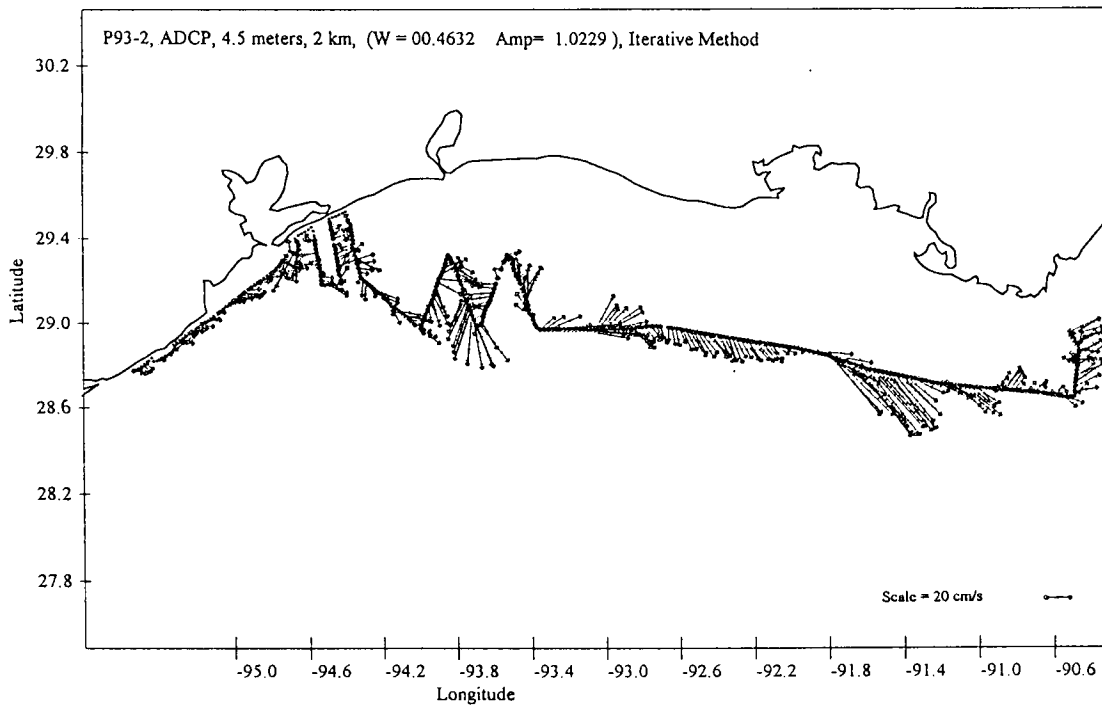
Figure 46. Current vectors along the Cruise IV track at the bin centered at 4.5 m depth (2 m bins).

4. Vertical Sections

Table 2 shows the start and end time of each line for Cruise IV.

Table 2. Times and dates of survey lines, Cruise IV. All times are in GMT (GMT is CDT plus 5 hours). Dates are noted in Julian days.

Line	Start Time	Start Date	End Time	End Date
S1 Hypoxia	0747	13 July	1058	13 July
Hypoxia	1058	13 July	0750	14 July
S1	1022	14 July	1642	14 July
T2	1642	14 July	2352	14 July
S2	2352	14 July	0816	15 July
T3	0816	15 July	1310	15 July
S2B	1310	15 July	1821	15 July
T4	1821	15 July	2332	15 July
S3	2332	15 July	0621	16 July
T5	1621	15 July	1121	16 July
S3B	1121	16 July	1512	16 July
T6	1512	16 July	1900	16 July
S4	1900	16 July	1325	17 July
T7	1325	17 July	1008	17 July
S5	1008	17 July	1928	17 July
T8	1928	17 July	0119	18 July
S6	0119	18 July	1001	18 July
T9	1001	18 July	1820	18 July
S7	1820	18 July	2155	18 July
T10	2155	18 July	0532	19 July
S8	9532	19 July	0905	19 July
Galveston Plume	1713	19 July	1345	20 July
Convergence Study	1708	20 July	1027	21 July

a. S1. The salinity distribution at S1 (Figure 47) shows an 8-10m thick broad band of low salinity water (<30 psu) that extends across the entire 80 km long section. This fresh water layer is underlain by a 5m thick halocline, which itself is underlain by a deep, fairly homogeneous layer of high salinity (34-36 psu) Gulf water. The currents (Figure 46) are strongly eastward (upwelling favorable), which is consistent with the up-to-the coast slope of the pycnocline and the top of the deep layer. Within the first 25 km from the coast, low salinity isohalines (21-25 psu) outcrop at the sea surface, suggestive of a very local regime of downwelling in the shallowest water near the coast. This interpretation is supported by the ship winds that are clearly onshore during the S1 transect (Figure 30). The dominant flow component is in the zonal (roughly alongshore) direction, and Figure 48 shows this component to the depth where bottom tracking was lost. The surface and halocline layers are flowing strongly eastward, from the coast out to 60 km. An intense jet exceeding 50 cm/sec is centered over the sharp break in slope 45 km offshore. There is strong indication of a counter current in the high salinity deep layer.

b. T2. The deep water tie-line T2 (data not shown) displays, over its entire 85 km length, a salinity structure very similar to the outer end of S1; namely, (1) a pycnocline zone near the surface with salinities of 25 psu increasing to 33 psu at depth of 14-18 m and (b) a relatively homogeneous deep layer of 34-36 psu extending from the base of the pycnocline to the bottom at 48-58 m water depths. Because of the lack of bottom track along T2 there is, as of yet, no ADCP velocity data.
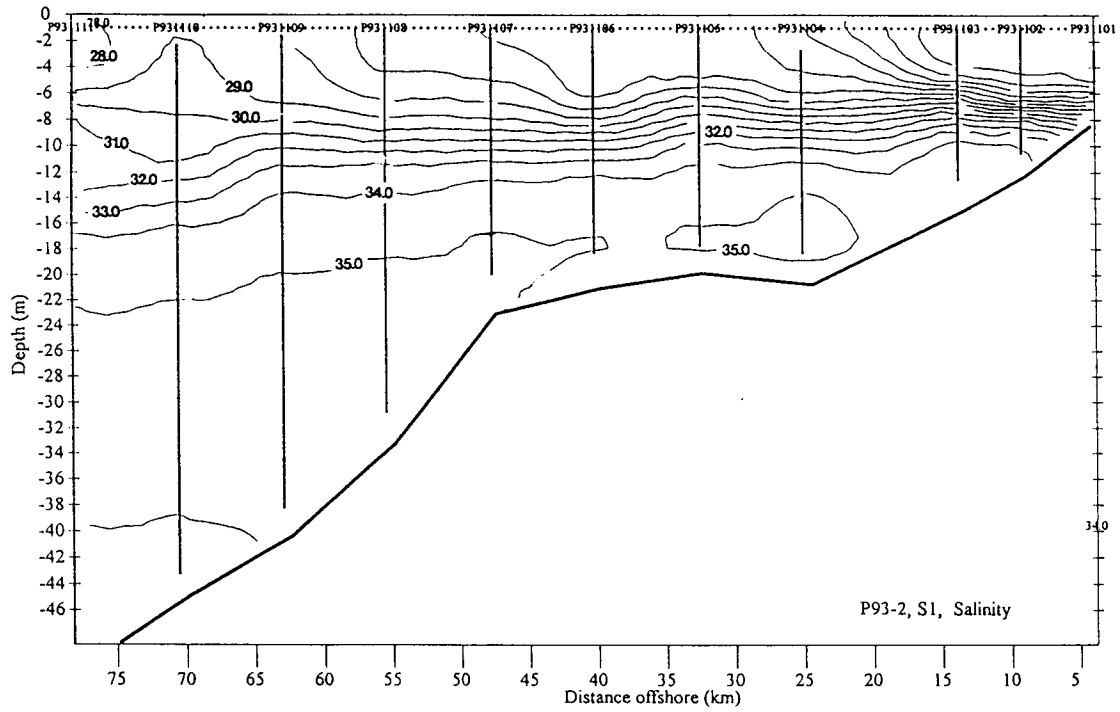
Figure 47. Salinity (psu) along line S1.
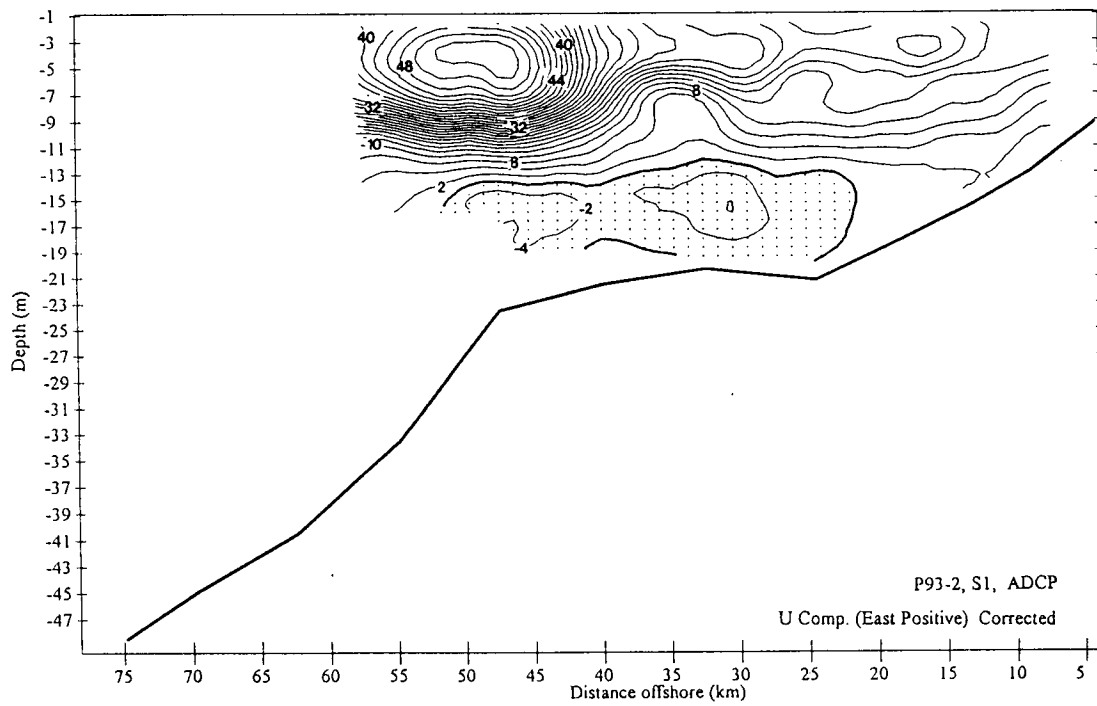
Figure 48. Zonal velocity component (positive-east) along line S1.

48

c. S2. The salinity structure at S2 (Figure 49) shows essentially the same three layers as observed at S1 except that the surface layer salinities are at least 4 psu lower because of proximity to the Atchafalaya River mouth. The intense upcoast jet in the along-shore ADCP speed observed at S1 is absent at S2. Instead we see in Figure 50 a broad area of moderate up coast (eastward) speeds extending from the inshore shallows out to the 65 km mark. A surface counter current centered at the 75 km offshore mark coincides with a deep zone of the well-mixed surface layer (Figure 49). It is notable that the vertical shear in the current in the upper 10m is such that upcoast speeds increase with increasing depth. Inspection of Figure 30, the ship winds, indicates that a strong wind stress, opposing the regional upcoast current during the S2 leg, is likely decelerating the top of the water column.

d. S2B. Line S2B which cuts obliquely through the Atchafalaya River outflow plume shows strong southeastward currents on Figure 46 (the near surface ADCP map). Figures 51 and 52 show the salinity and meridional (roughly cross-shore) ADCP speeds along S2B in vertical section. The salinity clearly shows the low salinity (11 psu) river plume entering at the inshore end of S2B and extending about 70 km offshore with a vertical thickness of about 10 m. The flow in S2B is strongly southeastward over nearly the entire section. The plume water has a strong southward component (Figure 52), as does the water underlying the plume.

e. S3. Line S3 is also dominated by the 8-10 m thick Atchafalaya River outflow as shown in the salinity distribution (Figure 53). The river plume water overlies an 8 m thick halocline in which the salinity increases from 24 psu up to about 32 psu. A wedge of high salinity (32-35 psu) water occupies the deep offshore part of this section. Currents are generally south eastward over the section (Figure 46). The eastward speed component reaches 30 cm/sec in a subsurface jet at the offshore edge (Figure 54). An anomalous westward counter current in the surface layer between the 40 and 55 km mark is associated with a lens of low salinity water centered at the 40 km mark. The ship winds along S3 (Figure 30) indicate a ~ 5 m/sec easterly wind (counter to the prevailing coastal current), which is consistent with the vertical shear observed along most of the section, i.e., eastward speeds increasing with depth.

f. S3B. Section S3B is filled over its entire length and down to the 8 m depth with nearly isohaline water of 23-24 psu. This unusual salinity distribution is associated with very strong southwestward currents at the seaward ends of both S3B and T5 (Figure 46). It is not clear what is causing this seaward jetting of the 23-24 psu water. One possibility is that the intrusion of higher salinity water from the west illustrated in Figure 43 (the surface salinity map) could be squeezing this modified Atchafalaya River water seaward around the more recent Atchafalaya plume water.

g. S4. Further west at S4 the complexity of structures in the salinity distribution (Figure 55 suggests the presence of a similarly complex velocity field. Salient features are (1) a nearshore low salinity wedge with downwelling inclined isohalines confined to within 20 km of the coast; (2) a weak, low salinity feature in the surface layer centered at 35 km offshore mark; (3) a salinity in version in the surface layer offshore where a lens of 24-26 psu water is located in the upper 8 m between 70 and 40 km offshore; (4) a down-to-the-coast slope of the base of the halocline (cf. the 30 and 31 psu isohalines): and, (5) a large volume of homogenous water ~ 26 psu occupying the center of the section from 4-12 m depth range between 20-45 km offshore.

The zonal velocity component at S4 (Figure 56) does indeed reflect these complexities in the salinity field. Inshore of the 45 km mark and beneath the 17 m depth level offshore there is a broad area of upcoast flow, which reflects the coastward dip of the halocline (item 4 above) and occupied by the homogenous water mass of item 5 above. The offshore lens of low salinity water, item 3 above, is directly associated with a intense downcoast jet reaching speeds of 40 cm/sec. Clearly, this is an eddy or filament of low salinity water that has intruded into the coastal current domain, perhaps from the mid shelf. The nearshore low salinity wedge and the patch of low

49
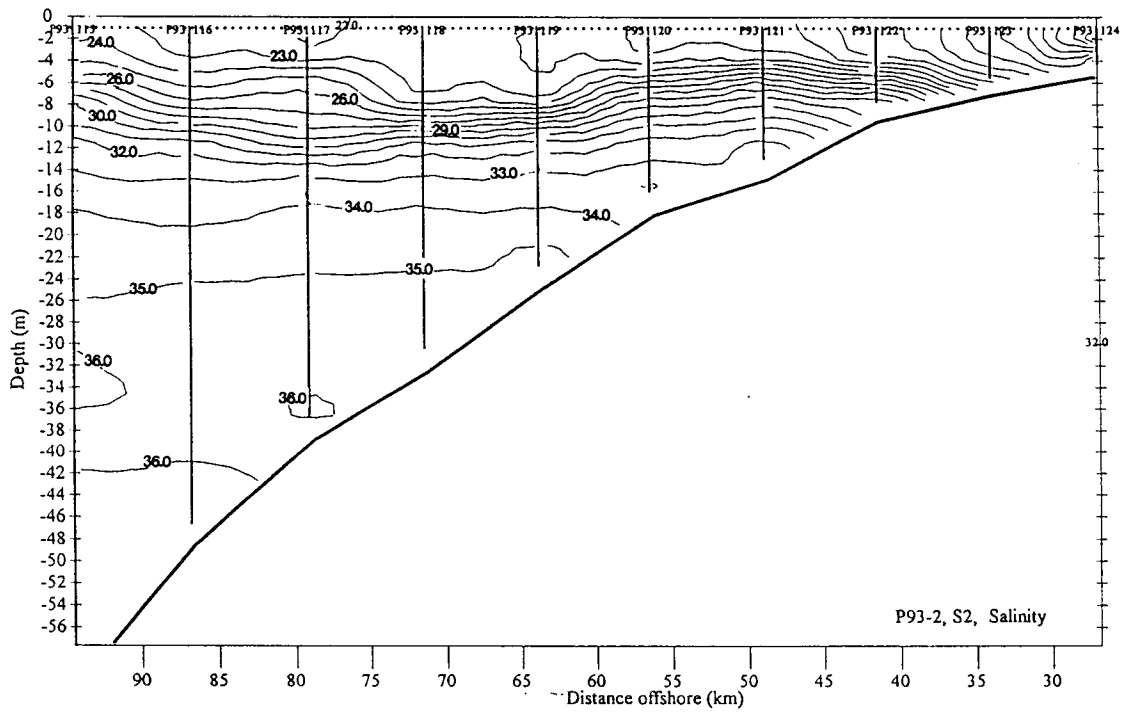
Figure 49. Salinity (psu) along line S2.
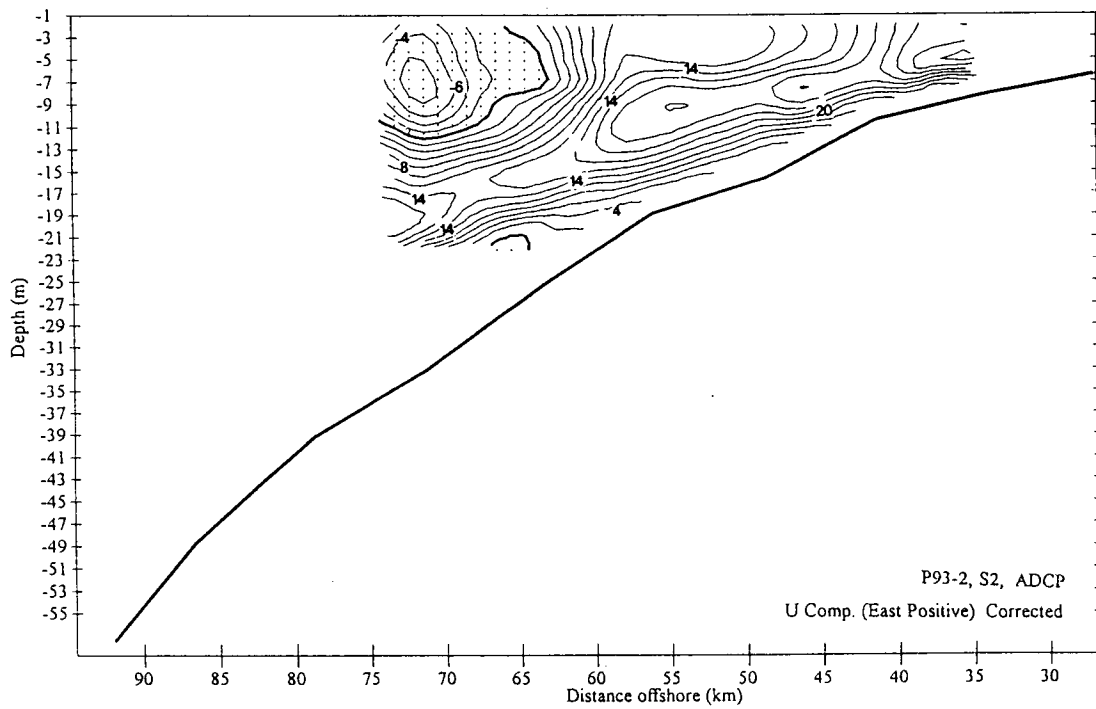
Figure 50. Zonal velocity component (positive-east) along line S2.

50
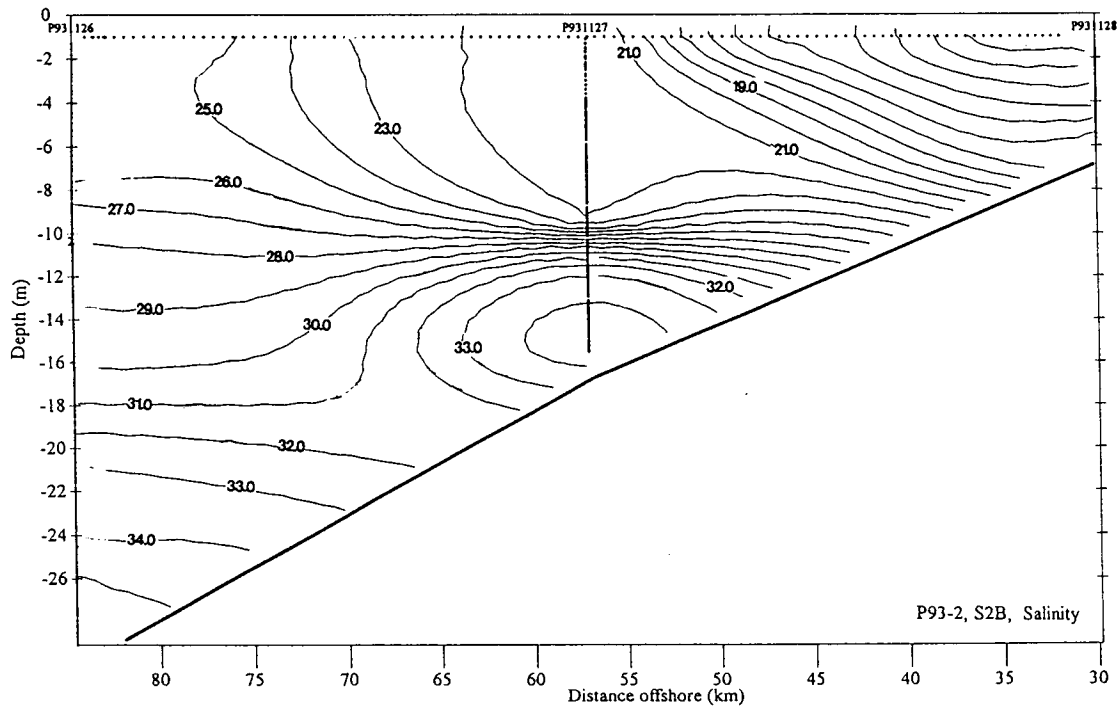
Figure 51. Salinity (psu) along line S2B.
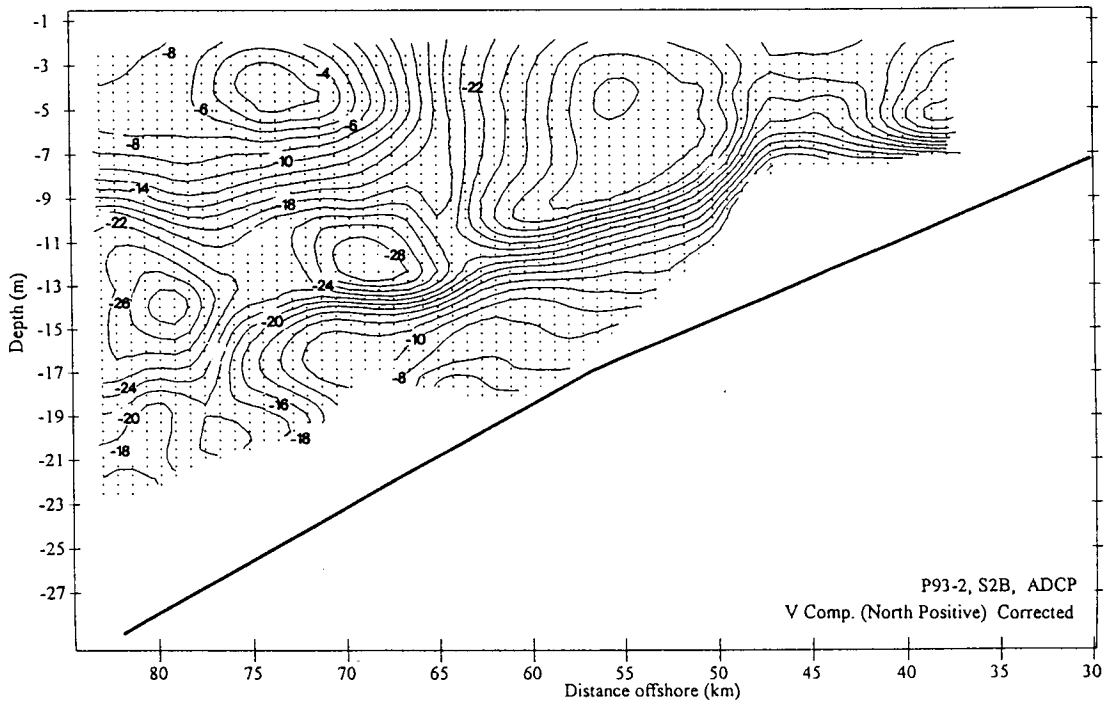
Figure 52. Meridional component (positive-north) along line S2B.

51
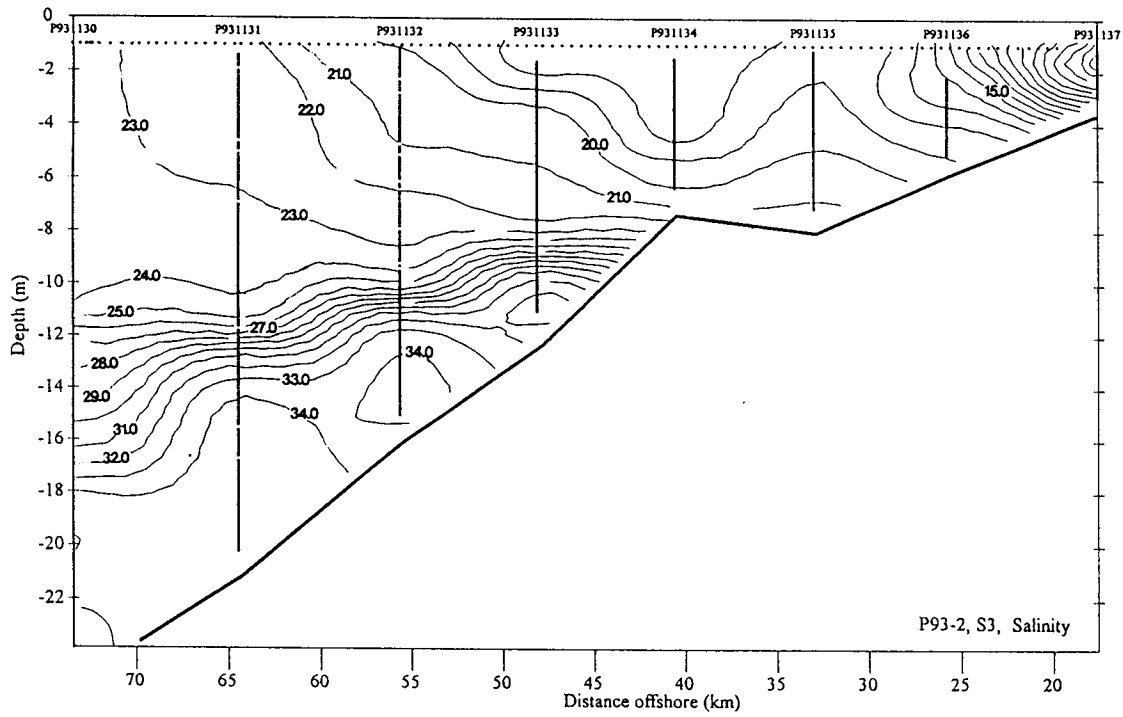
Figure 53. Salinity (psu) along line S3.
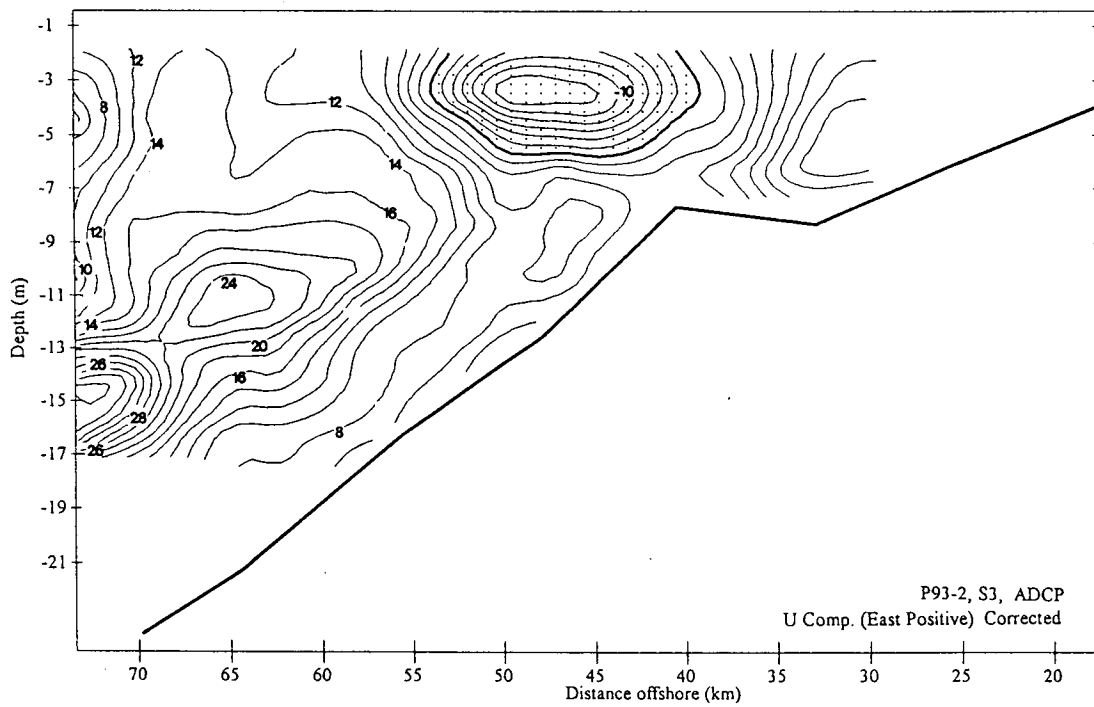
Figure 54. Zonal velocity component (positive-east) along line S3.

52
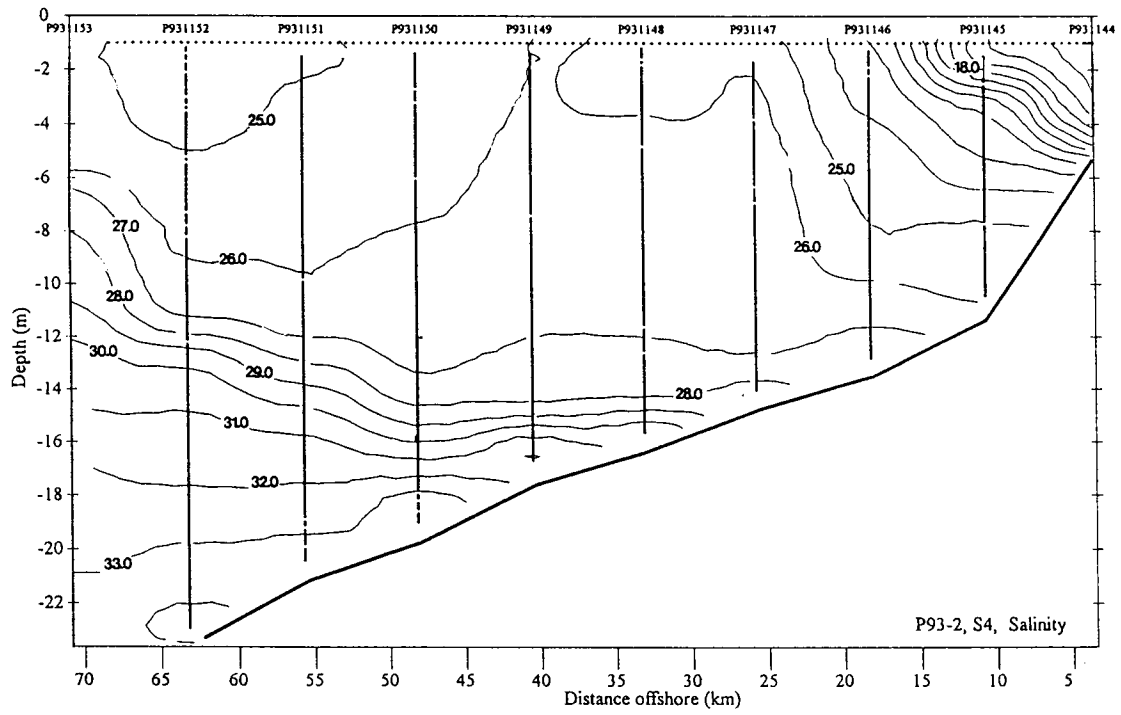
Figure 55. Salinity (psu) along line S4.
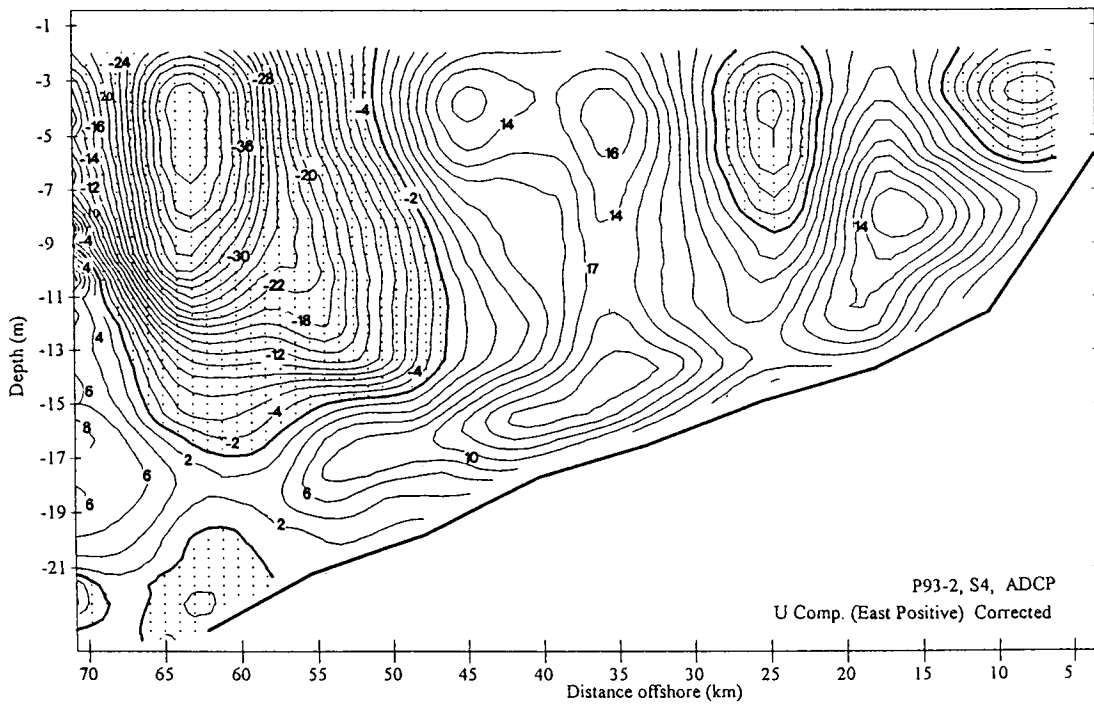
Figure 56. Zonal velocity component (positive-east) along line S4.

salinity at 35 km offshore (items 1 and 2 above) are both local zones of distinct downcoast currents flowing counter to the upcoast flow they are imbedded in.

h. T7. The salinity and ADCP velocities along T7 are consistent with the presence of an anticyclonic eddy in the S4-T7-S5 region. Salinity in the upper 10 m is < 27 psu, and this water is advecting westward on the south limb of the eddy. The flow turns northward on the west end of T7 where isohalines rise abruptly. For example, the 27 psu isohaline rises from 12 m to 1 m over the westernmost 20 km of T7, signaling the outer edge of the eddy.

i. S5. The S5 line (Figure 57 and 58) is similar to S4 in that its outer 30 km are dominated by the anticyclonic eddy present along S4 and T7. There is a sharp discontinuity in the velocity field at about km 63 (Figure 58) between the eddy and the coastal current located shoreward. The water in the eddy appears to have a higher salinity (Figure 57) (28-29 psu), compared to 25-27 psu in the eddy in S4. On shore of km 63 along S5 there is a prevalent and deep eastward flow (Figure 58) of water with salinities in the 20-28 psu range. Local (ship) winds are westerly during the ship transit of S5, maximizing the tendency toward eastward flow.

Ship winds indicate a shift to moderate (5-7 m/sec) southerly winds along T8-S6-T9. The inshore tie-line T8 shows a distinct parabathic current flowing eastward, returning low salinity (20-28 psu) water from Texas that apparently had advected down coast earlier.

j. S6. The onshore winds along S6 (Figure 59 and 60) appear to have strongly affected the structure of the flow. The upper 8 m of the water column is dominated by the onshore flow component, while below 8 m the prevailing eastward flow is clearly dominant over the entire section (Figure 60). The isohalines reflect the impact of the downwelling favorable winds, the inner 55 km being filled with a homogenous mass of water of 28-29 psu (Figure 59). Steep down-to-the-coast slopes of the 29, 30, and 31 psu isohalines also reflect the downwelling regime. The strong zonal upcoast flows below 8 m, however, illustrate the continued importance of the larger scale forces during the summer regime which produce the prevailing eastward flow.

k. S7. It is very instructive to inspect the salinity distribution in S6, T9 and S7 in sequence to see the rapid transition from lower salinity water south of Sabine to the higher salinity (32-33 psu) that completely occupies the S7 section (Figure 61). The 30 km section of S7 is very well-mixed in accord with the higher wind energy levels exhibited in Figure 32. The upcoast flow that dominates S7 (Figure 62) is illustrated with the more energetic zonal component which features a 10 km scale intense jet (24 cm/sec) confined within 12 km of the coast.

l. S8. Sixty km along the coast to the southwest, line S8 demonstrates a penetration into even higher salinity waters. In Figure 63 the 35 psu isohaline is seen only 23 km offshore at the 10 m depth level. This high salinity water at S8 is also returning upcoast (Figure 64), but S8 is also heavily influenced by strong onshore flows of high salinity shelf water. These filaments of offshore water intruding into the near-coast water are clearly seen as a major feature along T10 (Figure 46). This feature is continuous with the onshore flow at the seaward edge of S8. It is not clear whether this feature is an isolated intrusive filament or is associated with an anticyclonic eddy which is impinging on the coast.

m. Return Leg. After finishing the survey of the Galveston plume, the ship transited back to the east to home port on July 21 and 22. On this return leg a large saw tooth pattern was run through the outer edge of the S5-S6 box to investigate in more detail the strong cross-shore motions frequently observed in this region. Figure 65 shows the ADCP vectors at the 4.5 m depth level. There are, as anticipated, very strong (40-50 cm/sec) cross-shore motions along the saw tooth. South of the Atchafalaya Bay at 91°W and 91.6°W there are also zone of high speed current on the return track. The surface salinity trace (Figure 66) indicates there are high speed jets of very low salinity (5-8 psu) emanating from the Atchafalaya River outflow plume. Several of the pre-
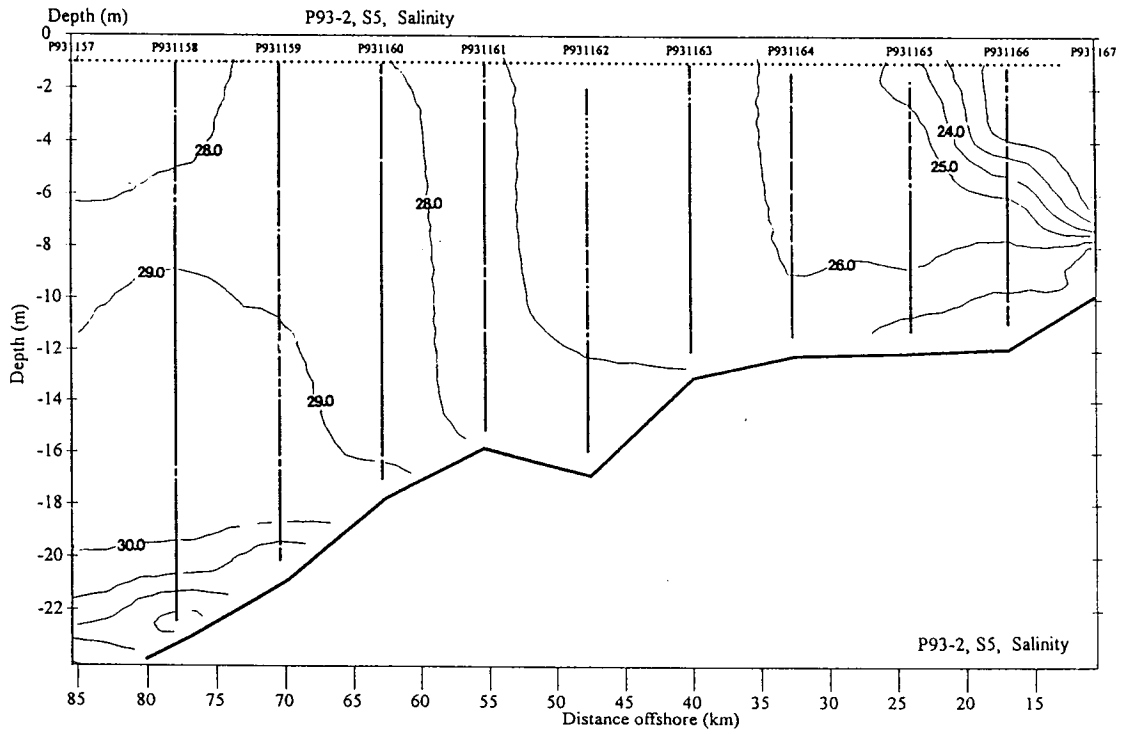
Figure 57. Salinity (psu) along line S5.
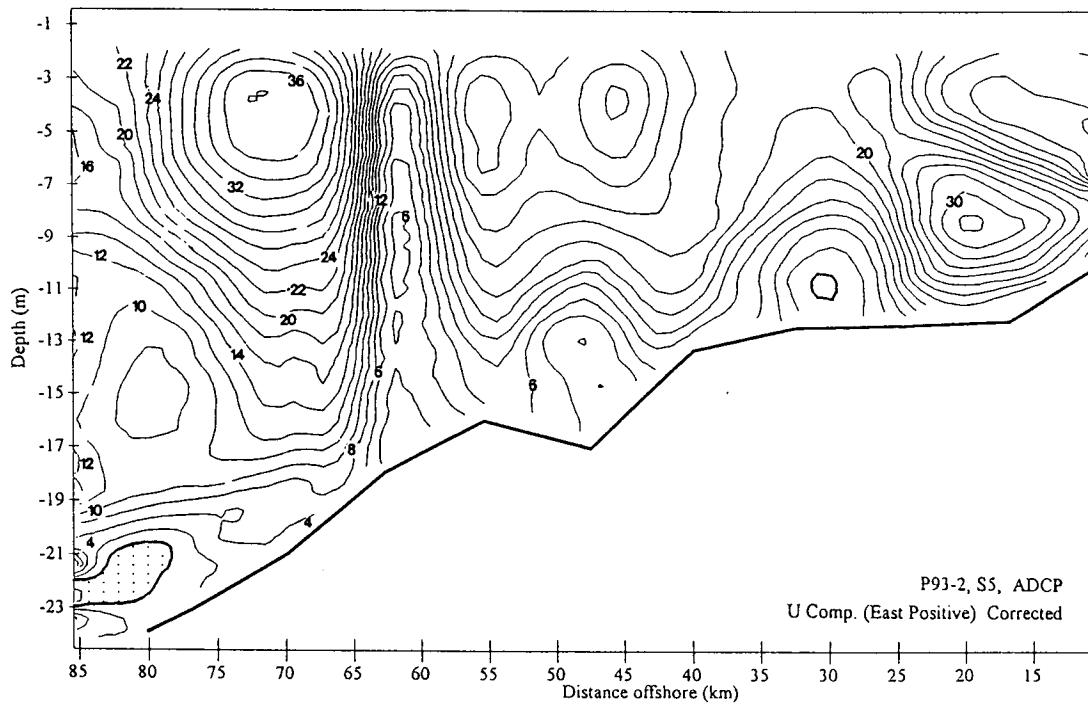
Figure 58. Zonal velocity component (positive-east) along line S5.
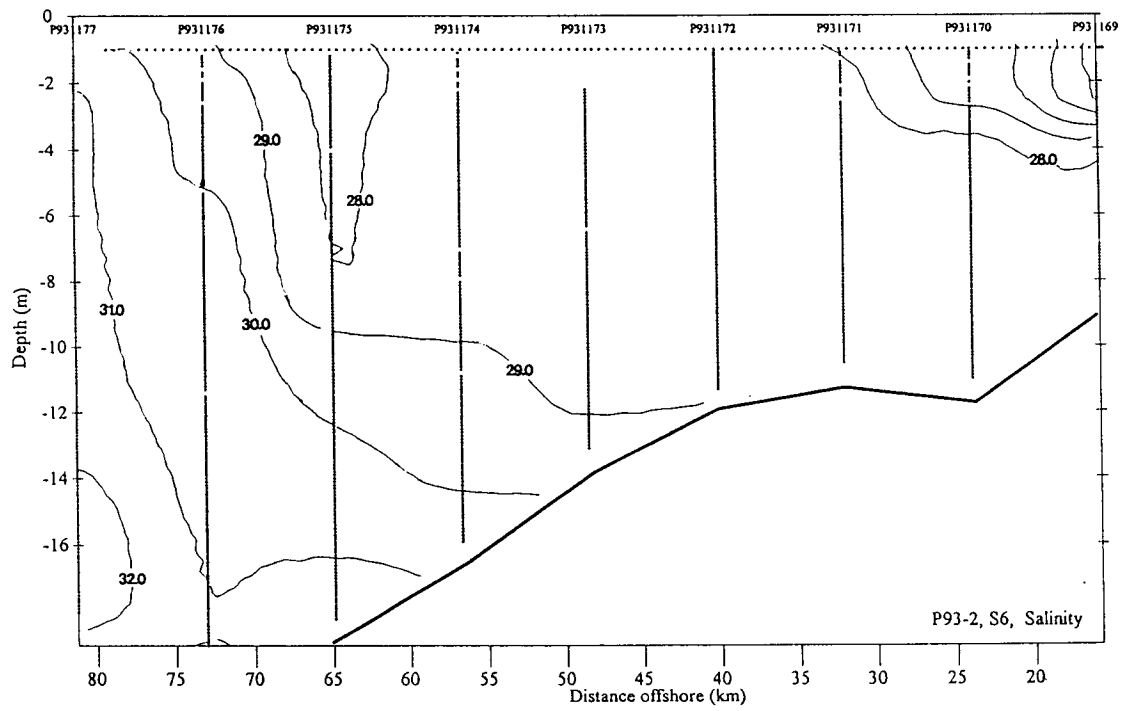
Figure 59. Salinity (psu) along line S6.
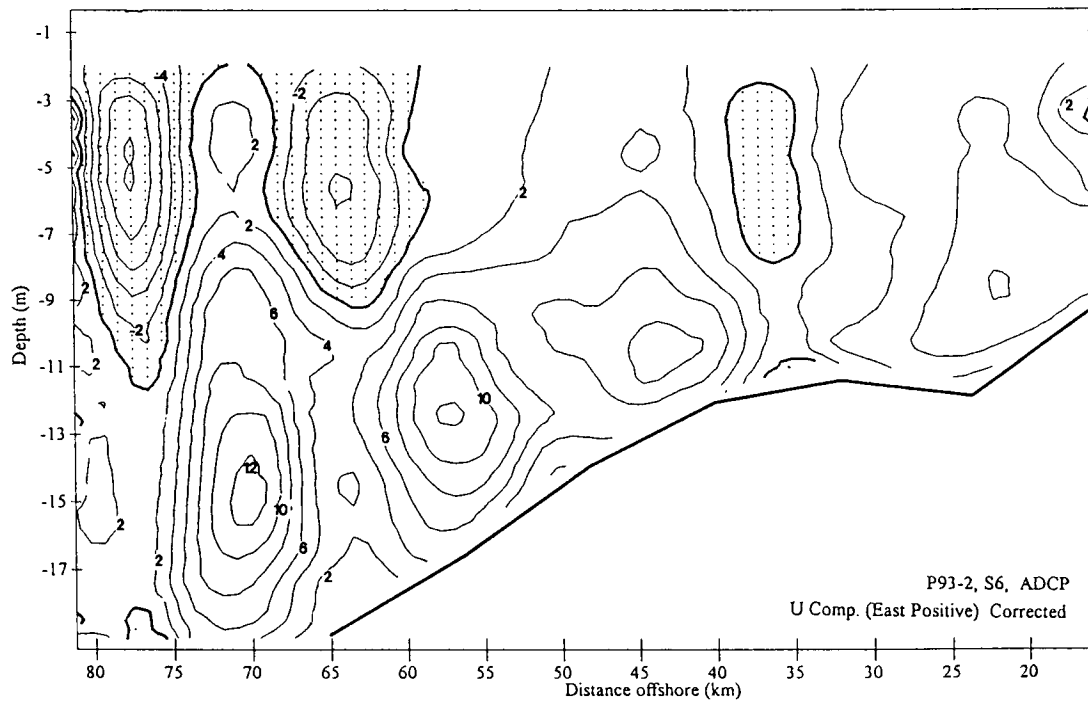
Figure 60. Zonal velocity component (positive-east) along line S6.

56
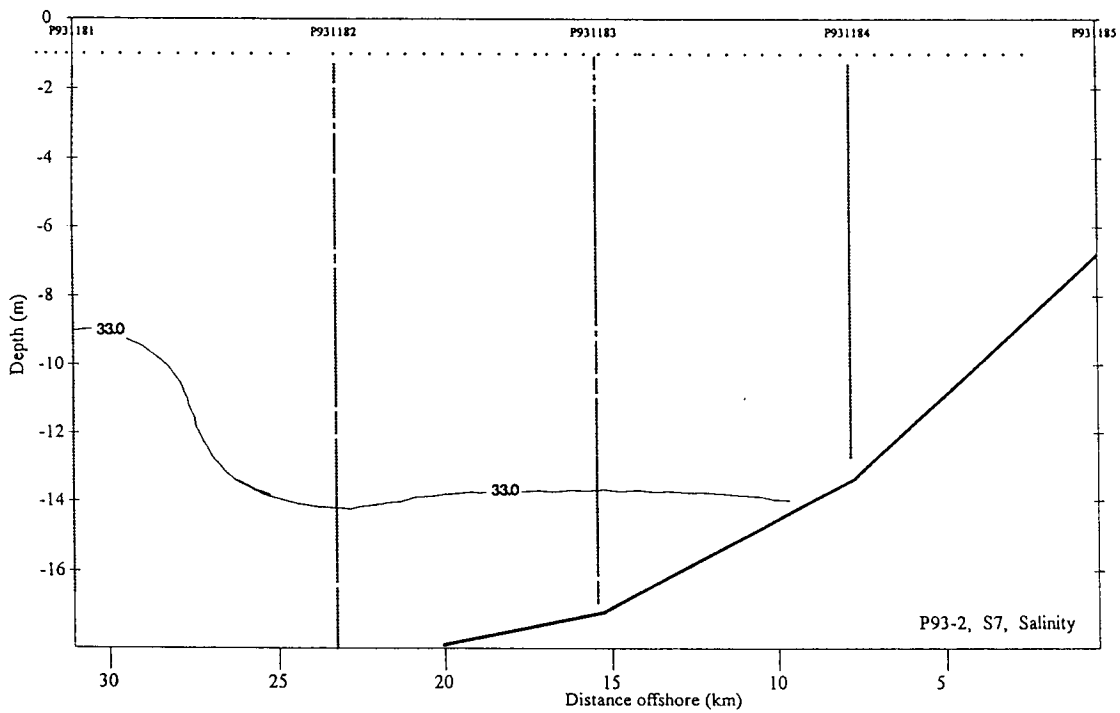
Figure 61. Salinity (psu) along line S7.
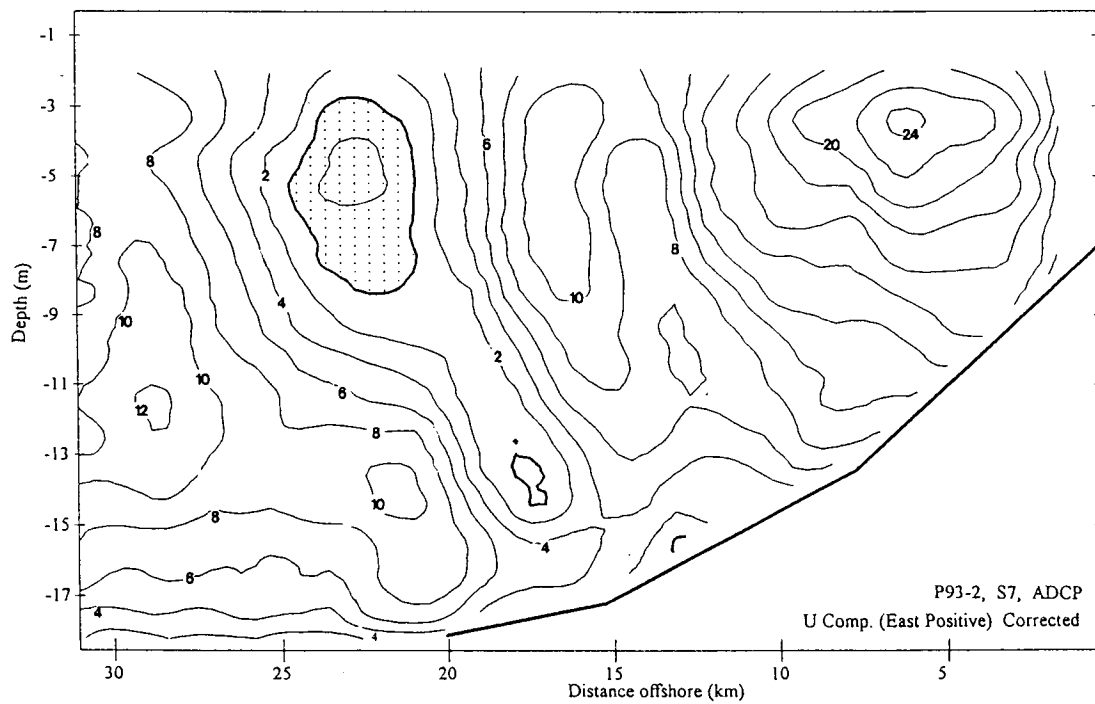
Figure 62. Zonal velocity component (positive-east) along line S7.

57
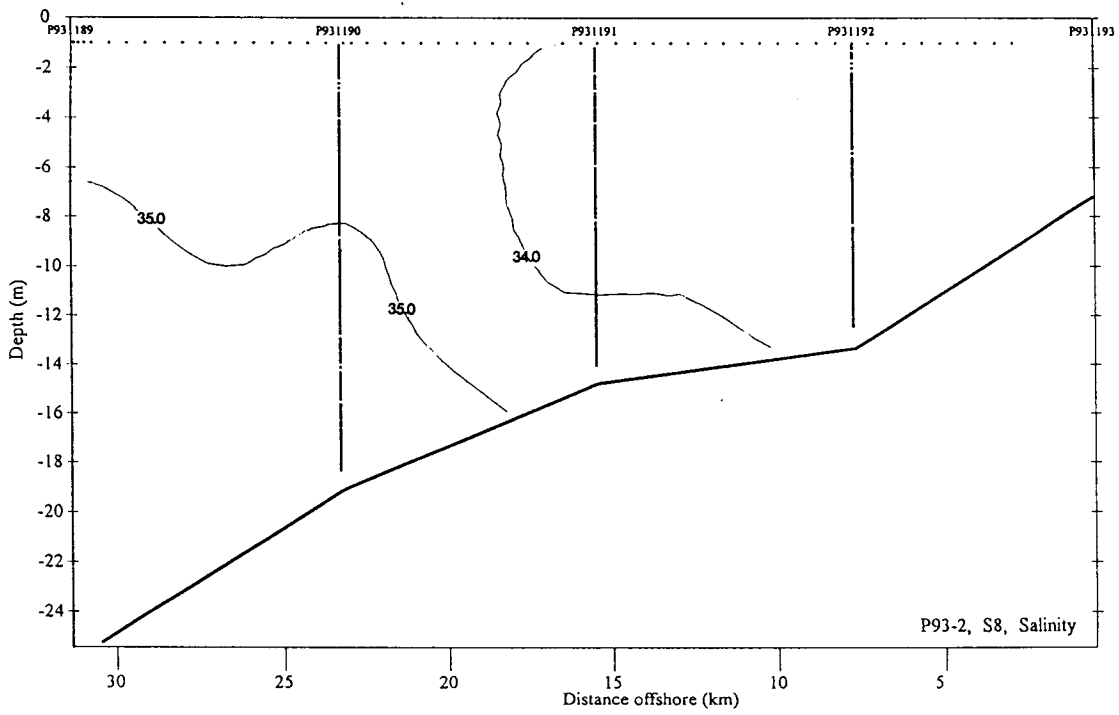
Figure 63. Salinity (psu) along line S8.
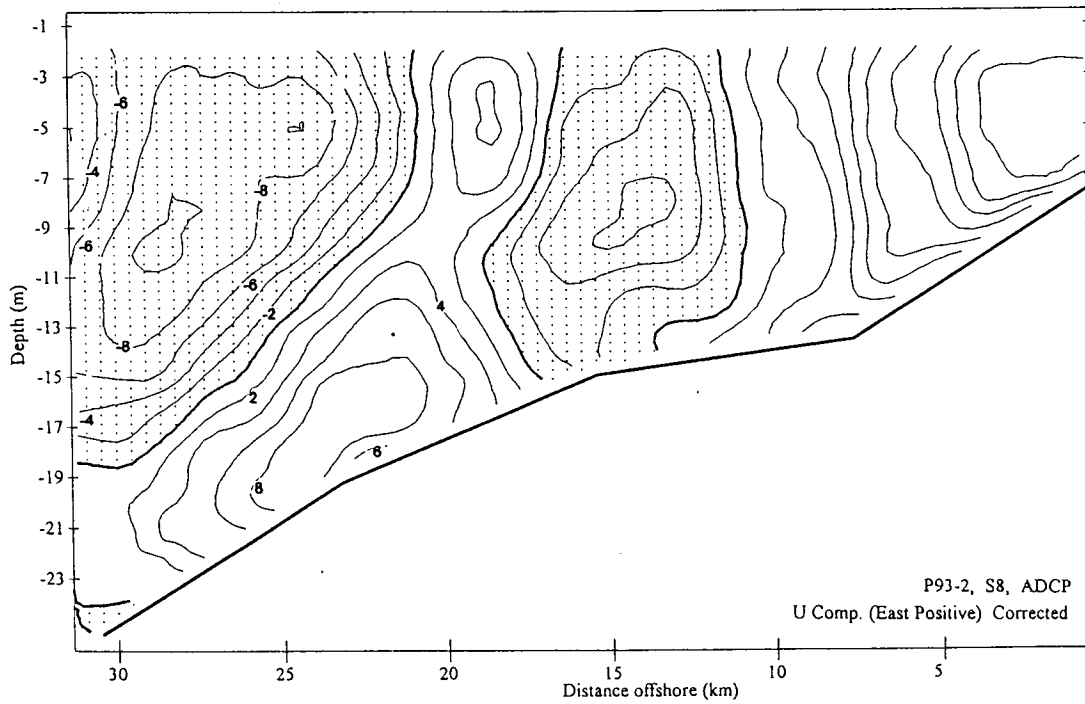
Figure 64. Zonal velocity component (positive-east) along line S8.

58
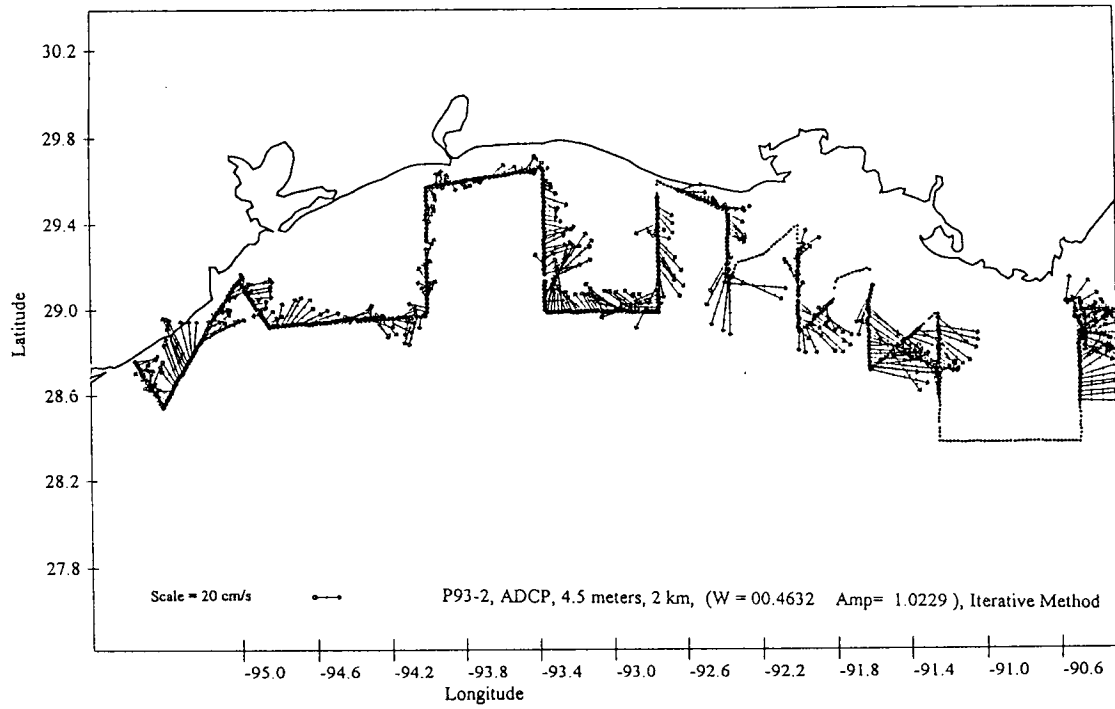
Figure 65. Velocity vectors (ADCP) at the 4.5 m depth along the return leg cruise track.
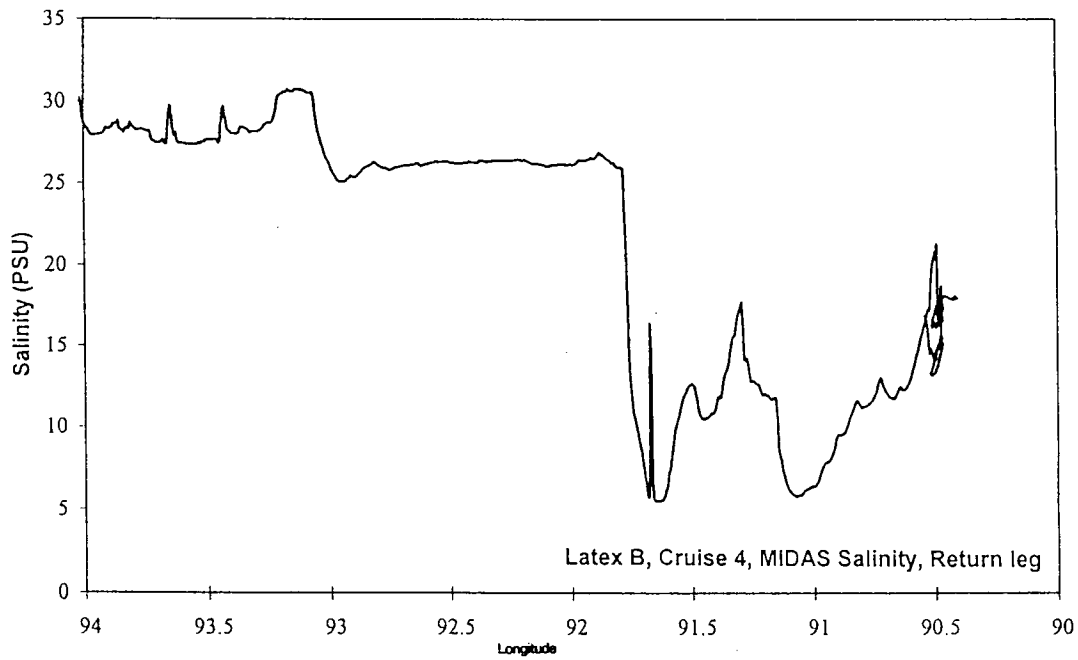
Figure 66. Salinity along the return leg south of Atchafalaya Bay showing the two low salinity pulses associated with the current jets in Figure 29.

59

SCULP drifters, trapped for several weeks on the western edge of the Atchafalaya plume, broke free during this outflow event and transited rapidly to the southeast and east. The cause of these fresh outflow plumes being so far offshore when they were absent on the outgoing leg is not certain. A drop-out of the winds along the ship track and northerly winds along the coast (Figure 32) points to the responses to change in wind forcing as the likely mechanism.

C. Preliminary Summary and Conceptual Synthesis

The hydrographic conditions in the LATEX B study region are discontinuous in the vicinity of Galveston Bay. To the east, the hydrographic distributions may be characterized as retrograde and are characteristic of a coastal region that is dominated by a freshwater plume. In contrast, to the west of Galveston the 1993 hydrographic field shows little influence of the massive runoff from the Mississippi and Atchafalaya Rivers. In this region the stratification is typical of other coastal regions in which the offshore stratification is altered and deformed by coastal mixing and upwelling and downwelling cycles. This partial decoupling of the east and west LATEX inner shelves is not a feature peculiar to the spring season of 1993. However, the location and degree of east/west discontinuity apparently varies year to year and season to season.

The freshwater outflow from the Mississippi and Atchafalaya Rivers during Cruise III (April, 1993) was approximately double that which occurred during Cruise I (April, 1992). While there were local areas of lower salinity along the Louisiana coast during the 1993 survey, the principal effect of the greater fresh water input was the broadening and, to a lesser extent, deepening of the buoyant coastal plume.

The presence of a buoyant coastal boundary layer along the Louisiana coast may be expected to be associated with a downcoast buoyancy-driven coastal current (e.g., Pettigrew and Murray, 1986). By making a two-layer approximation, the strength of the near-surface flow within in the buoyant plume may be estimated via simple scaling arguments. The elevation of the sea surface associated with the coastal freshening (η) may be scaled as εH (Csanady, 1971) where ε is the proportional density defect across the plume front, defined as $\Delta\rho/\rho$, and H is the characteristic water depth. The relevant form of the geostrophic equation is $u' = - g/f \, \partial\eta \, / \, \partial y$, where u' is the upper layer velocity, f is the Coriolis parameter, and η is the sea-surface elevation. We may express the relevant velocity scale as $(g/f) \, \varepsilon H/L$, where L is the characteristic width of the buoyant coastal boundary layer. Using empirical parameter values (obtained from the April 1993 cruise data) of: H= 20 m; ε= 5 x 10^{-3}; L=50 km, the velocity associated with the buoyant plume along the Louisiana shelf is scaled as 0.25 m/s. Thus, under high spring runoff conditions, massive westward thermohaline transport along the Louisiana shelf is the underlying circulation to which may be added components arising from wind-stress driving and/or pressure forcing from the offshore regime.

Although the freshwater plume was, at all locations and times, a dominant feature of the Louisiana coastal hydrography, the associated thermohaline circulation was not the dominant circulation process in this region. Direct wind-stress forcing had a clear and considerable impact upon both the hydrographic and velocity fields. In fact, upcoast wind driving was generally able to quickly halt and reverse the background downcoast buoyancy-driven flow. During the early stages of shifts in wind direction and magnitude, the coastal currents were observed to respond with a downwind acceleration. At greater elapsed time, the effects of rotation exerted influence and the signatures of coastal upwelling and downwelling became more apparent.

Because the study survey area is so large and the meteorological time scales short, the survey data are a complex mix of spatial and temporal variation. In order to analyze such a complex mixture of temporal and spatial variability, a crucial first step is the comparison of the

observations to elementary theoretical models that can to help organize the information in terms of the lowest-order dynamics. Several simple constructs are examined in the discussion below with the goal of helping to organize and summarize some of the main features of the data set.

1. The Lens-shaped Halocline

The salinity section shown in Figure 14 is a clear example of the lens-shaped hydrographic distributions originally reported to occur in the coastal boundary layer of the North American Great Lakes (Csanady, 1971). During data collection, winds along the S4 line were upwelling favorable varying from westerly (inshore) to northwesterly (offshore) at approximately 20 knots. Under the influence of a strong enough upwelling favorable wind-stress impulse (defined as the time integral of the wind-stress forcing) the retrograde front associated with coastally-trapped buoyancy driven current systems can be upwelled to intersect the surface, and the buoyant water mass moved bodily offshore (Csanady, 1974). Shipboard Doppler currents confirm an upwelling transverse circulation pattern (Figure 15). These data show that the full upwelling of the Mississippi/Atchafalaya plume can occur along the Louisiana shelf. During this process, the alongshore flow reversed to the downwind direction as is consistent with the theory.

2. Coastal Undercurrents

One of the most striking phenomenon observed during Cruise III is the presence of undercurrents in the eastern region of the LATEX inner shelf. These undercurrents were observed to occur both as bottom intensified upcoast currents and as "deep" counter currents, in either the up- or downcoast direction, opposing a near-surface downwind flow. The bottom intensified upcoast currents were observed to occur after a switch from the downcoast to upcoast wind direction.

The best example of the intensified undercurrent was observed at S4 (see Figure 16). A plausible explanation of this flow structure may be found by considering the interplay of two forcing functions in the alongshore momentum balance. As was shown in Figure 17, along this section of the Louisiana inner shelf, the increasing salinity toward the Texas coast contributes to an eastward baroclinic pressure gradient force. Because the salinity gradient exists at all depths along line T7, the strength of the pressure gradient force toward the east increases with increasing depth. Under typical conditions, the eastward alongshore pressure gradient opposes the westward buoyancy-driven flow toward the west. The result is a westward flow that decreases in magnitude with depth.

A second (related) mechanism for the generation of transient undercurrents deals with the difference in time scales associated with modification of barotropic and baroclinic pressure fields. After a coastal wind shift, changes in the pressure field are generated at the coastal boundary and propagate seaward (Pettigrew, 1981). Sea-surface adjustment occurs very rapidly since the signal propagates at the barotropic long-wave speed. However, internal adjustments take more time to extend offshore since they travel at the much slower internal wave speeds. The result is that, at distances from shore exceeding the internal Rossby radius, the modified surface pressure field can begin geostrophic adjustment before the changes in the baroclinic field have begun. Thus, within a few hours of the onset of upcoast winds, the barotropic pressure field may have reversed while the baroclinic field remains, temporarily, in the prior condition. The result is a transient state in which the barotropic and baroclinic flow components add constructively, resulting in subsurface maxima in the downwind current. Determining which, if either, of the above scenarios describes the basic dynamical origin of these exciting observations awaits further study and theoretical development.

A second, even more striking, rendition of coastal undercurrents are those that flow counter to the direction of the surface current. A clear example of this phenomenon is illustrated in Figure 21, which shows the alongshore component of the Doppler currents at S5. The surface layer

61

shows downwind flow in the core exceeding 0.16 m/s, while in the lower layer upwind currents as high as 0.14 m/s are found. The strong current reversal is especially striking in that it occurs in shallow (< 20 m) water. The picture is even more intriguing when one looks at the currents at section S5B, some 30 miles to the west (Figure 24). Not only do the currents at this section reverse with depth , but they are also 180° out of phase with the currents at S5. Thus between sections S5 and S5B there existed an alongshore convergence in the upper layer and a divergence in the lower layer.

Reference to MIDAS winds in Figure 6 shows that there was a convergence in the wind field between these two locations, so that in both instances the surface currents were downwind, and the deeper currents upwind. Reference to time series measurements of CMAN stations at Grand Isle and Sabine suggests that this meteorological convergence is real during the survey period, rather than merely an artifact of aliasing of a time-varying field.

The wind-stress convergence near the Louisiana/Texas border appears to be the dynamical origin of these spectacular lower-layer counter currents in the LATEX inner shelf region. Alongshore variations in the windstress or in coastline orientation may be expected to generate longshore pressure gradients with high pressure in regions of convergence and lows in regions of divergence (e.g., Pettigrew and Murray, 1986). As shown in a theoretical paper by Crepon and Richez (1982), in regions of convergence the adverse pressure gradient so established propagates back along the coast, as a combination of barotropic and baroclinic waves. Since the barotropic wave has far greater phase speed, its influence is quickly felt as it slows the otherwise linear growth of the downwind coastal jet (see Csanady, 1977; Pettigrew and Murray, 1986). The barotropic wave establishes an adverse pressure gradient that acts uniformly over the water column. Because the coastal jet is a surface-intensified feature, the adverse pressure gradient overpowers the flow in the lower layer, generating an upwind under current. This undercurrent continues to accelerate upwind until the arrival of the baroclinic pressure wave that arrives in a time scale given by T=Y/f R2, where Y is the distance from the convergence, f is the inertial frequency, and R2 is the internal Rossby radius of deformation defined as the ratio of the internal wave celerity to f.

The mechanism outlined above would generate oppositely directed undercurrents on either side of the convergence and would be operable whether the convergence were caused by wind variability or changes in coastline orientation. It is interesting to note that the result is a convergence of upper layer flow and a divergence of the lower layer flow, as was observed in the data. If these flow patterns are characteristic of the region, they may provide a partial explanation for the abrupt change in hydrography between the eastern and western LATEX regions.

III. BIOLOGICAL CHARACTERISTICS SURVEY

A. Phytoplankton Pigments *(Nancy N. Rabalais)*

1. Introduction

A useful, standard and easy method for determining phytoplankton biomass in sea water is to estimate the amount of chlorophyll (usually as chlorophyll *a*). Our methods followed those of Parsons et al. (1984) fluorometric determination. Chlorophyll degradation products, phaeopigments, were also determined fluorometrically after acid treatment of the chlorophyll extract. Fluorometry is not a good indicator of phycocyanin- or phycourobilin, phycoerythrin-containing organisms in the phytoplankton community, individuals of which may often be abundant (e.g., July 1993). The small coccoid cyanobacteria have less chlorophyll and more of the other photosynthetic pigments than the larger-sized phytoplankton. And, while fluorometric measurements do not provide the detail of pigment speciation available from high performance liquid chromatography, most of the larger-sized fractions of phytoplankton, which usually contribute proportionally more to phytoplankton biomass, do contain chlorophyll *a*. Thus, the fluorometric method of estimating phytoplankton biomass is suitable for comparison to electronic measures (CTD and MIDAS) and for comparison with salinity and nutrient data, to identify trends in biological communities.

2. Methods

Water samples were collected by bucket for the surface or by 5-1 Niskin bottles for near-bottom or selected depths. The middle of the Niskin bottle was approximately 1-m above the CTD Sea Tech fluorescence probe. MIDAS samples were collected from tubing (outflow or inflow) closest in proximity to the point of measurement of *in vivo* fluorescence in the system (Turner Designs fluorometer). The volume of water filtered through GF/F filters was 100 ml, or less if turbid. The filters were extracted in 5 ml of 40/60 DMSO (dimethyl sulfoxide)/90% acetone solution for a minimum of 1 hour and not more than 5 hours. Extracts were measured, before and after acidification, on a Model 10 Turner fluorometer. The fluorometer was calibrated with a chlorophyll *a* standard (Sigma, *Anacystis* chlorophyll *a*) on a Varian DMS80 UV, visible spectrophotometer.

Electronic measurements of *in vivo* fluorescence were collected from the LUMCON SeaBird CTD Sea Tech fluorometer, and the LUMCON MIDAS system Turner Designs fluorometer. Surface water salinity values were determined on an AutoSal, maintained and calibrated by the LSU Coastal Studies Institute Shop.

3. Results

a. Cruise III, April 1993. Surface chlorophyll *a*, phaeopigments, and total pigment distributions indicated strong cross-shelf gradients from offshore of Terrebonne Bay (S1) to offshore of Sabine estuary (S6) (Figure 67). To the west of Sabine estuary, surface chlorophyll *a* concentrations were uniformly below 5 μg/l. Similar trends in surface water chlorophyll *a* and phaeopigments are visible in a longitudinal plot (Figure 68). Surface pigments were composed primarily of chlorophyll *a*. The percentage of phaeopigments in the surface water samples increased with distance from the east (below 25%) to the west (20 to 45%) (Figure 68).

Bottom water chlorophyll *a* concentrations also displayed similar strong cross-shelf gradients as far west as Sabine, but higher phaeopigment concentrations were restricted to the area of the Atchafalaya River plume (Figure 69). Bottom water phaeopigment concentrations were higher than surface water values within the Atchafalaya River plume.

63
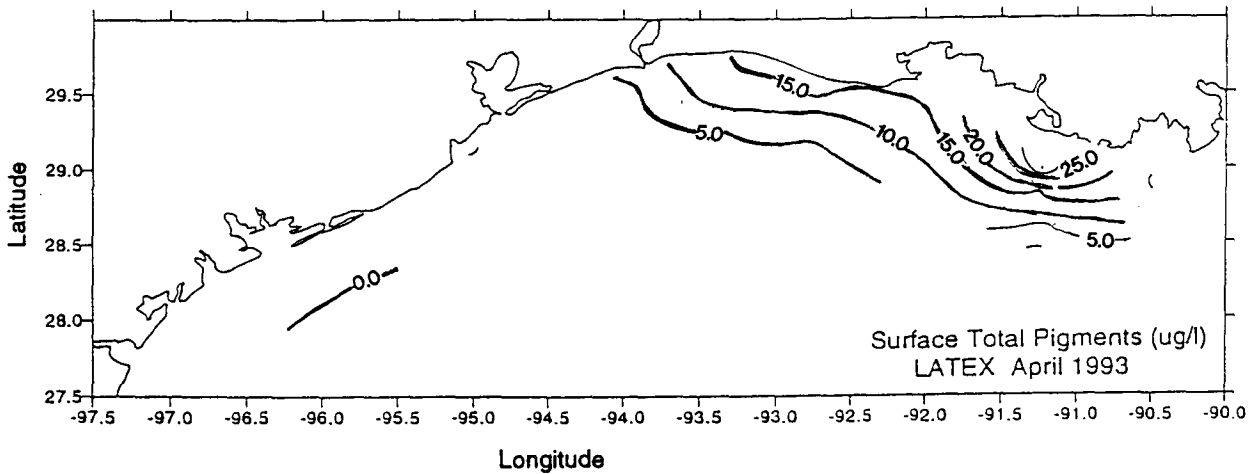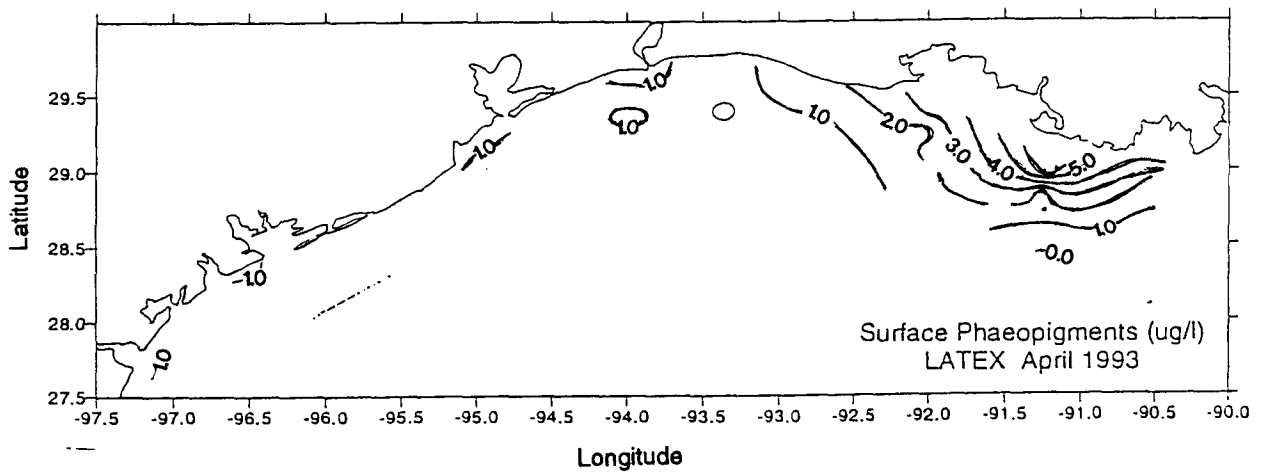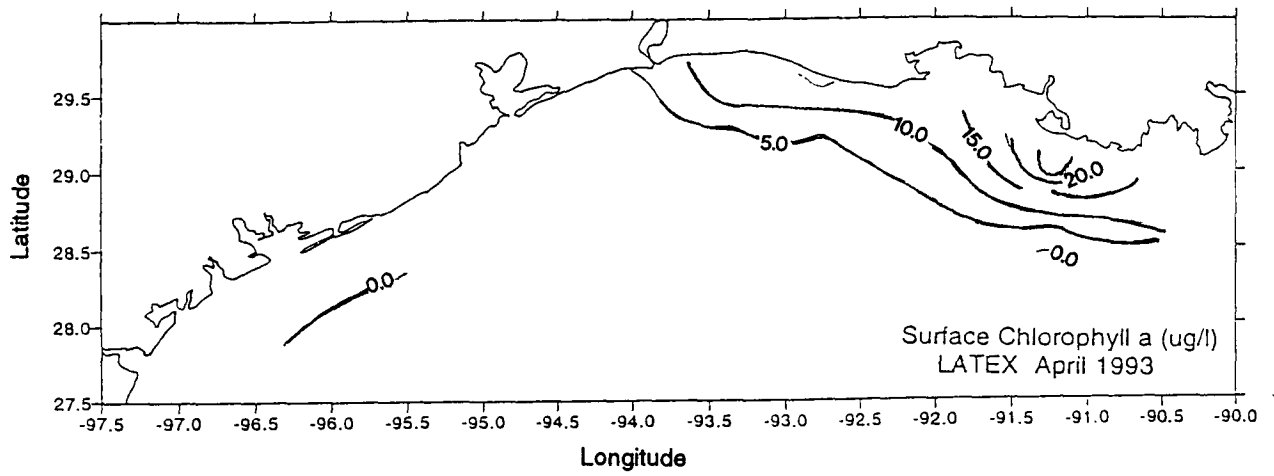
Figure 67. Distribution of surface water chlorophyll *a*, phaeopigments and total
pigments for Cruise III.

Mean Surface Chlorophyll a vs Longitude
LATEX April 1993

Mean Surface Phaeopigments vs Longitude
LATEX April 1993

Mean Phaeopigment Percentage of Total Pigments vs Longitude
LATEX April 1993

65
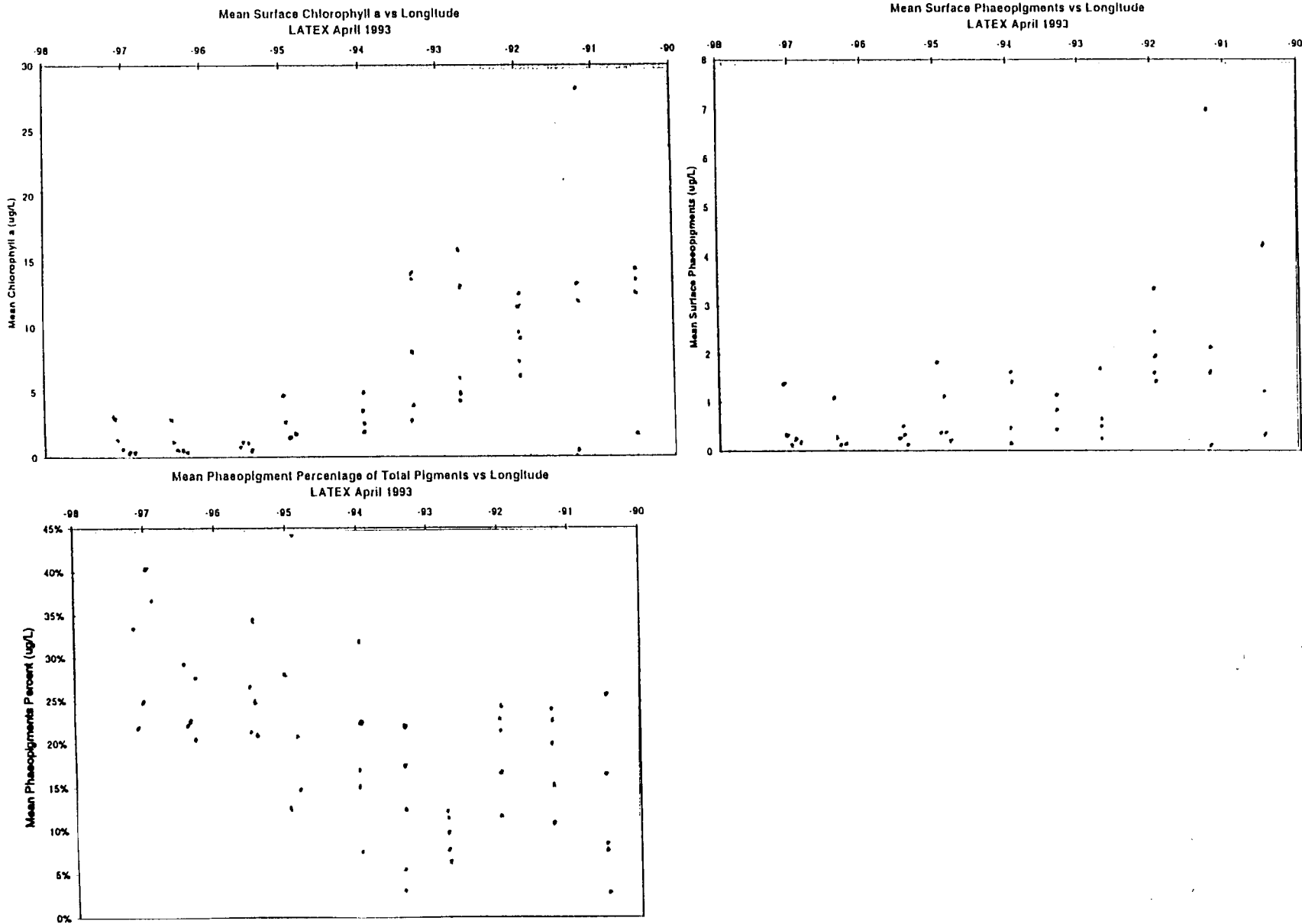
Figure 68. Distribution of surface water chlrophyll a, phaeopigments and percent phaeopigments of total pigments by longitude for Cruise III.
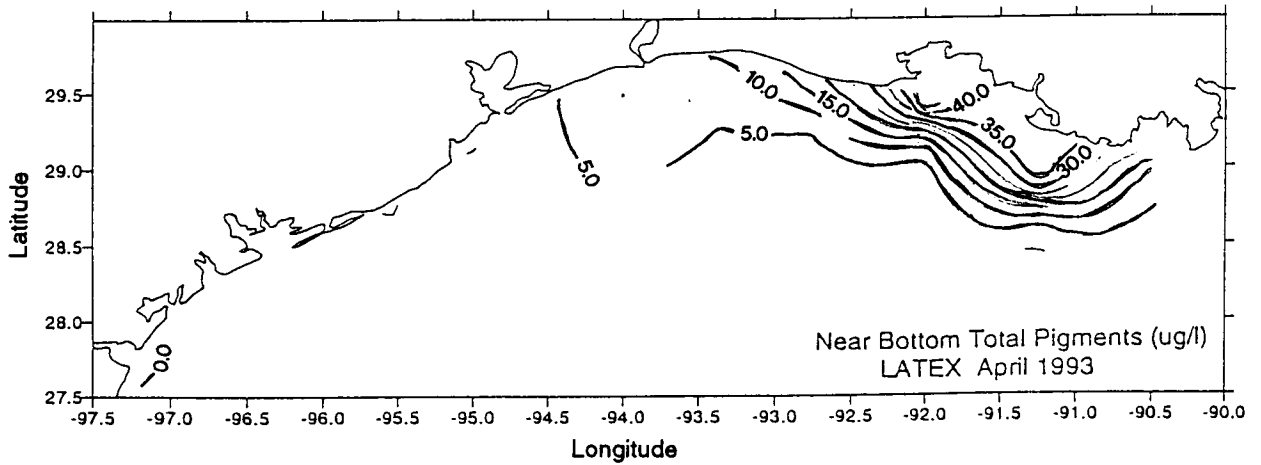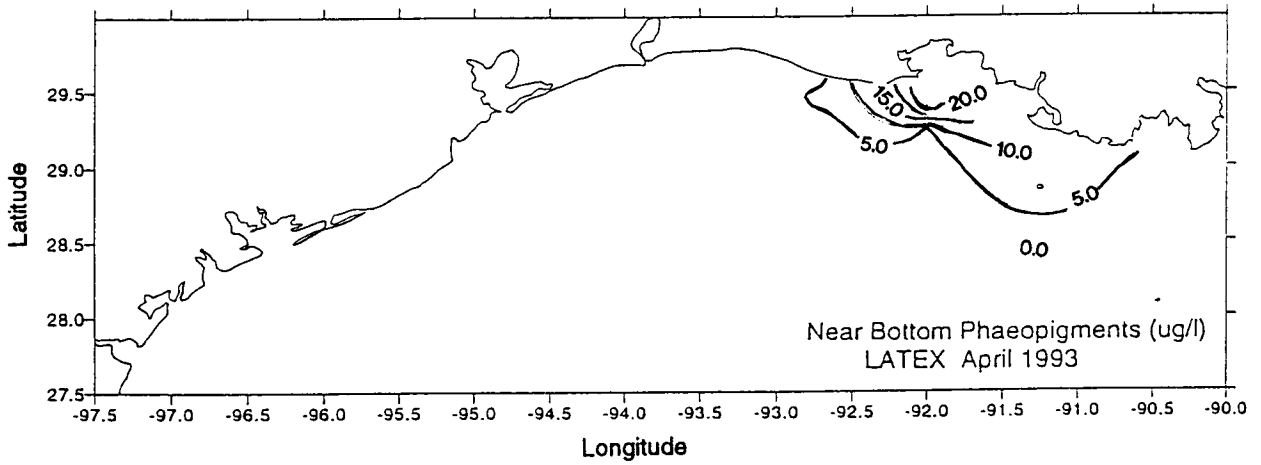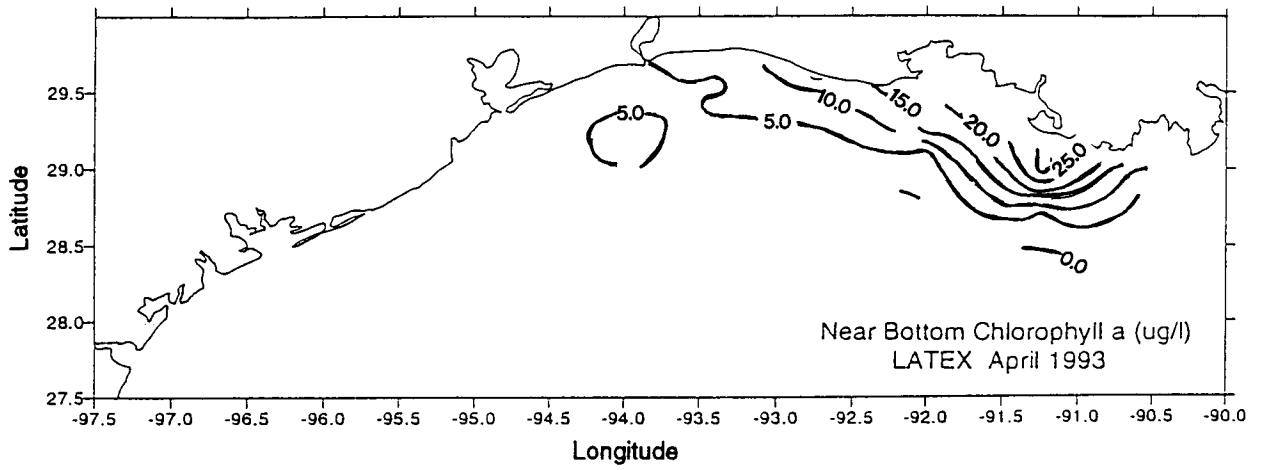
Figure 69. Distribution of near-bottom water chlorophyll a, phaiopigments and
total pigments for Cruise III.

Chlorophyll a concentrations in surface water samples (bucket-collected) were very similar to those obtained from the MIDAS flow-through system (Figure 70). Similar relationships were obtained for phaeopigments and total pigments (not illustrated). These relationships indicate that the flow-through system was collecting the same water mass as the surface bucket. On the other hand, the continuously-recording, electronically-derived *in vivo* chlorophyll a values from the MIDAS system did not correspond well with the absolute values obtained from the water samples (Figure 70), although the relationships were much more linear than the parabolic relationships established for Cruises I and II (Rabalais in Murray, 1994).

A similar comparison of the LUMCON CTD *in vivo* fluorescence probe to absolute concentrations of chlorophyll a showed fairly linear relationships below concentrations of 10 μg/l, but the relationships were different for surface and near-bottom waters (data not shown). Thus, caution must be taken in interpreting cross-shelf contours of CTD *in vivo* fluorescence as representative of the chlorophyll a biomass in the study area.

Surface water salinities were mostly in the 20 to 35 ppt range, with a few values between 5 and 13 ppt. Highest chlorophyll a biomass values were between 5 and 28 ppt, a rather broad range compared to other chlorophyll a biomass vs. salinity distributions (Figure 71).

The dissolved nutrients generally decreased with an increase in salinity away from the freshwater sources (data not shown). The dissolved inorganic nitrogen pool was dominated by nitrate (cf. Figure 71. Chlorophyll a biomass was high across a broad range of nutrient concentrations but generally decreased as nutrients were diluted on the seaward end of the plume, or coastal current (Figure 71).

b. Cruise IV, July 1993. Surface water pigment distributions for July 1993 were very similar to those of Cruise III in April 1993 (Rabalais in Murray, 1994). Surface chlorophyll a, phaeopigments, and total pigment distributions indicated strong cross-shelf gradients from offshore of Terrebonne Bay (S1) to offshore of Sabine estuary (S6) (Figure 72). To the west of Sabine estuary, surface chlorophyll a concentrations were uniformly below 5 μg/l. Similar trends in surface water chlorophyll a and phaeopigments are visible in a longitudinal plot (Figure 73). As on Cruise III, surface pigments were composed primarily of chlorophyll a; however, the percentage of phaeopigments in surface waters was much greater in July 1993 than in April 1993. Extremely high percentages of phaeopigments were found in surface waters on the hypoxia transect off Terrebonne Bay and as far west at 92°W off the Atchafalaya River plume (Figure 73).

Bottom water chlorophyll a concentrations also displayed similar strong cross-shelf gradients as far west as Sabine and were similar to those of Cruise III in April 1993 (Figure 74). Bottom water phaeopigments were surprisingly low, since they are often elevated during mid-summer, especially during hypoxic conditions as documented on this cruise (see Section VII). Bottom water phaeopigment concentrations in the vicinity of the Atchafalaya River plume were actually higher in April 1993 than in July 1993. Bottom water phaeopigment concentrations were similar to surface water values in July 1993.

As on Cruise III, chlorophyll a concentrations in surface water samples (bucket-collected) were very similar to those obtained from the MIDAS flow-through system (Figure 75). Similar relationships were obtained for phaeopigments and total pigments (data not shown). These relationships indicate that the flow-through system was collecting the same water mass as the surface bucket. On the other hand, the continuously-recording, electronically-derived *in vivo* chlorophyll a values from the MIDAS system did not correspond well with the absolute values obtained from the water samples (Figure 75), and was similar to the parabolic relationships established for Cruises I and II (Rabalais in Murray, 1994).
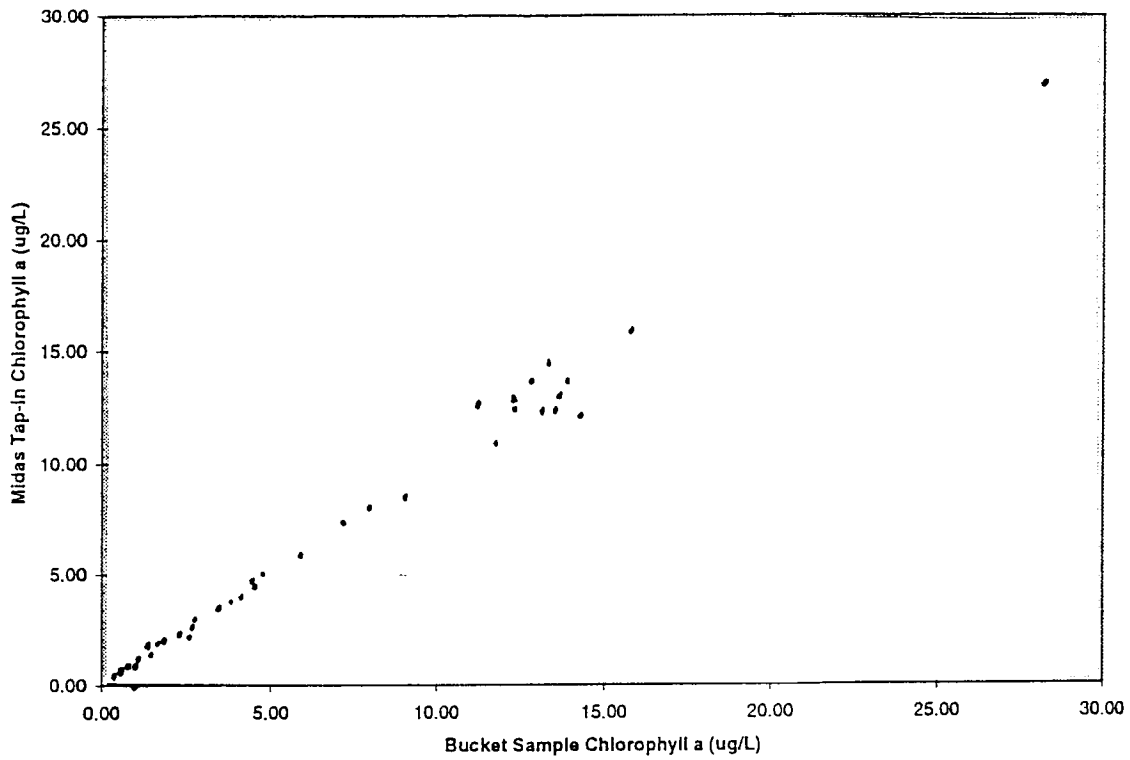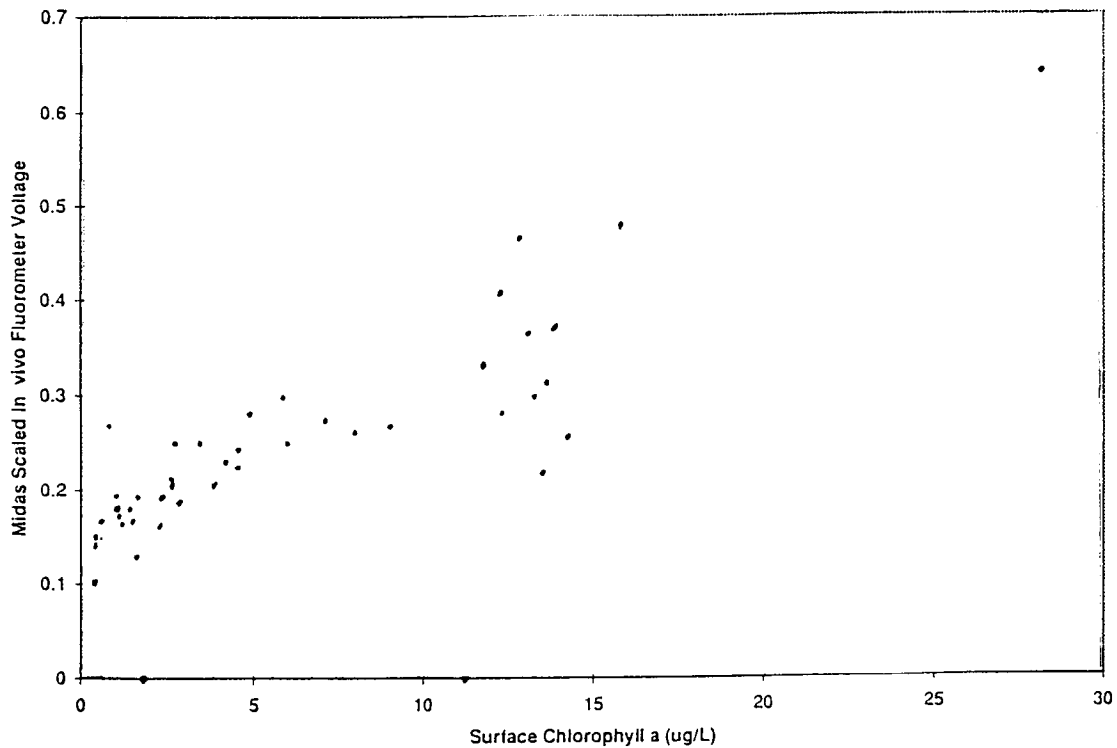
Figure 70. Relationship between surface chlorophyll *a* collected by bucket and MIDAS tap-in samples (upper panel) and between surface chlorophyll *a* and MIDAS scaled *in vivo* fluorescence voltage (lower panel) for Cruise III.

Surface Chlorophyll a vs Salinity
LATEX April 1993

Surface Chlorophyll a vs Dissolved Inorganic Nitrogen
LATEX April 1993

Surface Chlorophyll a vs Silicate:Nitrate Ratio
LATEX April 1993

Surface Chlorophyll a vs Silicate
LATEX April 1993

Chlorophyll a (ug/L)

Salinity (ppt)

NH4+NO2+NO3 (ug-at/L)

SIO4:NO3 Ratio

Silicate (ug-at/L)
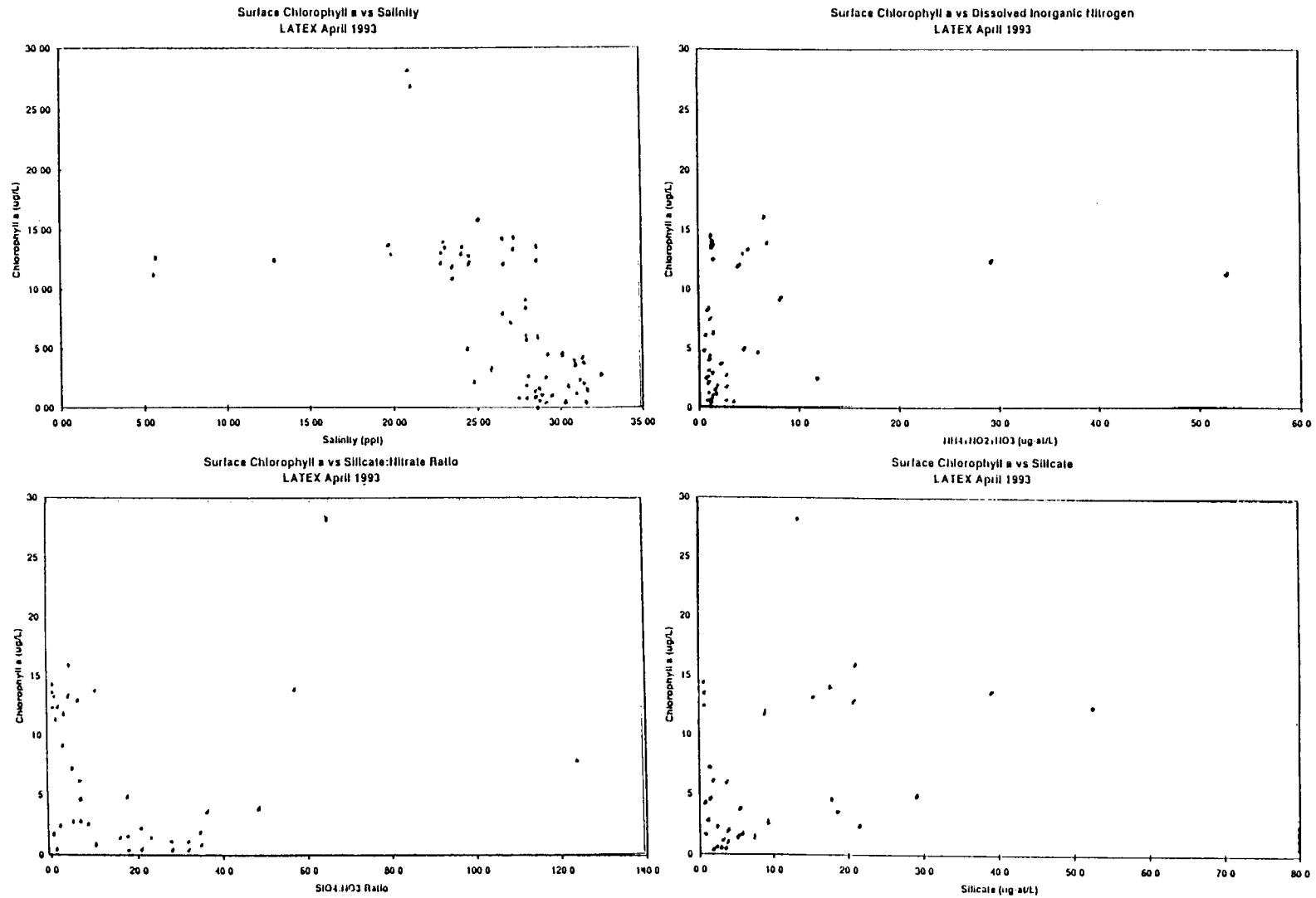
Figure 71. Distribution of chlorophyll *a* concentrations by salinity, dissolved
inorganic nitrogen ($NO_3+NO_2+NH_4$), silicate and the silicate:DIN
ratio for Cruise III.
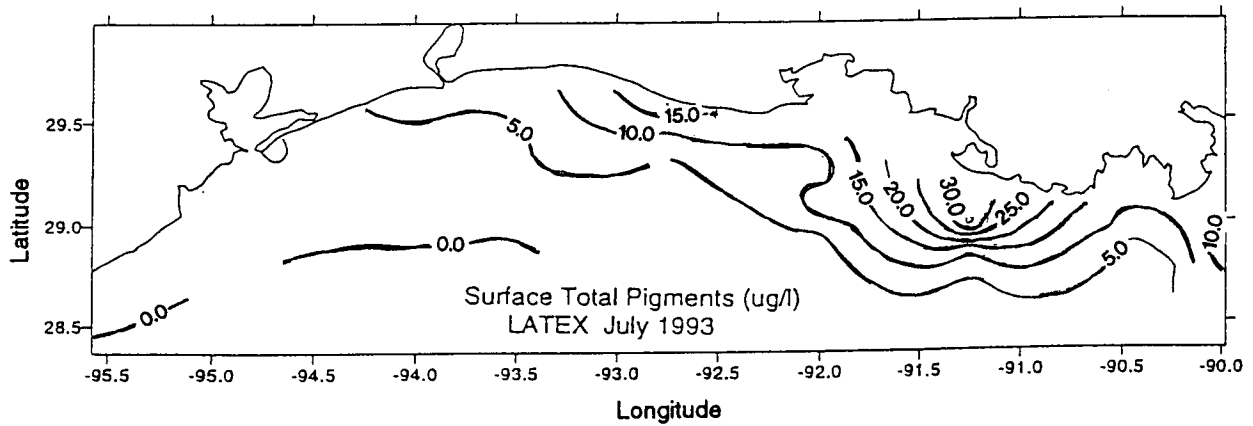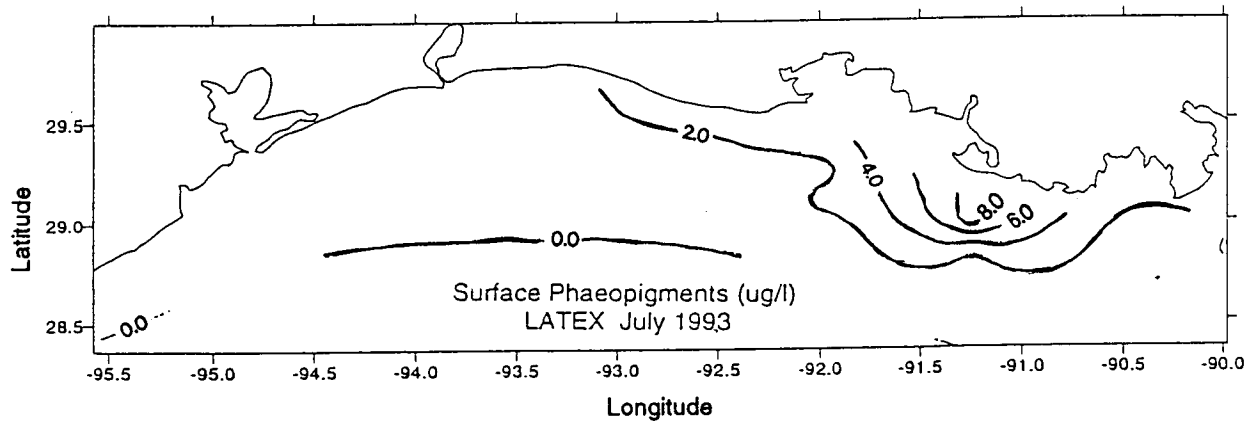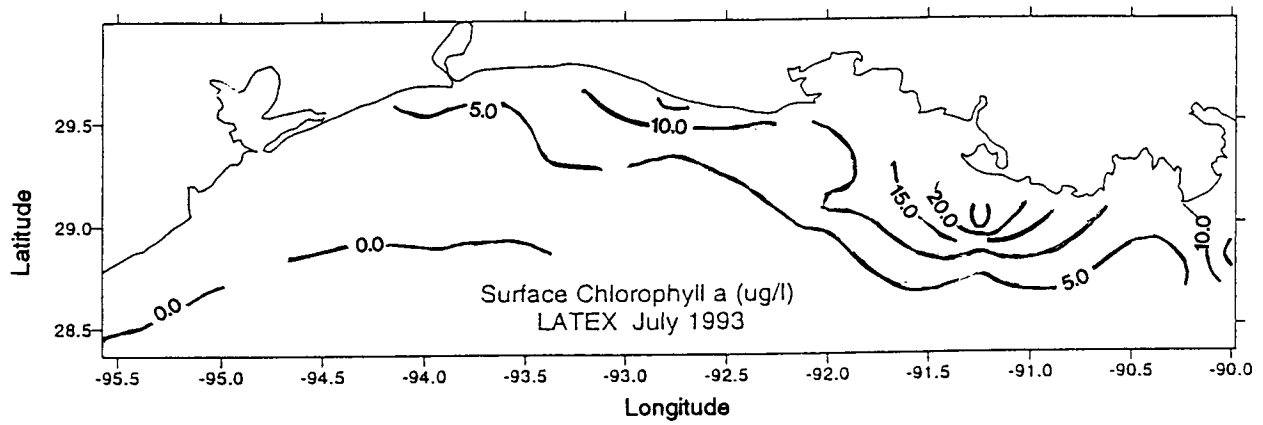
Figure 72. Distribution of surface water chlorophyll *a*, phaeopigments and total pigments for Cruise IV.
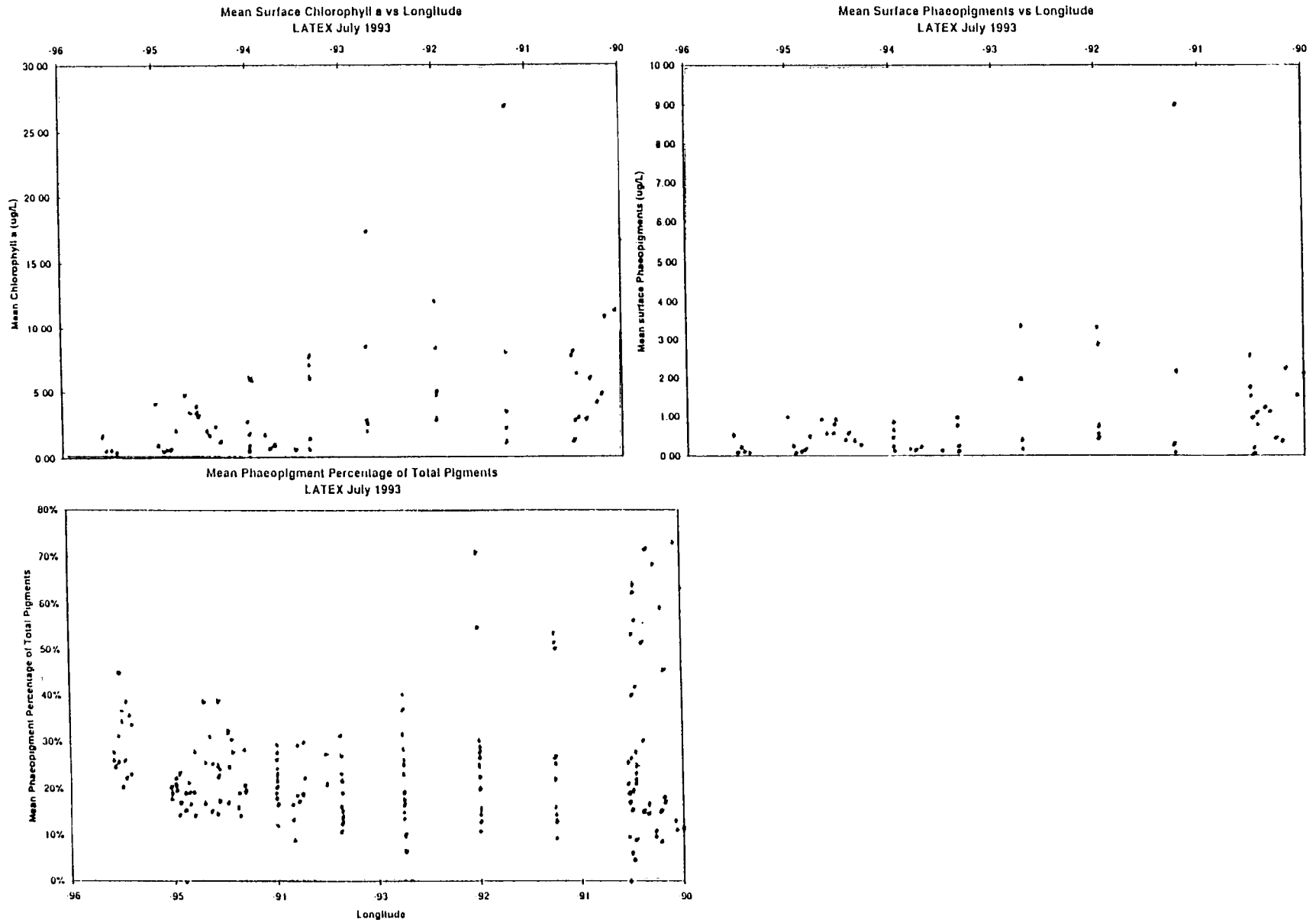
Figure 73. Distribution of surface water chlorophyll a, phaeopigments and percent phaeopigments of total pigments by longitude for Cruise IV.

71
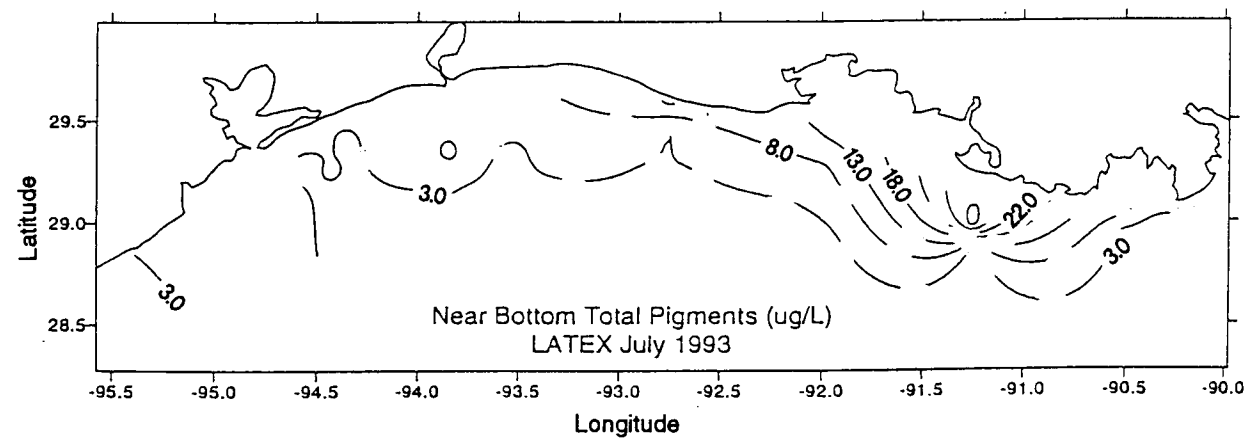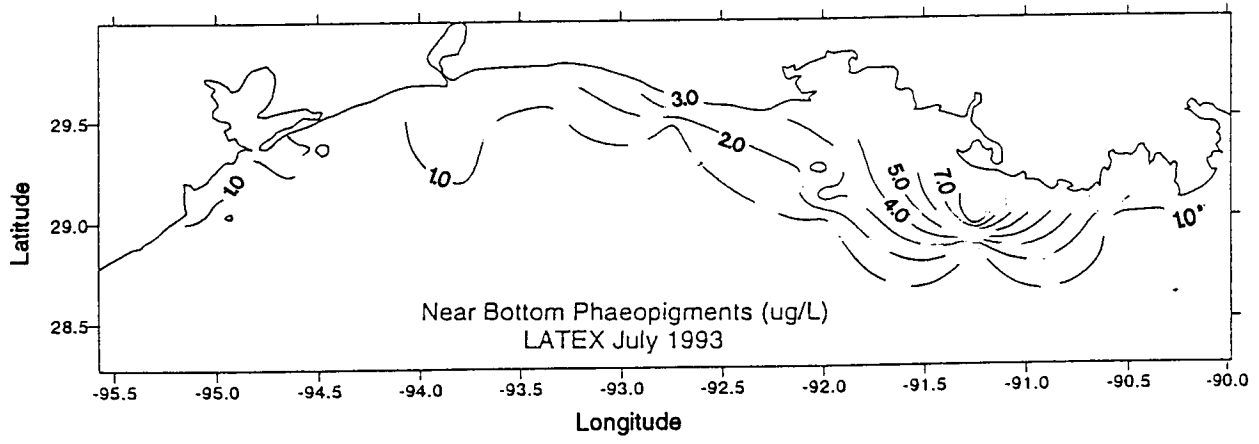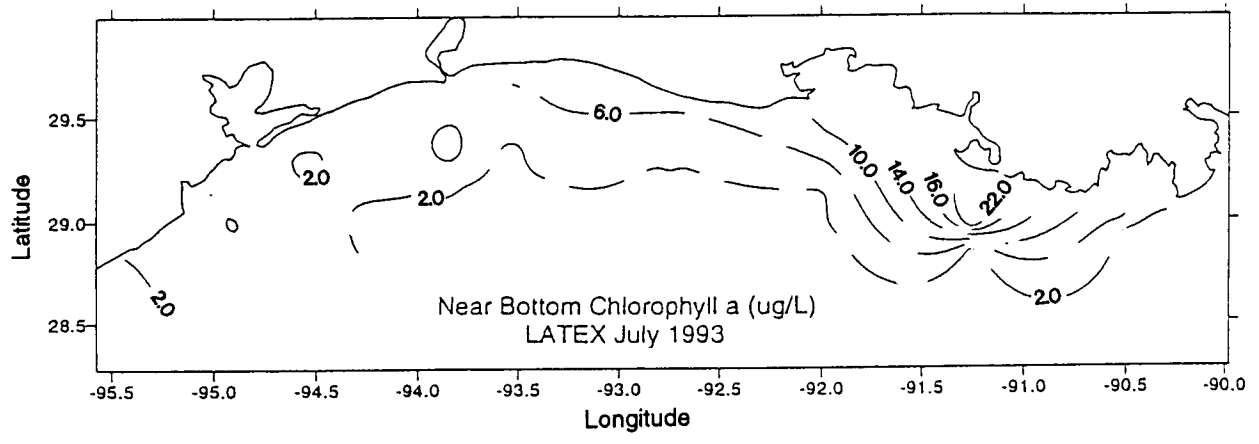
Figure 74. Distribution of near-bottom chlorophyll a, phaeopigments and total
pigments for Cruise IV.
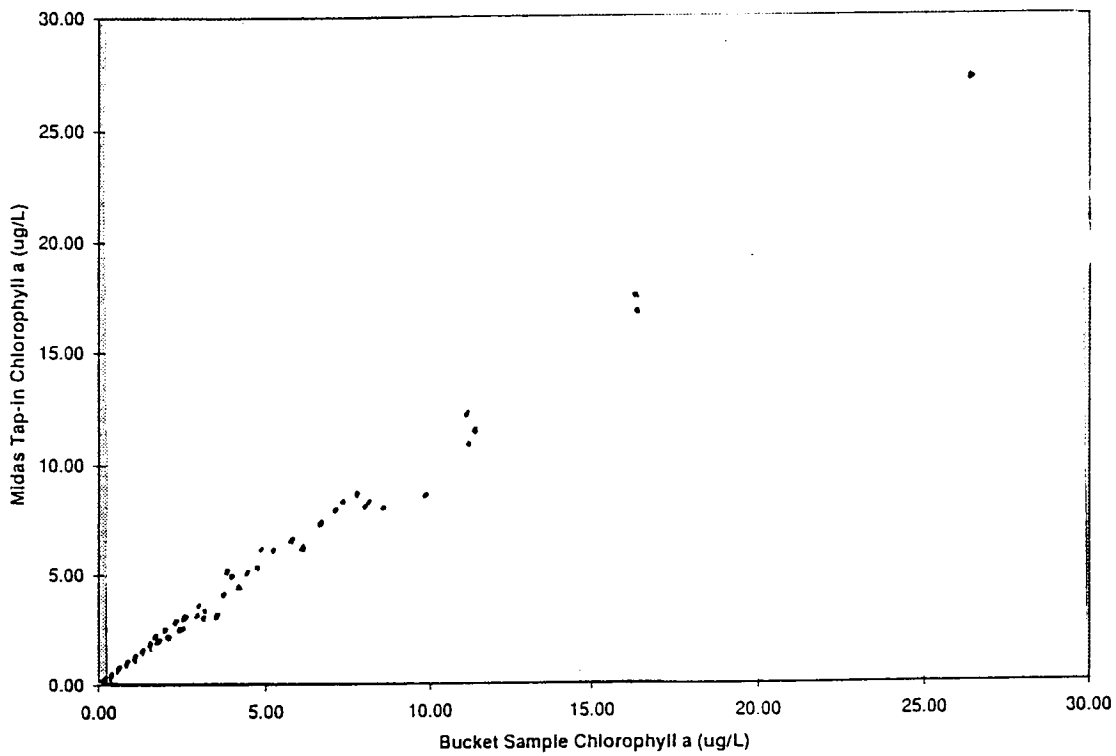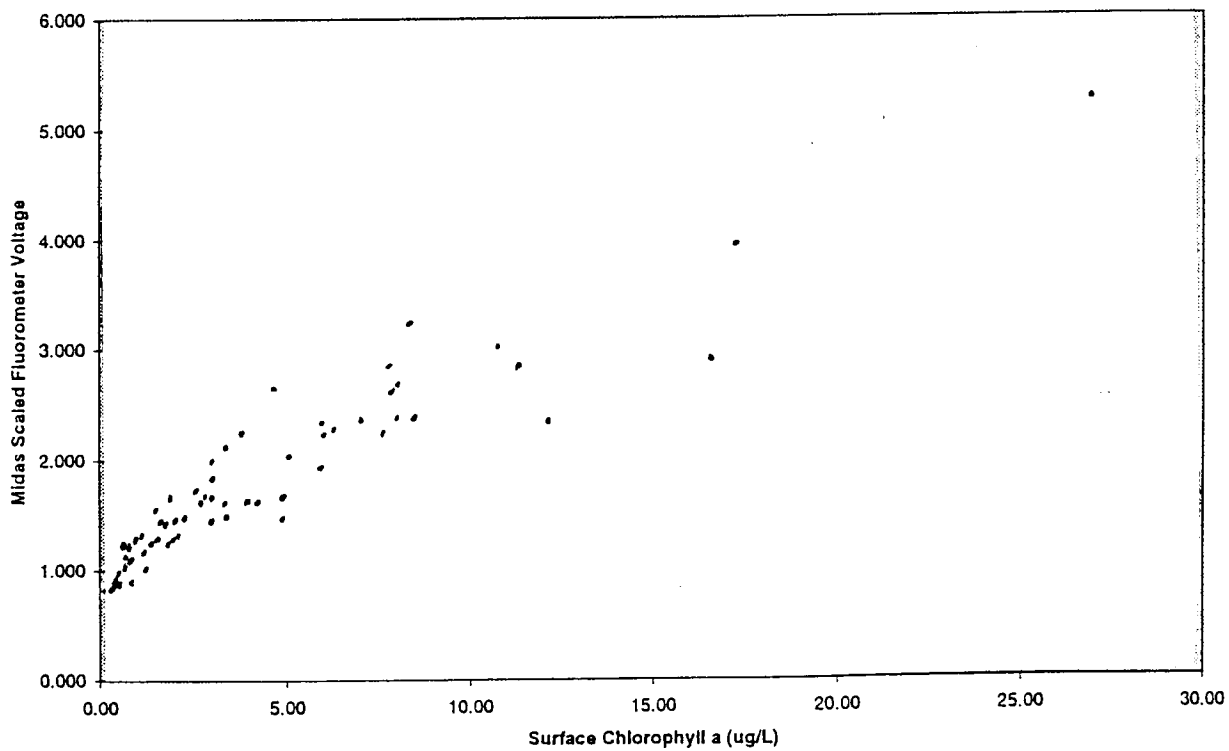
Figure 75. Relationship between surface chlorophyll a collected by bucket and
        MIDAS tap-in samples (upper panel) and between surface chlorophyll
        a and MIDAS scaled in vivo fluorescence voltage (lower panel) for
        Cruise IV.

A similar comparison of the LUMCON CTD *in vivo* fluorescence probe to absolute concentrations of chlorophyll *a* showed somewhat linear relationships, but the relationships were different for surface and near-bottom waters (data not shown). Thus, caution must be taken in interpreting cross-shelf contours of CTD *in vivo* fluorescence as representative of the chlorophyll *a* biomass in the study area.

Surface water salinities were mostly in the 20 to 35 ppt range, with a few values between 2 and 18 ppt. Highest chlorophyll *a* biomass values were between 8 and 20 ppt, a rather broad range compared to other chlorophyll *a* biomass vs. salinity distributions (Figure 76).

The dissolved nutrients generally decreased with an increase in salinity away from the freshwater sources (data not shown). The dissolved inorganic nitrogen pool was dominated by nitrate (cf. Figure 76). Chlorophyll *a* biomass was high across a broad range of nutrient concentrations but generally decreased as nutrients were diluted on the seaward end of the plume, or coastal current (Figure 76).

B. Phytoplankton Survey (Quay Dortch)

1. Introduction

The primary purpose for measuring phytoplankton species composition was to use phytoplankton as tracers of water masses and to extend information gained from other programs focused on the near river plume to the extended plume. In addition, this program offered an opportunity to compare the effects of the 1993 Mississippi River flood with non-flood periods and to compile more data on the occurrence of toxic and noxious algae in the region.

Some phytoplankton are characteristically found in certain types of water masses and can be used to trace the extent of movement of these water masses. This is especially true in the northern Gulf of Mexico where extremely different kinds of water often mix and range from highly eutrophic freshwater to extremely oligotrophic and saline waters offshore.

Dortch (1994a) has proposed a series of indicators, the most important of which are summarized in Table 3. The small (1-2 μm), coccoid cyanobacteria of the genus *Synechococcus* have a variety of photosynthetic pigments, besides chlorophyll *a*, which give them distinctive colors under epifluorescence microscopy (Dortch in Murray, 1994a). One group, containing the pigment phycocyanin (PC) (Waterbury et al., 1986; Vaulot and Ning, 1988), is usually the only cyanobacteria at low salinities in this area (Table 3). Phytoplankton in offshore waters are generally dominated by another group of small coccoid cyanobacteria, the high phycourobilin phycoerythrin-containing *Synechococcus* (High PU/PE) (Table 3) (Olson et al., 1988). Another group of cyanobacteria, those containing low phycourobilin and phycoerythrin (Low PU/PE), are intermediate in color and habitat. The pigment differences between these three groups have been hypothesized to be related to either salinity or light quality (Wood et al., 1985; Waterbury et al., 1986; Vaulot and Ning, 1988; Pick, 1991), but, regardless of the cause, they are specific indicators of water sources in this area (Dortch in Murray, 1994a). Thus, the degree to which the high-PU/PE or PC cyanobacteria dominate and are mixed with each other and the low-PU/PE cyanobacteria can indicate what types of water are mixing. Unfortunately, a time-scale cannot yet be put on the mixing because we do not yet have any data on survival rates after mixing.

74
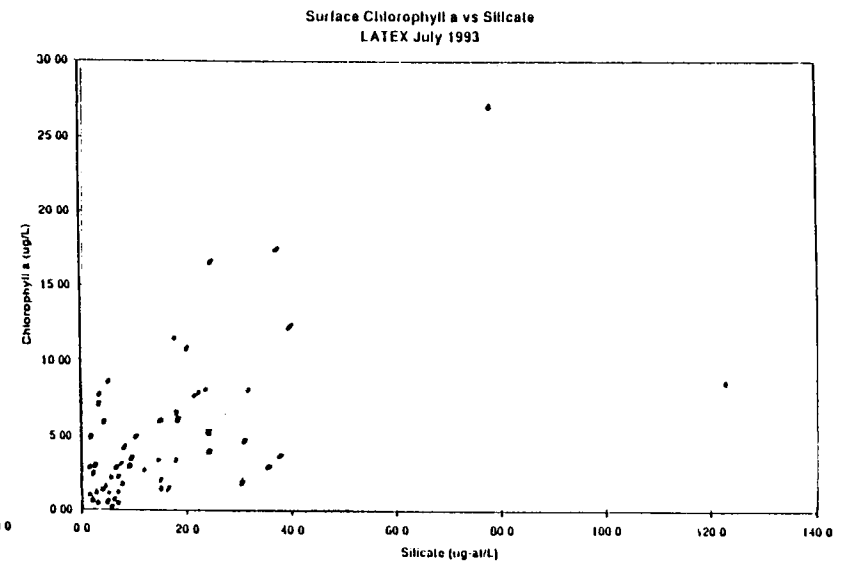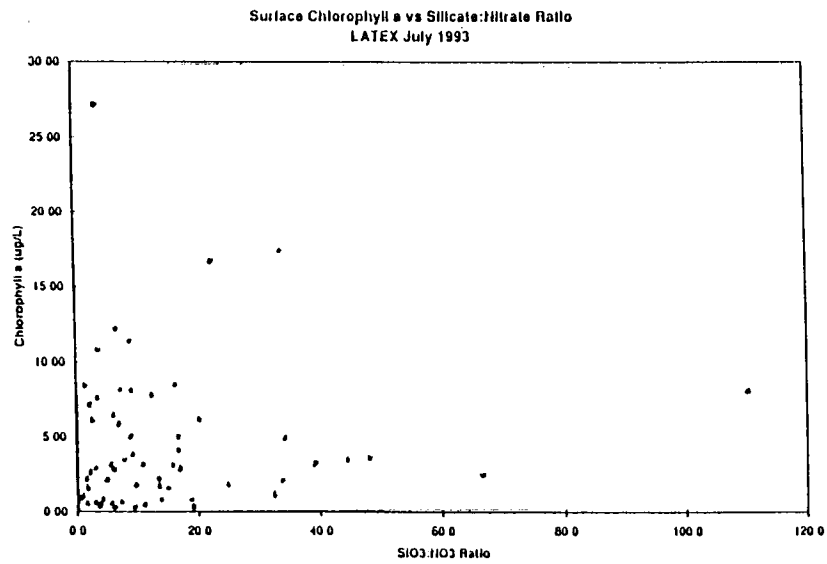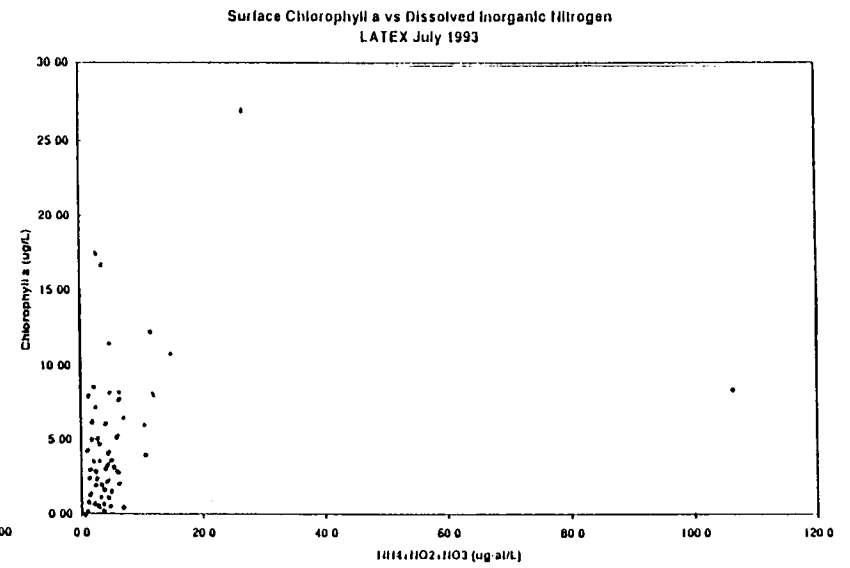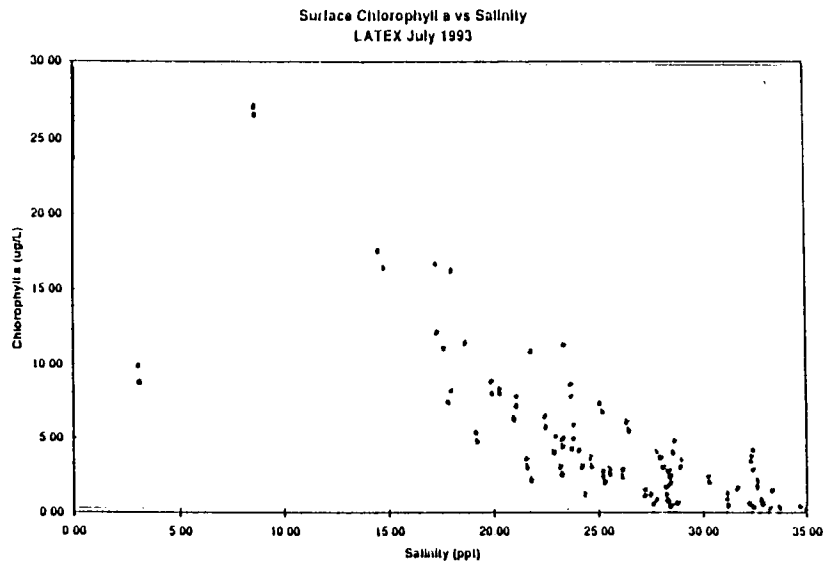
Figure 76. Distribution of chlorophyll a concentrations by salinity, dissolved inorganic nitrogen (NO3+NO2+NH4), silicate and the silicate:DIN ratio for Cruise IV.

Table 3. Phytoplankton groups or species which can be used to trace water masses and mixing in the LATEX area.

Group/Species	Indicator
Phycocyanin-containing *Synechococcus* (PC)	Direct river input
Skeletonema costatum	High productivity core of plume
% Diatoms/Total Autotrophs	River plume
High Phycouribilin/ Phycoerythrin-containing *Synechococcus* (High PU/PE)	High salinity water off shore

Because of the very low silicate concentrations in offshore waters, there are very few diatoms, especially in the large size fractions. Phytoplankton, especially diatom, biomass and growth is usually maximal at some distance from the river mouth because it is necessary for the sediment to settle out so there is enough light to stimulate photosynthesis. The first species to respond is almost always *Skeletonema costatum*, an opportunistic, fast-growing diatom. Growth of this species is then followed by that of other diatoms. Further down the axis of the plume the nutrients become depleted, and although there is plenty of light, there is insufficient nutrients to support high phytoplankton biomass. Thus, it can by hypothesized that high numbers of *S. costatum* will indicate the high productivity core of the plume, but that diatoms will dominate along the axis of the plume until the nutrients become depleted or diluted.

2. Method

The method for preserving and counting phytoplankton was adapted from Murphy and Haugen (1985), Shapiro and Haugen (1988), and Shapiro et al. (1989). Phytoplankton samples were collected at the surface using a bucket and at the bottom using 10 liter Niskin bottles on a CTD Rosette. If there was a mid-water fluorescence maximum (Sea Tech Fluorometer on seabird CTD), samples were also taken with a Niskin bottle. Between 0.1 and 1 liter was preserved with 50% glutaraldehyde to a final concentration of 0.5% (by volume) and refrigerated for at least 1 hour and not more than 24 hours prior to size fractionated filtration (Dortch in Murray, 1994a). Polycarbonate filters were used throughout. Phytoplankton in the 3 to 8 μm and > 8 μm size fraction were stained with proflavine monohydrochloride (Sigma P-4646, 0.33 g/200 ml distilled, deionized water). Before staining, samples < 25 ml were made up to 25 ml using 0.2 μm filtered seawater of approximately the same salinity. If possible, samples were filtered without vacuum, but if necessary < 100 mm vacuum was applied. The filters were transferred to slides and mounted with low fluorescence, low viscosity immersion oil. The 0.2-3 μm size fraction was counted immediately, the 3-8 μm size fraction was stored in the refrigerator and counted within several days. The > 8 μm filters were stored frozen and counted back in the lab within 60 days. Phytoplankton were counted on a BH2-RFA epifluorescence microscope with blue and green excitation (excitation filters BP-490 and BP-545, barrier filters O-515 and O-590, and dichroic mirrors DM500 and DM580). Table 4 outlines the types of organisms counted in each size fraction.

Table 4. Common phytoplankton groups counted in each size fraction.

Size	Phytoplankton Groups
0.2 to 3 μm (count immediately on ship)	Coccoid cyanobacteria--mostly *Synechococcus* Autotrophic eukaryotes Heterotrophic eukaryotes
3 to 8 μm (count on ship within several days)	Phytosynthetic flagellates and non-flagellates Heterotrophic flagellates and non-flagellates Cryptomonads Athecate dinoflagellates Diatoms Coccoid cyanobacteria
>8 μm (freeze and count in lab, detailed taxonomy to species, where possible)	Diatoms Dinoflagellates Ciliates Cryptomonads Colonial cyanobacteria Colonial, freshwater chlorophytes

3. Results

a. Cruise III, April 1993. Size Distribution. The distribution of total phytoplankton in the study area mirrored the distribution of the smallest phytoplankton (0.2-3 μm) because they are numerically the most abundant in both surface and bottom waters (data not shown). The highest concentrations are observed on the shelf between the Atchafalaya River and Galveston Bay and at the western end of the study area. Maximum concentrations of 3 to 8 μm phytoplankton occur in the vicinity of the Atchafalaya River (data not shown). Large phytoplankton concentrations exceed 10^6 cells L^{-1} over much of the shelf east of Sabine Lake (data not shown). Thus, all size fractions were most abundant in the region between the Atchafalaya River and Sabine Lake (S2-S6), the smallest phytoplankton were also abundant off of south Texas (S8-X2), and the large phytoplankton were also abundant to the east of the Atchafalaya river (S2-S1).

Distribution of Specific Groups. As in the previous cruises (Dortch in Murray, 1994a), the two most abundant groups of phytoplankton were cyanobacteria and diatoms (Table 5). The cyanobacteria were relatively most abundant (# cyanobacteria/total #phytoplankton x 100) offshore (data not shown). The %High PU/PE cyanobacteria, indicative of inputs of offshore water, were relatively low and increased from east to west (Figure 77, upper panel). At the bottom the %High PU/PE was generally higher and the contours of similar concentrations paralleled the coast line, suggesting that offshore water pushed further up on the shelf at depth and was overlain by water that was strongly influenced by riverine input even at long distances from the river. In contrast, the %PC cyanobacteria, indicative of direct riverine input, was highest off of Terrebonne Bay, the Atchafalya River, and Calcasieu Lake and were similar at both surface and bottom (Figure 78).
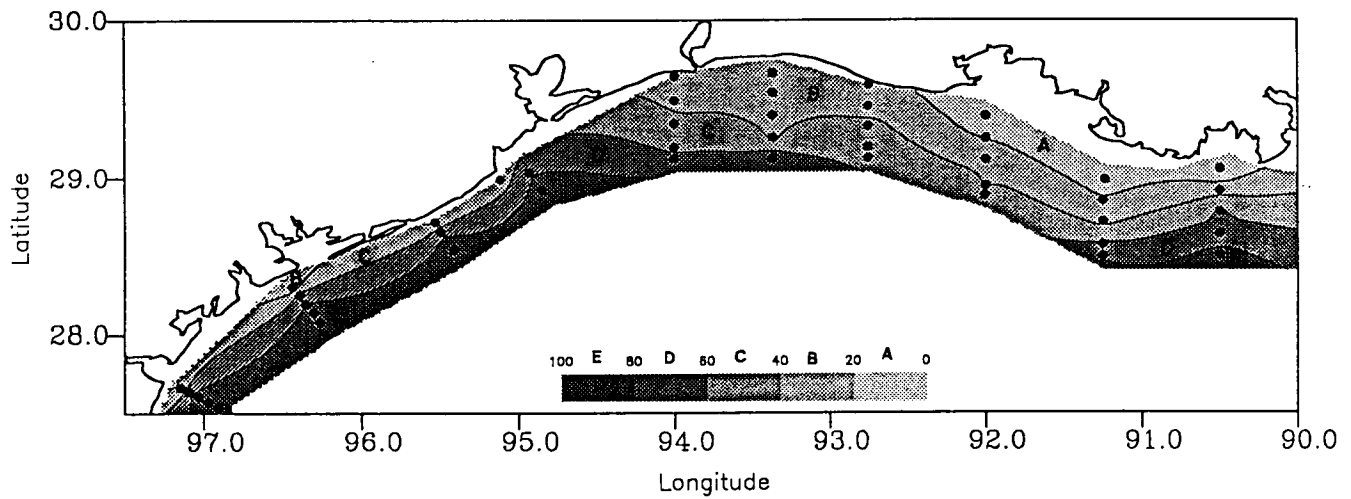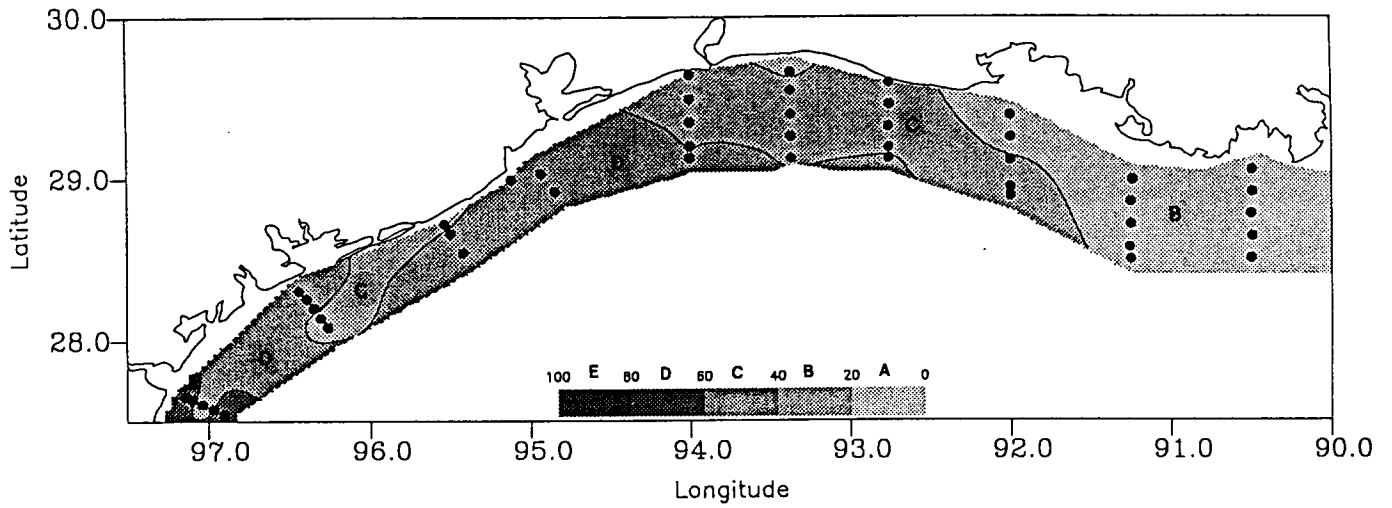
Figure 77. Contours of percent High PI/PE cyanobacteria/total cyanobacteria (0.2-3.0 μm) during Cruise III: surface (upper panel); bottom (lower panel).
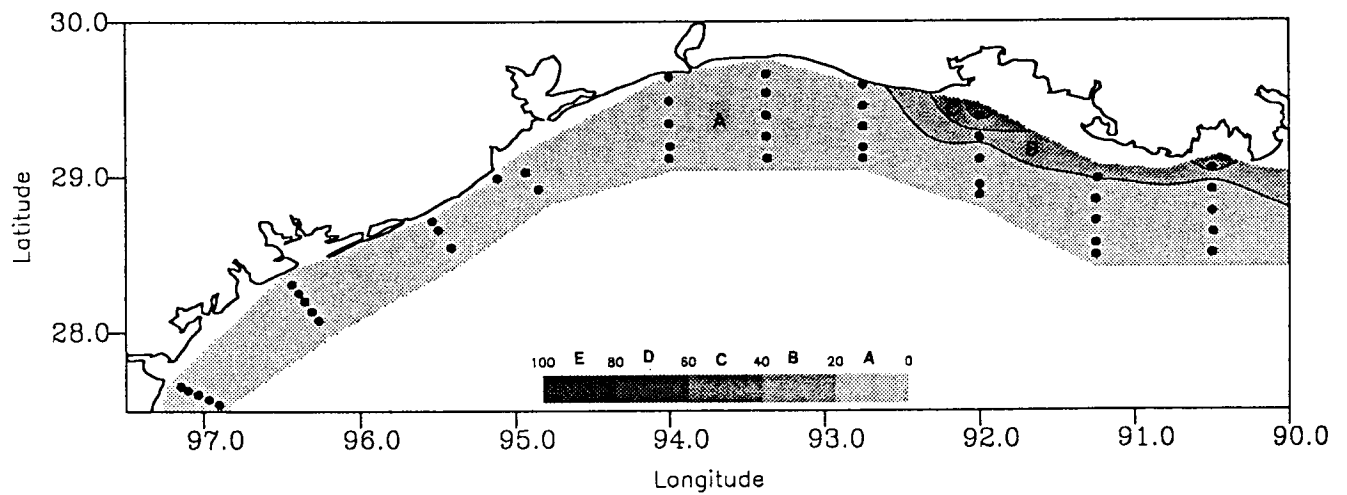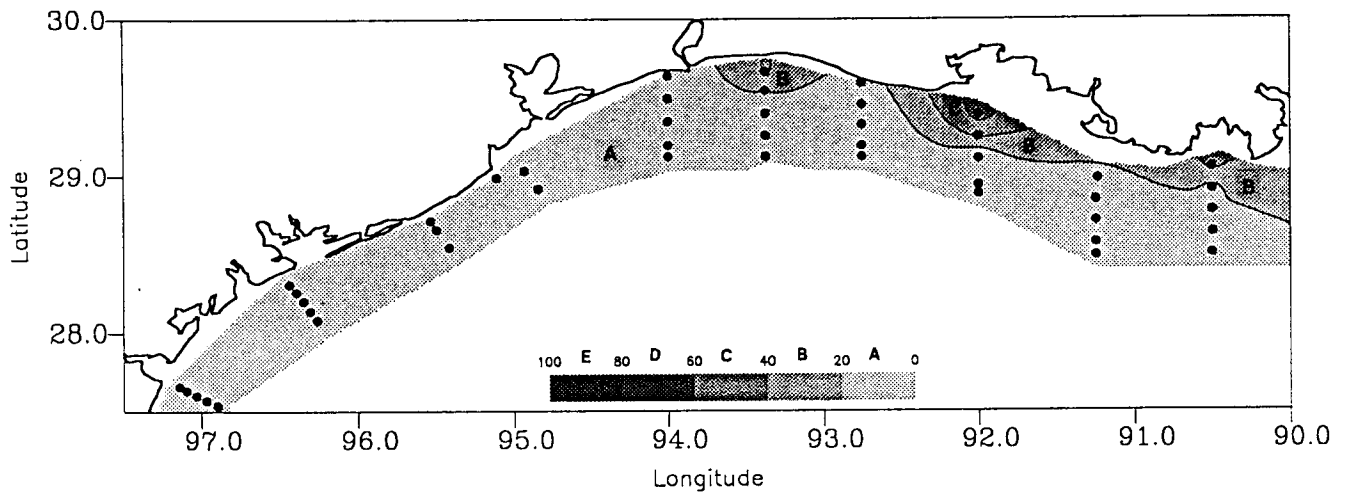
Figure 78. Contours of percent PC cyanobacteria/total cyanobacteria (0.2-3.0 μm) during Cruise III: surface (upper panel); bottom (lower panel).

Table 5. Comparison of mean phytoplankton abundance (#cells L⁻¹) and relative abundance (#cells L⁻¹ for a particular group/total #cells L⁻¹ autotrophs x 100) for all cruises in 1992 and 1993.

	April 1992	October 1992	April 1993	July 1993
Abundance				
0.2 to 3 μm	7.50×10^7	2.14×10^8	3.06×10^7	6.91×10^8
3 to 8 μm	5.36×10^6	1.12×10^7	1.31×10^6	2.62×10^7
> 8 μm	4.32×10^6	1.41×10^6	2.04×10^6	4.20×10^6
Total	8.46×10^7	2.26×10^8	3.40×10^7	7.21×10^8
Relative Abundance				
% Diatoms				
> 8 μm	56.2	22.4	63.4	6.6
Total	7.0	0.4	9.8	0.1
% Cyanobacteria				
Total	82.9	95.3	74.5	97.1
Number Samples	79	79	93	130

Skeletonema costatum, an indicator of the high productivity core of riverine/estuarine plumes, were most abundant off of the Atchafalya River and Calcasieu Lake (Figure 79). The larger plume area is indicated by high % diatoms/autotrophs >8μm (Figure 80). This corresponds to the same areas where large phytoplankton were most abundant (data not shown).

On this cruise a potentially toxic diatom genus, *Pseudo-nitzschia*, was especially abundant (Figure 81). Concentrations exceeded 10^6 cells L⁻¹ over large portions of the shelf to the east of Sabine Lake (S6), in the areas most influenced by riverine input. Concentrations in the surface layer greatly exceeded those at depth (Figure 81).

b. Cruise IV, July 1993. Size Distribution. Phytoplankton concentrations were more than an order of magnitude higher and even more dominated by small phytoplankton in July than in April (Table 5). At the surface the highest concentrations of total phytoplankton and small phytoplankton (0.2 to 3 μm) were observed from transect S2 to the east, i.e., in the region between the Atchafalaya and Mississippi Rivers (data not shown). The area of high abundance of the two larger size fractions was restricted to a smaller area closer to the Atchafalaya River (data not shown). In the bottom water, elevated concentrations of all size fractions were confined to shallow stations near the Atchafalya (data not shown), perhaps reflecting the very strong stratification.

Distribution of Specific Groups. The cyanobacteria were by far the most numerically abundant phytoplankton group, averaging 97% of the phytoplankton (Table 5) and exceeding 98% of the phytoplankton over most of the shelf at the surface and 95% in the bottom water (data not shown). At the surface the %High PU/PE cyanobacteria was high in the region strongly influenced by the Atchafalya plume in the eastern part of the study area (Figure 82). Instead of the usually gradual increase in %High PU/PE to the west, there is an abrupt increase, suggesting intrusion of Gulf
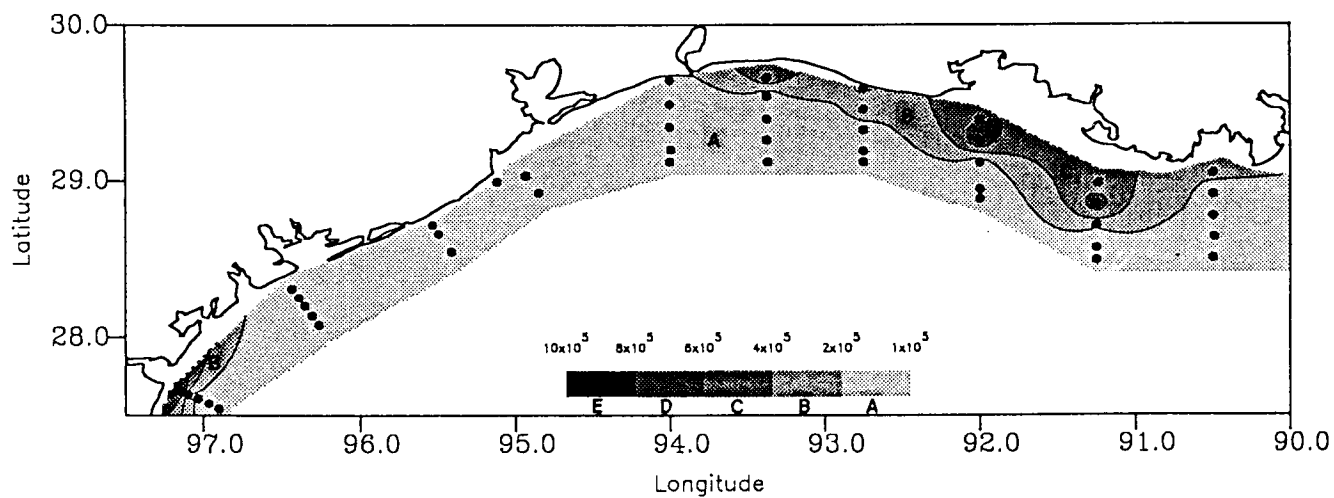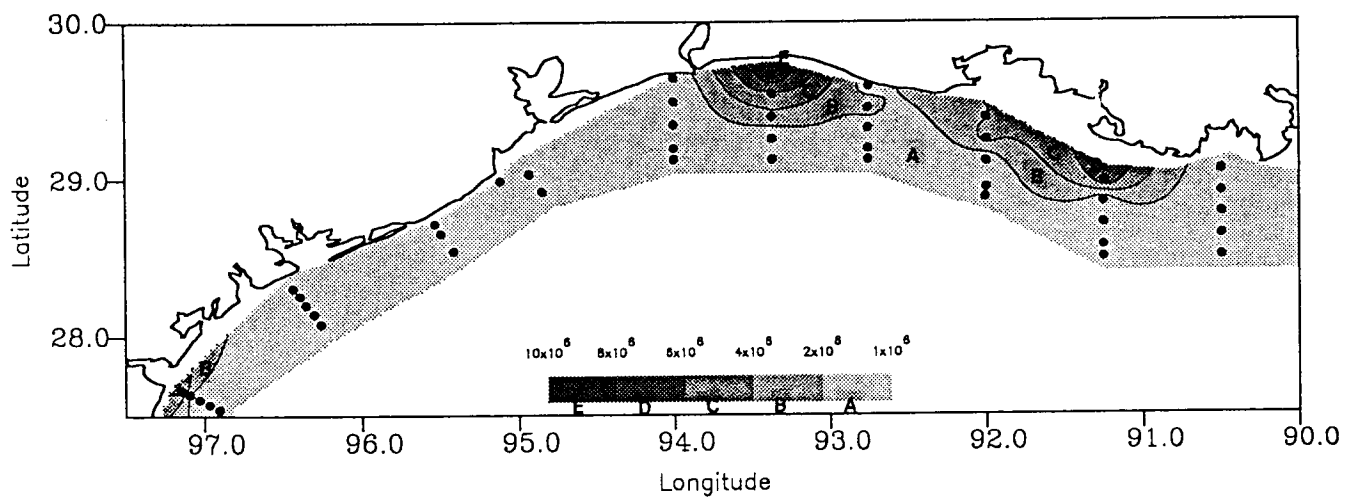
Figure 79. Contours of numbers of *Skeletonema costatum* (number L⁻¹) during
Cruise III: surface (upper panel); bottom (lower panel).

81
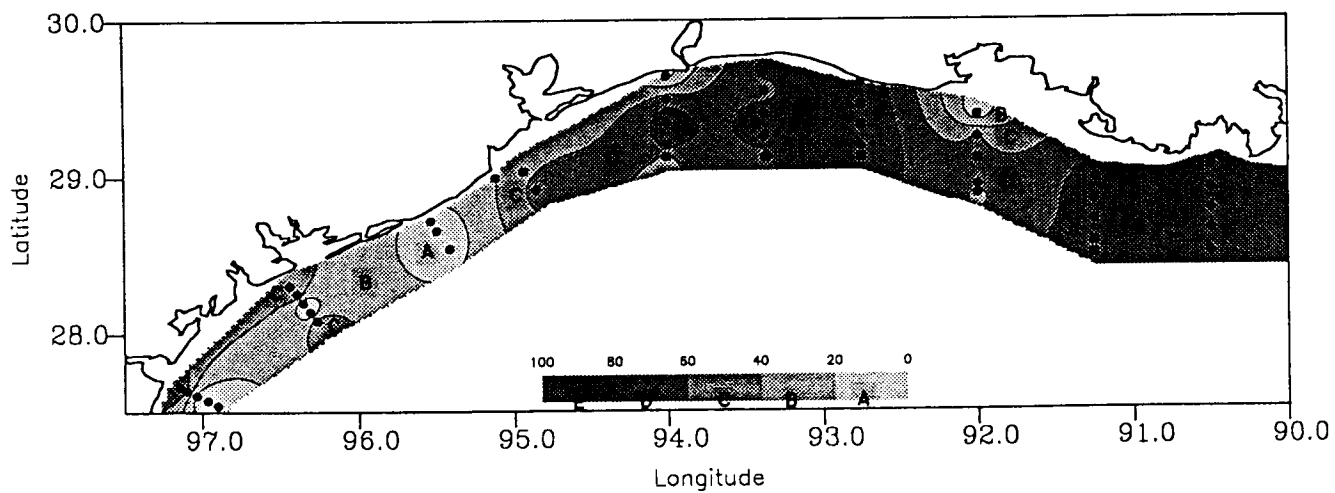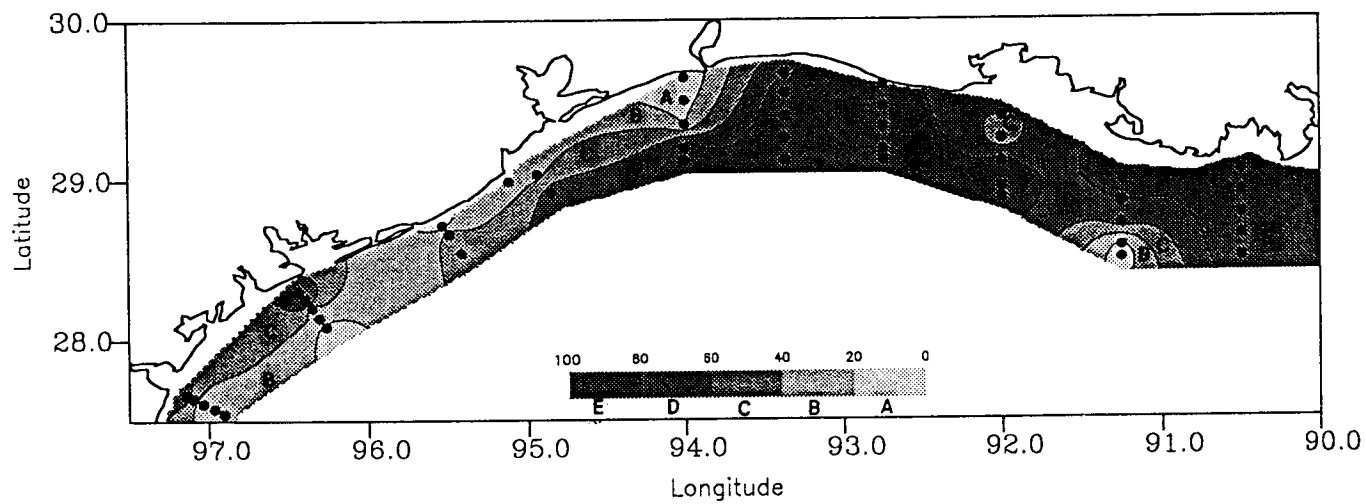
Figure 80. Contours of percent Diatoms/phytoplankton > 8 μm during Cruise III: surface (upper panel); bottom (lower panel).
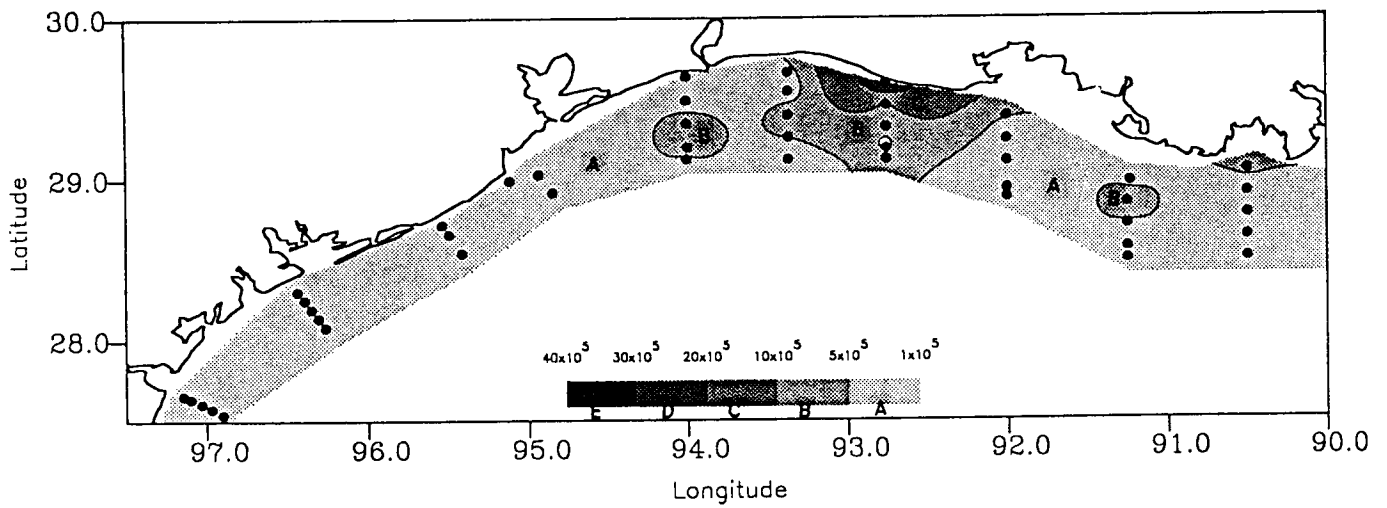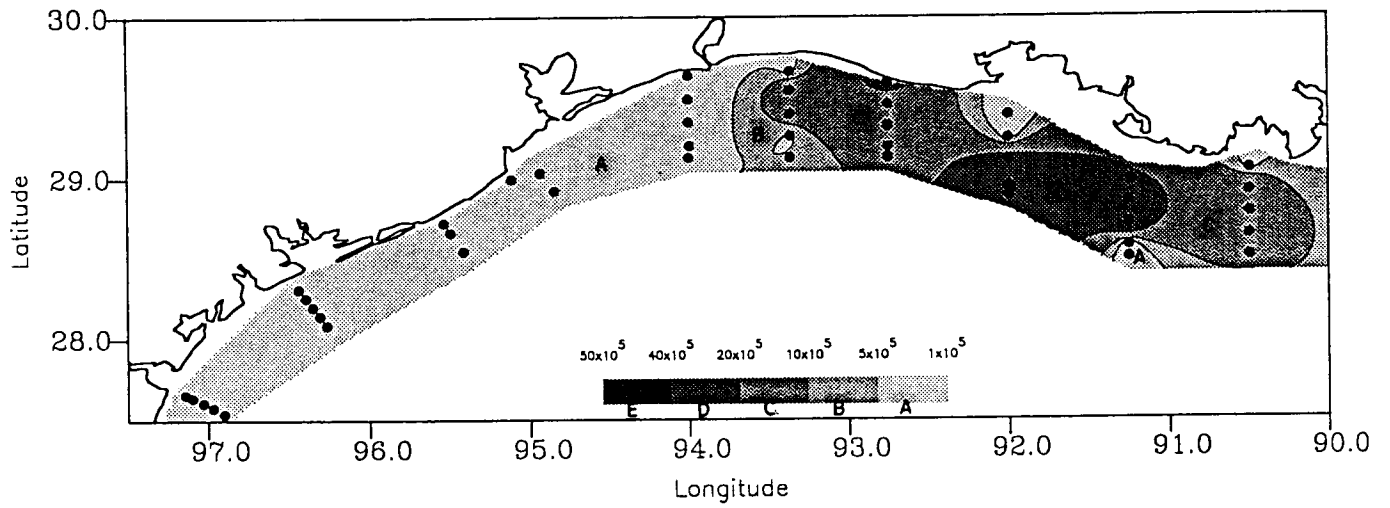
Figure 81. Contours of numbers of *Pseudo-nitzschia* spp. (number L⁻¹) during
Cruise III: surface (upper panel); bottom (lower panel).
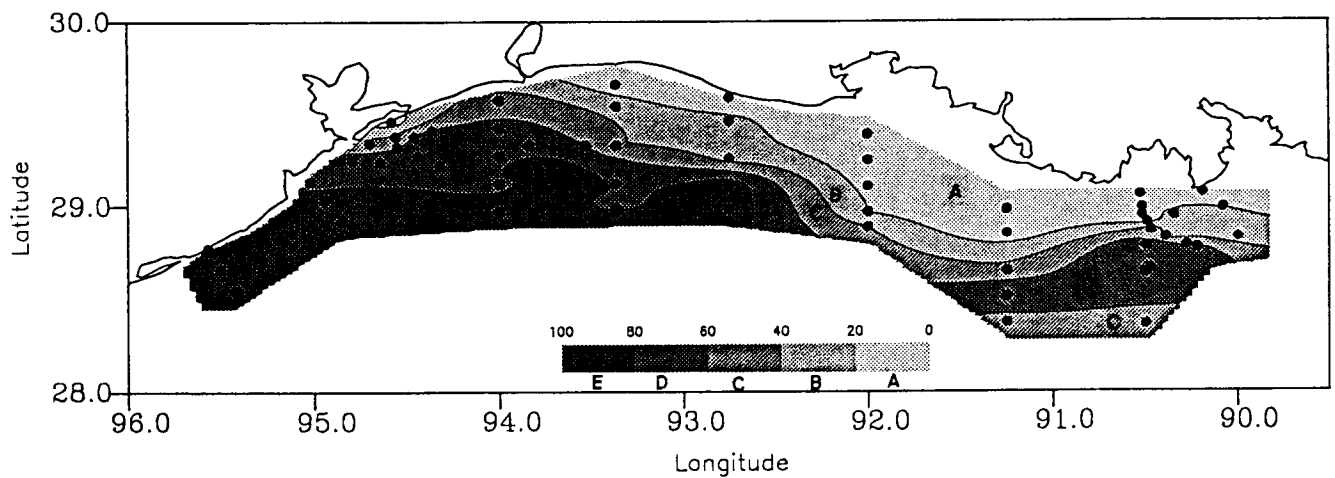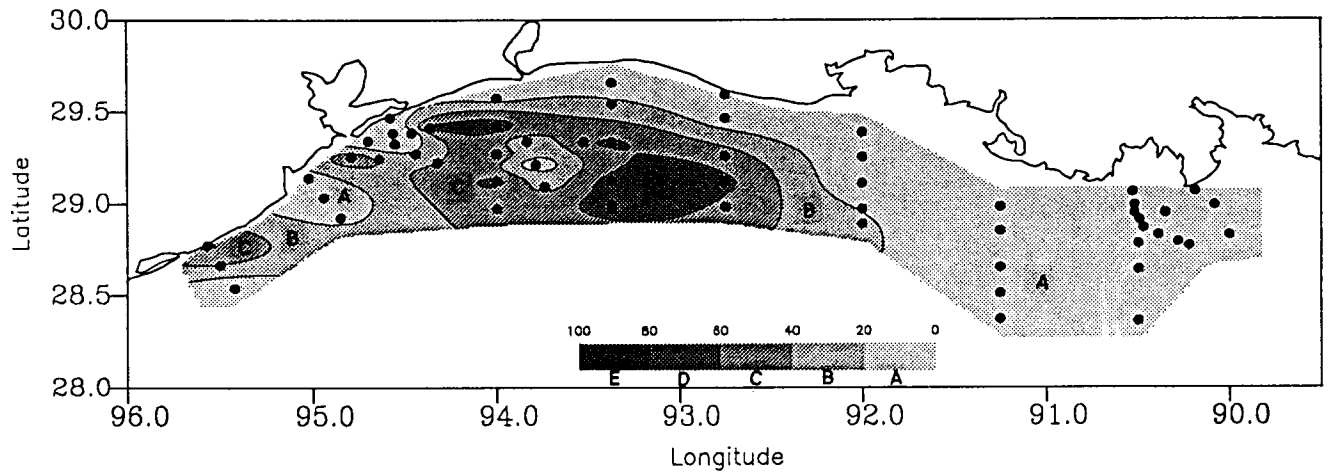
Figure 82. Contours of percent High PU/PE cyanobacteria/total cyanobacteria
(0.2-3.0 μm) during Cruise IV: surface (upper panel); bottom (lower
panel).

water at the surface on the shelf (Fig. 82, upper panel). The July 17 AVHRR SST images show similar structures in that area (Walker, pers. comm.). The bottom contours do not show the same structure (Fig. 82, lower panel). The %PC outline the areas most strongly influenced by the high river runoff that was occurring during this cruise (Fig. 83).

Because of large increases in cyanobacteria, and to some extent, other phytoplankton, diatoms were relatively less abundant, both in the large size fraction (>8 μm) and in the total phytoplankton (Table 5). Thus, in this unusual year with high river flow in mid-summer, neither the distribution of *S. costatum* (Fig. 84) nor % diatoms (Fig. 85) are good indicators of the location of the river plume.

4. Discussion

a. Using Phytoplankton as Indicators of Water Sources and Mixing. It was originally hypothesized that the coastal boundary current would separate the shelf into areas that were strongly influenced by either riverine inputs or offshore Gulf water with distinctive phytoplankton communities and sharp, strong gradients between them. The gradients are less strong than expected, although phytoplankton distributions, especially the distribution of cyanobacterial pigment types, clearly indicates the areas of riverine and offshore influence. Especially interesting was the intrusion of Gulf water onto the shelf at the surface in the summer, which was clearly shown by the % High PU/PE cyanobacteria, hinted at in the remote sensing data, and not apparent at all in the hydrographic data. In the two 1992 cruises (Dortch in Murray, 1994a) and the April 1993 cruise, the abundance of *Skeletonema costatum*, an opportunistic diatom, and the relative abundance of diatoms, also delineated the areas of riverine influence, but in the summer of 1993, this pattern was not repeated, despite the huge riverine input.

b. Seasonal Differences and the Effect of the 1993 Flood. The seasonal differences observed on the four cruises to date are summarized in Table 5. Overall phytoplankton numbers are higher in summer and fall than in spring. The species composition also changes substantially from spring to summer/fall. Large phytoplankton, primarily diatoms, become much less abundant, and small phytoplankton, primarily cyanobacteria, become much more abundant.

The effect of the 1993 Mississippi River flood was to create spring-like conditions of water and nutrient input during the summer when temperatures and light levels were high. Between samples collected as part of LATEX B and other programs (NOAA NECOP), sufficient data exist for one station in the core of the hypoxic zone (C6B; Dortch, 1994b; Rabalais et al., 1994) to evaluate the impact on phytoplankton populations. Total phytoplankton, cyanobacteria, and diatom abundance all increased (Table 6). However, cyanobacteria abundance increased much more than any other group. Calculations of biomass, based on crude estimates of cell volume from cell counts in different size fractions, showed that in summer 1993, the biomass of cyanobacteria exceeded that of diatoms. Consequently, the flood resulted in increased overall phytoplankton biomass, but also a change in the size distribution of the biomass. Both of these could have impacts on higher trophic levels and on the extent, severity, and duration of hypoxia.
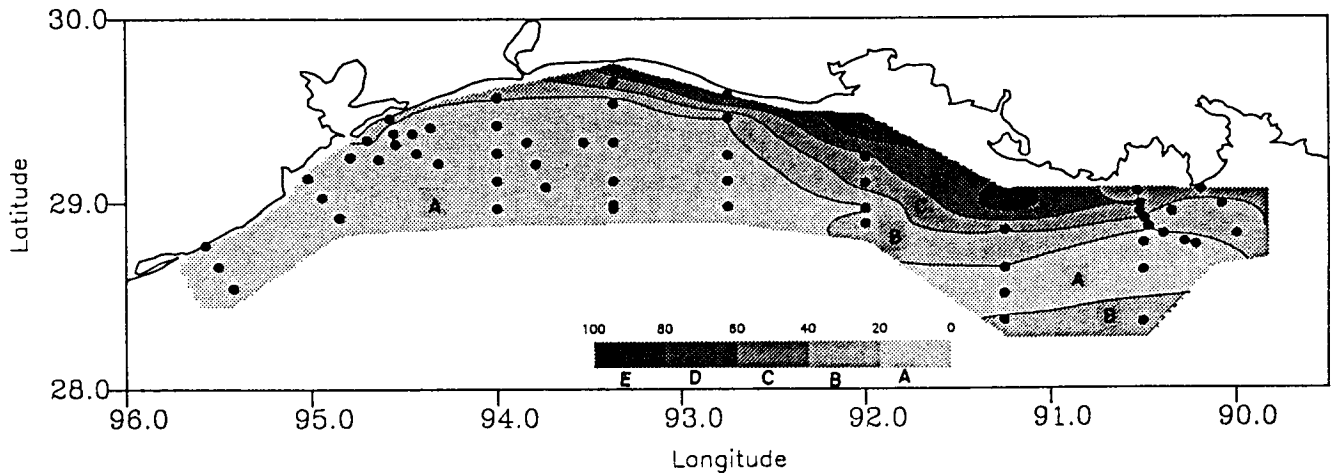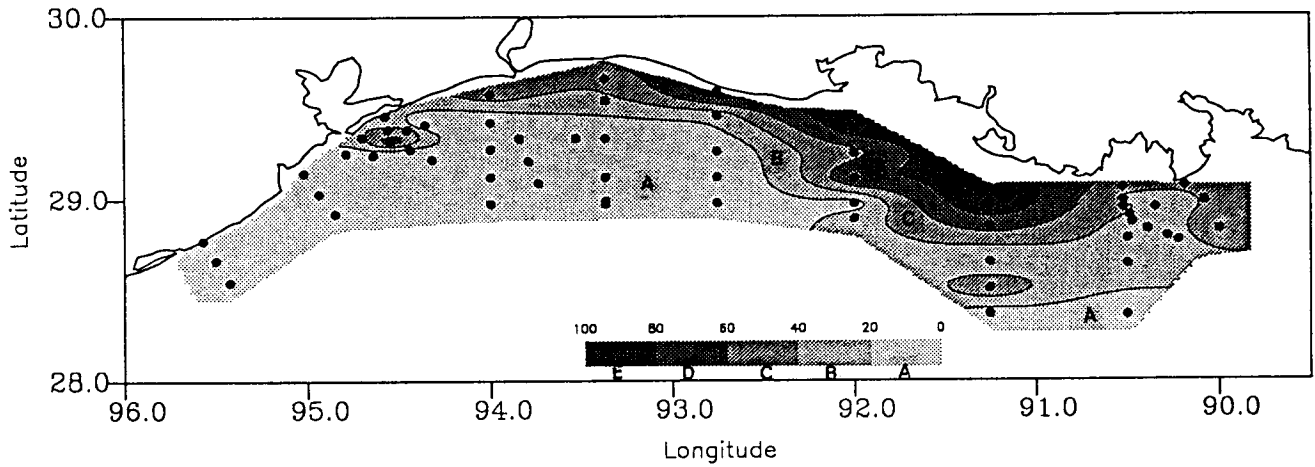
Figure 83. Contours of percent PC cyanobacteria/total cyanobacteria (0.2-3.0 μm)
during Cruise IV: surface (upper panel); bottom (lower panel).
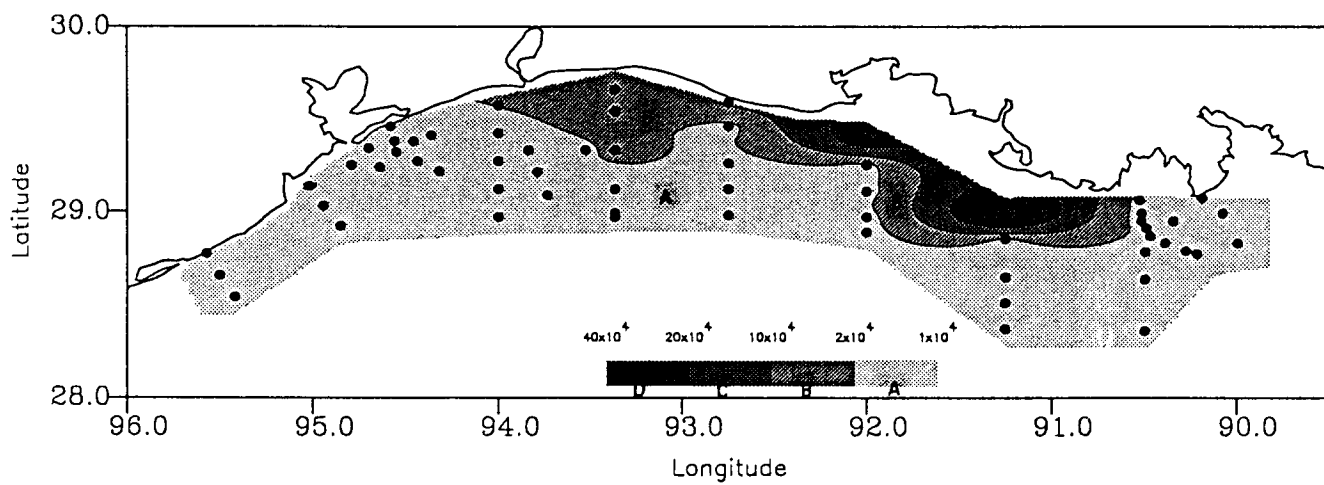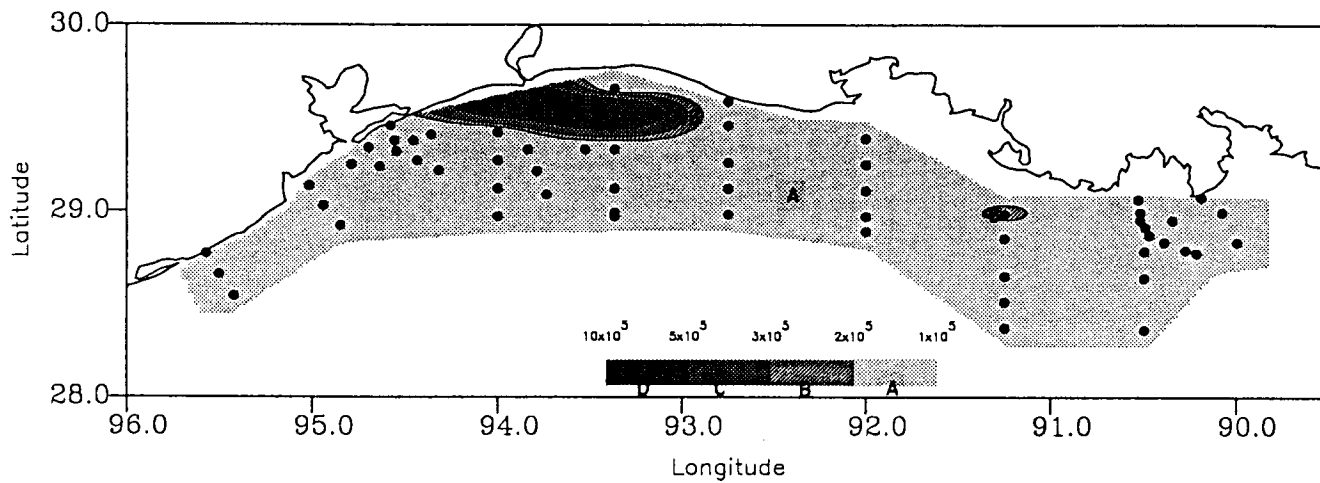
Figure 84. Contours of *Skeletonema costatum* (number L⁻¹) during Cruise IV: surface (upper panel); bottom (lower panel).
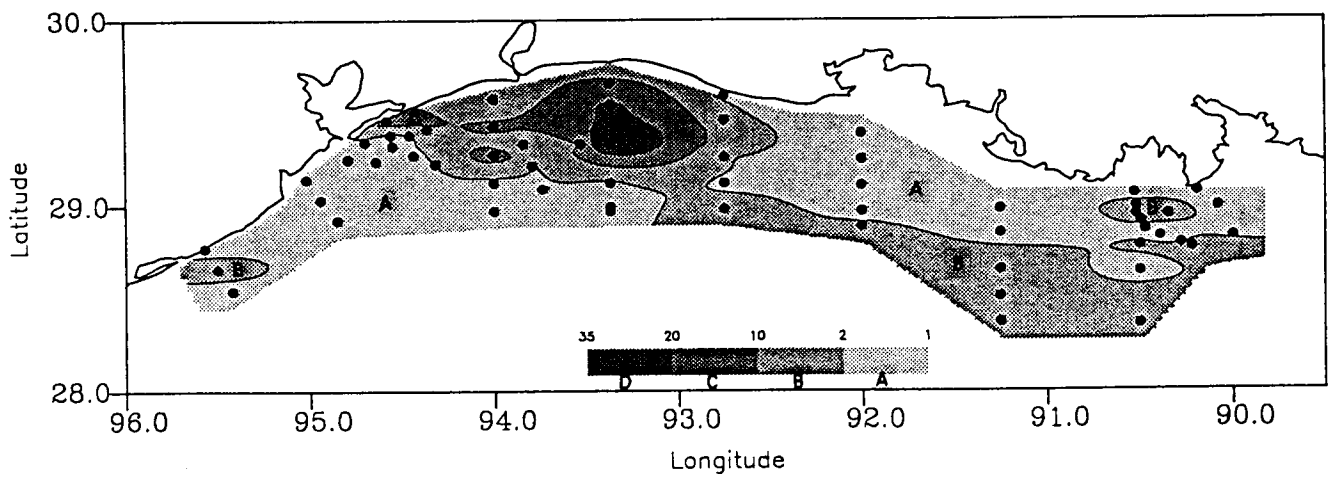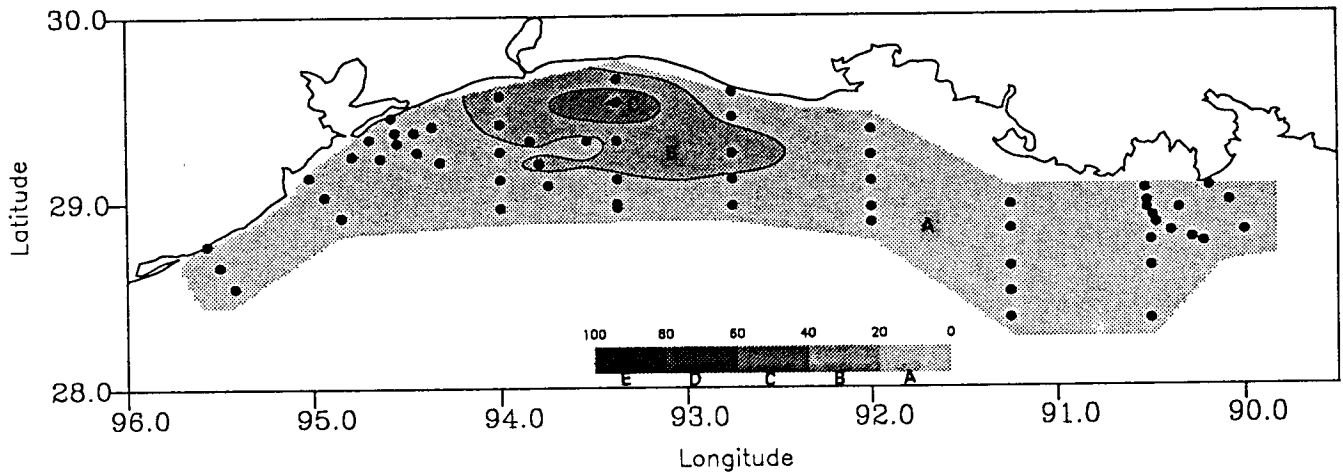
Figure 85. Contours of percent Diatoms/phytoplankton > 8 μm during Cruise IV:
surface (upper panel); bottom (lower panel).

Table 6. Average cell numbers and estimated biomass in all samples collected in July through September in the core of the hypoxic region in non-flood and flood years. Adapted from Dortch (1994b).

Cell Numbers (#L^{-1})	Non-Flood	Flood 1990-92	% Change 1993
Total Phytoplankton	1.3 x10^8	18 x 10^8	1385
Cyanobacteria	0.8 x 10^8	18 x 10^8	2250
Diatoms	0.4 x 10^6	1.6x 10^6	400
Biomass (μgCL^{-1})*			
Cyanobacteria	46.8	1007	2140
Diatoms	263	953	360

*Estimated from approximate cell volume

c. **Toxic and Noxious Phytoplankton Abundance.** These cruises provide an opportunity to survey the Louisiana and Texas continental shelves for the occurrence of toxic and noxious phytoplankton. These data have been supplied to both the Barataria-Terrebonne Bay and the Corpus Christi Bay National Estuary Programs to aid in determining the potential threat from toxic and noxious algae in those areas, as part of their assessment of Current Status and Trends.

No blooms resulting in water discoloration were observed on these cruises. However, *Pseudo-nitzschia* spp., potentially toxic diatoms, reached bloom concentrations during the April cruise (Figure 81; Table 7), especially on the shelf in the areas most immediately influenced by the Mississippi and Atchafalaya Rivers and were present in 97% of all samples. They were present in almost 50% of samples in the summer as well, but were much less abundant (Table 7). Dortch et al. (submitted) have shown that peak abundance of this organism occurs every April. Determining if the species that are present are toxic requires scanning electron microscopy or toxin analysis, neither of which have yet been done on a routine basis, so it is unknown whether the April peak contains toxic species. Both toxic and sometimes toxic forms have been identified in the northern Gulf of Mexico (Fryxell et al., 1990; Dortch et al., submitted).

A number of other potentially toxic and noxious phytoplankton were also observed on these cruises (Table 7). In particular species possibly associated with Diarrhetic Shellfish Poisoning in humans occurred frequently in samples, both in the spring and the summer. In addition, *Gymnodinium sanguineum*, a dinoflagellate associated with fish kills and oyster mortality, which caused a major red tide and fish kill in the spring of 1994 (Robichaux and Dortch, submitted), was also observed at many locations.

Table 7. Abundance[1] and frequency[2] of occurrence of toxic and noxious phytoplankton observed during cruises. A ? by Problem indicates that there is evidence implicating this species in causing this problem, but the link is not conclusive.

Taxon	April 13-19,1993		July 13-21,1993		Problem
	Maximum Abundance[1]	% Frequency[2]	Maximum Abundance[1]	% Frequency[2]	
Pseudo-nitzschia spp.	4.40×10^6	96.8	8.89×10^4	47.7	ASP[3]
Prorocentrum compressum	8.12×10^4	79.6	2.47×10^4	53.9	DSP[4]?
Prorocentrum micans	3.25×10^4	54.8	7.55×10^3	32.3	DSP[4]?
Dinophysis caudata	6.67×10^2	8.6	5.41×10^3	27.7	DSP[4]?
Gymnodinium sanguineum	1.66×10^3	9.7	2.99×10^3	14.6	Ichthyotoxic Oyster mortality
Dinophysis ovum	4×10^2	4.3	2.4×10^1	0.8	DSP[4]?
Ceratium spp.	3.25×10^3	39.8	9.44×10^3	37.7	DSP[4]? Hypoxia
Oscillatoria spp.	0	0	1.73×10^6	16.9	Discolored Water Ichthyotoxic

[1]Maximum abundance observed on cruise in # cells L^{-1}

[2]% Frequency = # samples with species/total # samples x 100

[3]Amnesic Shellfish Poisoning, short term memory loss, seizures, death (Hallegraeff, 1993)

[4]Diahretic Shellfish Poisoning, gastrointestinal distress, but not fatal; also a tumor promoter (Hallegraeff, 1993)

C. Zooplankton Survey *(Richard F. Shaw)*

1. Materials And Methods

Oblique plankton tows were made with a 60-cm diameter paired-bongo frame modified to accommodate a 20-cm ring. Bongo-net meshes were 153 and 335 μm, while a 63-μm mesh net was lashed to the 20-cm ring. Nets were lowered to the bottom as rapidly as possible before retrieving at a ship speed of 1 knot and an ascent of approximately 1 m/s. The 153- and 335-μm nets were fitted with a torpedo-type flowmeter for volume-filtered estimates. Volume-filtered estimates were not determined for the 63-μm net because of the potential of clogging (Taylor, 1976; Tranter and Smith, 1968). Upon retrieval, nets were thoroughly rinsed from the outside, concentrating the sample within the cod-end. The 63- and 153-μm samples were initially preserved in 4% formaldehyde and transferred to 70% ethanol after 24 hours. The 335-μm samples were preserved in 70% non-denatured buffered ethanol, placed on ice, and transferred to fresh 70% ethanol 24 hours later. This method is suitable for larval fish otolith and growth analysis (Butler, 1992; Methot and Kramer, 1979).

Biomass estimates were performed on one-half of all samples. All plankton splits were made with a Folsom plankton splitter (McEwen, et al., 1954). Halves were randomly selected for analysis. The three mesh sizes used in the study were analyzed in order to evaluate differences in zooplankton-size fractionations. To determine the relationship between volumetric and gravimetric

techniques, volume displacements (Yentsch and Hebard, 1957) were conducted on a randomly-selected third of the stations from each cruise prior to dry weight determination. Dry weights were determined for all samples by oven-drying at 60° C to constant weight (Lovegrove, 1966). Zooplankton density was calculated for both gravimetric (mg/m^3) and volumetric (ml/m^3) biomass estimates for the 153- and 335μm samples as:

Zooplankton Density = Biomass Estimate/Volume Filtered,

where Volume Filtered=volume filtered (m^3) by the net. Volume filtered was calculated as:

Volume Filtered = Net Area x Δ Counts x Rotor Constant,

where Net Area=area of net's mouth (m^2), Δ Counts=number of flowmeter rotor revolutions, and Rotor Constant=0.5102. Zooplankton density was not determined for the 63-μm (20-cm net) samples since volume filtered estimates were not recorded for these samples.

Larval fish and squid were removed from halves of all 335-μm samples and were identified to the lowest taxonomic level possible. If a 335-μm mesh sample was not available at a particular station, the 153-μm sample was sorted if available. If the number of fish sorted from a half sample was less than five, the other half of the sample was sorted if available. For each station, larval density (#/m^3) was calculated for each species as:

Density = (# Species$_x$/Volume Filtered),

where # Species$_x$ = the number of larvae of the xth species at that station. For each cruise, percent catch was calculated for each species as:

% Catch = (# Species$_x$/Σ(# Species$_x$)) X 100.

All halves (minus the fraction used in the zooplankton analysis for the 153-μm samples and larval fish and squid for the 335-μm samples) not used for biomass estimates were archived in 70% ethanol for future ecological studies.

2. Results

a. Overview. Two hundred and eighty-seven samples were obtained from 96 biological stations during LATEX B Cruises III and IV (Table 8) at station depths ranging between 2.9 and 57.7 m. Forty-four genera of larval and juvenile fish and 2 squid genera, from 30 families, were identified collectively (Table 9). From the half-split samples, 2268 fish were identified and 2073 were measured, while 19 squid were identified and measured. Curiously, squid were only present during the April cruise. An estimated 4495 larval and juvenile fish and 38 squid were captured after taking splits into account.

Zooplankton dry weight densities were significantly higher in April than in July within the 153-size fraction; however, no difference was found between the cruises for the 335-size fraction (t-test, $\alpha=0.05$). Since the data violated the assumptions for parametric regression even after appropriate transformations, the relationship between zooplankton dry weight and volume displacement was evaluated by Kendall Partial Rank-Order Correlation Coefficient ($T_{xy.z}$; Siegel and Castellan, 1988). Analysis revealed a strong positive relationship ($\tau=0.81$, p<0.001) between the two biomass determinations. Thus, the two biomass estimates are linearly related with little variability. However, dry weight may lead to the best estimate since it tends to be less variable and more reproducible statistically, and more useful for ecological studies from an energetic standpoint, than volume displacement estimates (Laurence, 1976).

b. Cruise III, April 1993. One hundred and thirty-one samples from 44 biological stations were obtained during the April 1993 cruise (Table 8), a high-river discharge period. Samples were collected from the Mississippi Delta (S1) to Corpus Christi, Texas (X3), the southwestern-most portion of the plume's range (Figure 86).

91

Table 8. Samples (63-, 153-, and 335-μm mesh) obtained at each station during Cruises III and IV. X=sample collected. PL= Galveston Plume Survey. CV=Convergence Survey.

APRIL

Station	Transect	Mesh (μm) 63	153	335
931101	S1	X	X	X
931103	S1	X	X	X
931105	S1	X	X	X
931107	S1	X	X	X
931109	S1	X	X	X
931113	S2	X	X	
931114	S2	X		X
931116	S2	X	X	X
931118	S2	X	X	X
931120	S2	X	X	X
931127	S3	X	X	X
931129	S3	X	X	X
931131	S3	X	X	X
931133	S3	X	X	X
931140	S4	X	X	X
931142	S4	X	X	X
931144	S4	X	X	X
931146	S4	X	X	X
931147	S4	X	X	X
931151	S5	X	X	X
931153	S5	X	X	X
931155	S5	X	X	X
931157	S5	X	X	X
931159	S5	X	X	X
931168	S6	X	X	X
931169	S6	X	X	X
931171	S6	X	X	X
931173	S6	X	X	X
931175	S6	X	X	X
931179	S7	X	X	X
931181	S7	X	X	X
931183	S7	X	X	X
931187	S8	X	X	X
931189	S8	X	X	X
931191	S8	X	X	X
931195	X1	X	X	X
931197	X1	X	X	X
931199	X1	X	X	X
931202	X2	X	X	X
931204	X2	X	X	X
931206	X2	X	X	X
931209	X3	X	X	X
931211	X3	X	X	X
931213	X3	X	X	X

JULY

Station	Transect	Mesh (μm) 63	153	335
932101	S1	X	X	X
932103	S1	X	X	X
932105	S1	X	X	X
932107	S1	X	X	X
932111	S1	X	X	X
932115	S2	X	X	X
932117	S2	X	X	X
932119	S2	X	X	X
932122	S2	X	X	X
932124	S2	X	X	X
932130	S3	X	X	X
932131	S3	X	X	X
932133	S3	X	X	X
932135	S3	X	X	X
932137	S3	X	X	X
932144	S4	X	X	X
932146	S4	X	X	X
932149	S4	X	X	X
932151	S4	X	X	X
932153	S4	X	X	X
932157	S5	X	X	X
932159	S5	X	X	X
932162	S5	X	X	X
932165	S5	X	X	X
932167	S5	X	X	X
932169	S6	X	X	X
932171	S6	X	X	X
932173	S6	X	X	X
932175	S6	X	X	X
932177	S6	X	X	X
932181	S7	X	X	X
932183	S7	X	X	X
932185	S7	X	X	X
932189	S8	X	X	X
932191	S8	X	X	X
932193	S8	X	X	X
932401	PL	X	X	X
932403	PL	X	X	X
932405	PL	X	X	X
932407	PL	X	X	X
932408	PL	X	X	
932409	PL	X	X	X
932413	PL	X	X	X
932415	PL	X	X	X
932420	PL	X	X	X
932423	PL	X	X	X
932601	CV	X	X	X
932604	CV	X	X	X
932605	CV	X	X	X
932606	CV	X	X	X
932610	CV	X	X	X
932613	CV	X	X	X

Table 9. Estimated larval fish and squid densities by cruise from data obtained during Cruises III and IV. Both cruises were combined for number caught and measured. Length statistics were based upon number measured. Also included by cruise are the number of stations with volume filtered estimates, volume filtered, and total estimated number of fish and squid caught. If the median of the density was not equal to zero, it was included after pos stn. Total catch, number caught, and densities were calculated after splits were accounted for. sd=standard deviation. pos stn=number of stations at which that species was identified.

					Apr-93	Jul-93
# STATIONS					44	50
VOLUME FILTERED (M3)					1067	928
TOTAL CATCH					1634	2899
SPECIES	#	#	Size Range	Mean Length	Mean Density	Mean Density
	Caught	Measured	(mm)	(mm; s.d.)	(#/100 m³) (sd, pos stn)	(#/100 m³) (sd, pos stn)
ANGUILLIFORMES (eels and morays)	4	2	5.3-6.5	5.90 (0.71)		0.43 (2.20; 2)
CLUPEIFORMES (herrings and anchovies)	51	25	1.8-7.0	4.08 (1.53)	4.47 (15.09; 6)	1.21 (7.24; 2)
OSTEICHTHYES (bony fishes)	28	12	1.0-3.0	1.50 (0.67)		2.18 (7.50; 5)
PERCIFORMES (perciform fishes)	46	19	1.3-4.9	1.84 (0.96)	4.21 (8.55; 13)	0.76 (5.36; 1)
ATHERINIDAE (silversides)	2	1	6.2	6.2	0.12 (0.79; 1)	
BLENNIDAE (blennies)	18	9	2.0-3.2	2.22 (0.44)	0.55 (2.59; 2)	1.18 (4.14; 4)
Ophioblennius atlanticus (redlip blenny)	4	2	2.2-2.5	2.35 (0.00)	1.02 (6.77; 1)	
Scartella cristata (molly miller)	2	1	9.8	9.8		0.17 (1.24; 1)
BOTHIDAE (lefteye flounders)	27	14	1.6-2.6	1.79 (0.43)	2.27 (7.15; 7)	0.17 (1.23; 1)
Citharichthys spilopterus (bay whiff)	2	1	8.5	8.5		0.17 (1.24; 1)
Citharichthys spp. (whiffs)	10	5	1.7-9.0	5.00 (3.81)	1.61 (7.56; 2)	0.33 (2.36; 1)
Engyophrys senta (spiny flounder)	2	1	6.4	6.4		0.09 (0.66; 1)
Etropus crossotus (fringed flounder)	57	32	2.0-9.1	4.16 (1.97)	1.12 (3.44; 5)	3.82 (10.14; 10)
Syacium gunteri (shoal flounder)	40	20	1.8-10.5	2.55 (2.39)		3.09 (20.76; 2)
Syacium spp. (lefteye flounders)	40	20	1.1-5.8	1.60 (1.05)	1.04 (5.74; 2)	1.87 (7.94; 4)
Trichosetta ventralis (sash flounder)	4	2	2.4-2.9	2.65 (0.00)		0.31 (2.18; 1)
BREGMACEROTIDAE						
Bregmaceros cantori (codlet)	64	32	1.5-48.0	12.09 (10.45)	4.44 (13.63; 7)	
Bregmaceros spp. (codlets)	10	5	2.0-11.4	7.00 (4.64)		0.52 (2.28; 3)
CARANGIDAE (jacks)	2	1	2.9	2.9		0.21 (1.47; 1)
Chloroscombrus chrysurus (Atlantic bumper)	130	68	1.2-4.9	2.15 (0.65)		13.84 (29.17; 18)
CLUPEIDAE (herrings)	2	1	1.8	1.8		0.82 (5.77; 1)

Table 9 cont'd

SPECIES	# Caught	# Measured	Size Range (mm)	Mean Length (mm; s.d.)	Apr-93 Mean Density (#/100 m³) (sd, pos stn)	Jul-93 Mean Density (#/100 m³) (sd, pos stn)
# STATIONS					44	50
VOLUME FILTERED (M3)					1067	928
TOTAL CATCH					1634	2899
Brevoortia patronus (gulf menhaden)	142	67	5.2-23.5	20.15 (2.69)	10.09 (55.86; 4)	
Harengula jaguana (scaled sardine)	94	47	3.3-17.0	9.96 (3.75)	0.11 (0.75; 1)	6.27 (22.15; 8)
Opisthonema oglinum (Atlantic thread herring)	128	64	3.6-13.8	7.47 (2.62)	0.07 (0.48; 1)	15.18 (40.88; 10)
CONGRIDAE (conger eels)	2	1	38	38		0.14 (1.01; 1)
ELEOTRIDAE						
Dormitator maculatus (fat sleeper)	4	2	1.7-2.4	2.05 (0.71)	0.23 (1.49; 1)	
ENGRAULIDAE (anchovies)	2052	858	1.7-16.2	5.33 (2.47)	83.18 (174.32; 26; 17.97)	160.6 (280.18; 37; 67.42)
Anchoa cubana (Cuban anchovy)	26	12	4.5-12.3	6.67 (2.19)	6.66 (44.18; 1)	
Anchoa hepsetus (striped anchovy)	82	41	3.5-19.5	6.78 (3.17)	0.12 (0.79; 1)	7.72 (50.46; 3)
Anchoa nasuta (longnose anchovy)	14	7	15.0-35.0	19.71 (6.87)		1.53 (8.00; 2)
Anchoa spp. (anchovies)	180	83	1.8-11.5	5.14 (2.07)	20.82 (61.31; 7)	4.05 (20.35; 2)
Anchoviella perfasciata (flat anchovy)	132	66	5.0-25.0	8.56 (4.66)	0.84 (4.77; 2)	8.25 (53.88; 3)
GOBIESOCIDAE						
Gobiesox strumosus (skilletfish)	6	3	3.7-9.7	7.00 (3.46)	0.45 (2.10; 2)	
GOBIIDAE (gobies)	98	48	1.5-10.5	5.67 (3.51)	4.84 (11.52; 1)	2.41 (6.41; 9)
Gobiosoma bosc (naked goby)	2	1	9	9		0.12 (0.87; 1)
LOLIGINIDAE						
Loligo spp. (inshore squids)	30	15	1.0-1.9	1.00 (0.00)	2.25 (6.21; 7)	
Lolliguncula brevis (w. Atlantic brief squid)	8	4	1.1-2.6	1.50 (0.58)	0.96 (3.97; 3)	
LUTJANIDAE (snappers)	4	2	2.4-6.5	4.45 (2.83)		0.35 (1.89; 2)
Lutjanus spp. (snappers)	8	4	3.0-8.4	4.75 (2.36)		0.54 (2.39; 3)
MICRODESMIDAE						
Microdesmus lanceolatus (lancetail wormfish)	11	6	2.5-13.0	5.83 (4.62)		0.88 (3.82; 3)
MUGILIDAE						
Mugil curema (white mullet)	2	1	2.9	2.9	0.16 (1.08; 1)	
OGCOCEPHALIDAE (batfishes)	2	1	3.5	3.5		0.12 (0.82; 1)
OPHICHTHIDAE (snake eels)	6	3	5.0-49.5	22.67 (23.25)	0.13 (0.88; 1)	0.25 (1.26; 2)
Aplatophis chauliodus (tusky eel)	1	1	38	38		0.07 (0.52; 1)
Myrophis punctatus (speckled worm eel)	4	2	51.0-71.0	61.00 (14.14)	0.73 (3.66; 2)	
Ophichthus spp. (snake eels)	2	1	75	75	0.16 (1.03; 1)	

Table 9 cont'd

SPECIES	# Caught	# Measured	Size Range (mm)	Mean Length (mm; s.d.)	Apr-93 Mean Density (#/100 m^3) (sd, pos stn)	Jul-93 Mean Density (#/100 m^3) (sd, pos stn)
# STATIONS					44	50
VOLUME FILTERED (M3)					1067	928
TOTAL CATCH					1634	2899
OPHIDIIDAE (cusk-eels)	2	1	2.5	2.5		0.27 (1.93; 1)
Lepophidium spp. (cusk-eels)	12	6	2.9-7.5	4.00 (1.67)		1.01 (3.14; 5)
Ophidion selenops (mooneye cusk-eel)	2	1	35	35		0.13 (0.90; 1)
Ophidion spp. (cusk-eels)	12	6	2.1-13.3	4.50 (4.32)	1.18 (4.52; 4)	
SCIAENIDAE (drums)	30	14	1.2-4.3	2.14 (1.03)	2.95 (9.20; 5)	0.52 (2.72; 2)
Cynoscion arenarius (sand seatrout)	385	194	1.4-21.5	2.75 (2.18)	25.77 (39.64; 24; 5.88)	15.00 (52.88; 16)
Cynoscion nebulosus (spotted seatrout)	16	8	2.4-3.9	2.38 (0.52)		1.31 (5.88; 3)
Cynoscion nothus (silver seatrout)	8	4	2.9-4.5	3.00 (0.82)		0.78 (3.35; 3)
Cynoscion spp. (seatrouts)	4	2	4.4-11.5	7.95 (4.95)	0.29 (1.90; 1)	0.09 (0.66; 1)
Larimus fasciatus (banded drum)	2	1	2.3	2.3		0.15 (1.07; 1)
Menticirrhus spp. (kingfishes)	16	8	1.4-4.2	2.38 (0.92)	1.04 (3.17; 5)	0.70 (3.08; 3)
Micropogonias undulatus (Atlantic croaker)	26	13	2.2-7.2	4.31 (1.49)	0.98 (5.78; 2)	
Pogonias cromis (black drum)	16	8	2.4-4.7	2.88 (0.64)	2.86 (15.13; 2)	
Stellifer lanceolatus (star drum)	68	35	2.1-6.3	3.46 (1.07)		8.88 (24.93; 11)
SCOMBRIDAE						
Auxis spp. (mackerels)	16	8	2.0-7.5	2.88 (1.73)		1.16 (5.75; 3)
Euthynnus alletteratus (little tunny)	4	2	4.1-4.3	4.20 (0.00)		0.31 (1.51; 2)
Scomberomorus cavalla (king mackerel)	2	1	4.5	4.5		0.15 (1.07; 1)
Scomberomorus maculatus (Spanish mackerel)	20	10	1.2-4.5	2.60 (1.17)	0.11 (0.75; 1)	2.25 (8.38; 6)
SCORPAENIDAE						
Scorpaena spp. (scorpionfishes)	2	1	8.5	8.5		0.15 (1.09; 1)
SERRANIDAE (sea basses)	44	22	1.2-5.0	2.14 (0.94)	0.42 (1.96; 2)	3.03 (10.02; 6)
Serraniculus pumilio (pygmy sea bass)	2	1	2.1	2.1		0.12 (0.84; 1)
SOLEIDAE						
Achirus lineatus (lined sole)	2	1	3.3	3.3		0.12 (0.87; 1)
Symphurus plagiusa (blackcheek tonguefish)	11	6	2.0-12.5	4.33 (3.88)		1.22 (5.94; 3)
Symphurus spp. (tonguefishes)	190	98	1.3-10.7	2.54 (1.37)	0.72 (2.33; 4)	15.83 (33.75; 23)
SPARIDAE (porgies)	4	2	4.5-6.1	5.30 (1.41)	0.22 (1.02; 2)	
STROMATEIDAE						
Peprilus burti (gulf butterfish)	4	2	2.1-2.2	2.15 (0.00)	0.35 (1.66; 2)	

95

Table 9 cont'd

SPECIES	# Caught	# Measured	Size Range (mm)	Mean Length (mm; s.d.)	Apr-93 Mean Density (#/100 m^3) (sd, pos stn)	Jul-93 Mean Density (#/100 m^3) (sd, pos stn)
# STATIONS					44	50
VOLUME FILTERED (M3)					1067	928
TOTAL CATCH					1634	2899
SYNGNATHIDAE						
Syngnathus spp. (pipefishes)	2	1	11	11	0.14 (0.95; 1)	
SYNODONTIDAE (lizardfishes)	16	8	3.2-9.0	5.13 (2.03)		0.94 (5.78; 2)
Synodus foetens (inshore lizardfish)	8	4	2.5-3.2	2.55 (0.50)	0.42 (2.82; 1)	
Synodus spp. (lizardfishes)	14	7	2.4-7.3	4.71 (1.70)	0.26 (1.32; 2)	0.47 (3.29; 1)
TETRAODONTIDAE						
Sphoeroides spp. (puffers)	4	2	2.3-8.2	5.25 (4.24)	0.18 (1.20; 1)	0.09 (0.66; 1)
TRICHIURIDAE						
Trichiurus lepturus (Atlantic cutlassfish)	2	1	7.5	7.5	0.07 (0.48; 1)	
TRIGLIDAE						
Prionotus spp. (searobins)	2	1	8.6	8.6	0.13 (0.88; 1)	
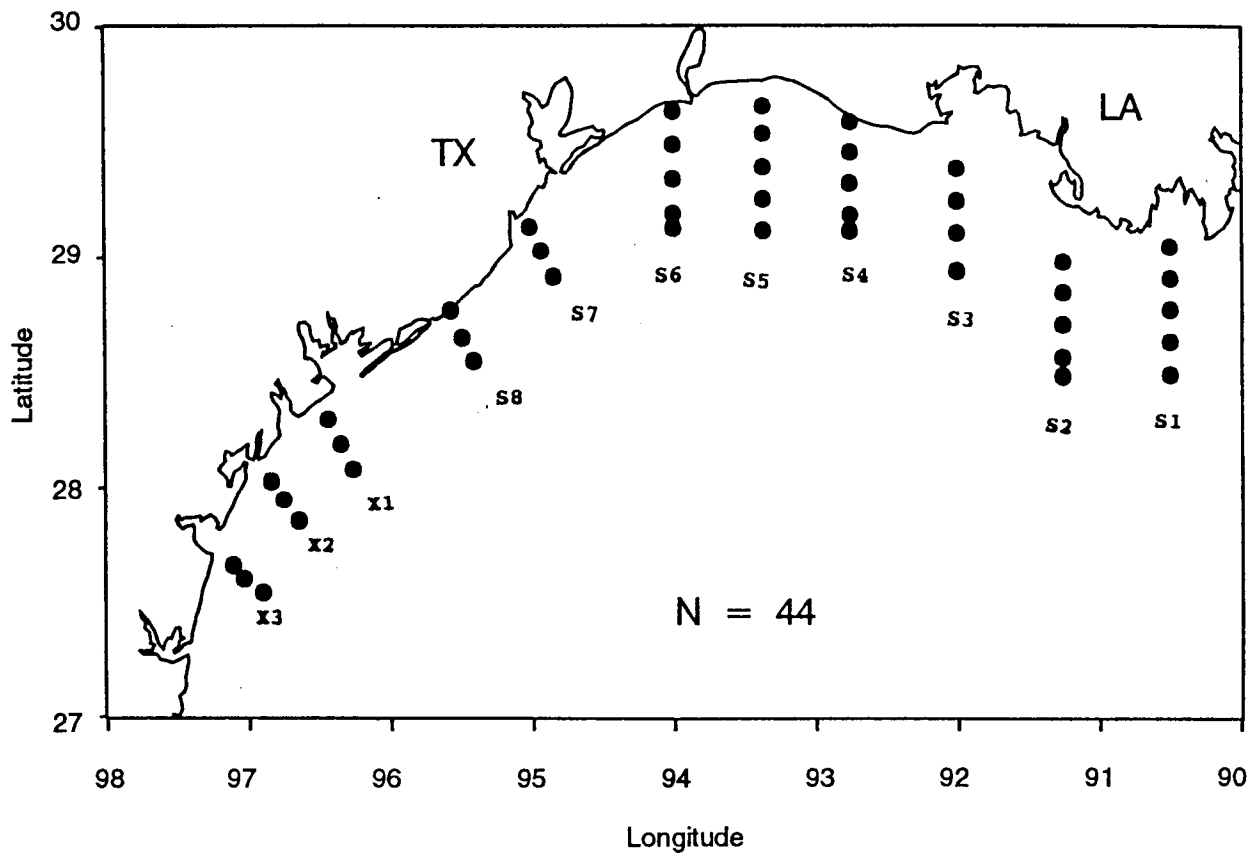
Figure 86. LATEX B biological stations during Cruise III, April 1993.

Zooplankton biomass tended to be high in the central portion of the study area, from Atchafalaya Bay (S2) to slightly west of Sabine Lake (S6), for both the 153- and 335-μm samples (Figures 87 and 88). Zooplankton dry-weight density for the 153-μm samples ranged from 16.77 to 1213.70 mg/m³ (mean=149.21, s.d.=201.89), while the 335-μm samples ranged from 6.91 to 400.69 mg/m³ (mean=40.07, s.d.=61.37; Table 10).

An estimated 1596 larval and juvenile fish and 38 squid were collected during the April cruise. Larval fish densities were highest off Atchafalaya Bay (S2 and S3) and along the Texas coast (S7 through X2; Figure 89), ranging from 0.05 to 9.36 larvae/m³ (mean=1.91, s.d.=1.95; Table 10). April samples were dominated by the unidentified engraulids (%Catch = 36.34 %), although *Cynoscion arenarius* (14.79 %), *Anchoa* spp. (11.66 %), and *Brevoortia patronus* (8.90 %) were also abundant (Table 9). These percentages are similar to Cruise I (April 1992) results, where engraulids (74%) and *Cynoscion arenarius* (14.4 %) dominated the catch. Listed below is a breakdown of the cruise by transect.

S1. The 153-μm dry-weight densities were fairly low and increased with increasing distance from shore, ranging from 49.48-93.40 mg/m³. The 335-μm biomass estimates showed no discernible trend, ranging from 24.23-45.16 mg/m³. Total larval fish density also increased with increasing distance from shore, ranging from 0.99-2.08 larvae/m³.

S2. No trend was observed for zooplankton biomass. The 153-μm zooplankton densities ranged from 43.74-281.89 mg/m³, while the 335-μm dry weights ranged from 22.68-70.18 mg/m³. However, larval fish densities decreased with increasing distance from shore, ranging from 1.92-4.42 larvae/m³.

S3. The highest zooplankton densities were found along the coast for both mesh sizes. Dry weights ranged from 26.90-627.73 mg/m³ for the 153-μm samples and from 13.53-400.69 mg/m³ for the 335-μm samples. This was a maximum for the 335-μm mesh size and the second largest value recorded for the 153-μm samples; however, the net hit substrate during towing and mud in the sample probably increased the estimate unrealistically. Ichthyoplankton densities were high throughout the transect, ranging from 3.61-7.59 larvae/m³.

S4. The 153-μm biomass estimates were highest in the center portion of the transect, ranging from 68.94-214.78 mg/m³. The 335-μm biomass density decreased as distance from shore increased, decreasing from 57.93 to 15.08 mg/m³. Larval fish density also tended to decrease from shore and ranged from 0.45-1.70 larvae/m³.

S5. No noticeable trend was observed for the density estimates. Zooplankton biomass estimates ranged from 16.77-332.12 mg/m³ for the 153-μm samples and from 6.91-48.57 mg/m³ for the 335-μm samples. Ichthyoplankton densities ranged from 0.16-1.55 larvae/m³.

S6. While no trend was discernible for the densities, zooplankton biomass estimates were high throughout the transect. The 153-μm samples ranged from 122.44-1213.70 mg/m³, a cruise maximum, while the 335-μm biomass estimates ranged from 13.38-157.29 mg/m³. Again, this cruise maximum was affected by mud in the sample. Larval fish densities remained low, ranging from 0.06-1.37 larvae/m³.

S7. The 153-μm biomass estimates ranged from 88.44-125.43 mg/m³. The 335-μm biomass densities decreased with increasing distance from shore, ranging from 9.65-35.10 mg/m³. Larval fish density also increased in the shoreward direction to a cruise maximum, increasing from 0.48-9.36 larvae/m³.
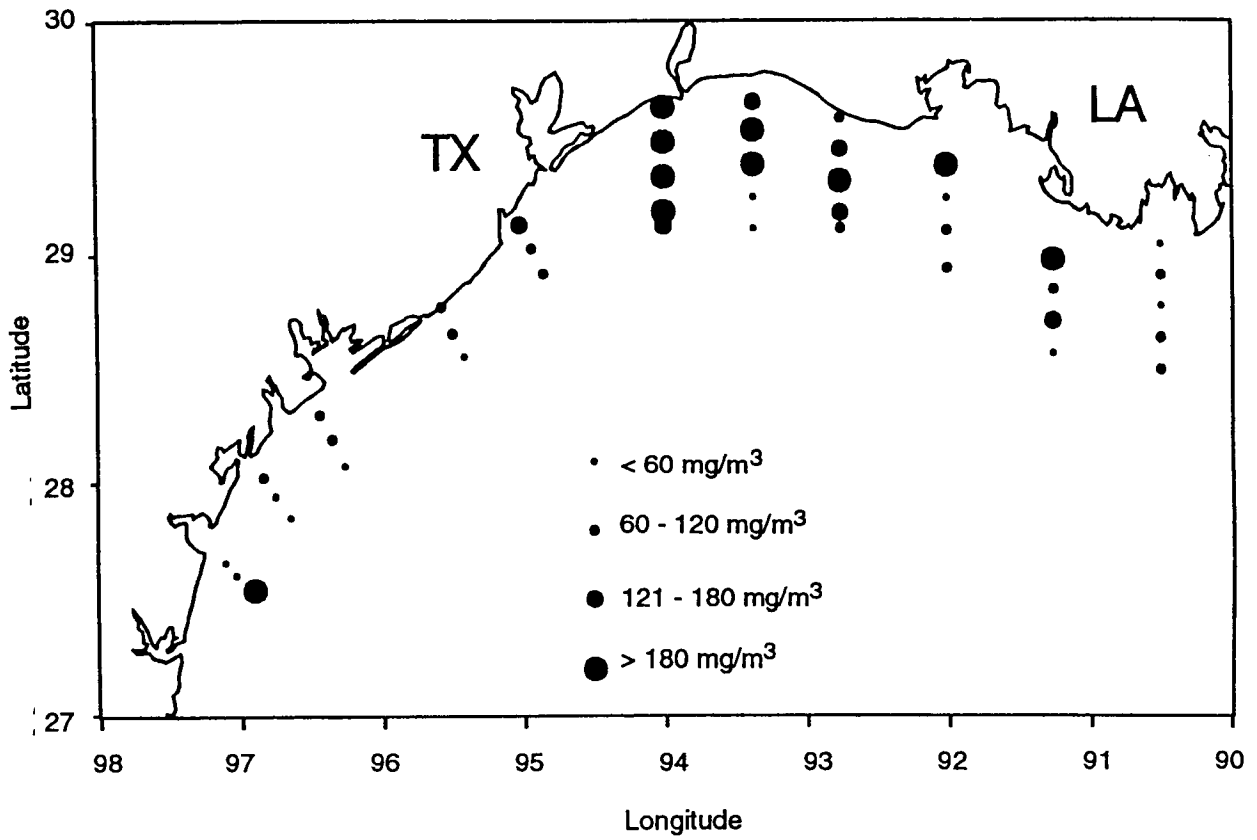
Figure 87. Plankton biomass (mg/m^3) for 153 μm mesh samples collected during Cruise III.
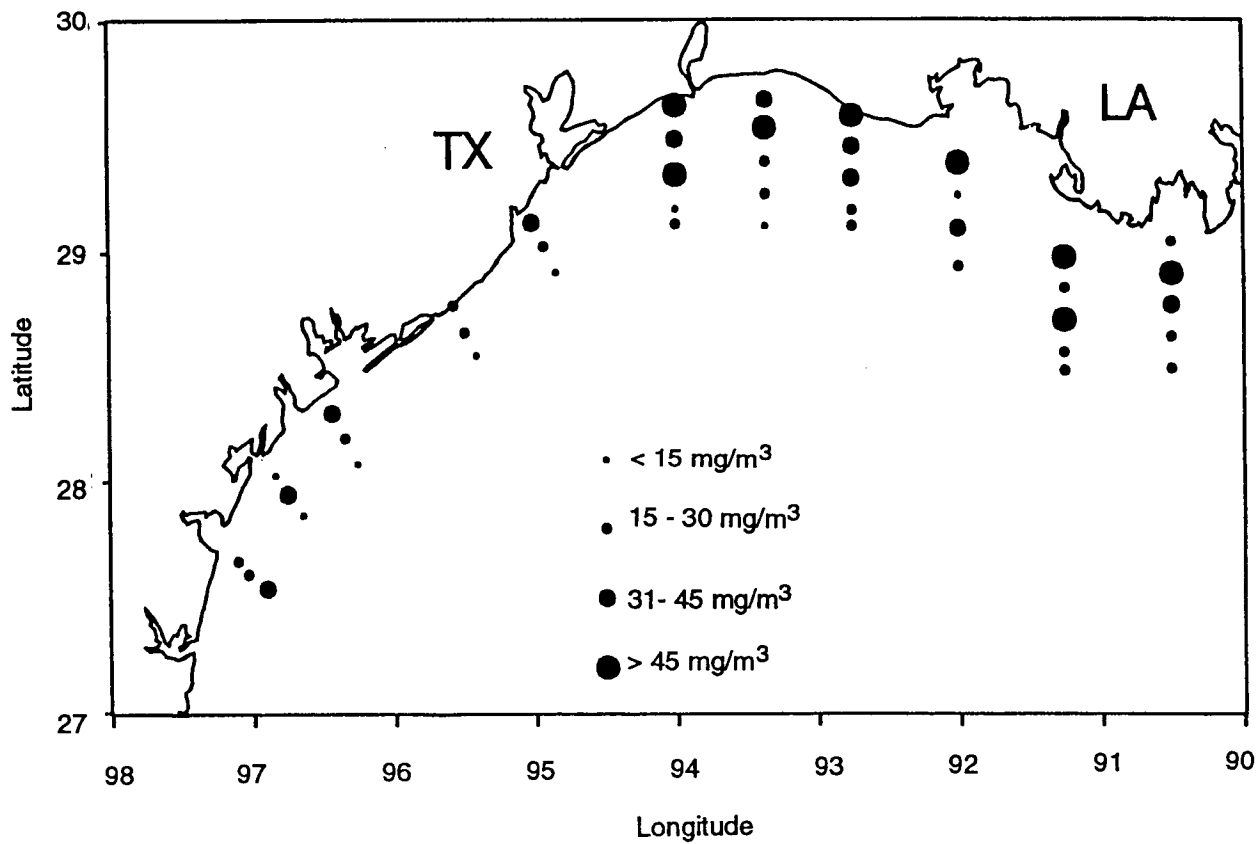
Figure 88. Plankton biomass (mg/m³) for 335-μm mesh samples collected during Cruise III.

100
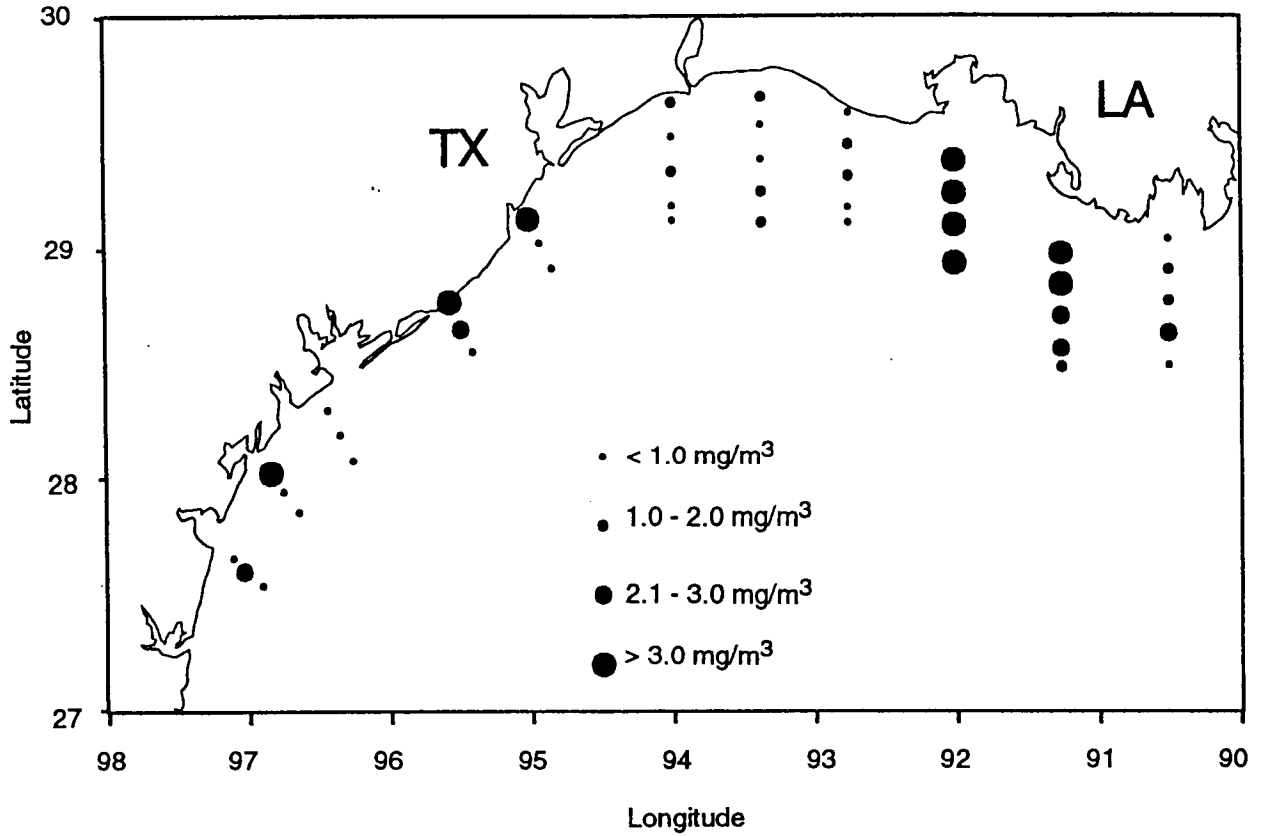
Figure 89. Total larval fish density (#/m³) for Cruise III zooplankton samples.

Table 10. List of zooplankton dry weight densities (mg/m³) for 153-μm and 335-μm mesh samples, total larval fish and squid densities (#/m³) at each station sampled during Cruises III and IV. ("-"= data not available; PL=Galveston Plume Survey; CV = Convergence Survey.

APRIL Station	Transect	153μ Dry	Densities 335μ Dry	Larval	JULY Station	Transect	153μ Dry	Densities 335μ Dry	Larval
931101	S1	49.48	29.75	0.99	932101	S1	239.98	44.39	4.44
931103	S1	93.40	45.15	1.37	932103	S1	117.07	34.36	16.85
931105	S1	59.39	31.27	1.77	932105	S1	46.55	25.37	0.52
931107	S1	70.80	24.23	2.08	932107	S1	44.83	15.54	0.30
931109	S1	71.18	28.25	0.99	932111	S1	-	10.33	0.41
931113	S2	-	28.78	1.92	932115	S2	27.52	14.47	1.50
931114	S2	43.74	22.68	2.27	932117	S2	67.49	8.37	1.07
931116	S2	159.10	70.18	2.94	932119	S2	66.59	12.60	1.26
931118	S2	74.77	24.86	4.42	932122	S2	171.49	10.02	1.67
931120	S2	281.89	45.52	4.14	932124	S2	141.46	90.70	0.26
931127	S3	111.04	27.97	7.59	932130	S3	28.36	17.86	0.07
931129	S3	106.30	40.90	3.88	932131	S3	47.24	6.43	0.06
931131	S3	26.90	13.53	3.61	932133	S3	151.12	8.87	2.36
931133	S3	627.73	400.69	4.77	932135	S3	261.11	108.11	0.64
931140	S4	69.01	57.93	0.97	932137	S3	24.65	0	2.40
931142	S4	120.02	37.93	1.70	932144	S4	91.43	51.60	9.03
931144	S4	214.48	30.42	1.01	932146	S4	44.05	17.80	0.11
931146	S4	138.73	16.18	0.81	932149	S4	47.26	12.44	0.10
931147	S4	68.94	15.08	0.45	932151	S4	189.01	88.34	1.04
931151	S5	42.70	6.91	1.55	932153	S4	30.16	21.17	1.44
931153	S5	16.77	25.13	1.08	932157	S5	50.99	25.39	2.67
931155	S5	182.14	24.99	0.16	932159	S5	71.68	39.96	1.00
931157	S5	332.12	48.57	0.69	932162	S5	81.93	11.77	0.74
931159	S5	178.04	40.44	1.35	932165	S5	105.56	25.95	2.16
931168	S6	122.44	21.02	0.10	932167	S5	75.39	35.34	4.08
931169	S6	212.64	13.38	0.43	932169	S6	39.90	20.14	2.85
931171	S6	270.61	157.29	1.04	932171	S6	100.23	29.31	4.06
931173	S6	1213.70	44.74	0.06	932173	S6	176.22	73.34	8.52
931175	S6	368.48	96.09	1.37	932175	S6	133.84	79.38	5.29
931179	S7	92.34	9.64	0.48	932177	S6	71.56	14.85	4.71
931181	S7	88.44	16.37	0.91	932181	S7	45.87	16.42	6.69
931183	S7	125.43	35.10	9.36	932183	S7	41.00	19.10	5.19
931187	S8	49.36	10.66	0.74	932185	S7	16.19	8.15	0.82
931189	S8	73.14	15.65	2.61	932189	S8	28.00	10.09	3.03
931191	S8	83.36	18.99	4.07	932191	S8	45.76	23.94	0.27
931195	X1	30.93	8.53	0.71	932193	S8	80.44	15.34	3.07
931197	X1	66.15	19.53	0.94	932401	PL	42.66	63.56	1.19
931199	X1	76.70	38.05	0.54	932403	PL	58.71	26.46	1.50
931202	X2	33.51	13.94	0.62	932405	PL	39.00	16.95	0.94
931204	X2	38.11	31.23	0.31	932407	PL	46.73	6.60	0
931206	X2	87.99	8.33	3.33	932408	PL	53.04	10.15	0.30
931209	X3	186.16	30.49	0.05	932409	PL	57.04	13.10	2.43
931211	X3	40.04	21.48	2.85	932413	PL	7.89	16.67	6.27
931213	X3	17.72	15.12	0.88	932415	PL	143.35	28.90	1.38
					932420	PL	72.76	21.19	7.37
					932423	PL	76.13	56.61	0.84
					932601	CV	30.33	13.93	1.22
					932604	CV	123.13	25.17	1.36
					932605	CV	56.33	12.59	0.84
					932606	CV	38.17	8.62	0.57
					932610	CV	171.45	88.21	4.81
					932613	CV	36.97	9.43	6.73

102

S8. All density estimates increased as distance from shore increased. Dry weight densities ranged from 49.36-83.36 mg/m^3 for the 153-μm samples and from 10.66-18.99 mg/m^3 for the 335-μm samples. Ichthyoplankton density increased from 0.74 to 4.07 larvae/m^3.

X1. Dry weight estimates decreased with increasing distance from shore. Biomass estimates ranged from 30.93-76.70 mg/m^3 for the 153-μm fraction and from 8.53-38.05 mg/m^3 for the 335-μm samples. Larval fish density varied between 0.54 and 0.94 larvae/m^3.

X2. The 153-μm dry weight density decreased with increasing distance from shore, ranging from 33.51-87.99 mg/m^3. The 335-μm biomass estimates ranged from 8.33-31.23 mg/m^3, while larval fish densities ranged from 0.31-3.33 larvae/m^3.

X3. Dry weight estimates increased with increasing distance from shore. Biomass densities ranged from 17.72-186.16 mg/m^3 for the 153-μm samples and from 15.13-30.49 mg/m^3 for the 335-μm samples. Larval fish densities ranged from 0.05 to 2.85 larvae/m^3.

c. *Cruise IV, July 1993.* One hundred and fifty-six samples were collected from 52 stations during July 1993 (Table 8), typically a period of high biological activity. Samples were collected from the Mississippi Delta (S1) to south of Galveston Bay, Texas (S8), as well as during the Plume and Convergence surveys (Figure 90).

High zooplankton biomass estimates for both the 153- and 335-μm mesh samples were found scattered throughout the central and eastern portion of the cruise (S1-S6; Figures 91 and 92). Biomass for the 153-μm samples ranged from 16.19-261.11 mg/m^3 (mean=79.72, s.d.=57.13) and 335-μm samples ranged from 0-108.11 mg/m^3 (mean=28.18, s.d.=25.53; Table 10).

An estimated 2899 larval and juvenile fish were obtained during the July 1993 cruise (Figure 93). Larval fish densities were highest west of Sabine Lake (S6-S8), ranging from 0-16.85 larvae/m^3 (mean=2.85, s.d.=3.25; Table 10). Again, unidentified engraulids made up the bulk of the catch (%Catch = 50.78 %; Table 3). *Symphurus* spp. (6.21 %), *Cynoscion arenarius* (5.14 %), *Chloroscombrus chrysurus* (4.48 %), *Opisthonema oglinum* (4.35 %), and *Anchoviella perfasciata* (4.28 %) were also common in July samples. Listed below is a breakdown of the cruise by transect.

S1. Zooplankton biomass decreased with increasing distance from shore. Dry weight densities for the 153-μm samples ranged from 44.83-239.98 mg/m^3, while the 335-μm samples ranged from 10.33-44.39 mg/m^3. No trend was discernible for larval fish densities, ranging from 0.30-16.85 larvae/m^3, the cruise maximum.

S2. Dry weight density for the 153-μm samples was higher at near-shore stations, ranging from 27.52-171.49 mg/m^3. The 335-μm biomass estimates ranged from 8.37-90.70 mg/m^3, while ichthyoplankton densities ranged from 0.26-1.67 larvae/m^3.

S3. Cruise maximums were obtained for both the 153- and 335-μm fractions at station 135. Dry weight densities ranged from 24.65-261.11 mg/m^3 for the 153-μm samples and from 0-108.11 mg/m^3 for the 335-μm fraction. Larval fish densities ranged from 0.06-2.40 larvae/m^3.

S4. No obvious trend was noted for the three density estimates. Zooplankton biomass estimates for the 153-μm fraction ranged from 30.16-189.01 mg/m^3, while the 335-μm estimates ranged from 12.44-88.34 mg/m^3. Larval fish densities ranged from 0.10-9.03 larvae/m^3.
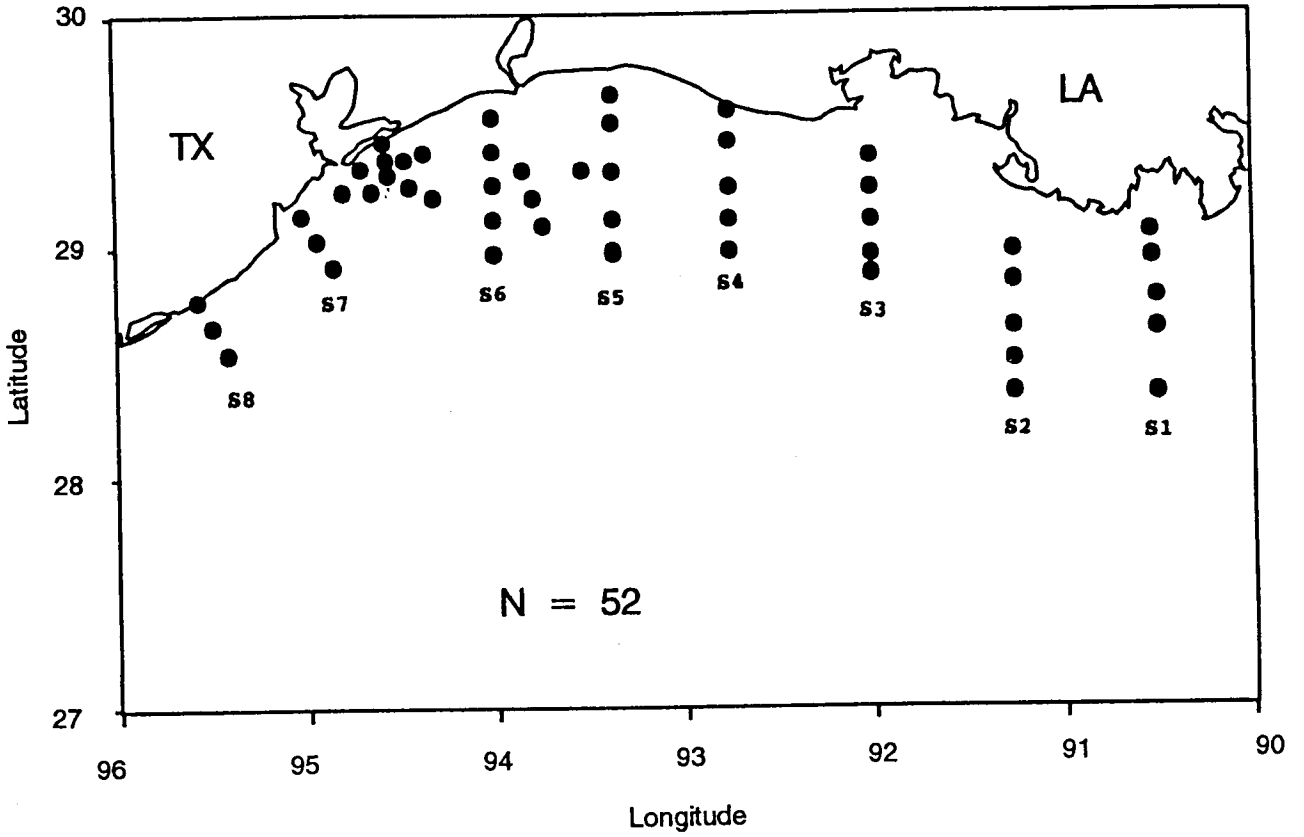
Figure 90. LATEX B biological stations during Cruise IV, July 1993.
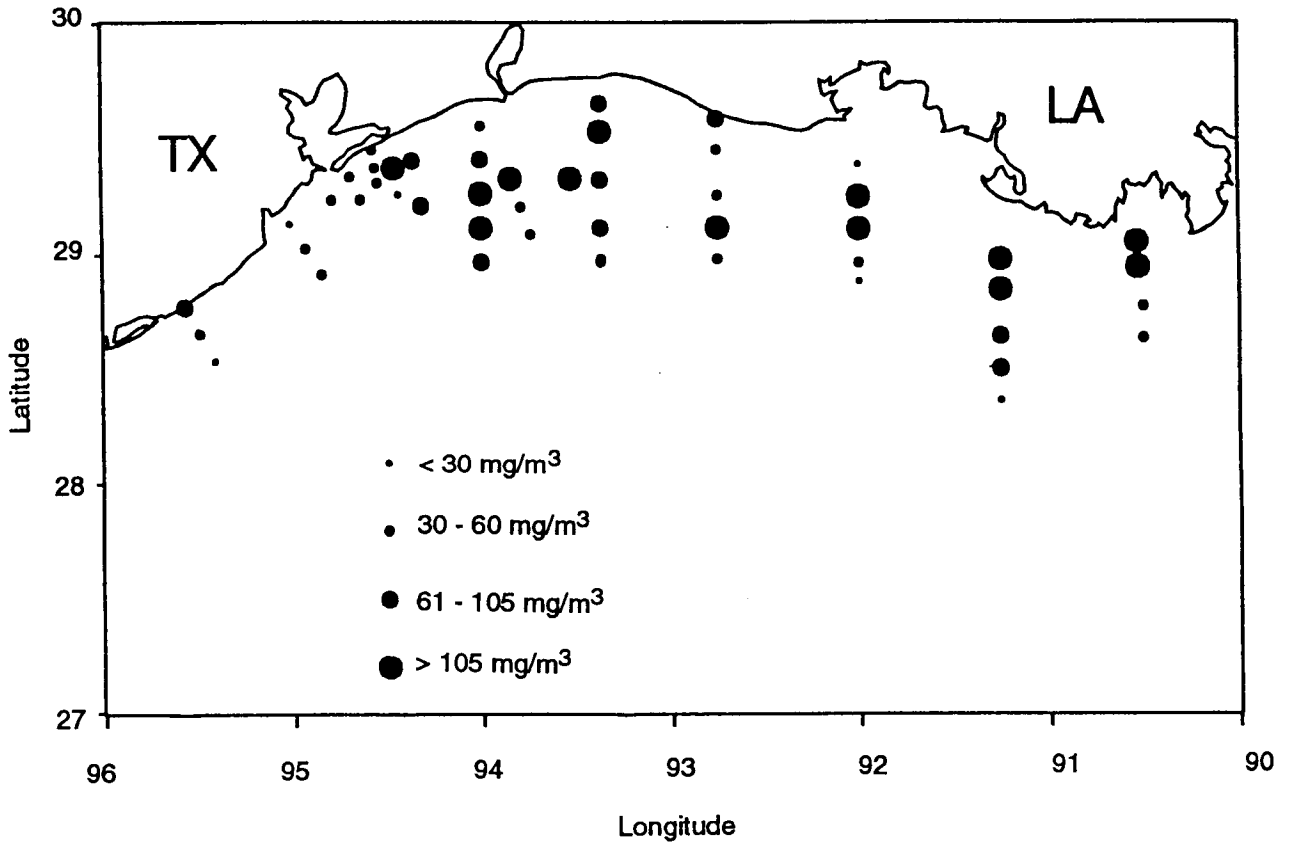
Figure 91. Plankton biomass (mg/m3) for 153-μm samples collected during Cruise IV.
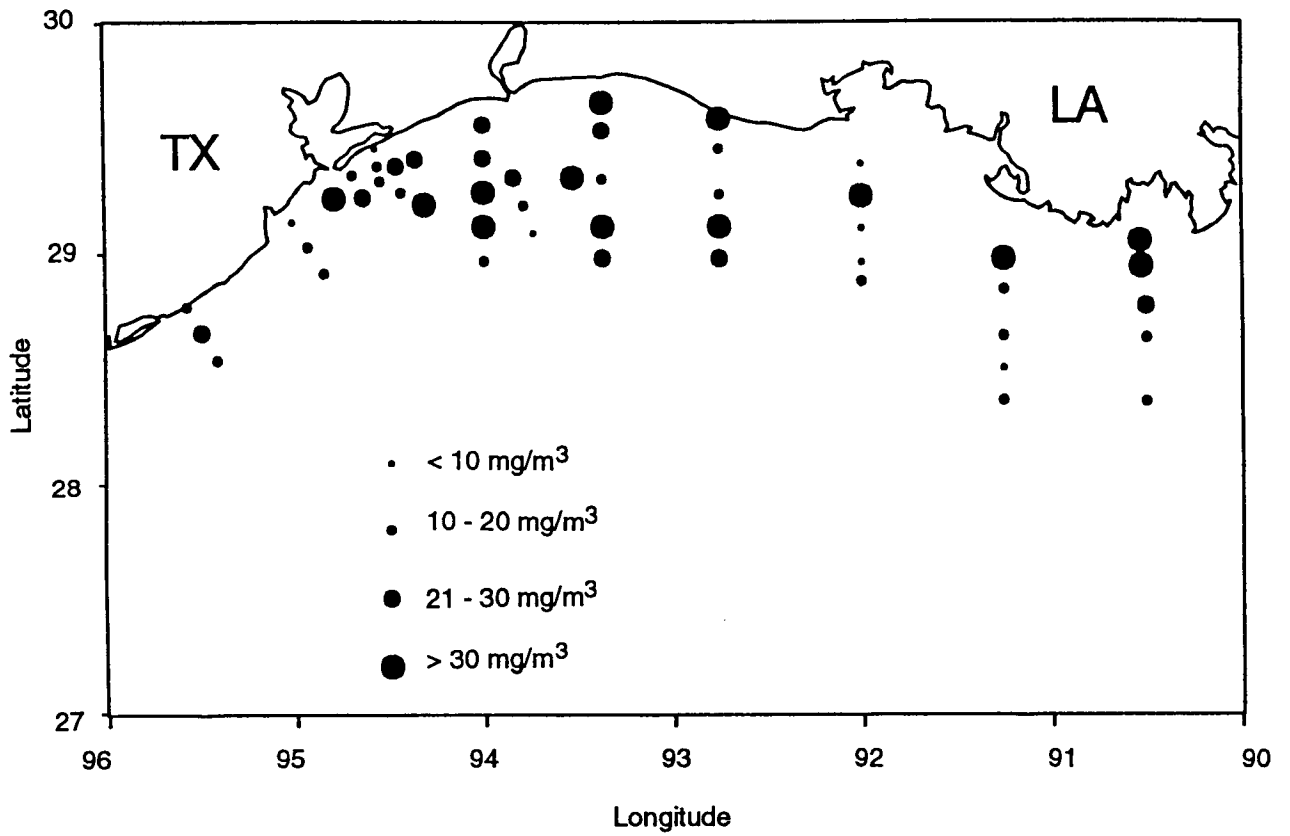
Figure 92. Plankton biomass (mg/m³) for 335-µm mesh samples collected during Cruise IV.
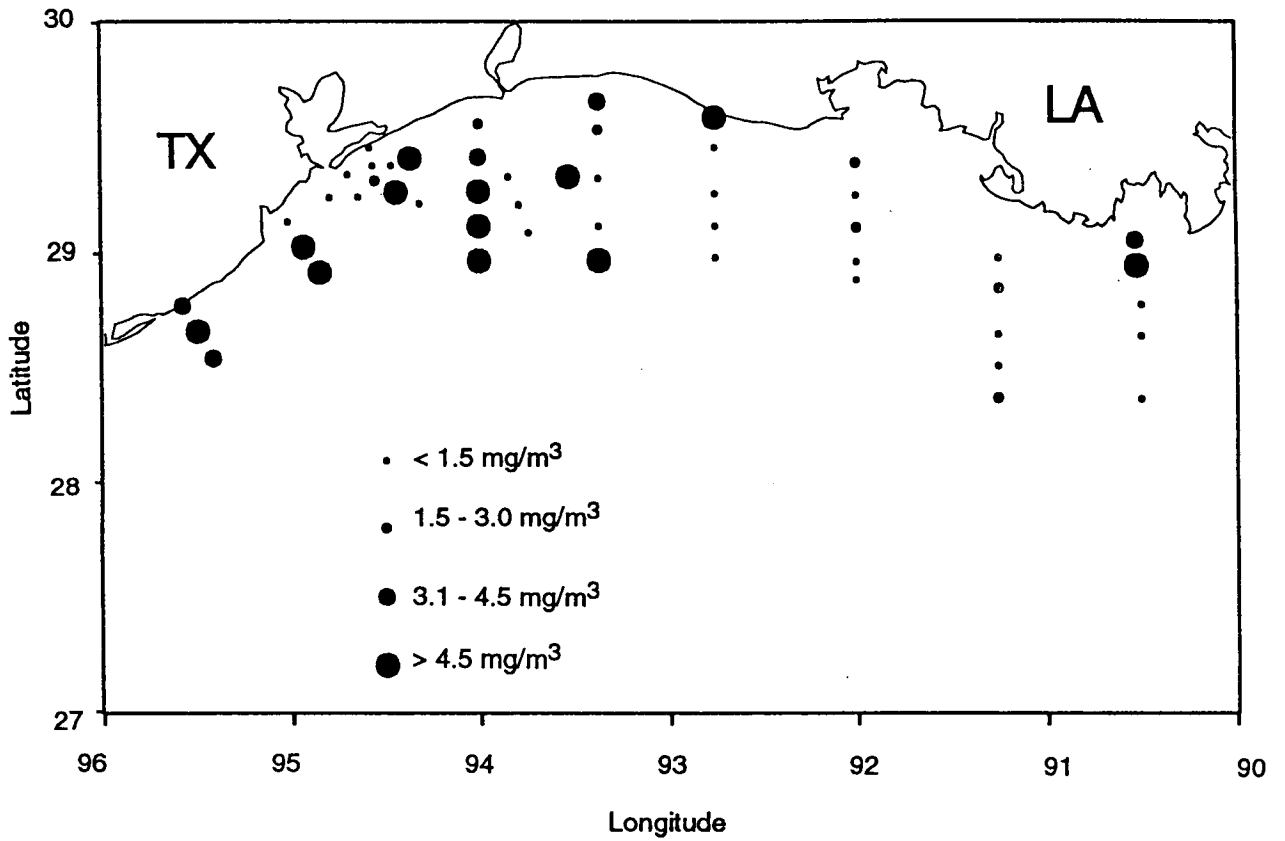
Figure 93. Total larval fish density (#/m³) for Cruise IV zooplankton samples.

$\underline{S5}$. Again, no trend was observed for the density estimates. The 153-μm fraction ranged from 50.99-105.56 mg/m^3 and the 335-μm samples ranged from 11.77-39.96 mg/m^3. Larval fish densities ranged from 0.74-4.08 larvae/m^3.

$\underline{S6}$. The 153-μm biomass estimates were highest in the central portion of the transect, ranging from 39.90-176.22 mg/m^3. The 335-μm samples tended to increase with increasing distance from shore, ranging from 14.85-79.38 mg/m^3. Ichthyoplankton densities were fairly high throughout the transect and ranged from 2.85-8.52 larvae/m^3.

$\underline{S7}$. Density estimates for the 153-μm fraction and for fish larvae increased with distance from shore. The 153-μm biomass increased from 16.19-45.87 mg/m^3, while the 335-μm fraction ranged from 8.15-19.10 mg/m^3. Larval fish densities ranged from 0.82-6.69 larvae/m^3.

$\underline{S8}$. The 153-μm densities increased offshore, ranging from 28.00-80.44 mg/m^3. Density estimates were highest at the central station for both the 335-μm samples and fish larvae. Dry weight densities ranged from 10.09-23.94 mg/m^3 for the 335-μm samples, while larval fish densities ranged from 3.03-10.27 larvae/m^3.

IV. FIELD MEASUREMENTS OF BOTTOM BOUNDARY LAYER PROCESSES AND SEDIMENT SUSPENSION ON THE LOUISIANA INNER CONTINENTAL SHELF

L.D. Wright, R. W. Sternberg, and C. Sherwood

As a small component of the LATEX-B study, we obtained direct field measurements of near-bottom flows, bed stresses, and sediment transporting processes by means of an instrumented tetrapod system deployed at a depth of 15.5 m in spring of 1992 and 20.5 m in spring and summer of 1993. In all three deployments, the tetrapod supported five Marsh McBirney electromagnetic current meters (EMCM's; 3.8-cm probe diameter) situated within the lower 100-113 cm of the water column; two Paroscientific pressure sensors; a flux-gate compass; an array of 5 Downing optical backscatterance (OBS) turbidity sensors, located within the lower 100-113 cm of the water column; and, a Datasonics digital sonar altimeter (DSA; 300 kHz) to measure changes in bed elevation. All sensors were interfaced to Onset data loggers. Table 11 summarizes the information concerning sensor elevations, burst duration, sampling frequency, burst interval and total length of "good data" records for each deployment.

Consistent with the results of others, our measurements show that near-bed flows were very weak under non-storm conditions. Bed stresses were typically too low to resuspend bed sediments. However, the advection of high-turbidity layers or plumes past the instrumentation apparently caused a sustained period of high suspended sediment concentration throughout the log layer in spring of 1993. In the absence of wave activity or high suspended-sediment concentrations, boundary layer profiles showed the bed to have been hydraulically very smooth with $z_0 < 0.1$ cm. However, wave agitation, combined with increased suspended sediment concentration caused hydraulically rough conditions with $z_0 \geq 1.0$ cm.

Time series of smoothed near-bottom current vectors measured during the spring 1993 deployment are shown in Figure 94; notably, the near-bottom flows set persistently to the northerly quadrants throughout the period. Figure 95 summarizes the mean-current and bottom orbital speeds for the same period. An episode of moderate wave activity produced orbital speeds that remained above 10 cm s^{-1} over a 30-hour period centered around hour 216. Examples of logarithmic near-bottom velocity profiles obtained during the spring 1993 deployment are shown in Figure 96. During the early phase of the record, when wave activity was negligible, hydraulic roughness was extremely low with z_0 values less than 0.01 (drag coefficients, $C_D(100)$ ~ 2 x 10^{-3}). However, with the onset of moderate wave activity, z_0 increased by up to two orders of magnitude to over 1 cm episodically. Figure 96b shows one hour of high value for z_0; corresponding $C_D(100)$ ~ 7 - 10 x 10^{-3}). In summer of 1993, z_0 remained < 0.01 cm.

No local resuspensions were apparent during the spring 1992 or summer 1993 deployments. However, the moderate wave event of spring 1993 initiated a prolonged period of high suspended sediment concentration as shown in Figure 97. Following the onset of the moderate wave energy "event," which began at hour 216 (Figure 95), concentrations increased dramatically at z_0=23 cm and continued to increase after the event subsided and skin friction stresses dropped below 0.05 Pa. Eventually, the high turbidity spread throughout the lower 114 cm of the water column. Notably, the time of maximum concentration, centered around hour 504 (Figure 97), coincided with a time of minimal bed stress. Additionally, the peak concentrations were similar at all elevations. This suggests that the high turbidities were more likely related to a wide-spread turbid water mass advected past the tetrapod rather than to local resuspension.

Our data are limited to normal fairweather or *non-storm* conditions. For such conditions we conclude: (1) benthic flows over the inner shelf are weak;
(2) bed stresses induced by mean currents are too weak to suspend sediments;

Table 11. Data summary.

Spring 1992   **28°56.29 N**   **90°28.81 W**   **April 22-30-1992**

Sensor		Elevation above bed	Samples per burst	Sampling interval	Bursts every	Number of bursts	Total Duration
635	press	250 cm	2048	0.5 sec	2 hr	37	72 hr
626	vel 1	2	2048	0.5	2	35	68
	vel 2	33	2048	0.5	2	35	68
	vel 3	63	2048	0.5	2	35	68
	vel 4	93	2048	0.5	2	35	68
OBS	C1	2	2048	0.5	2	41	80
	C2	35	2048	0.5	2	41	80
	C3	60	2048	0.5	2	41	80
	C4	93	2048	0.5	2	41	80
	C5	118	2048	0.5	2	41	80

Spring 1993   **28°56.22 N**   **90°27.72 W**   **May16-June 15, 1993**

Sensor		Elevation above bed	Samples per burst	Sampling interval	Bursts every	Number of bursts	Total Duration
635	press	245cm	4096	0.2 sec	4 hr	180	716 hr
626	vel	53	4096	0.2	4	180	716
626	press	245	1024	1.0	4	180	716
626	vel 1	18	1024	1.0	4	180	716
	vel 2	48	1024	1.0	4	180	716
	vel 3	78	1024	1.0	4	180	716
	vel 4	113	1024	1.0	4	180	716
OBS	C1	23	1024	1.0	4	180	716
	C2	49	1024	1.0	4	180	716
	C3	49	1024	1.0	4	180	716
	C4	49	1024	1.0	4	180	716
	C5	114	1024	1.0	4	180	716

Summer 1993   **28°52.20 N**   **90°27.72 W**   **May16-June 15, 1993**

Sensor		Elevation above bed	Samples per burst	Sampling interval	Bursts every	Number of bursts	Total Duration
635	press	228cm	4096	1.0 sec	4 hr	53	208 hr
626	vel	65	4096	1.0	4	53	208
626	press	228	2048	0.5	4	53	208
626	vel 1	4	2048	0.5	4	53	208
	vel 2	34	2048	0.5	4	53	208
	vel 3	64	2048	0.5	4	53	208
	vel 4	100	2048	0.5	4	53	208
OBS	C1	5	2048	1.0	4	53	208
	C2	34	2048	1.0	4	53	208
	C3	64	2048	1.0	4	53	208
	C4	100	2048	1.0	4	53	208
	C5	126	2048	1.0	4	53	208
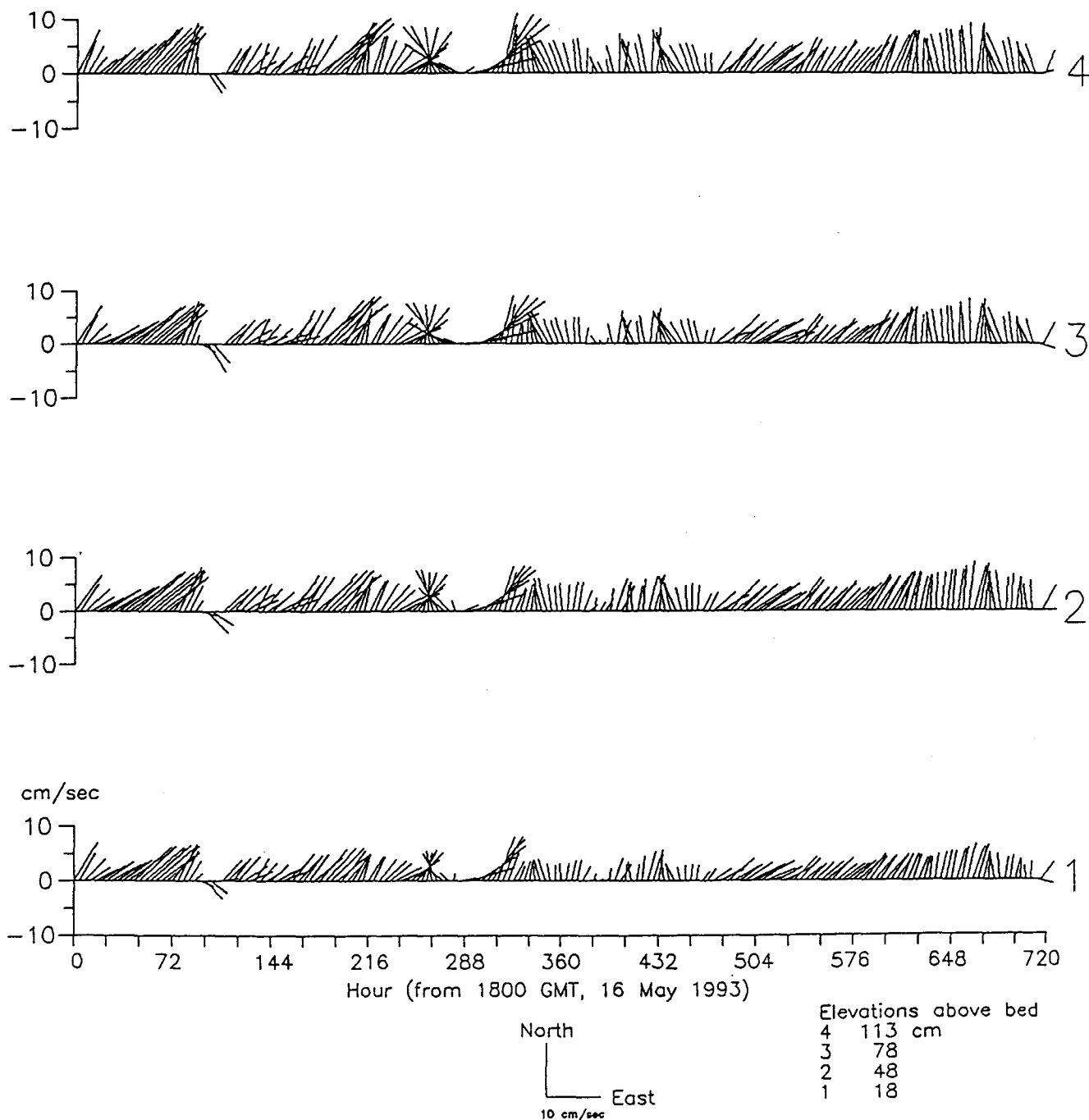
Figure 94. Vector diagram of near-bottom flows measured in spring 1993 at 20.5 m. The series has been smoothed over time.

111
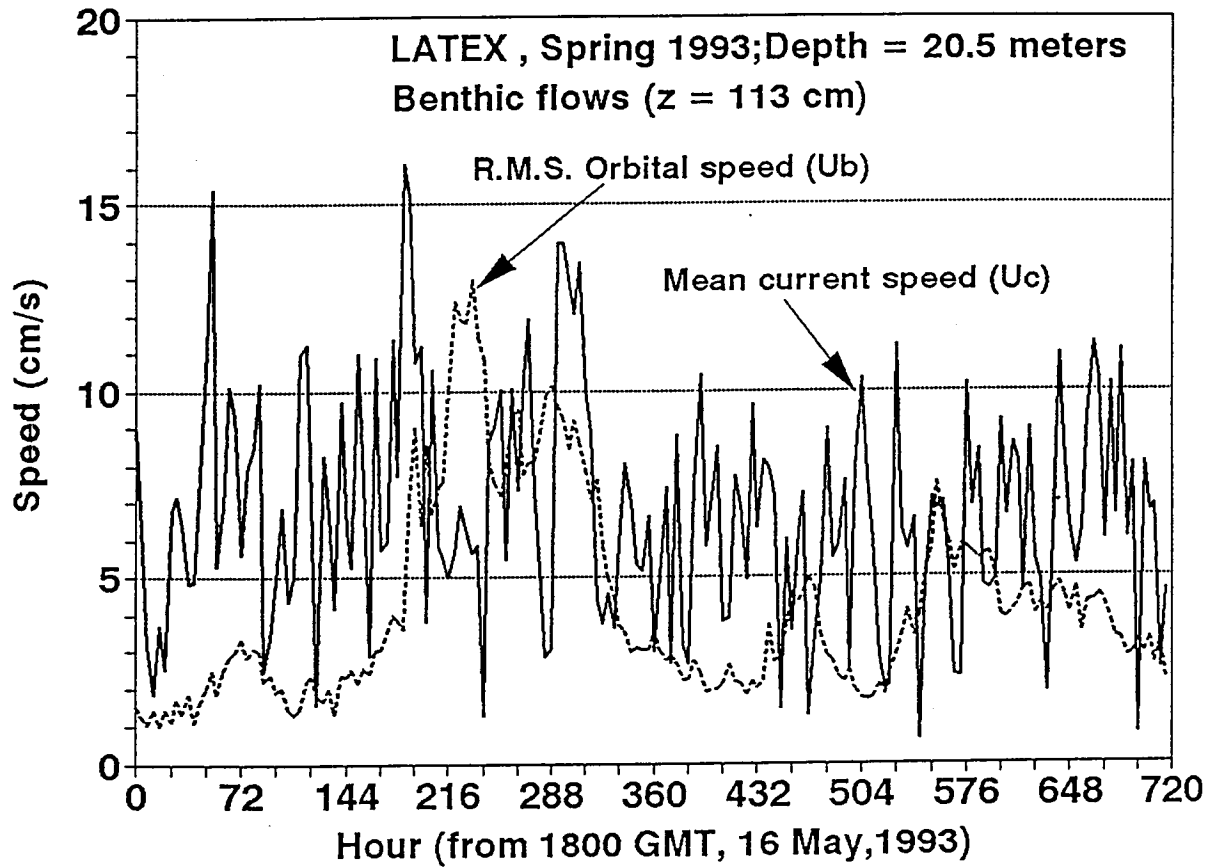
Figure 95. Time series of mean current and bottom orbital speeds near the bed at 20.5 m in spring 1993.
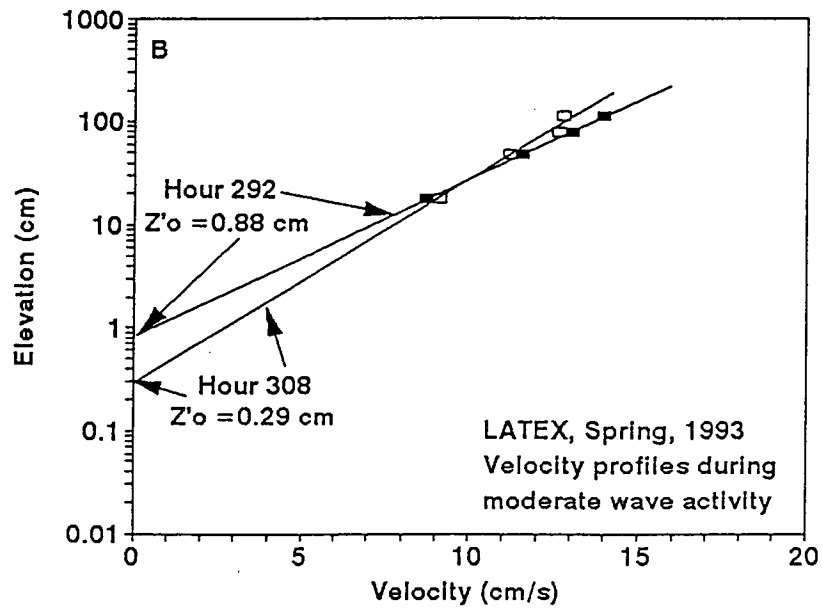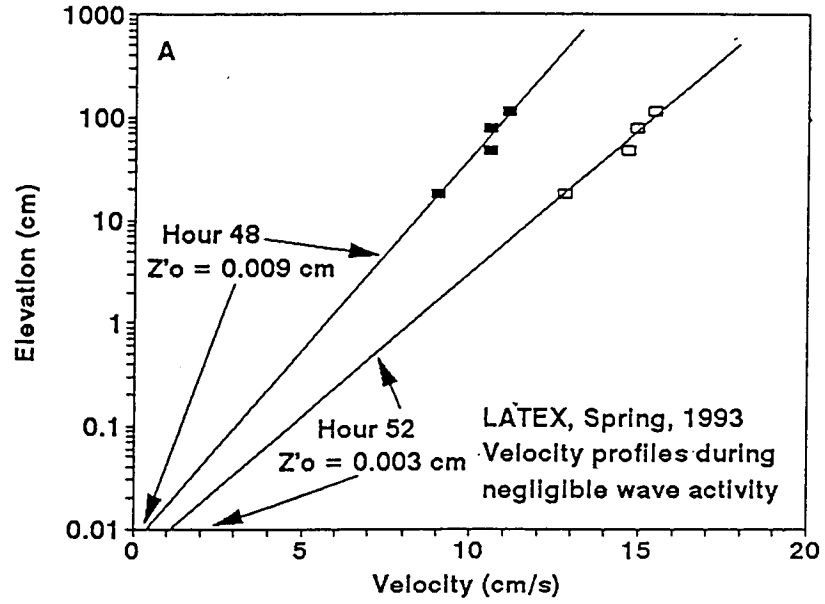
Figure 96. Near-bottom velocity profiles from the 20.5 m site in spring 1993.

113
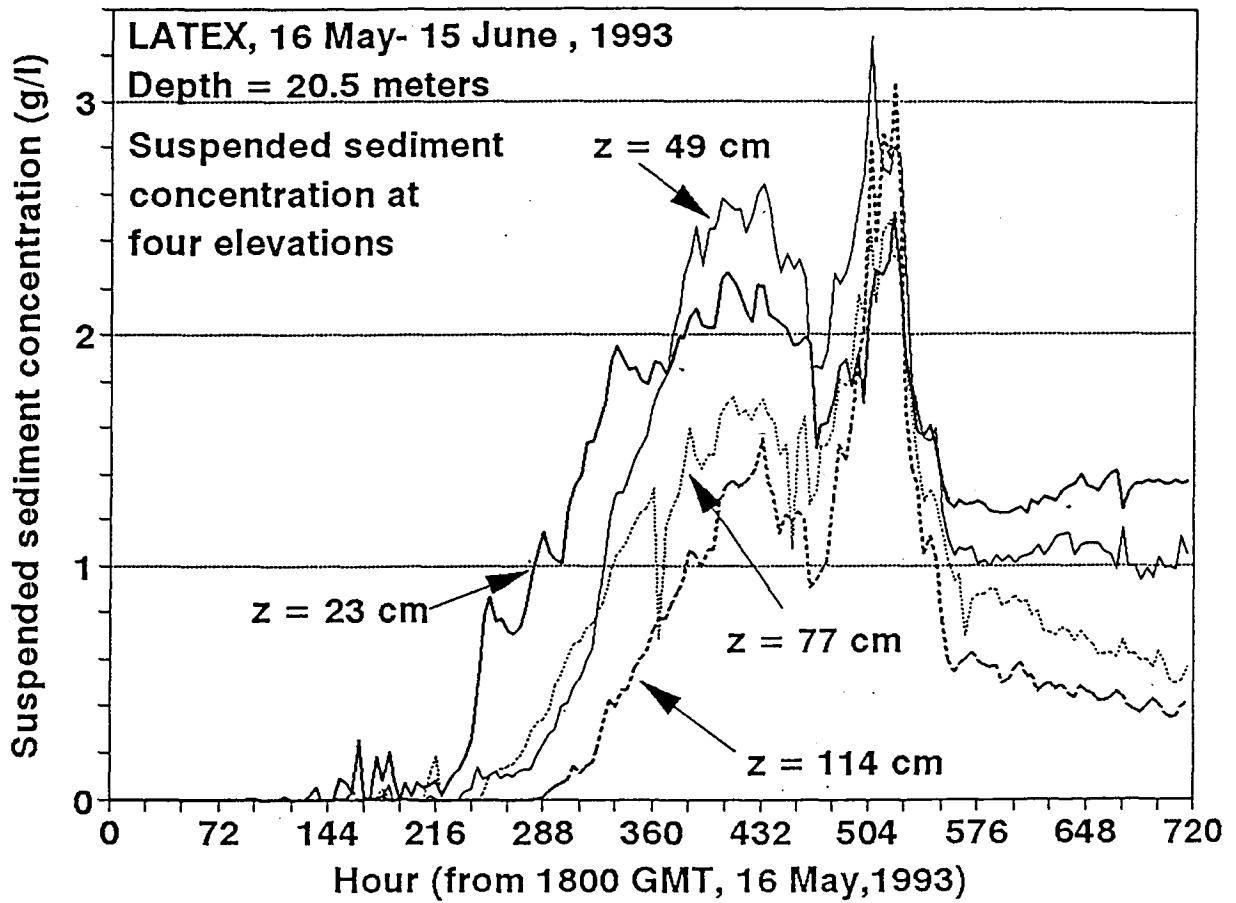
Figure 97. Time series of burst-averaged suspended sediment concentration measured at four elevations above the bed at the 20.5 m site in spring 1993.

114

(3) stresses induced by combined wave-induced and mean (tidal or wind-driven) boundary layer flows probably resuspend sediments at times of moderate wave activity;

(4) under low wave activity and in the absence of high near-bed turbidity, the bottom boundary layer is hydraulically smooth with $z < 0.1$ cm; and,

(5) hydraulic roughness increases by one or more orders of magnitude when wave agitation is significant and when near-bed concentrations of sediment are high.

V. HYPOXIA

Nancy N. Rabalais

A. Introduction

Hypoxia ($\leq$ 2 mg/l dissolved oxygen) is a seasonally dominant feature of the inner- to mid-continental shelf of Louisiana, most widespread and severe during June-August, but occurring as early as February and as late as October (Rabalais et al. 1991, 1992). Hypoxia forms as a result of and is maintained by a combination of physically controlled density structures (mediated by the high freshwater inputs of the Mississippi and Atchafalaya Rivers) and biological processes that contribute to productive coastal water masses and oxygen depletion of the lower water column. The configuration of hypoxic water masses can be related to large-scale circulation patterns, river flow, density structure, and biological features (in particular patterns of phytoplankton biomass, the flux of surface-produced organic matter to the lower water column, and decomposition of organic material).

B. Methods

Dissolved oxygen concentrations were recorded electronically by the LUMCON SeaBird CTD unit. The precision of measurements for the SeaBird oxygen probe is 0.1 ml/l. The upper and lower dissolved oxygen limits of the probe were determined by the LUMCON Marine Technician prior to each cruise and incorporated into the configuration files for the SeaBird software. Calibration of the oxygen probe was accomplished by Winkler titrations on water collected in 5-1 Niskin bottles from the CTD/rosette across the range of values observed. Replicate titrations from replicate 300-ml BOD bottles were made on a Mettler DL21 automatic oxygen titrator. Mean chemically-derived values were compared to the processed SeaBird oxygen data for the depth at which the water sample was collected. A regression equation was developed by which the SeaBird oxygen data were corrected or not, depending on the goodness of fit of the regression equation and its deviation from a 1:1 relationship.

A protocol was developed for extracting usable oxygen data from the SeaBird CTD unit. This methodology was used to delete oxygen data from the upper parts of CTD casts where the oxygen probe had not stabilized adequately prior to the downcast, where the oxygen probe had not stabilized adequately prior to the collection of a near-bottom water sample, and where the oxygen data for the entire cast were suspect. The remaining oxygen data were processed by the same protocols for the other SeaBird parameters. Near-bottom oxygen values for the SeaBird CTD unit are those recorded at the end of the downcast, after the oxygen probe stabilized, and just prior to the tripping of Niskin bottles or just prior to the beginning of the upcast. These values are usually 1-1.5 m above the bottom, but may be as much as 2-3 m above the seabed in rough sea conditions.

A Hydrolab Surveyor 3 multi-parameter CTD unit was used on Cruise IV in July 1993 to obtain dissolved oxygen measurements closer to the seabed than available from the SeaBird CTD unit. The Hydrolab was deployed on every station, unless the depth exceeded the capabilities of the 50-m cable. Hydrolab readings were made at the bottom, for 0.5-m increments to a depth of 2 m above the bottom, and at the surface. The precision of measurements for the Hydrolab oxygen probe is 0.2 mg/l. The Hydrolab oxygen probe is calibrated before and after each cruise.

Comparative hydrographic data were available from the NOAA NECOP Hypoxia Monitoring and Related Process Studies of Rabalais, Turner and Wiseman (e.g., Rabalais et al. 1992, 1994). These data were collected with a Hydrolab Survey 3. Transect C of Rabalais et al. parallels the nearshore end of the LATEX-B S1 line, then turns to the southeast. Similar station depths are occupied along the two transects and provide suitable data to examine temporal and/or small-scale

spatial variability. LATEX-B stations 505 and 104 were comparable in location and depth to station C6B of the NOAA NECOP study.

C. Results

1. Cruise III, April 1993

A broad range of dissolved oxygen concentrations (1.9-10.2 mg/l) was obtained for the development of a regression equation of CTD oxygen values versus Winkler titrations. The relationship (data not shown) was strong with an intercept near zero (y = -0.143 + 1.017x, r^2 = 0.995). The SeaBird CTD data were not corrected for April 1993.

Near-bottom waters were generally well-aerated with no values falling below 2 mg/l dissolved oxygen, the upper limit for hypoxic waters (Figure 98). Near-bottom waters low in oxygen, but not hypoxic (2.0 < x ≤ 4.0 mg/l) were located along the S1, S2 and S3 lines, from offshore Terrebonne Bay to offshore Atchafalaya Bay. Lower oxygen concentrations (≤ 4.0 mg/l) were present along most of the length of S1 in the lowest 2-3 m of the water column (Figure 99). Similar low values were present on the S2 line between 13 and 26 m on the outer end of the transect (Figure 99).

Several distinct patches of hypoxic bottom waters were observed during the NOAA NECOP cruise (April 26-30, 1993) that were not evident during the LATEX B cruise the previous week (April 12-22, 1993). The distribution of a low oxygen area off Terrebonne Bay (NECOP cruise) was consistent with the lower concentrations of dissolved oxygen along S1 in mid-April (LATEX B).

2. Cruise IV, July 1993

A broad range of dissolved oxygen concentrations (0.1-6.8 mg/l) was obtained for the development of a regression equation of CTD oxygen values versus Winkler titrations. The relationship (data not shown) was strong with an intercept near zero (y = -0.019 + 0.940x, r^2 = 0.994). The SeaBird CTD data were not corrected for July 1993.

There were extensive areas of near-bottom and bottom water hypoxia during Cruise IV in July 1993 (Figure 100). Hypoxia extended from the transects off Terrebonne and Timbalier Bays on the east to the western end of the study area off Freeport, Texas (95.5°W). The importance of obtaining oxygen concentration measurements as close to the bottom as possible, especially during expected conditions of hypoxia, is revealed in the comparative extent of near-bottom water hypoxia documented with the SeaBird CTD and the bottom water measurements made with the Hydrolab Surveyor 3 CTD (Figure 101). The areal extent of hypoxia is much greater based on the Hydrolab measurements.

During Cruise IV, the hypoxic water mass was confined close to the seabed (Figures 102 and 103), except along the inshore end of S1 where values less than 2 mg/l extended well up into the water column. Lower oxygen concentrations, but not hypoxic (2.0 < x ≤ 4.0 mg/l), were located well up into the water column along S1 and S2 (Figure 102), but not along S4 and S6 (Figure 103).

The areal extent of hypoxia documented during late July 1993 (NOAA NECOP cruise) was twice the size documented over the same station design for the previous eight years (Rabalais et al., 1994). During the NECOP cruise (July 24-28),the hypoxic water mass did not extend as far to the west as during the previous mid-July LATEX B cruise. Persistent winds from southerly and southwesterly directions had displaced much of the surface waters to the east (along with lowered

Near Bottom Dissolved Oxygen (mg/l)
LATEX April 1993
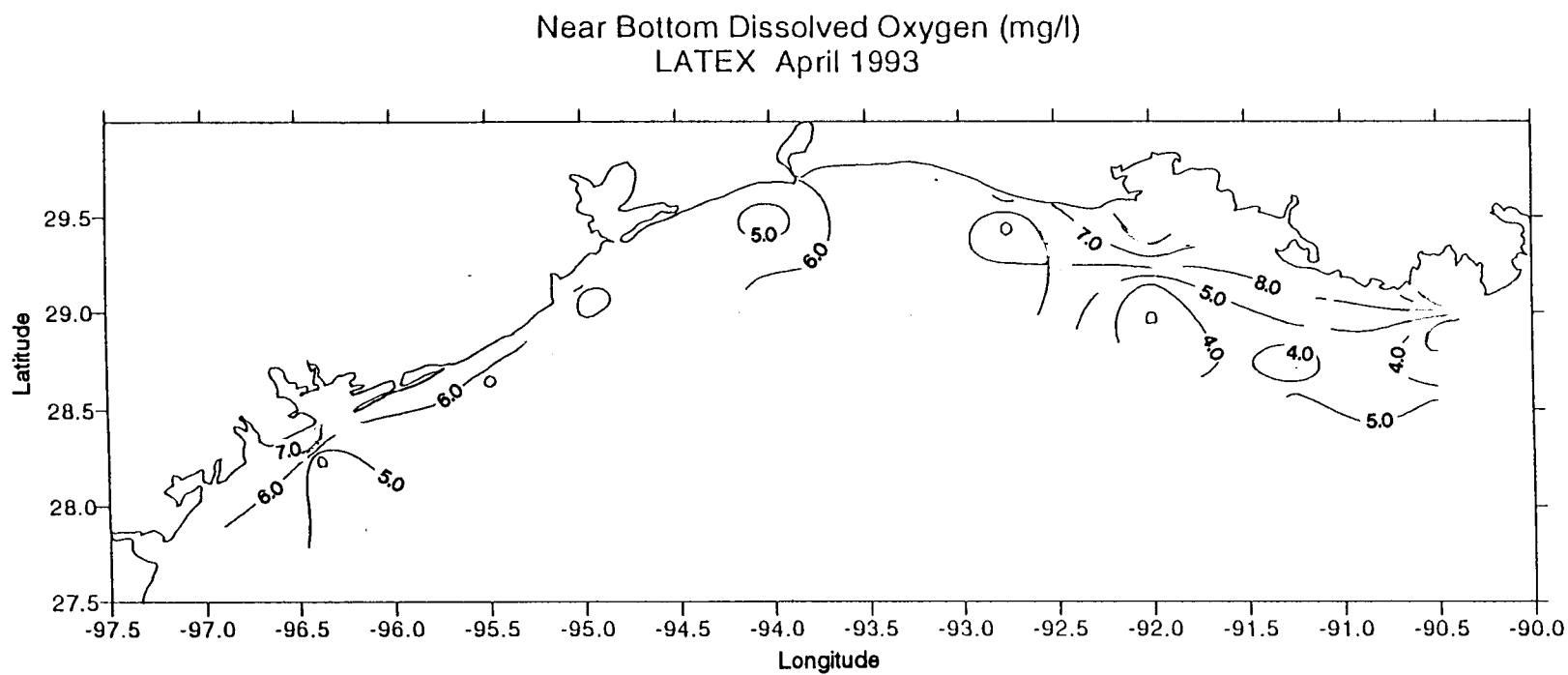
Figure 98. Distribution of near-bottom dissolved oxygen (mg/l) for Cruise III; SeaBird CTD data.
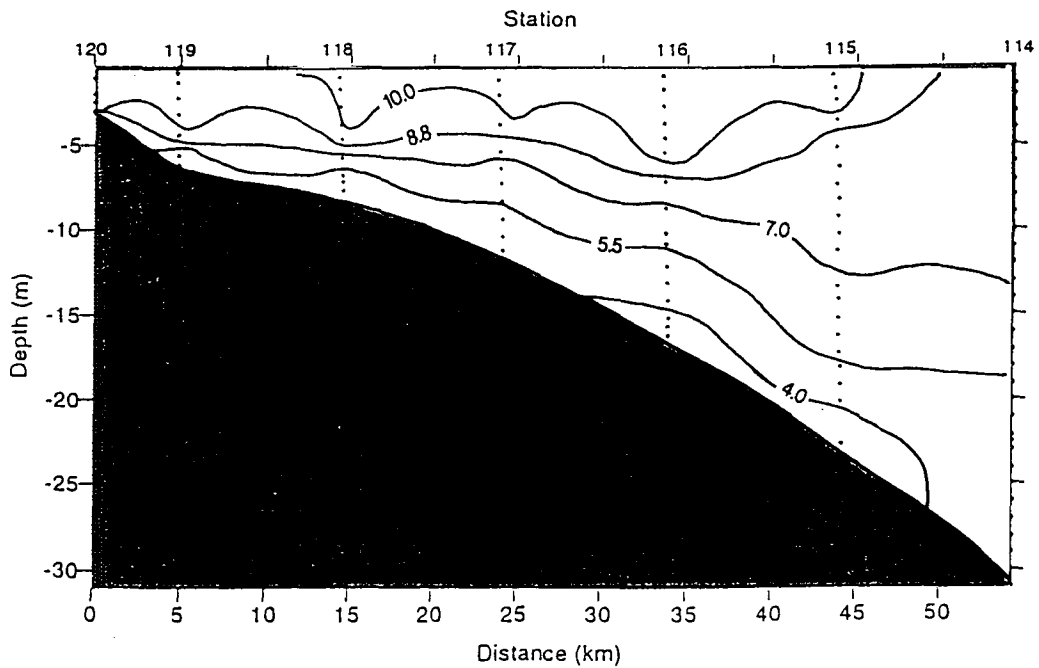
Figure 99. Cross-shelf profiles of dissolved oxygen (mg/l) for the S1 line (upper panel) and S2 line (lower panel) in April 1993, Cruise III.

120
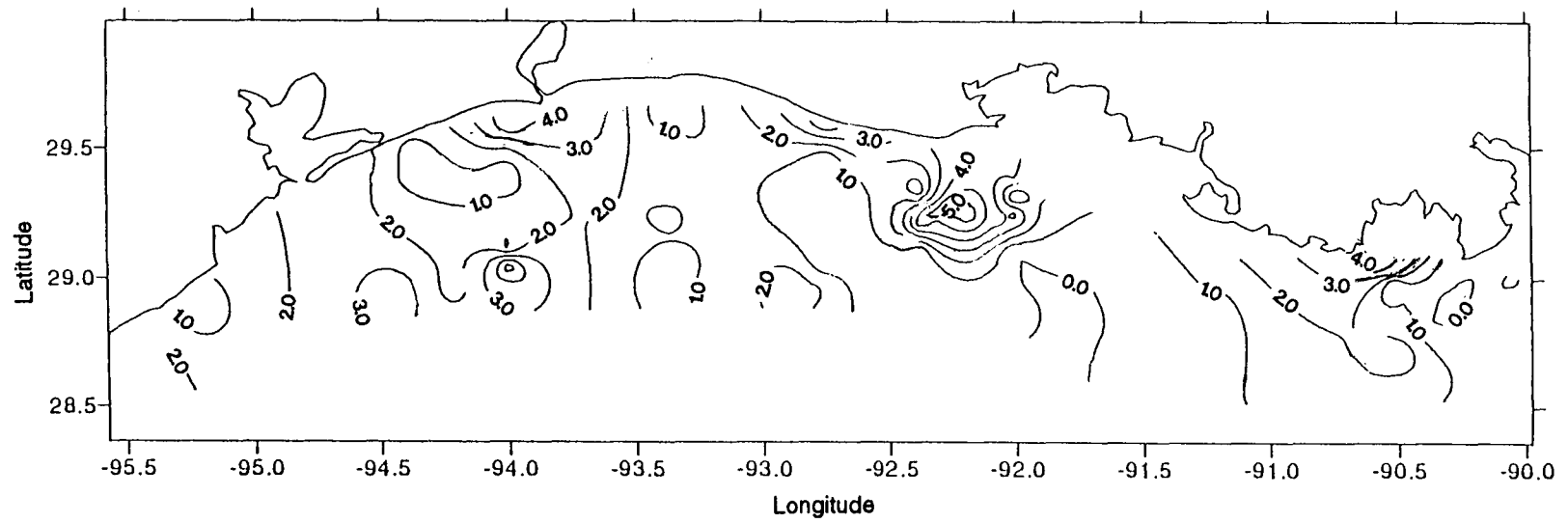
Figure 100. Distribution of near-bottom dissolved oxygen (mg/l) for Cruise IV;
Hydrolab's Surveyor 3 data.
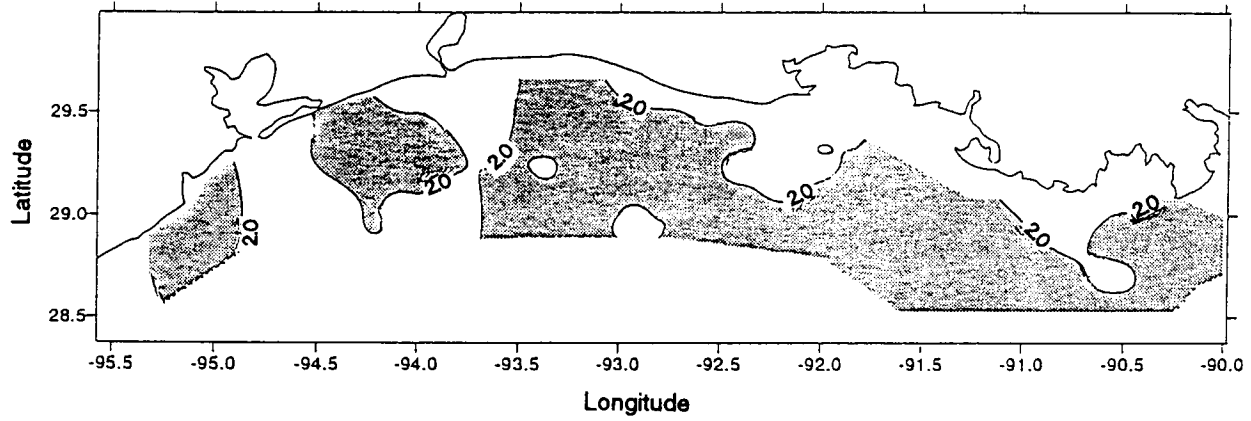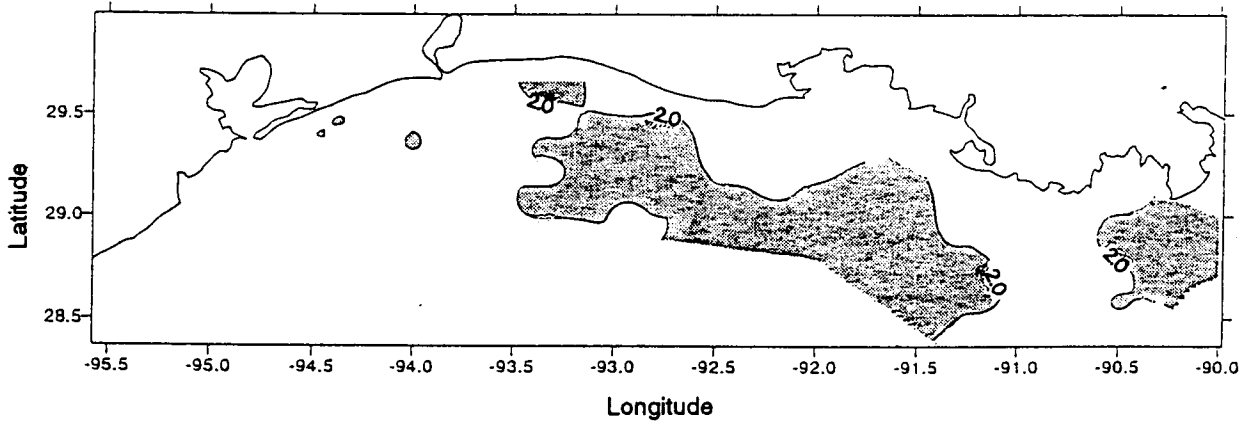
Figure 101. Extent of near-bottom water hypoxia (stippled area) documented with the SeaBird CTD (upper panel) and the bottom water measurements made with the Hydrolab Surveyor 3 CTD (lower panel).
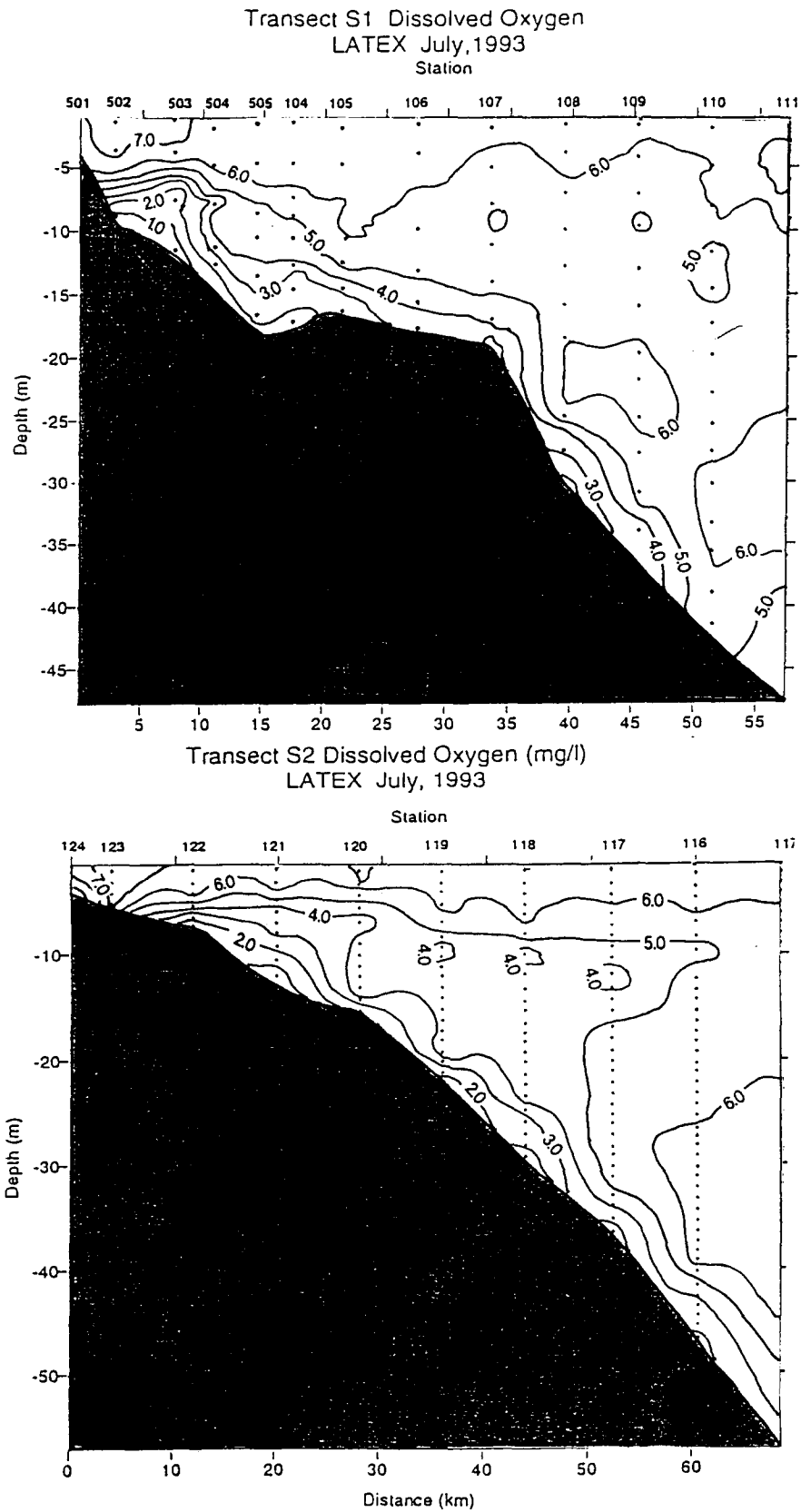
Figure 102. Cross-shelf profiles of dissolved oxygen (mg/l) for the S1 line (upper panel) and S2 line (lower panel) in July 1993, Cruise IV.

123

Transect S4 Dissolved Oxygen (mg/L)
LATEX July, 1993

Station

Distance (km)
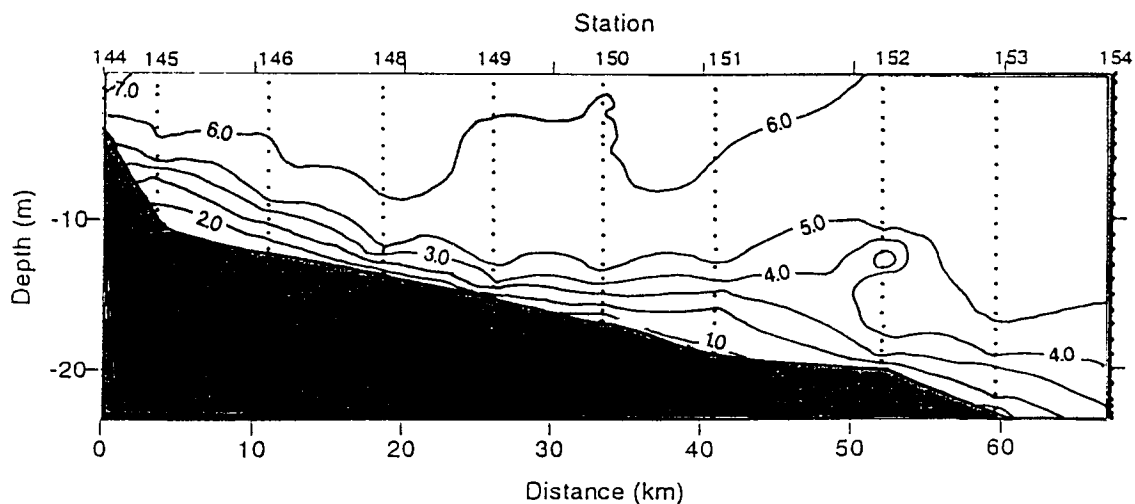
Transect S6 Dissolved Oxygen (mg/L)
LATEX July, 1993

Station

Distance (km)
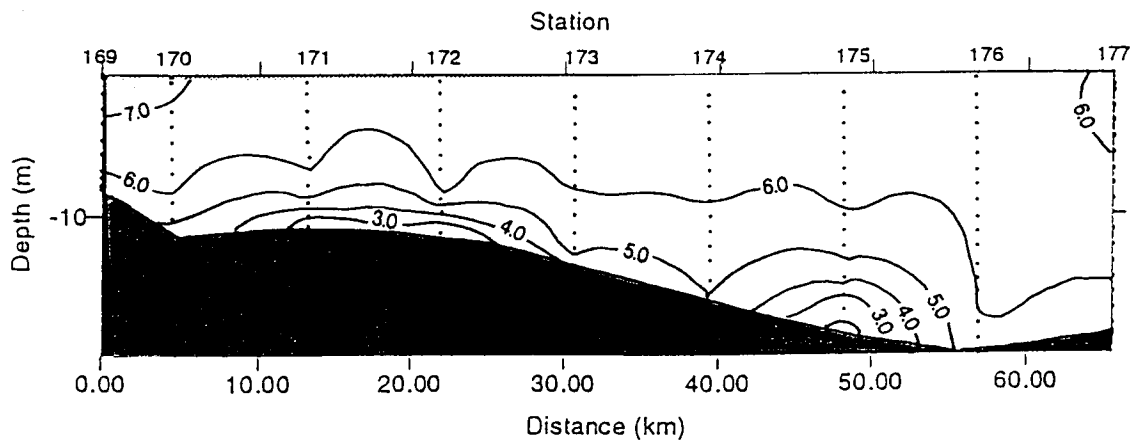
Figure 103. Cross-shelf profiles of dissolved oxygen (mg/l) for the S4 line (upper panel) and S6 line (lower panel) in July 1993, Cruise IV.

124

salinities and higher nutrients), as well as some of the bottom water hypoxia (Rabalais et al., 1994). While hypoxia was extensive during Cruise III, it was located near the seabed and was somewhat patchy in distribution. One week later during the NECOP cruise, hypoxia had become well-developed and was present in much of the lower water column, was severe (well below 0.5 mg/l at many stations), and was a continuous water mass. As freshwater inflow and nutrient flux to the coastal system from flooding of the Mississippi River extended well into August and September, the persistence, severity, and extent of bottom water hypoxia continued as well (Rabalais et al., 1994). The progression of hypoxia development is illustrated in Figure 104.

126
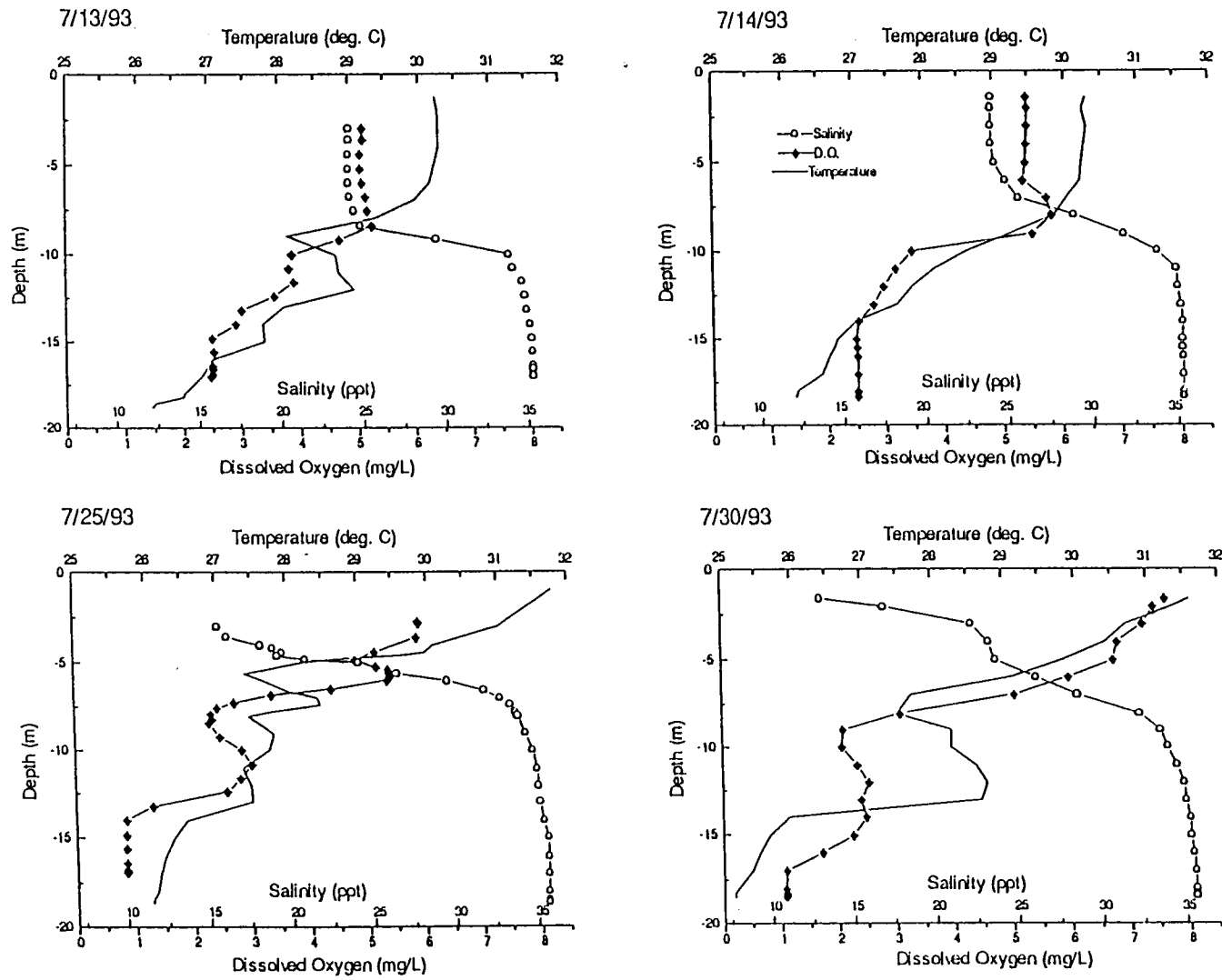
Figure 104. CTD profiles from Station C6B during LATEX-B Cruise IV (July 13-14, 1993) and during the NECOP cruise (July 25 and 30, 1993).

VI. REMOTE SENSING AND IMAGING

Nan D. Walker

A. Methodology and Image Analysis Synthesis

NOAA Advanced Very High Resolution Radiometer (AVHRR) satellite date coverage of the Gulf of Mexico is acquired several times each day at the Earth Scan Lab, Coastal studies Institute, Louisiana State University. These data are captured and archived suing a SUN Sparc II computer running Terascan [TM] software from Seaspace, San Diego, California. After capture, the thermal and visible channels are calibrated from count values to science units. The thermal infrared channels are converted to brightness temperatures in Celsius, and the visible channels are calibrated to percent albedo (Kidwell, 1991). The Gulf of Mexico portion of the image is automatically cut out of the raw data and placed on the Earth Scan Lab's newest computer, the SGI Crimson server with 85 mips and 144 mb RAM. All further processing and analysis of the satellite data is performed on this computer, accessed by Tektronix X-11 terminals. The data is screened for cloud cover and general image quality. A determination is made at this time whether further processing is to be performed. If an image is sufficiently free of cloud cover over an area of interest, the dataset is run through additional processing procedures, which include calculation of sea surface temperature (SST), calculation of reflectance (to reveal surface suspended sediment), and navigation/registration of the image to a standard rectangular map projection. Sea surface temperatures are computed using the multi-channel algorithms of McClain et al. (1985). Reflectance is obtained from the bias correction technique of Stumpf (1988, 1992). Estimates of suspended sediment concentrations are sometimes made using a calibration equation developed specifically for Mississippi River plume waters (Walker and Rouse, 1993). The satellite data processing procedures are summarized in Figure 105. Frontal analyses are routinely performed on the satellite image data with the assistance of the sobel filtering method and digitizing software, available within the Terascan image processing package. Information on coastal and river plume fronts, shelf fronts, squirts and jets, Loop eddies, and the Loop Current were digitized from the satellite image data.

```
Calibration of Visible and Thermal Infrared Channel Data
          from count values to science units
                         ↓
      Initial Screening of the Data for Cloud Cover
                         ↓
              Calculation of Reflectance
                         ↓
         Calculation of Sea Surface Temperatures
                         ↓
   Navigation/Registration of Images to Map Projection
                         ↓
                  Frontal Analyses
                         ↓
              Production of GIF images
                         ↓
               Archival of products
     (4mm tape, 35 mm slide film, and color prints)
```

Figure 105. Image processing procedure summary for NOAA AVHRR data.

Further processing of the frontal information for provision to the other LATEX tasks via GULF.MEX was performed on a PC using the OPCPLOT software (Dr. Murray Brown, pers. comm.). GIF images were routinely provided (corresponding to the GULF.MEX frontal

127

analyses) covering either the LATEX area or the entire Gulf of Mexico. They are made available via anonymous ftp on "nevado.srcc.lsu.edu." In support of the LATEX cruises or overflights, more detailed information was provided in either GIF image format, as line drawings (faxable) or as color prints. In 1993, 55 frontal analyses were posted to GULF.MEX (Table 12) and GIF images corresponding to these analyses were made available via anonymous ftp. In addition, support was provided for the LATEX B April 1993 and July 1993 cruises.

An additional component of the satellite data analysis is to analyze a representative sample of the historical NOAA AVHRR data sets within the Earth Scan Lab archive, which begins in July 1988. During 1992, approximately 2 images/day were uploaded from the archive tapes between July 1988 and January 1992, totaling 3000 images. The images were screened for image quality and the best images were processed for further analysis by the investigators. In the next section of this report analysis of historical data, as well as data collected during the LATEX program, is presented.

B. Historical Analysis: Annual and Interannual Variability of Surface Temperatures and Fronts

1. Introduction

Surface temperature structure across the Louisiana and Texas continental shelves varies considerably throughout the year. During winter, surface temperature variability is maximized as winter storms move over the northern Gulf of Mexico and remove heat from shelf water masses. Inner shelf waters cool most rapidly as a result of their depth-limited heat storage capacity (Huh et al., 1984). This results in a pronounced temperature structure across the shelf with coolest waters close to the coast and warmest waters offshore. In contrast, during summer, almost no surface temperature structure is discernible over the continental shelves of Louisiana and Texas. An exception is the southeast Texas coastline where relatively cool upwelled waters contrast in temperature to ambient Gulf of Mexico waters during the summer months.

In this section, the seasonal and interannual variabilities of surface temperatures and surface temperature fronts will be discussed using satellite image data for three years; 1989/90, 1992/93 and 1993/4. These three years were chosen as they demonstrate the range of meteorological conditions experienced by the continental shelf of the northwestern Gulf of Mexico. Climatological air temperature information from Lake Charles, Louisiana, coinciding with the satellite image archive within the Earth Scan Laboratory (beginning in June 1988) was used to select the years for investigation. Figure 106 illustrates the monthly mean air temperatures from Lake Charles from June 1988 through June 1994, plotted against the 30-year (1961-1990) climatological monthly means. These data reveal that the 1989/90 winter season was much colder than average. The most anomalous air temperatures were recorded in December 1989 when the monthly mean was about 5° C lower than the climatological mean. The 1992/93 winter season was warmer than normal, and the 1993/94 winter season was near normal.

For this study, surface temperatures were extracted from 5 profile lines corresponding to the LATEX-A mooring lines (Locations, Figure 107). The year is defined here as beginning in September and ending in August to focus on the winter season and to facilitate the investigation of the autumn cooling and spring warming on the shelf. An attempt was made to locate at least two cloud-free images across the entire LATEX region for each month

It is relevant to point out at this stage that although the satellite radiometer senses the ocean's skin temperature, this measurement is generally representative of the surface mixed layer, particularly in the presence of wind and/or at night. In addition, several comparisons of LATEX-B cruise data with contemporaneous satellite frontal information have demonstrated that the satellite-observed fronts were indicative of boundaries between water masses of different densities.

Table 12. Frontal Analyses and GIF files provided to LATEX personnel in 1993.

Date	Feature(s) of Interest
1 Jan 93	LATEX fronts/ squirt
9 Jan 93	LATEX fronts/ squirt
16 Jan 93	LATEX fronts/Eddy V
17 Jan 93	Eddy U/ Loop Current
26 Jan 93	LATEX fronts/ squirt
31 Jan 93	LATEX fronts
8 Feb 93	LATEX fronts
12 Feb 93	LATEX fronts/ Eddy V and W
21 Feb 93	LATEX fronts/ Loop Current
23 Feb 93	Eddy V/ Loop Current
4 Mar 93	LATEX fronts/ Eddy V and squirt/ Loop
7 Mar 93	LATEX fronts/ Eddy V and squirt/ Loop
9 Mar 93	LATEX fronts/ Eddy V/ cyclonic eddy/ Loop
14 Mar 93	LATEX fronts/ squirt
22 Mar 93	Eddy V
25 Mar 93	Mississipppi plume front
27 Mar 93	Eddy V/ Loop Current
1 Apr 93	Eddy V/ Mississippi plume/ Loop Current
10 Apr 93	Eddy V/ cyclonic eddy/ Loop Current
18 Apr 93	Eddy V / Loop Current
3 May 1993	Eddy V/ squirt/ Loop Current
21 May 1993	Loop Current
23 May 1993	Loop Current and filaments
30 May 1993	Loop Current
31 May 1993	Formation of Eddy W
6 June 1993	Eddy W
8 June 1993	Eddy W
24 June 1993	Eddy W
25 June 1993	Eddy W / Loop Current
7 July 1993	Texas upwelling/ River plume fronts
28 July 1993	LATEX fronts/ Loop Current
1 August 1993	Eddy V and W/ River plumes
5 August 1993	Eddy W/ Texas upwelling
10 August 1993	River plumes
12 August 1993	Eddy W
17 August 1993	LATEX fronts/ Cyclonic eddy
18 August 1993	Texas upwelling
22 August 1993	Loop Current
29 August 1993	Loop Current and Eddy X
2 September 1993	Texas upwelling
21 September 1993	LATEX fronts
22 September 1993	Loop Current
29 September 1993	LATEX fronts/Eddy X
5 October 1993	LATEX fronts/ Eddy X
18 October 1993	Loop Current/Eddy X
1 November 1993	LATEX fronts
7 November 1993	LATEX fronts
11 November 1993	LATEX fronts/ Eddy W/Eddy X
14 November 1993	Loop Current
17 November 1993	LATEX fronts/ Eddy W/ squirt
21 November 1993	LATEX fronts
28 November 1993	LATEX fronts/Eddy V/W and X/ Loop
5 December 1993	LATEX fronts/ Eddy X/ squirt/ Loop Current
15 December 1993	LATEX fronts/ Eddy V/W and squirt
20 December 1993	Loop Current

129
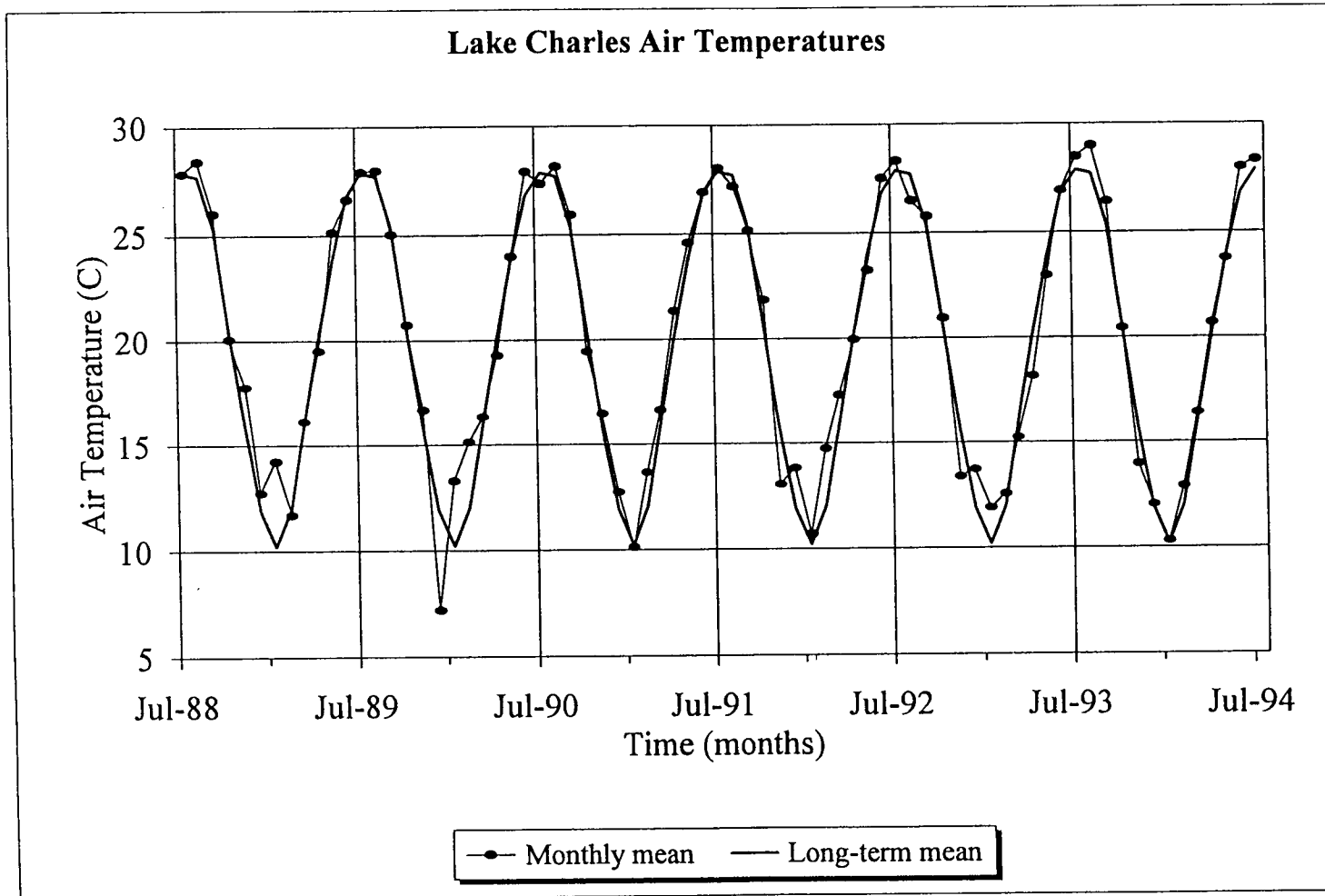
Figure 106. Monthly mean air temperatures compared with long-term monthly mean air temperatures recorded at Lake Charles, Louisiana, from July 1988 through June 1994.
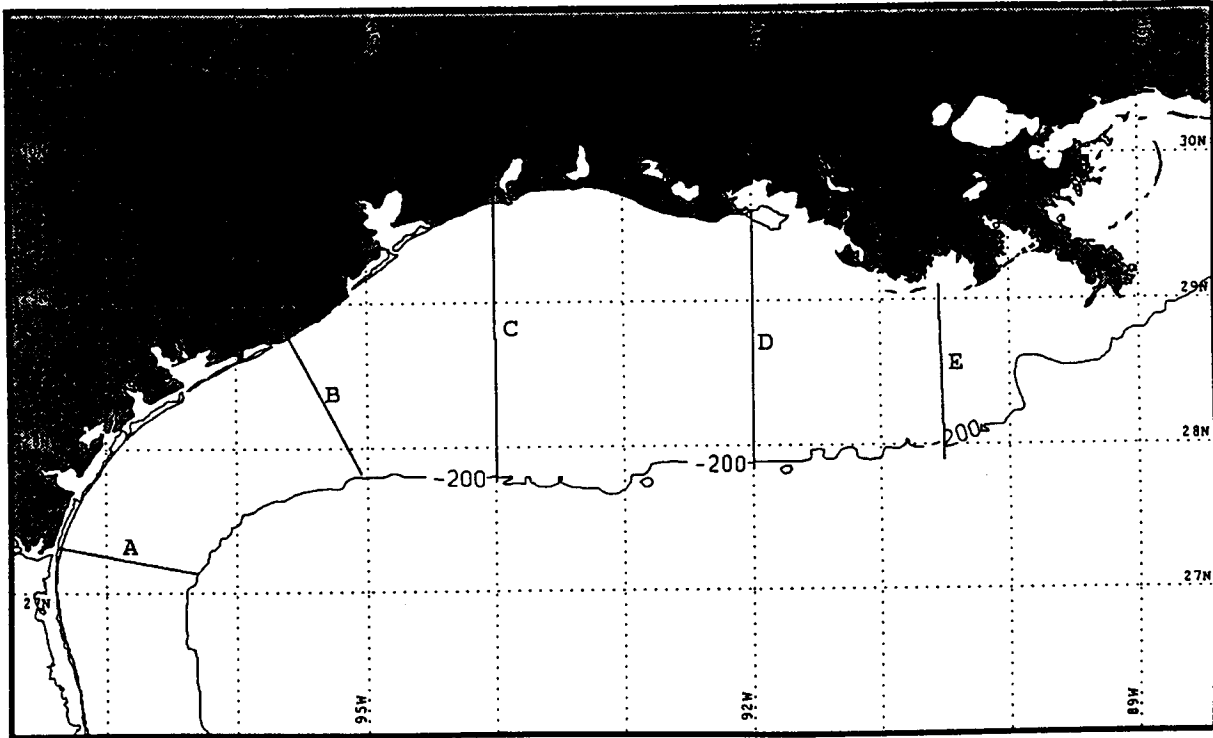
Figure 107. Map depicting the location of LATEX A mooring lines along which SSTs were extracted in this study.

Comparisons of the ADCP near-surface currents obtained during the October 1992 LATEX-B cruise indicate that the main SST front may mark the outer boundary of the coastal current. The strongest currents within the westward-flowing Louisiana coastal current were found in close proximity and shoreward of the strongest SST front on the LATEX shelf (Walker et al. in Murray, 1994).

2. Shelf Temperature Changes, Frontal Characteristics and Circulation Observations during 1989-90

The episodically cold winter of 1989-90 was investigated to reveal surface temperature structure across the shelf, frontal intensities and locations, as well as associated circulation patterns. Although SST information was extracted from 23 images during the 1989-90 year, only the most informative SST profiles will be referred to in this discussion. For the September through December 1989 period, SST information, extracted from five images, is presented for profile lines A and D (Figure 108a,b). The image dates shown are September 18 (1900 UTC), October 20 (2000 UTC), November 10 (2000 UTC), December 14 (0700 UTC), and December 26 (2000 UTC).

The September 18, 1989, image data revealed very little temperature structure as SSTs were 27° to 28° C across the entire LATEX region, a situation typical of summer. The first significant cold-air outbreak of the autumn season moved southeastwards over the study region on October 18 when coastal air temperatures measured at Grand Isle dropped from 24° C on October 18° to 8° C on October 20. SST information extracted from the October 20 image demonstrated that substantial cooling of continental shelf waters resulted from passage of this winter storm. Cooling across the inner shelf ranged from 4° C to 9° C, whereas cooling of 2° C to 3° C was observed across the outer portions of the shelf. The greatest temperature changes were observed on the inner shelf seaward of Atchafalaya Bay where river water and cool bay water were forced onto the shelf by westerly and northwesterly (offshore) winds during this winter storm. SST gradients appeared across the shelf as the deeper offshore waters chilled less rapidly than shallower waters. On October 20, relatively weak SST fronts were observed on profile lines A, B, and D. Along line A, an SST front of 3° C over 20 km was observed mid-shelf (Figure 108). Along line B, an SST front of 1° C over 5 km was observed about 40 km offshore (not shown). The frontal intensities were greatest along line D where Atchafalaya River and Atchafalaya Bay waters had been discharged onto the shelf (Figure 3b). Multiple fronts were observed along line D approximately 15, 35, and 55 km from the coast (see F1, F2, F3, on Figure 108). The inner shelf front was the strongest, approximately 3° C over 8 km.

Between October 20 and November 10, only one weak winter storm passed over the area and, as a result, little temperature change was observed over the continental shelf. Although coastal waters were 1° C to 4° C cooler than offshore waters, no distinct SST fronts were observed, indicating that the fronts had weakened between October 20 to November 10.

Six winter cold air outbreaks were experienced between the November 10 and the December 14 images. The temperature changes that resulted were impressive. The inner shelf waters responded most rapidly with temperature changes ranging from 6° C on lines A and B (in the west) to 8 to 10° C on lines C, D, and E (in the east). The lowest shelf temperatures (8° C) were again observed seaward of Atchafalaya Bay (Figure 108). On line D, multiple fronts were again observed. Near the coast, an SST front of 3° C over 6 km was observed (Figure 108, see F4). SST fronts were also observed 35 km and 80 km from the coast (Figure 3, See F5 and F6). Along line E, a front of 3° C in 10 km was observed near the coast and a sharper front (2° C in 4 km) was observed about 80 km from the coast (not shown). Along the other lines, surface temperatures increased gradually in an offshore direction with no major SST gradient features.
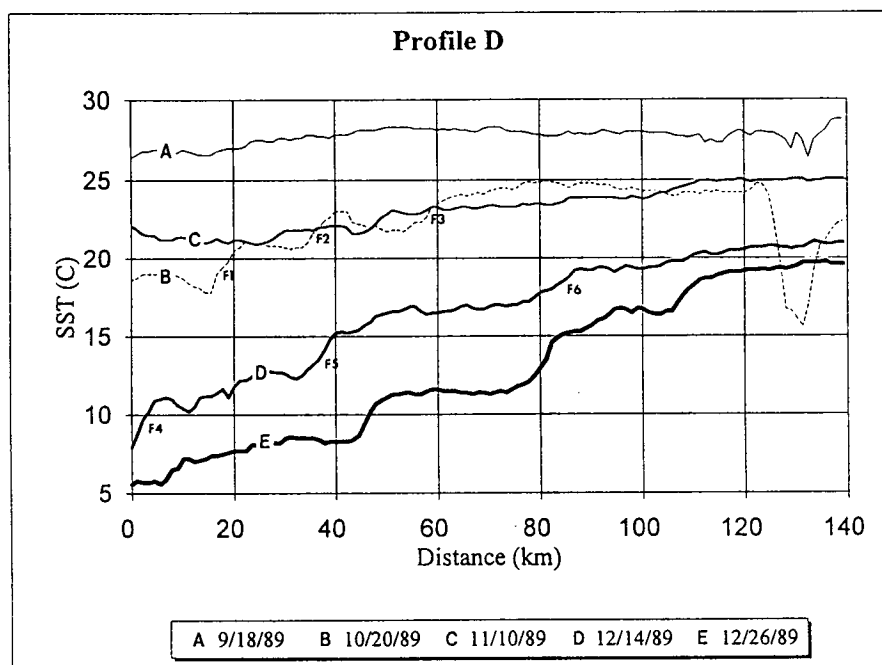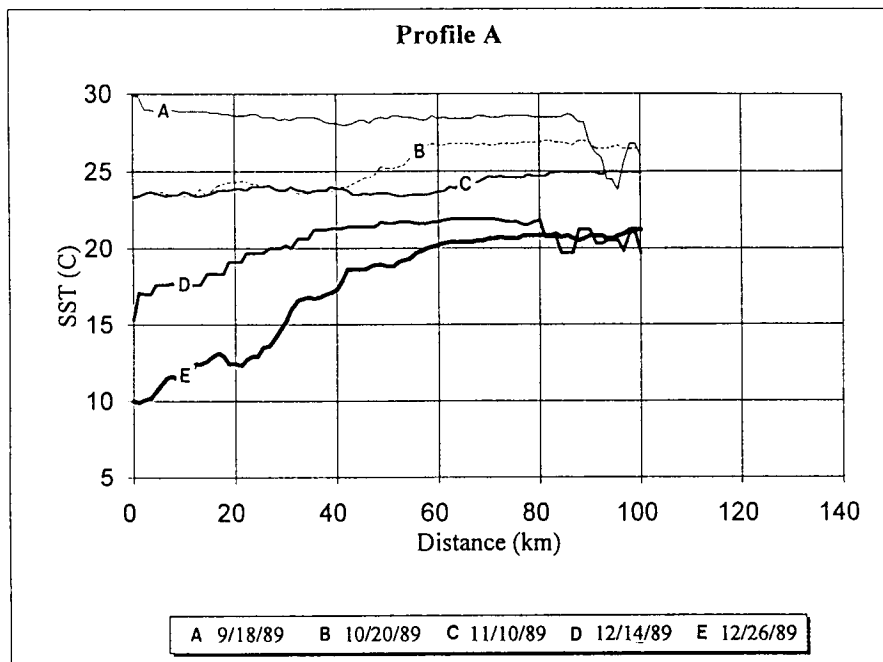
Figure 108. SST information extracted from satellite image data for line A (upper panel) and line D (lower panel) between September 1989 and December 1989. F1-F6 are fronts referred to in the text.

Between December 14 and December 26, an episodic winter storm moved through the study region. Air temperatures at Grand Isle fell below freezing from December 22 through December 25 (Figure 109) and accompanying offshore northwesterly winds exceeded 10 m/s for 2 days. Along lines A and B, cooling from this cold air outbreak was similar to that of the six minor winter storms which occurred between November 10 and December 14. Along the inner shelf of south Texas, cooling of 5° C to 6° C was experienced. (Figure 108). In contrast, comparatively little temperature change occurred offshore. Distinct SST fronts were observed after this winter storm. Along line A (Figure 3a), two SST fronts were observed within 40 km of the coast. The first front measured 3° C in 15 km and the second stronger front was 6° C in 20 km.. Temperatures seaward of Atchafalaya Bay fell below 6° C (Figure 108b), and inner shelf waters along line C were below 10° C 60 km from the coast (not shown). During this event, ice several inches thick formed in shallow bays and in nearshore coastal areas of Louisiana (Edward Weeks, pers. comm.). The mid-shelf temperature fronts previously observed on December 14 along line D (Figure 108, F5, F6) increased in strength and moved seaward between December 14 and 26. Analysis of the image data reveals that line D was located west of the strongest SST front associated with the Atchafalaya plume. The strong northwesterly winds had forced the coldest portion of the plume towards the southeast where an SST front of 14° C over 20 km was observed (not shown).

Three minor winter storms occurred between the December 26 and January 10 images. It is of interest that the inner shelf waters of line A experienced further cooling, whereas the inner shelf waters of C, D, and E warmed considerably over the two week period between images (Figure 110). The most likely explanation is that the cooler water masses on the inner along lines A and B resulted from advection of cooler water from the northeast, transported by the Louisiana-Texas coastal current. This seems the most likely source of cold water since atmospheric forcing was relatively weak and, therefore, local heat loss could not have explained the cooling which took place on the inner shelf. On January 10 along line A, a very sharp SST front (6° C over a few km) was observed 35 km from the coast (Figure 110), replacing the somewhat weaker multiple front structure observed on December 26. Along line D (Figure 110b), the inner shelf waters had warmed by 2° C to 3° C, while the mid-shelf waters remained essentially unchanged. In contrast, the outer shelf waters (80-140 km) had cooled substantially (3° C to 4° C). The profile data extracted from line D also show that the SST fronts were located further seaward on January 10.

To investigate changes in frontal structure across the entire LATEX shelf between December 26 and January 10, the main SST fronts were digitized and are displayed in Figure 111. The outer Atchafalaya plume front moved seaward as much as 35 km over the 2 week period. Further west, the wavy front observed south of Galveston on December 26 had become further deformed such that several "mini-squirts" were observed with length scales of 35 km and separation distances of 50-70 km. Further south, an elongated cool feature was observed extending seaward to the 200 m isobath. This region is a preferential area for squirt formation as it is influenced by strong currents associated with warm core eddies that often reside in close proximity to the edge of the shelf.

Between January 10 and February 23, a warming trend was observed over most of the continental shelf. Temperature change was most rapid in shallower regions of the shelf, as would be expected. Warming of the inner shelf was most rapid on line A (furthest south) where 10° C water on January 10 was replaced by 16° C water by February 23. In addition, the strong SST fronts observed between December 26 and January 26 had disappeared. Subsequently, warming of the shelf waters continued and by April 20 the shelf was nearly isothermal with temperatures across the shelf near 22° C. Between April 20 and August 5, surface temperatures increased by about 10° C on all parts of the shelf, which remained virtually isothermal.

The analysis of temperature data during the 1989/90 year has shown that the inner shelf waters of the LATEX region cool rapidly in response to the passage of winter storms. The differential cooling of shelf waters (as a result of depth differences) results in a transition from coldest waters near the coast to warmer waters offshore. The lowest temperatures were observed seaward of

134
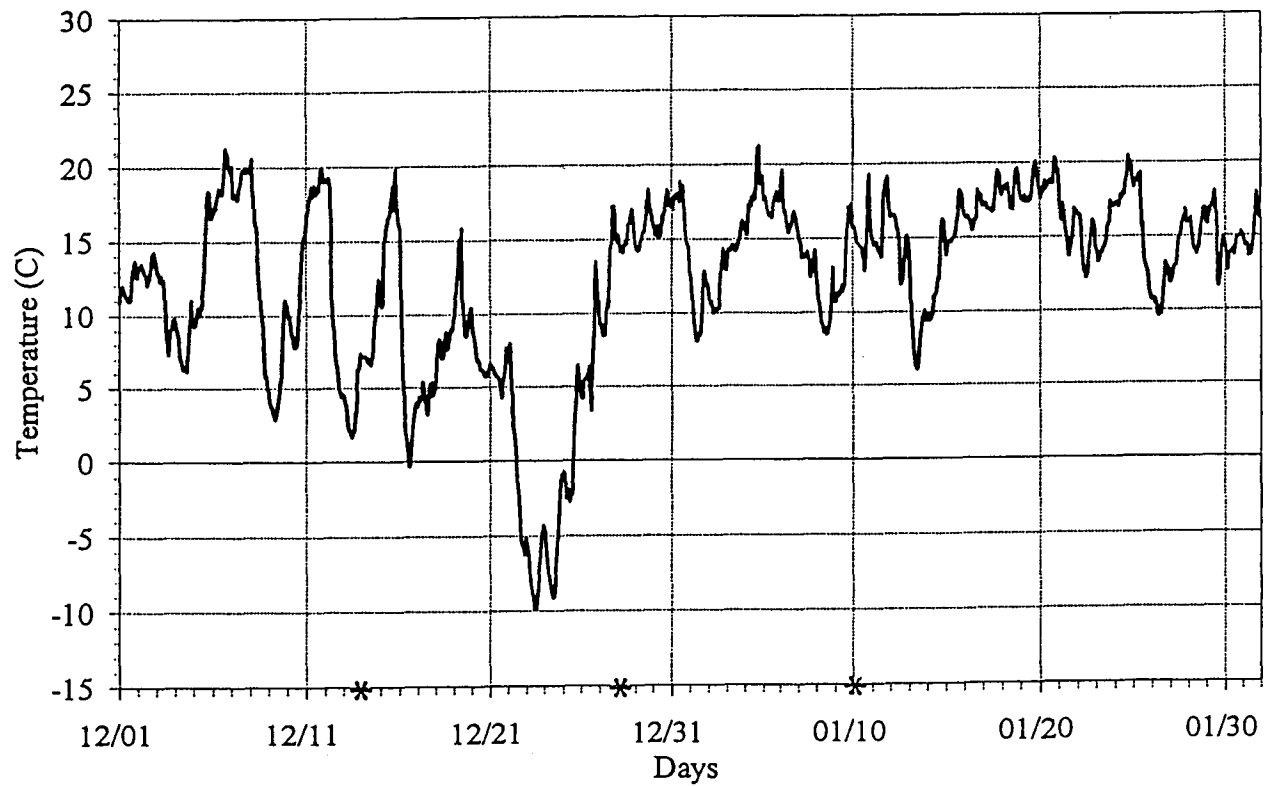
Figure 109. Hourly air temperatures recorded at Grand Isle, Louisiana, during December 1989 and January 1990. The astericks depict times of satellite image acquisition, discussed in the text.
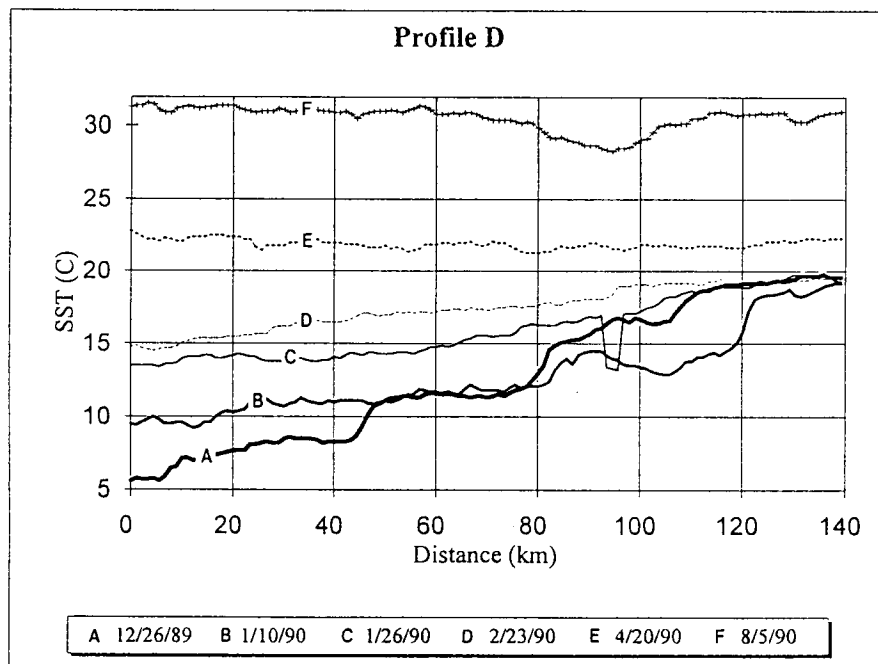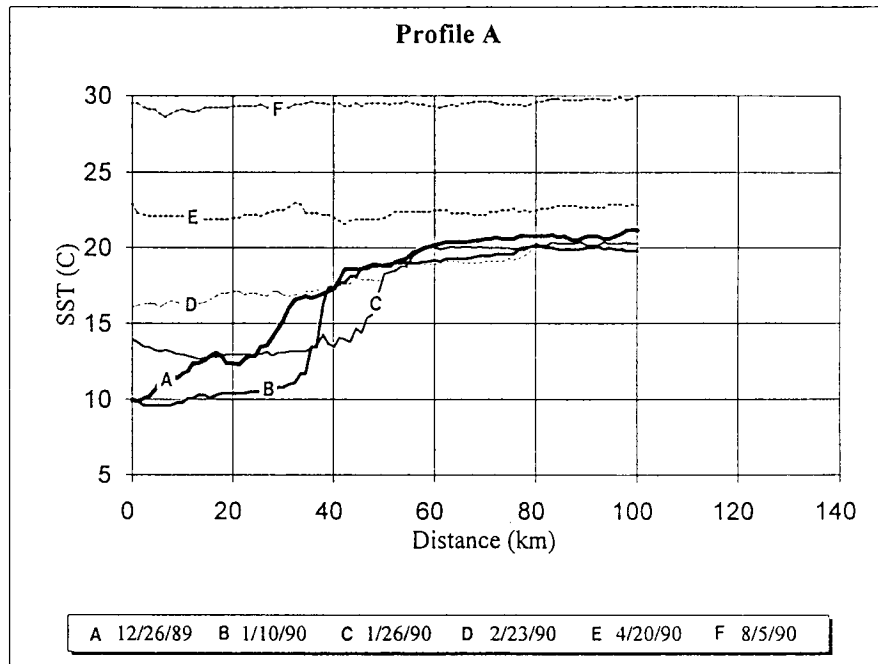
Figure 110. SST information extracted from satellite image data for line A (upper panel) and line D (lower panel) between December 1989 and August 1990.
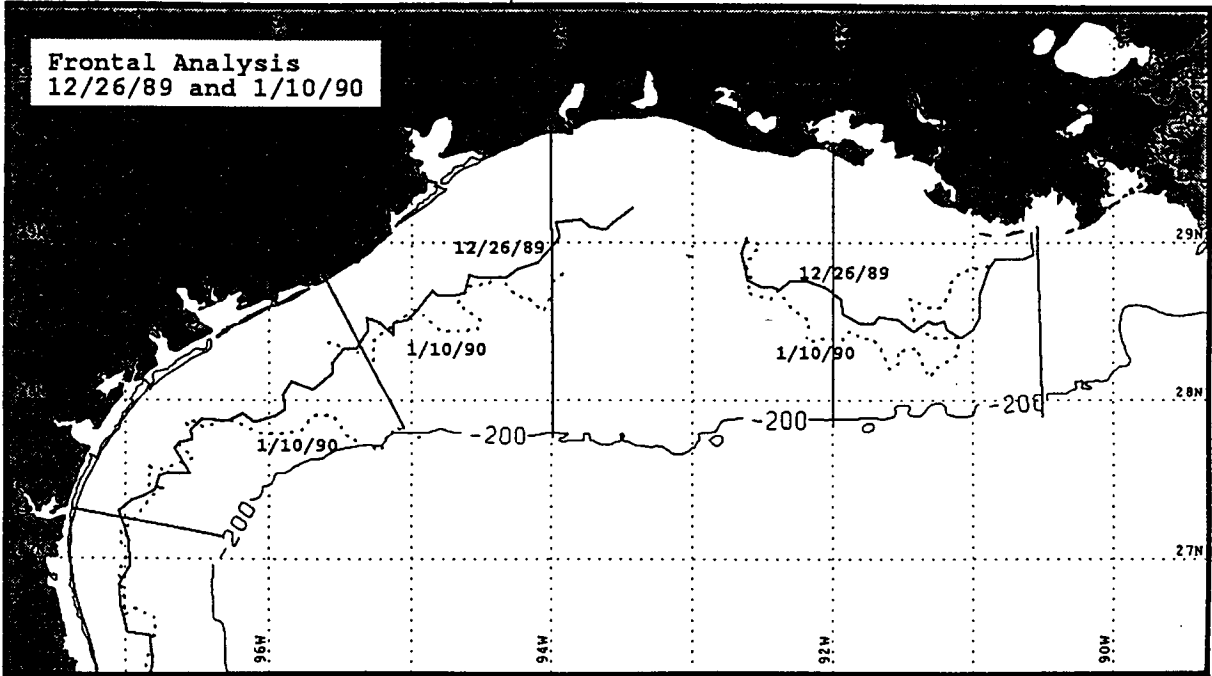
Figure 111. Schematic depicting the location of major SST fronts in December 26, 1989, and January 10, 1990, in relation to the shelf break and the LATEX A mooring lines.

Atchafalaya Bay where inner shelf waters reached 6° C. Along line A on the south Texas shelf, temperatures reached 10° C. Minimum temperatures on the outer shelf were about 20° C. Strongest fronts were observed along lines A, B and D. A series of strong fronts was observed seaward of Atchafalaya Bay where the cool plume had been forced offshore by northerly winds associated with the winter storm episodes. These fronts may be generated by seaward pulsing of the cool bay water by consecutive frontal passages. Further west, a continuous SST front was observed between lines C and A. The frontal structure in this area was not straight, but rather exhibited a wavy structure with "wavelengths" of 30-40 km. After repeated cold front passages the undulations grew in the offshore direction measuring approximately 35 km in length with wavelengths of about 50 km. A major site for offshelf movement of cool shelf water was noted between lines A and B, where long thin squirts were observed extending offshore to the 200 m isobath. This site of squirt formation corresponds with the well-known "graveyard" eddy zone in the northwest GOM. The anticyclonic motion associated with eddies in this region appear to enhance the movement of inner shelf waters previously initiated by winds associated with cold front passages.

The strongest SST fronts were observed subsequent to the most intense winter storms. Under conditions of repeated westerly or northwesterly wind forcing, the main SST fronts moved seaward. However, relaxation of the wind forcing or a wind shift to the more frequent easterly wind regime resulted in frontal retreat towards the coast.

3. Interannual Variability of Temperature Structure and Fronts

The interannual variability in temperatures and frontal structure was investigated by comparing the temperature profile data along lines A and D, which exhibited the lowest inner shelf temperatures for the 1989/90, 1992/93 and 1993/94 winters. It is apparent from this analysis that temperatures on the inner shelf were abnormally cold during the 1989/90 winter. Along line A inner shelf temperatures were 4° C to 5° C lower during 1989/90 for a distance of 30 km (Figure 112, upper panel). Along line D, shelf temperatures were several degrees colder out to 80 km (Figure 112, lower panel). The same pattern was not observed on the outer portions of the shelf where the temperatures during 1989/90 were not necessarily colder than the other years studied.

There is an indication from this analysis that the SST fronts generated along line A were stronger during 1989/90 and located further offshore than during the other years (Figure 112, upper panel). This was not, however, obviously the case along line D. In contrast to line A, which exhibited one main front, line D exhibited a series of strong multiple fronts during the "average" winter of 1993/94, as well as the cold winter of 1989/90 (Figure 112, lower panel).

4. Frontal Summary Based on 1989-90, 1992-93 and 1993-1994 Satellite Data

In order to synthesize frontal information, it was necessary to define front. For this study, a front had to meet the following criteria. First, the SST gradient in an offshore direction had to exceed 1° C/10 km. Secondly, the total temperature change across the front had to exceed 1° C. This analysis is based on extracting frontal information from the lines A-E. An attempt was made to choose satellite imagery which was clear over the entire LATEX region. If this was not possible, imagery as closely spaced in time was used. Approximately two images/ month were used in the analysis. The total images used varied from a low of 23 in 1989-90 to a high of 30 in 1992-93.

The average frontal intensity along each line for each year is shown in Table 13. This data compilation suggests that the average frontal intensity was somewhat greater on lines A,B, and D. Line C exhibited the weakest fronts. There was no indication that the average front across the shelf changed from year to year, as the averages only varied from 1.9° C and 2.0° C. Table 14 shows the maximum frontal intensities along each line for each year and their averages. The strongest SST fronts occur along lines A, B, and D, while the weakest fronts occur along Line °C. Line

Profile A

A 1/10/90   B 2/8/93   C 2/18/94

Profile D

A 12/26/89   B 1/31/93   C 1/14/94
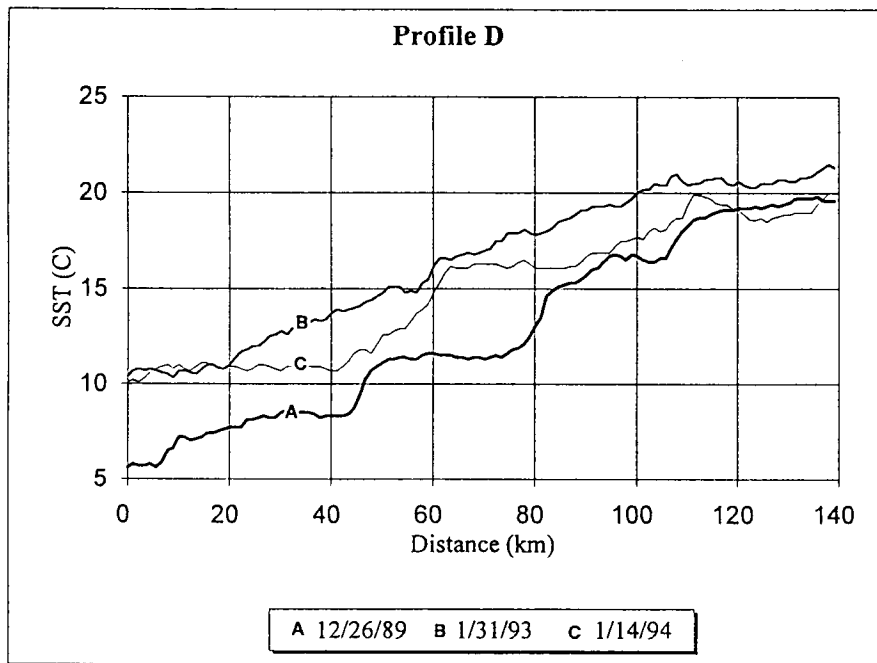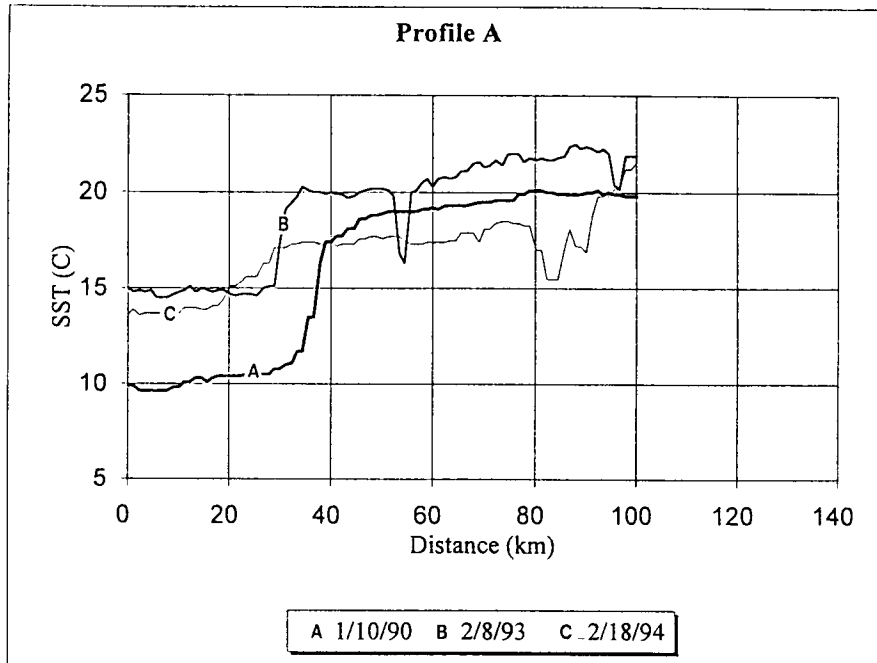
Figure 112. Surface temperatures extracted from line A (upper panel) and line D (lower panel), which exemplify the lowest temperatures on the inner shelf for each of the years 1989-90, 1992-93 and 1993-94.

139

Table 13. Average frontal intensity (°C) during 1989-90, 1992-93 and 1993-94.

Year	A	B	Average Frontal Intensity (°C) C	D	E	Mean
89-90	2.5	2.1	1.4	2.2	1.7	2.0
92-93	2.4	2.0	1.6	2.2	2.0	2.0
93-94	2.1	1.9	1.7	2.0	1.8	1.9
Mean	2.3	2.0	1.6	2.1	1.8	

Table 14. Maximum frontal intensity (°C) during 1989-90, 1992-93 and 1993-94.

Year	A	B	Maximum Frontal Intensity (°C) C	D	E	Mean
89-90	8.3	5.8	2.5	4.0	3.3	4.8
92-93	5.1	4.8	2.8	4.5	4.0	4.2
93-94	4.3	5.9	3.5	5.3	3.5	4.5
Mean	5.9	5.5	2.9	4.6	3.6	

E does not really represent the Atchafalaya or Mississippi River plumes because it lies in the zone of mixing between them. There was some indication that the maximum frontal intensity was correlated with cold-front intensity (at least in terms of air temperature) as the relatively cold 1989-90 winter exhibited the strongest fronts and the relatively warm 1992-93 winter exhibited the weakest fronts. Table 15 gives information on frontal distance from the coast. The fronts along line A were closest to the coast and exhibited the least variability in location, whereas those along line C were furthest from the coast and exhibited the most variability in location. There was no obvious relationship between severity of the winter and average frontal location across the entire LATEX shelf.

Table 15. Average frontal distance from the coast (km) during 1989-90, 1992-93 and 1993-94.

Year	A	B	Average Frontal Distance from Coast C	D	E	Mean
89-90	45	56	78	60	50	58
92-93	41	58	54	60	62	55
93-94	33	56	66	49	41	49
Mean	40	57	66	56	51	
s(X)	20	29	39	36	34	

A schematic summarizing the average position of shelf fronts along each line and position variability (one standard deviation from the mean) are depicted in Figure 113. It is interesting to note that although Line A fronts are closest to the coast, they lie in deeper water than those of Lines C, D, and E. The mean location of fronts along Line C were furthest from the coast; however, in terms of bathymetry the fronts were in the shallower water than those across the rest of the shelf. What is noteworthy is that the mean frontal position along Line B is in considerably deeper water than that of Line C, perhaps indicating a preferential site for seaward movement in this region, either caused by convergences or wind-forced flows. Indeed, the 1989-90 image data showed this region to be a preferential site of mini-squirt formation. The fronts along line A may lie closer to the coast as a result of the frequent occurrence of anticyclonic eddy activity along the seaward end of this line. Warm eddy filaments are often observed spilling onto the shelf in this region, a process that would inhibit the offshore movement of coastal waters. However, just north of line A where the depth contours curve sharply to the east, a preferential region for squirt formation has been observed. This region lies on the northern flank of the detached anticyclonic eddy zone and thus eastward currents associated with the north side of the eddy would enhance offshore movement of shelf water.

It is important to note that the standard deviations of the frontal positions are very high for all lines except line A. The frequent occurrence of multiple fronts along these lines explains a large part of this observed variability. Scattergrams of frontal locations and intensities along each line are shown in Figures 114 through 118.

5. Conclusions

The analyses of annual and interannual variability of shelf fronts and temperature structure on the LATEX shelf have demonstrated the following:

1. Shelf fronts result from differential cooling of shelf water caused by winter storms and subsequent convergence of water masses of contrasting temperature.
2. Shelf fronts exceeding 1° C are generally observed on the shelf between October and March.
3. The strongest shelf fronts occur from December through February, coinciding with the most severe winter storm events.
4. The frontal locations and intensities across the LATEX shelf are complex and change rapidly.
5. The Atchafalaya plume front responds rapidly to wind forcing. It moves seaward under conditions of westerly and northwesterly wind forcing and landward under conditions of southeasterly wind forcing.
6. The strongest SST fronts along the middle portion of the Texas shelf often exhibit a wavy character. This region, between lines A and C, has been observed to be a preferential region for offshelf flow during winter.

141
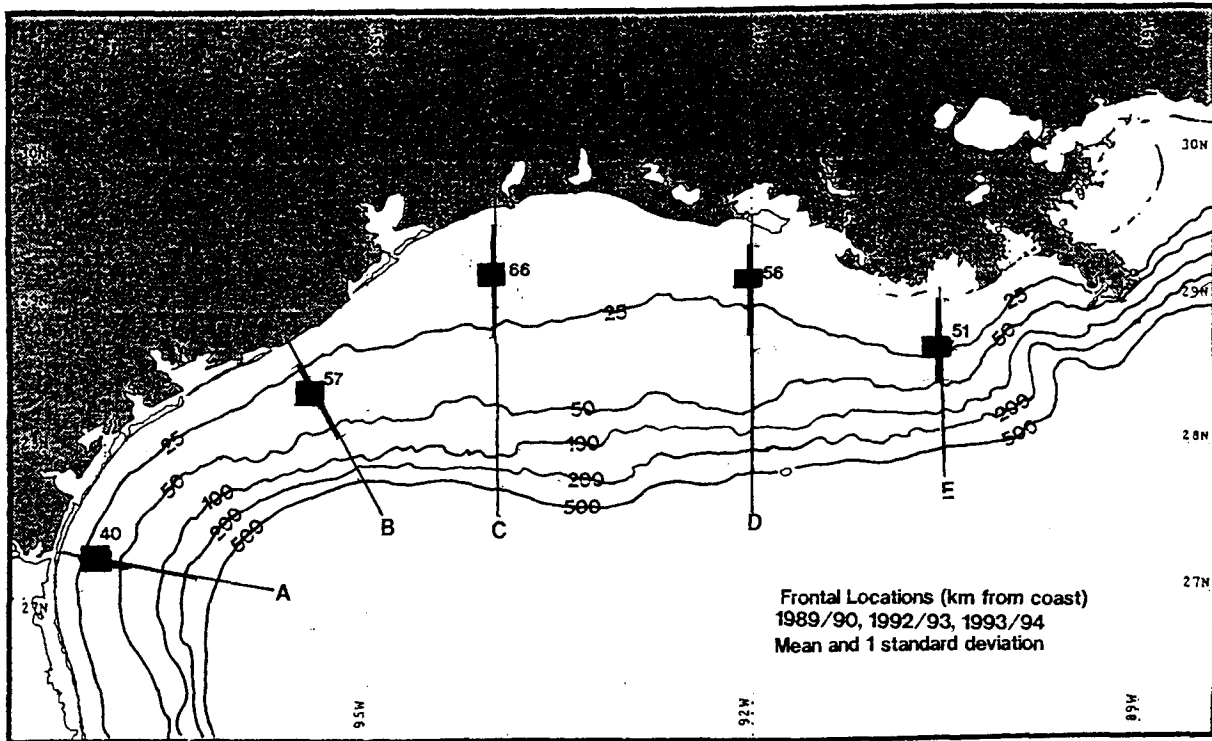
Figure 113. Summary figure depicting the average position of fronts along lines A through E as well as one standard deviation for 1989-90, 1992-93 and 1993-94.

Profile A
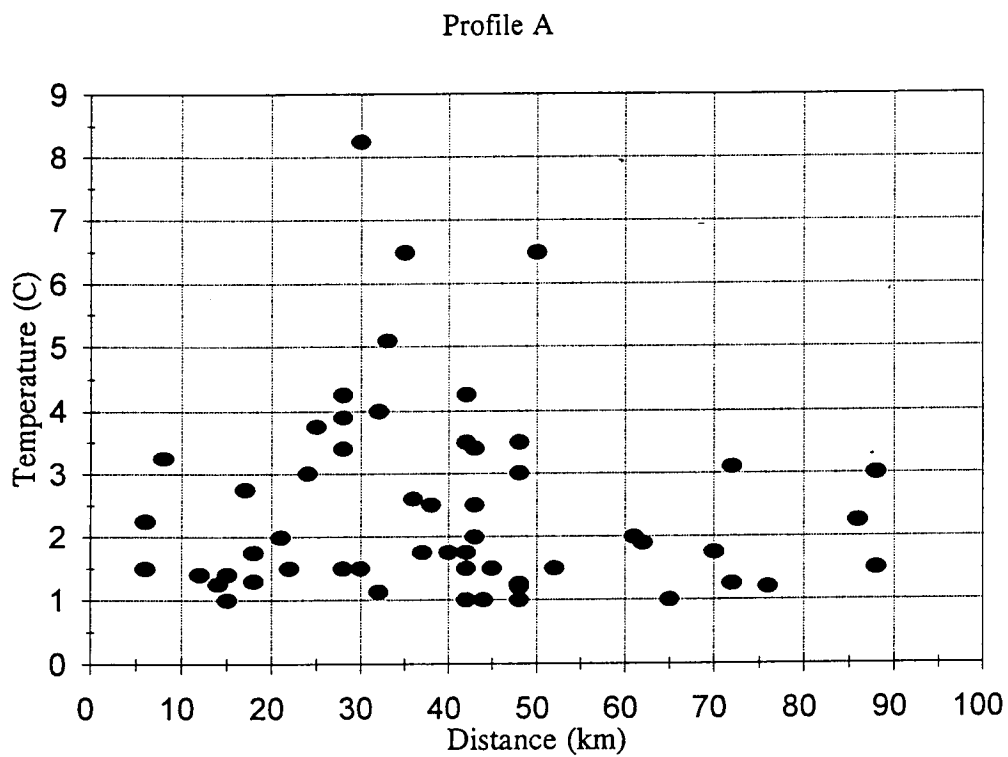
Figure 114. Scattergram showing positions of fronts and their intensities based on all data from 1989-90, 1992-93 and 1993-94 for line A.

143

Profile B
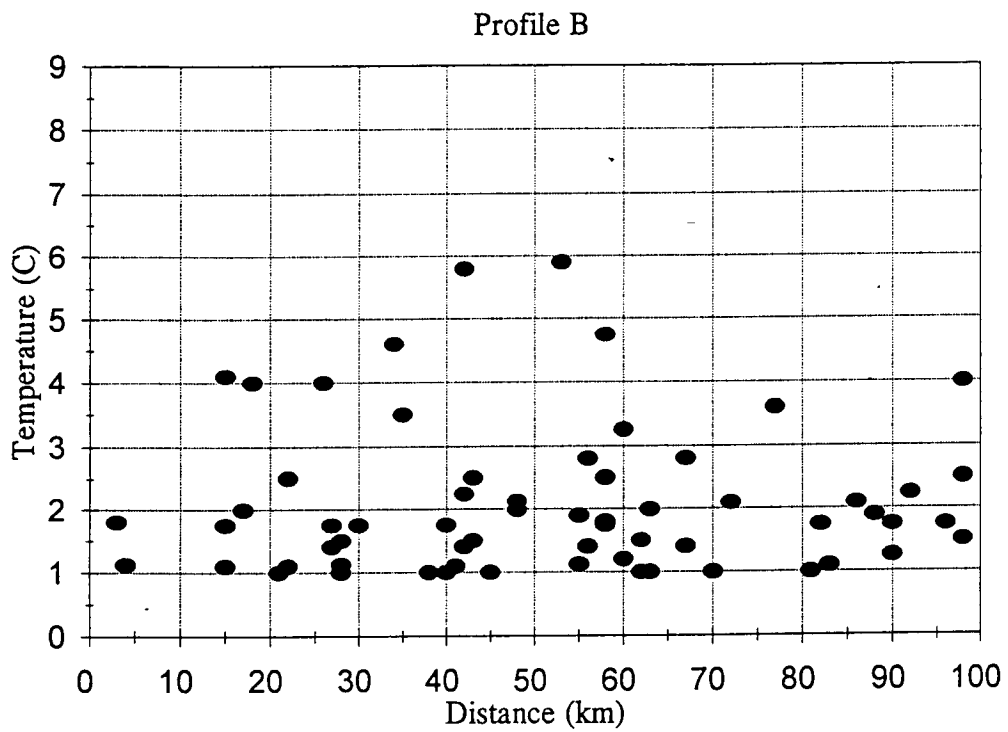
Figure 115. Scattergram showing positions of fronts and their intensities based on
all data from 1989-90, 1992-93 and 1993-94 for line B.
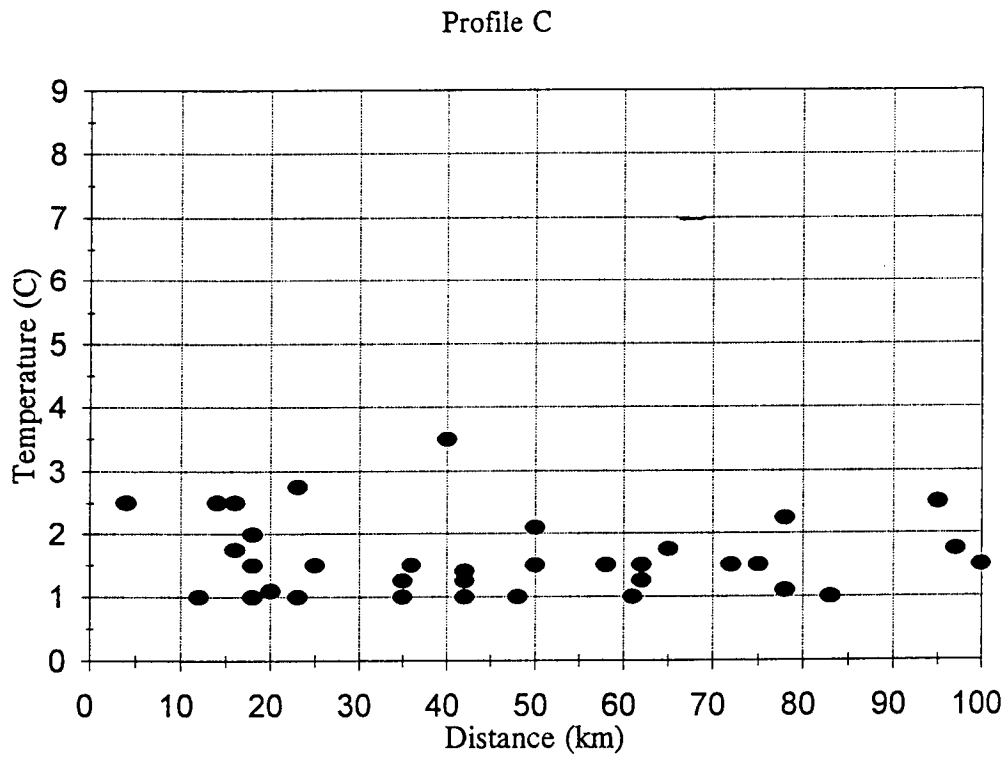
Profile C

Figure 116. Scattergram showing positions of fronts and their intensities based on all data from 1989-90, 1992-93 and 1993-94 for line C.

145

Profile D
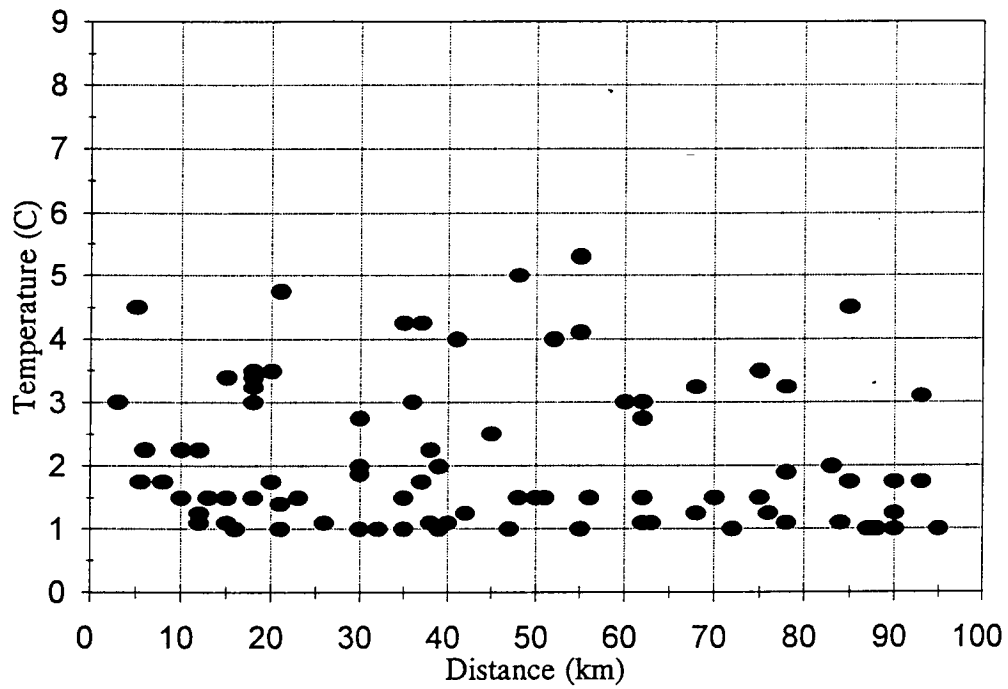
Figure 117. Scattergram showing positions of fronts and their intensities based on all data from 1989-90, 1992-93 and 1993-94 for line D.

Profile E
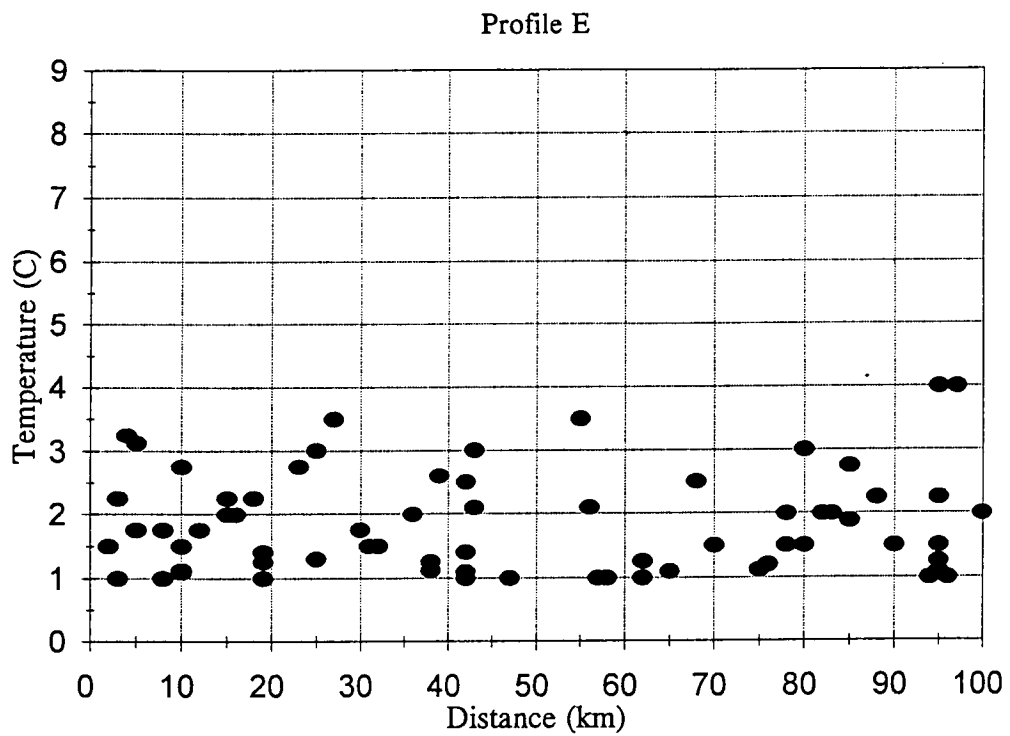
Figure 118. Scattergram showing positions of fronts and their intensities based on
all data from 1989-90, 1992-93 and 1993-94 for line E.

147

VII. HIGHER RESOLUTION SURVEY OF THE GALVESTON PLUME AREA AND ADJACENT AREA OF CONVERGENCE

Curtis C. Ebbesmeyer, Eddie Weeks, Walter Johnson, Peter Niiler

A. Objective

Plumes exiting the bays, estuaries, and rivers along the coast contribute significant quantities of sediments, organic material, and chemicals to the coastal plume of the Louisiana-Texas shelf. To investigate these plumes, surveys of the position and characteristics of several plumes were planned as a part of the LATEX B program. The Calcasieu Plume was the first of these to be surveyed and has been reported in the first annual report (Cox and Ebbesmeyer in Murray, 1994). The second to be sampled was that in the approached to the Galveston ship channel.

Because the Convergence Survey was conducted close to the Plume Survey, and because water exiting Galveston Bay appears to feed the convergence zone, analysis of the two surveys has been combined.

B. Parameters Measured

The object of the Plume and Convergence Surveys was to characterize the plume by sampling the plume's water structure, sediments, biology, and circulation.

To monitor the plume, four approximately north-south transects were conducted off the mouth of the Galveston ship channel during approximately twenty hours on July 19 and 20, 1993. Immediately after completing the transects the Convergence Survey was completed with a sawtooth pattern spaced between Sections S5 and S6 during approximately 17 hours on July 20-21, 1993. The combined Plume and Convergence Surveys lasted approximately 37 hours on July 19-21. Because of their proximity in time and space, presentations of data for the Plume and Convergence surveys are combined in this report.

While underway, surface water temperature, conductivity, light transmission, and chlorofluorescence were sampled with LUMCON's Multi-Interface Data Acquisition System (MIDAS), while currents were measured with the 1200 kHz ADCP. Salinity and density (sigma-theta) were calculated from the temperature and conductivity data.

For additional description of the flow field, drifter trajectories were superposed on maps of the water properties.

C. Plume Survey Results

1. Water Properties

The near-surface characteristics of the Galveston plume may be distinguished using temperature, salinity, and ADCP velocities. Plan view contours of the MIDAS data are presented in Figure 119 and 120; ADCP vectors at the shallowest depth sampled by the ADCP (4.5 meter depth), superimposed with pre-SCULP trajectories, are presented in Figure 121.

Effluent from the Galveston Ship Channel was distinguished by temperatures warmer than approximately 30.8° C and salinities between 28-29 psu. Using these contours to define the plume, the MIDAS temperatures indicate that the plume can be traced approximately 20 kilometers to the east of the Ship Channel's mouth.

149
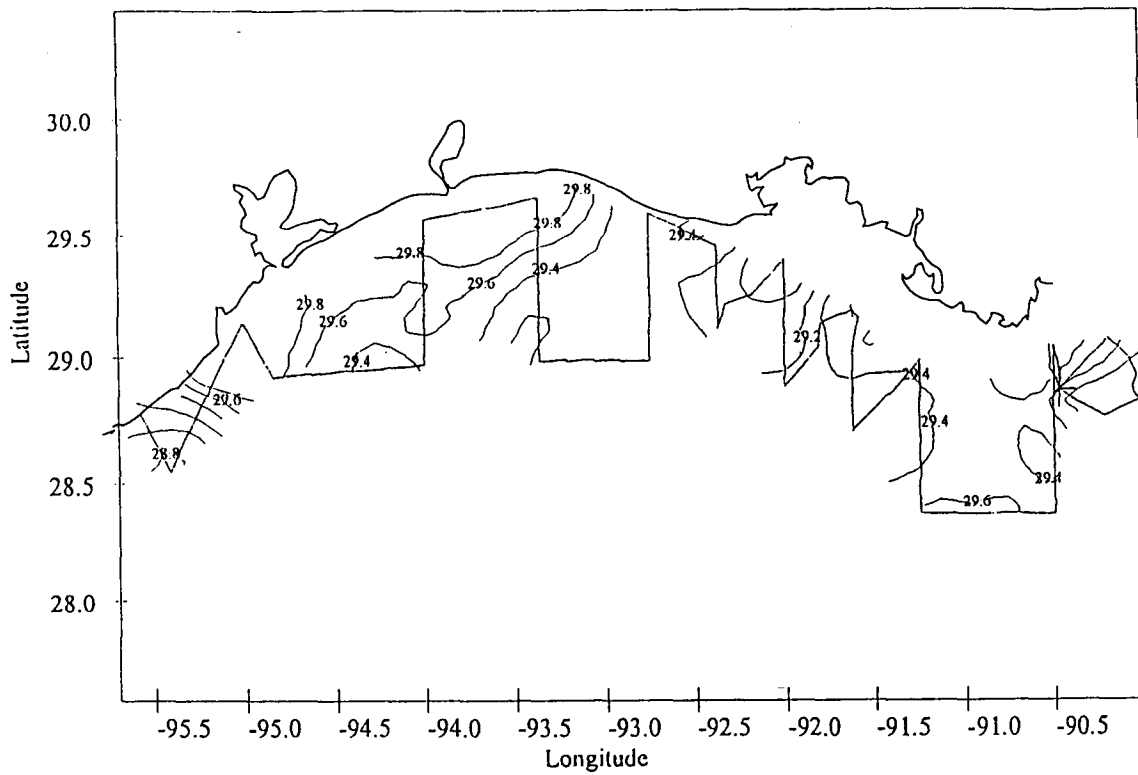
Figure 119. Plume and convergence surveys: map of sea surface temperature from MIDAS, Cruise IV.
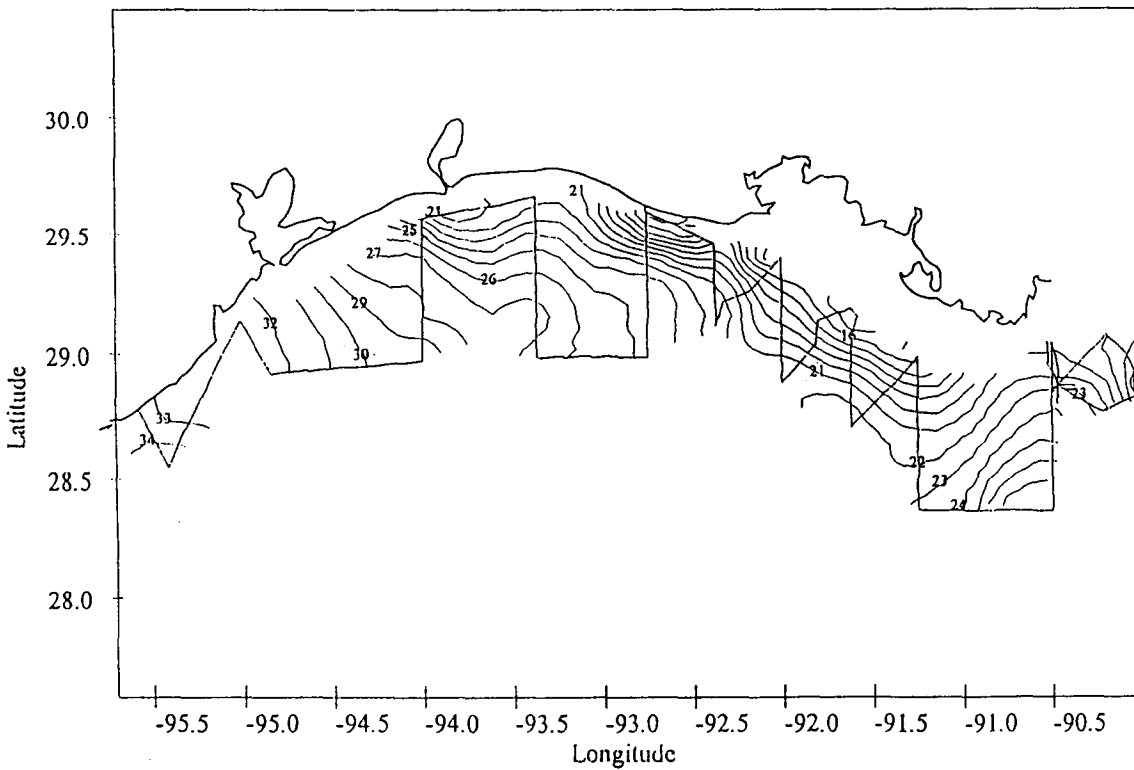
Figure 120. Plume and convergence surveys: map of sea surface salinity from MIDAS, Cruise IV.

150

29.6

29.2

28.8

211

210

206

208

204

200

199

197

198

202

203

204

205

206

196

197

199

200

195

197

195

□·······□ Buoy 20017
○————○ Buoy 20021

Scale = 20 cm/s   ○→→

P93-2, ADCP, 4.5 meters, 2 km, (W = 00.4632   Amp= 1.0229), Iterative Method

-94.6   -94.2   -93.8   -93.4

Longitude

Latitude

151
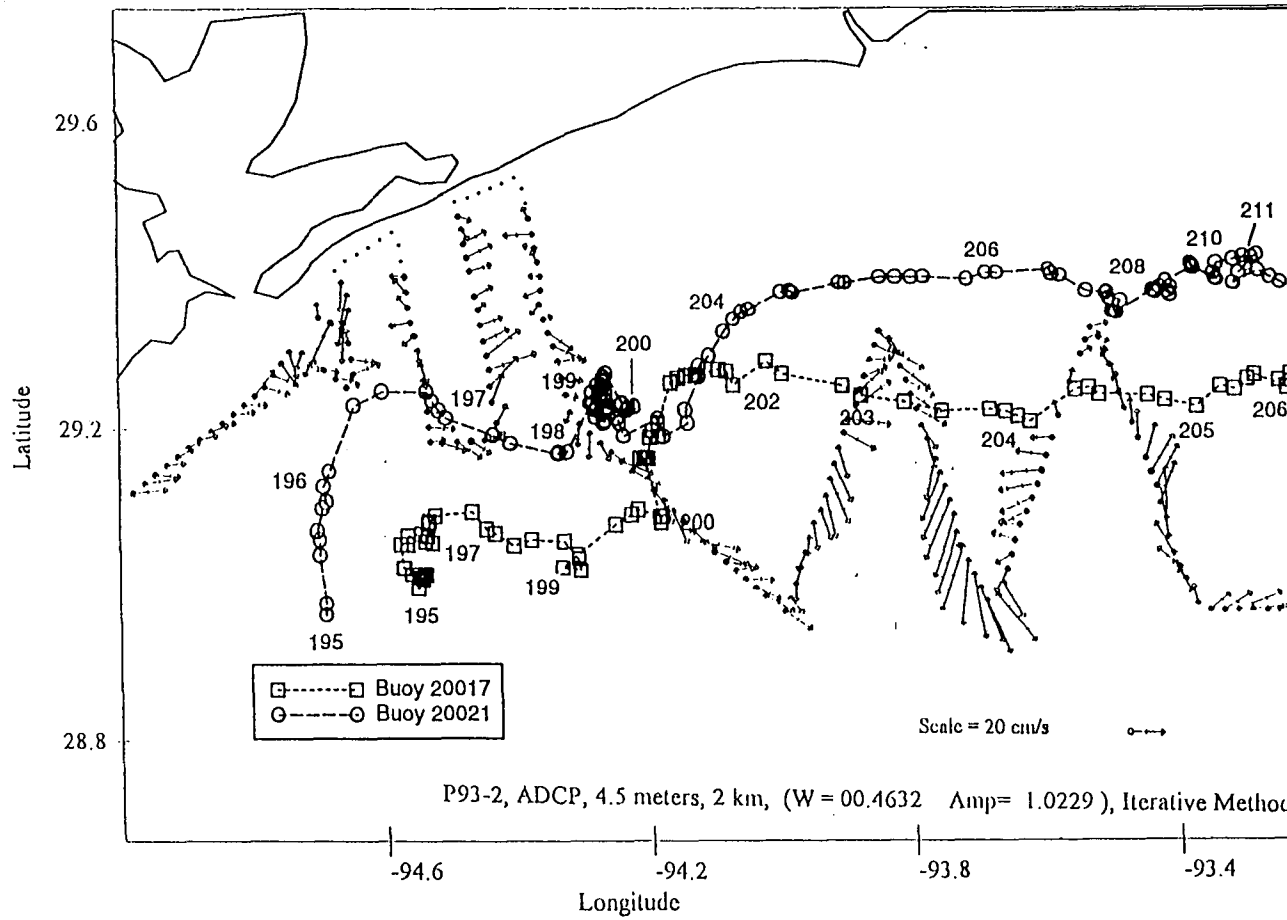
Figure 121. Plume and convergence surveys: ADCP current vectors at 4.5 meter depth and pre-SCULP trajectories, Cruise IV.

The salinity field indicates that the Galveston plume is sandwiched between two other water masses, one to the north and the other to the south. To the south, much saltier water is being advected northeastward along the coast under the prevailing southerly winds. To the north the salinities less than 29 psu indicate a plume of water from another coastal source of freshwater.

2. Circulation

Various aspects of the flow field were resolved by the water properties, ADCP, and pre-SCULP drifters. The near-surface fields of temperature and salinity suggest that Galveston Plume water flowed offshore in an "S" pattern into the area sampled in the Convergence Survey. South of the plume, the ADCP vectors at 4.5 meters depth showed the northward flowing, saline water. Two pre-SCULP buoys (Nos. 20017 and 20021) were transported from the south, skirted the plume, and entered the convergence area.

In the convergence area the ADCP vectors indicate regions of offshore flow. However, the two pre-SCULP buoys appear to have passed north of this offshore flow and continued drifting to the east of the convergence area.

3. Phytoplankton Pigments and Associated Environmental Variables *(Nancy N. Rabalais)*

During Cruise IV, Stations 401 through 423 were occupied to document the biological characteristics of the Galveston plume and their associated water quality parameters. Surface water temperature was uniformly high across the area with a slight cooling towards the seaward edge of the plume study area (2° C) (data not shown). Salinities ranged from 24-31.5 ppt and were lower in the northeast quadrant of the study area and were higher to the southwest. Light transmission paralleled the salinity distributions, with the most turbid waters being associated with the lower salinities in the northeast quadrant of the study area. Scaled in vivo fluorescence from the MIDAS flowthrough system differed from the salinity/turbidity trends. The highest fluorescence was located centrally in the station grid, was fairly high in the northwest quadrant and decreased seaward in all directions (data not shown). For discrete water samples, the lowest chlorophyll a biomass was associated with the highest salinity (Figure 122), and higher chlorophyll a with the intermediate salinities. A similar relationship was observed with the MIDAS data in that the high peaks of scaled in vivo fluorometer voltage were associated with the lower salinities (Figure 122).

4. Zooplankton Characteristics *(Richard F. Shaw)*

Dry weight density for the 153-μm samples showed no trend associated with Galveston Bay's plume, which ranged from 17.89-143.35 mg/m³. The 335-μm biomass estimates were higher outside of the plume's influence, ranging from 6.60-63.56 mg/m³. Larval fish density increased as the distance from the bay increased and ranged from 0-7.37 larvae/m³.

D. Convergence Survey Results

1. Water Properties

The temperature and salinity contours of the Plume Survey appear to blend with those the Convergence Survey. As the saltier waters from the south collided with the fresher waters to the north, Galveston Plume water stained the union. Near the shore the two water masses met during Cruise IV near the mouth of the Galveston Ship Channel. The shapes of the salinity contours and the pre-SCULP drifter trajectories indicate that water in plumes from farther north continues to hug the coast under the influence of the earth's rotation (Coriolis acceleration). The saline water from
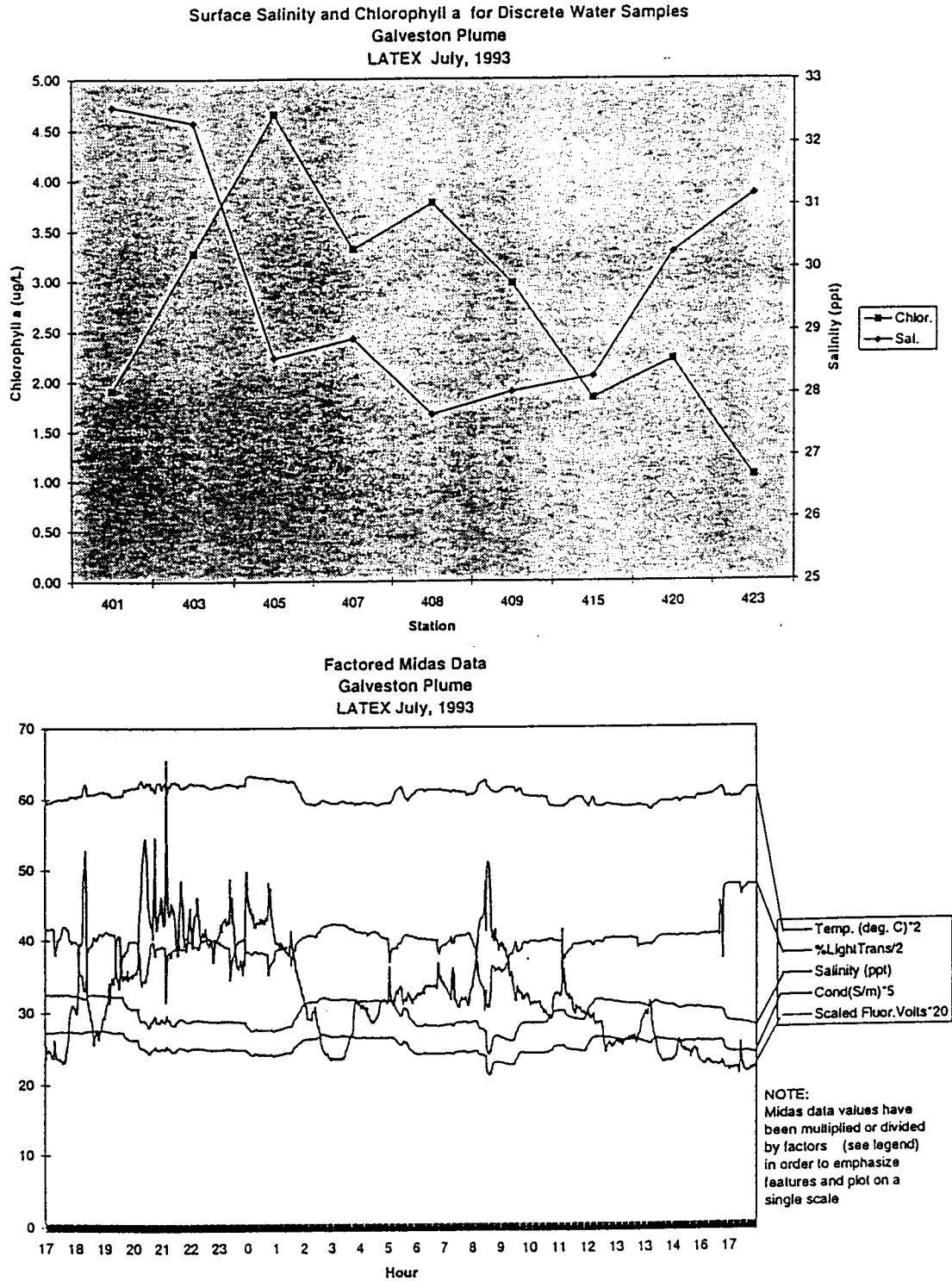
Figure 122. Comparison of chlorophyll *a* biomass to salinity for discrete water samples (upper panel) and of MIDAS scaled in vivo fluorescence and salinity (lower panel) for the Galveston plume survey.

153

the south, also under the effect of Coriolis acceleration, turns to the south, riding around the coastal plume water. Galveston plume water "stains" the junction of the two water masses.

The Galveston plume water appears to snake its way into the convergence area between Sections S5 and S6. This may be seen by following the band of water between salinities of 28-29 psu in Figure 123, and by water having temperatures exceeding 30.6° C.

2. Circulation

Both the ADCP vectors suggest the transport of Galveston Plume water into the convergence zone between Sections S5 and S6. The ADCP vectors (Figure 3) indicate a squirt-like region approximately 20 km wide between approximately 93.7° and 93.9° W. To the west of the offshore low, the saline waters from the south are carried offshore, and to the east, less saline coastal waters are also carried offshore. Therefore, the convergence area is a zone of offshore transport of three water types: saline water from the south, Galveston Plume water, and coastal brackish water from the coast.

As pre-SCULP buoy 20021 drifted northward, it intersected the Galveston plume on July 20. Upon meeting the plume, the buoy turned eastward, tracing with its trajectory the southern outline of the plume. Assuming that the buoys continue tracing the southern edge, it appears that the Galveston Bay water was advected to the east, north of the region of the convergence survey. This implies that the Galveston water lay north of the SCULP trajectory and offshore of the plume nearest the shore. It does not appear that the Galveston Bay water was ejected farther offshore in the squirt-like feature seen in the ADCP data.

3. Phytoplankton Pigments and Associated Environmental Variables *(Nancy N. Rabalais)*

Surface water temperature was uniformly high across the area with a slight cooling towards the eastern side of the study area (not diel related) (data not shown). Salinities and percent light transmission were also fairly uniform across the study area. The lowest percent light transmission was found in the northwest quadrant and associated with the highest in vivo scaled fluorometer voltage. This indicates that the turbidity was phytoplankton biomass. Similar lows in percent light transmission on the continuous MIDAS data were associated with peaks of in vivo scaled fluorometer voltage (Figure 123). There was no clear relationship between salinity and measured chlorophyll a biomass or in vivo scaled fluorometer voltage (Figure 123).

4. Zooplankton Characteristics *(Richard F. Shaw)*

For the 153- and 335-μm biomass estimates, no trend was associated with the convergence zone; however, higher densities were noted on the shoreward side of both water masses. Dry weight densities ranged from 30.33-171.45 mg/m^3 for the 153-μm fractions and from 8.62-88.21 mg/m^3 for the 335-μm fractions. Larval fish density was higher on the Louisiana side of the convergence. This contrasts the overall picture of ichthyoplankton densities, where the highest densities were found along the Texas shelf. Larval fish densities ranged from 0.57-6.73 larvae/m^3.
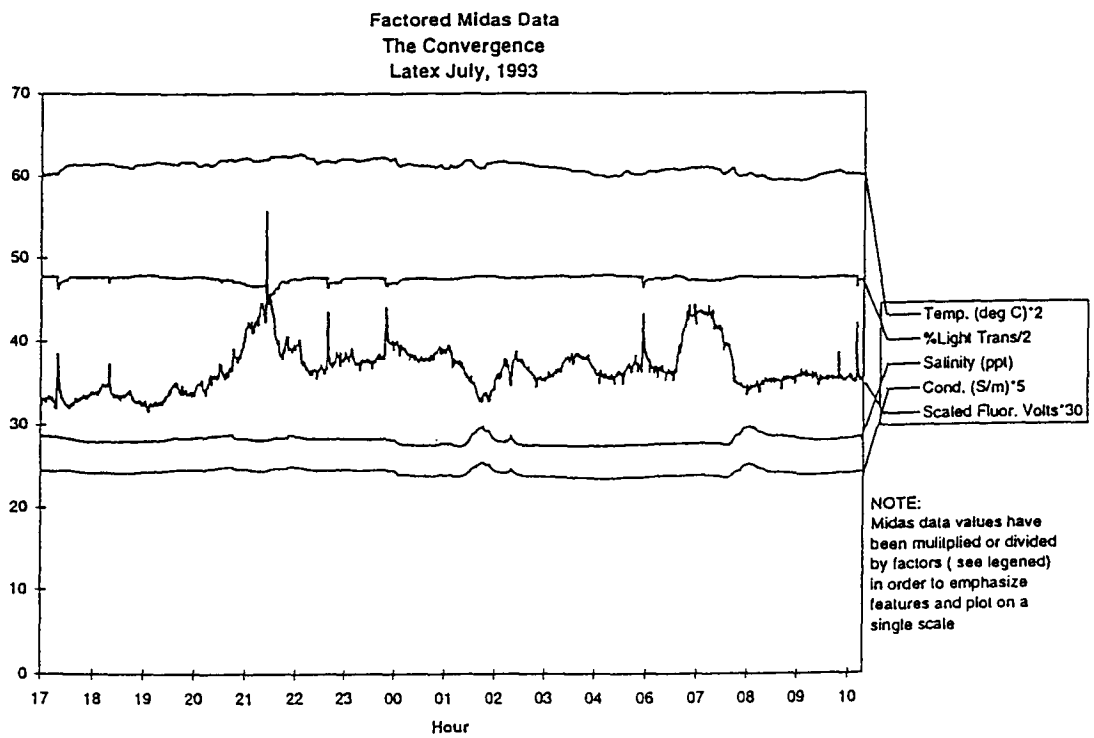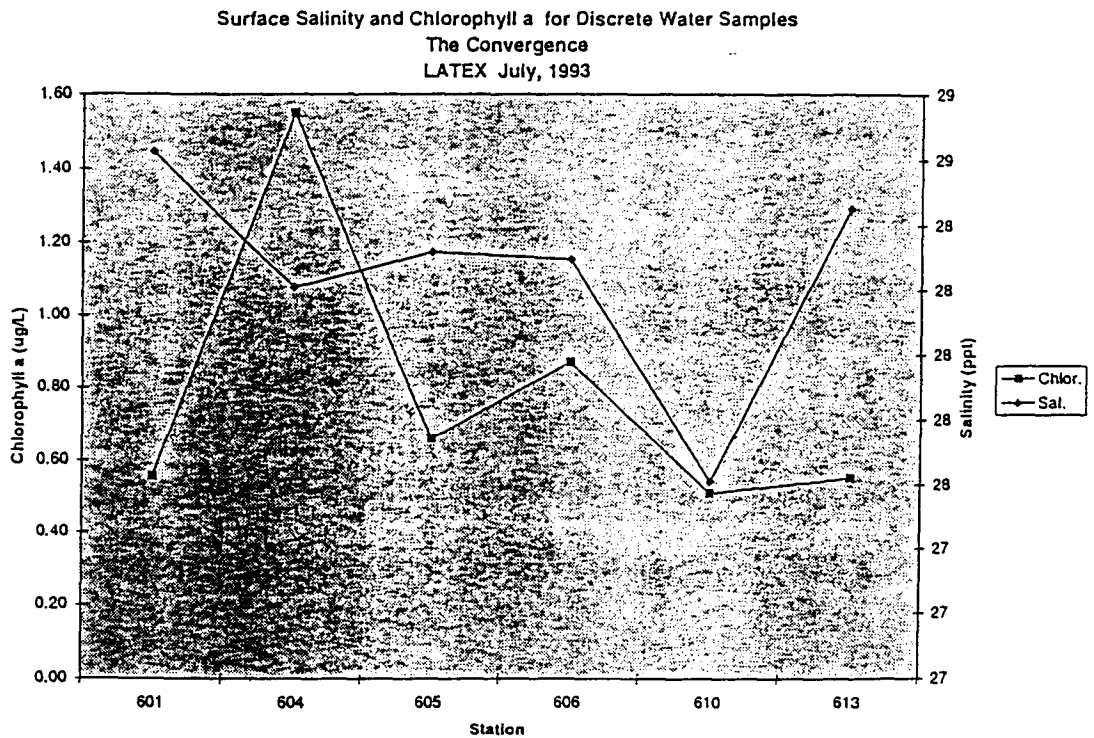
Figure 123. Comparison of chlorophyll *a* biomass to salinity for discrete water samples (upper panel) and of MIDAS scaled *in vivo* fluorescence and salinty (lower panel) for the convergence survey.

155

VIII. LITERATURE CITED

Butler, J.L. 1992. Collection and preservation of material for otolith analysis. pp. 13-17. In: Stevenson, D.K. and S.E. Campana (eds.). Otolith Microstructure Examination and Analysis. Can. Spec. Publ. Fish. Aquat. Sci. 117.

Cox, J. and C. Ebbesmeyer. 1994. MIDAS survey of the Calcasieu River plume. In: Murray, S.P. (ed.). Mississippi River plume hydrography: annual report. OCS Study MMS 94-0028. U.S. Dept. of the Interior, Minerals Mgmt. Service, Gulf of Mexico OCS Region, New Orleans, LA, pp. 211-219.

Crepon, M. and C. Richez. 1982. Transient upwelling generated by two-dimensional atmospheric forcing and variability in the coastline. JPO, 12, pp. 1437-1457.

Csanady, G.T. 1971. On the equilibrium shape of the thermocline in the shore zone. JPO, 1, pp. 263-270.

Csanady, G.T. 1974. Spring thermocline behavior in Lake Ontario during IFYGL, JPO, 4, pp. 425-445.

Csanady, G.T. 1977. The coastal jet conceptual model in the dynamics of shallow seas. In: Goldberg, E.D., I.N. McCave, J.J. O'Brien, and J.H. Steele (eds.). The Sea, 6, John Wiley, NY, pp. 117-144.

Dortch, Q. 1994a. Phytoplankton Survey. In: Murray, S.P. (ed.). Mississippi River plume hydrography: annual report. OCS Study MMS 94-0028. U.S. Dept. of the Interior, Minerals Mgmt. Service, Gulf of Mexico OCS Region, New Orleans, LA, pp. 124-142.

Dortch, Q. 1994b. Changes in phytoplankton numbers and species composition. In: Coastal oceanographic effects of 1993 Mississippi River flooding. Special NOAA Report. NOAA Coastal Ocean Office/National Weather Service, Silver Spring, MD, pp. 46-49.

Dortch, Q., R. Robichaux, S. Pool, D. Milstead, G. Mire, N.N. Rabalais, T. M. Soniat, G.A. Fryxell, R.E. Turner, and M.L. Parsons. Submitted. Abundance and vertical flux of *Pseudo-nitzschia* in the northern Gulf of Mexico. Marine Ecology Progress Series.

Fryxell, G.Q., M.E. Reap, and D.L. Valencic. 1990. *Nitzschia pungens* Grunow f. multiseries Hasle: observations of a known neurotoxic diatom. Beiheft zur Nova Hedwigia 100:171-188.

Hallegraeff, G.M. 1993. A review of harmful algal blooms and their apparent global increase. Phycologia 32:79-99.

Huh, O.K., L.J. Rouse, Jr., and N.D. Walker. 1984. Cold air outbreaks over the northwest Florida continental shelf: heat flux processes and hydrographic changes. J. of Geophysical Res. 89(C1):717-726.

Kidwell, K.B. 1991. NOAA polar orbiter data users guide. U.S. Dept. of Commerce, Satellite Data Service Division.

157

Laurence, G.C. 1976. Caloric value of some north Atlantic calanoid copepods. Fish. Bull. 74:218-220.

Lovegrove, T. 1966. The determination of the dry weight of plankton and the effect of various factors on the values obtained. pp. 429-467. In: Barnes, H. (ed.). Some Contemporary Studies in Marine Science. George Allen and Unwin Ltd., London.

McClain, E.P., W.G. Pichel, and C.C. Richardson. 1985. Comparative performance of AVHRR-based multichannel sea surface temperatures. J. Geophys. Res. 90:11,587-11,601.

McEwen, G.F., M.W. Johnson, and T.R. Folsom. 1954. A statistical analysis of the performance of the Folsom plankton sample splitter, based upon test observations. Arch. Met. Geophys. Bioklim, Series A. 7:502-527.

Meade, R.H. and R.S. Parker. 1985. Sediment in rivers of the United States. National Water Supply-Summary 1984. U.S. Geological Survey Water-Supply Paper No. 2275, U.S. Dept. of the Interior, Geological Survey, Washington, DC.

Methot, Jr., R.D. and D. Kramer. 1979. Growth of northern anchovy, *Engraulis mordax*, larvae in the sea. Fish. Bull. 77(2):413-423.

Murphy, L.S. and E.M. Haugen. 1985. The distribution and abundance of phototrophic ultraplankton in the North Atlantic. Limnol. Oceanogr. 30:47-58.

Murray, S.P. 1994. Mississippi River plume hydrography: annual report. OCS Study MMS 94-0028. U.S. Dept. of the Interior, Minerals Mgmt. Service, Gulf of Mexico OCS Region, New Orleans, LA, 229 pp.

NOAA. 1993. Climate Diagnostics Bulletins. U.S. Department of Commerce, National Weather Service, National Meteorological Center.

Olson, R.J., S.W. Chisholm, E.R. Zettler, and E.V. Armbrust. 1988. Analysis of *Synechococcus* pigment types in the sea using single and dual beam flow cytometry. Deep-Sea Res. 35:425-440.

Parsons, T.R., Y. Maita, and M. Lalli. 1984. A manual of chemical and biological methods for seawater analysis. Pergamon Press, NY, 173 pp.

Pettigrew, N.R. 1981. The dynamics and kinematics of the coastal boundary layer off Long Island. Ph.D. Dissertation, WHOI/MIT, 262 pp.

Pettigrew, N.R. and S.P. Murray. 1986. The coastal boundary layer and inner shelf. In: Mooers, C.N.K. (ed.). Baroclinic processes on continental shelves. Coastal and Estuarine Sciences, 3, AGU, pp. 95-108.

Pick, F.R. 1991. The abundance and composition of freshwater picocyanobacteria in relation to light penetration. Limnol. Oceanogr. 36:14570-1462.

Rabalais, N.N. 1994. Phytoplankton Pigments. In: Murray, S.P. (ed.). Mississippi River plume hydrography: annual report. OCS Study MMS 94-0028. U.S. Dept. of the Interior, Minerals Mgmt. Service, Gulf of Mexico OCS Region, New Orleans, LA, pp. 124-142.

158

Rabalais, N.N., R.E. Turner, W.J. Wiseman, Jr., and D.F. Boesch. 1991. A brief summary of hypoxia on the northern Gulf of Mexico continental shelf: 1985-1988. In Tyson, R.V. and T.H. Pearson (eds.). Modern and ancient continental shelf anoxia. Geological Society Special Publication No. 58, The Geological Society, London, pp. 35-47.

Rabalais, N.N., R.E. Turner, and W.J. Wiseman, Jr. 1992. Distribution and characteristics of hypoxia on the Louisiana shelf in 1990 and 1991. In: Nutrient enhanced coastal ocean productivity. Publ. No. TAMU-SG-92-109, Texas Sea Grant College Program, Galveston, TX, pp. 62-67.

Rabalais, N.N., R.E. Turner, and W.J. Wiseman, Jr. 1994. Hypoxic conditions in bottom waters on the Louisiana-Texas shelf. In: Coastal oceanographic effects of 1993 Mississippi River flooding. Special NOAA Report. NOAA Coastal Ocean Office/National Weather Service, Silver Spring, MD, pp. 50-54.

Renaud, M.L. 1986. Hypoxia in Louisiana coastal waters during 1983: implications for fisheries. Fish. Bull. 84(1):19-26.

Robichaux, R.J. and Q. Dortch. Submitted. Occurrence of *Gymnodinium sanguineum* in Louisiana and Texas coastal waters, 1989-1994. Contr. Mar. Sci.

SAS Institute Inc. 1985. SAS user's guide: basics, version 5. Cary, NC. 1,290 pp.

Shapiro, L.P. and E.M. Haugen. 1988. Seasonal distribution and temperature tolerance of *Synechococcus* in Boothbay Harbor, ME. Est. Coast. Shelf Sci. 26: 517-526.

Shapiro, L.P., E.M. Haugen, and E.J. Carpenter. 1989. Occurrence and abundance of green fluorescing dinoflagellates in surface waters of the Northwest Atlantic and Northeast Pacific Oceans. J. Phycol. 25:189-191.

Stumpf, R.P. 1988. Remote sensing of suspended sediments in estuaries using atmospheric and compsitional corrections to AVHRR data. In: Proceedings of the 21st Intl. Symp. on Remote Sensing of Environment. Ann Arbor, MI, pp. 205-222.

Stumpf, R.P. 1992. Remote sensing of water clarity and suspended in coastal waters. In: Proceedings of the First Thermatic Conference on Remote Sensing for Marine and Coastal Environments. 13 pp.

Siegel, S. and N.J. Castellan, Jr. 1988. Nonparametric statistics for the behavioral sciences, 2nd edition. McGraw-Hill, Inc., NY, 399 pp.

Smith, N.P. 1980. On the hydrography of shelf waters off the central Texas Gulf Coast. J. Physical Oceanogr. 10:806-813.

Smith, R.A., R.B. Alexander, and M.G. Wolman. 1987. Water-quality trends in the nation's rivers. Science 235:1607-1615.

Taylor, F.J.R. 1976. Appendix: Treatment of micro- and nanoplankton samples. In: Steedman, H.F. (ed.). Zooplankton fixation and preservation. Unesco Press, Paris, pp. 32-33.

Tranter, D.J. and P.E. Smith. 1968. Filtration performance. In: Zooplankton Sampling. Unesco Press, Paris, pp. 27-56.

Turner, R.E., R. Kaswadji, N.N. Rabalais, and D.F. Boesch. 1987. Long-term changes in the Mississippi River water quality and its relationship to hypoxic continental shelf waters. In: Estuarine and coastal management—tools of the trade. In: Proceedings, Tenth National Conference, The Coastal Society, October 12-15, 1986, New Orleans, LA, pp. 261-266.

Vaulot, D. and X. Ning. 1988. Abundance and cellular characteristics of marine *Synechococcus* spp. in the dilution zone of the Changjiang (Yangtze) River, China. Cont. Shelf Res. 8:1171-1186.

Walker, N.D. and L.J. Rouse, Jr. 1993. Satellite assessment of Mississippi River discharge plume variability. OCS Study MMS 93-0044. U.S. Dept. of the Interior, Minerals Mgmt. Service, Gulf of Mexico OCS Region, New Orleans, LA, 50 pp.

Walker, N.D., O.K. Huh, and L. J. Rouse, Jr. 1993. Warm-core eddy discovered in the Gulf of Mexico. EOS, Transactions, American Geophysical Union, 74(30):337-338.

Walker, N.D., L.J. Rouse, Jr., and O. K. Huh. 1994. Remote sensing and imaging. In: Murray, S. P. (ed.). Mississippi River plume hydrography: annual report. OCS Study MMS 94-0028. U.S. Dept. of the Interior, Minerals Mgmt. Service, Gulf of Mexico OCS Region, New Orleans, LA, pp. 191-209.

Walker, N.D., O.K. Huh, L.J. Rouse, and S.P. Murray. In press. Evolution and structure of a coastal squirt off the Mississippi River delta: northern Gulf of Mexico. J. Geophys. Res.

Waterbury, J.B.S., S.W. Watson, F.W. Valois, and D.G. Franks. 1986. Biological and ecological characterization of the marine unicullular cyanobacterium *Synechococcus*. In: Platt, T. and W.K.W. Li (eds.). Photosynthetic picoplankton. Can. Bull. Fish. Aquat. Sci. 214, pp. 71-120.

Wood, A.M., P.K. Horan, K. Muirhead, D.A. Phinney, C.M. Yentsch, and J.B. Waterbury. 1985. Discrimination between types of pigments in marine *Synechococcus* spp. by scanning spectroscropy, epifluorescence microscopy, and flow cytometry. Limnol. Oceanogr. 30:1303-1316.

Yentsch, C.S. and J.F. Hebard. 1957. A gauge for determining plankton volume by the mercury immersion method. J. Conseil. 22(2):184-190.

160

The Department of the Interior Mission

As the Nation's principal conservation agency, the Department of the Interior has responsibility for most of our nationally owned public lands and natural resources. This includes fostering sound use of our land and water resources; protecting our fish, wildlife, and biological diversity; preserving the environmental and cultural values of our national parks and historical places; and providing for the enjoyment of life through outdoor recreation. The Department assesses our energy and mineral resources and works to ensure that their development is in the best interests of all our people by encouraging stewardship and citizen participation in their care. The Department also has a major responsibility for American Indian reservation communities and for people who live in island territories under U.S. administration.

The Minerals Management Service Mission

As a bureau of the Department of the Interior, the Minerals Management Service's (MMS) primary responsibilities are to manage the mineral resources located on the Nation's Outer Continental Shelf (OCS), collect revenue from the Federal OCS and onshore Federal and Indian lands, and distribute those revenues.

Moreover, in working to meet its responsibilities, the **Offshore Minerals Management Program** administers the OCS competitive leasing program and oversees the safe and environmentally sound exploration and production of our Nation's offshore natural gas, oil and other mineral resources. The MMS **Royalty Management Program** meets its responsibilities by ensuring the efficient, timely and accurate collection and disbursement of revenue from mineral leasing and production due to Indian tribes and allottees, States and the U.S. Treasury.

The MMS strives to fulfill its responsibilities through the general guiding principles of: (1) being responsive to the public's concerns and interests by maintaining a dialogue with all potentially affected parties and (2) carrying out its programs with an emphasis on working to enhance the quality of life for all Americans by lending MMS assistance and expertise to economic development and environmental protection.